Linear optical properties of III-nitride semiconductors between 3 and 30 eV

vorgelegt von
Diplom-Physiker

Christoph Cobet

Berlin

Fakultät II – Mathematik und Naturwissenschaften

der Technischen Universität Berlin

zur Erlangung des akademischen Grades
Doktor der Naturwissenschaften
Dr. rer. nat.

genehmigte Dissertation

Promotionsausschuss:

Vorsitzender:	Prof. Dr. A. Hese
Berichter/Gutachter:	Prof. Dr. M. Dähne
Berichter/Gutachter:	Priv. Doz. Dr. N. Esser
Berichter/Gutachter:	Prof. Dr. W. Richter

Tag der wissenschaftlichen Aussprache: 25.10.2005

Berlin 2005

D 83

Parts of this work have already been published:

R. Goldhahn, A. T. Winzer, V. Cimalla, O. Ambacher, C. Cobet, W. Richter, N. Esser, J. Furthmüller, F. Bechstedt, H. Lu, and W. J. Schaff, *Anisotropy of the dielectric function for wurtzite InN, Superlattices and Microstructures*, **36**, 591 (2004).

C. Cobet, T. Schmidtling, M. Drago, N. Wollschläger, N. Esser, W. Richter, R. M. Feenstra, and T. U. Kampen, *Surface termination during GaN growth by metalorganic vapor phase epitaxy determined by ellipsometry, J. Appl. Phys.* **94**, 6997 (2003).

C. Cobet, T. Schmidtling, M. Drago, N. Wollschläger, N. Esser, W. Richter, and R. M. Feenstra, *In-situ ellipsometry: Identification of surface terminations during GaN growth, phys. stat. sol. (c)* **0**, 2938 (2003).

C. Cobet, N. Esser, J. T. Zettler, W. Richter, P. Waltereit, O. Brandt, K. H. Ploog, S. Peters, N. V. Edwards, O. P. A. Lindquist, and M. Cardona, *Optical properties of wurtzite $Al_xGa_{1-x}N$ ($x< 0.1$) parallel and perpendicular to the c axis, Phys. Rev. B* **64**, 165203 (2001).

N. V. Edwards, M. D. Bremser, A. D. Batchelor, I. A. Buyanova, L. D. Madsen, S. D. Yoo, T. Wethkamp, K. Wilmers, C. Cobet, N. Esser, R. F. Davis, D. E. Aspnes, and B. Monemar, *Optical characterization of wide bandgap semiconductors, Thin Solid Films* **364**, 98 (2000).

L. X. Benedict, T. Wethkamp, K. Wilmers, C. Cobet, N. Esser, E. L. Shirley, W. Richter, and M. Cardona, *Dielectric function of wurtizite GaN and AlN thin films, Solid State Commun.* **112**, 129 (1999).

T. Wethkamp, K. Wilmers, C. Cobet, N. Esser, W. Richter, O. Ambacher, M. Stutzmann, and M. Cardona, *Dielectric function of hexagonal AlN films determined by spectroscopic ellipsometry in the vacuum-uv spectral range, Phys. Rev. B* **59**, 1845 (1999).

C. Cobet, M. Rakel, T. Schmidtling, M. Drago, W. Richter, and N. Esser, *Optical Properties of thin InN layers, BESSY Annual Report* , 422 (2003).

R. Goldhahn, V. Cimalla, O. Ambacher, C. Cobet, W. Richter, N. Esser, H. Lu, and W. Schaff, *Anisotropy of the dieletric function for hexagonal InN, BESSY Annual Report* , 377 (2003).

T. Wethkamp, K. Wilmers, C. Cobet, N. Esser, W. Richter, O. Ambacher, and M. Cardona, *Optical properties of hexagonal GaN and AlN films at low temperature determined by VUV-ellipsometriy, BESSY Annual Report* , 228 (1997).

Contents

1. Introduction

In the last few years no other class of material of semiconductors has attracted so much scientific and commercial attention like the group III-nitrides. The increasing interest is due to its extraordinary physical properties, which can be used in many new electronic and optoelectronic devices. Very prominent examples are the short wavelength LED's and laser diodes, which take advantage of the wide band gap of GaN. Possible applications are full colour displays, laser printers, and high density information storage. Si, SiC, or other widely used III-V semiconductors are not suitable for the construction optoelectronic devices, which operate in the blue and ultraviolet spectral region. Their band gaps are either indirect or not large enough. ZnSe based semiconductors would also provide band gaps suitable for short wavelength optoelectronic devices, but the bond strength in the II-VI wide band gap semiconductors is often too low. In fact, the high thermal and chemical stability in combination with the high electron mobilities generates further applications of the group III-nitride semiconductors, for example, in high power transistors or field effect transistors.

The group-III-nitrides, which include GaN, AlN, and InN, is a class of materials with a remarkable variation in the optical band gap while the lattice constant is nearly the same. The band gap changes from the visible (near infrared) for InN over the near VUV for GaN (3.5 eV) to the deep VUV spectral range for AlN (6.2 eV). The very similar lattice constants make it possible to grow complex multilayer systems, as well as ternary and quaternary compounds. These properties can be utilised in the construction of laser devices for the visible and VUV spectral range, as well as the application in full colour displays by tuning the band gap and the optical/electronic properties.

The three nitrides tend to crystallise in the wurtzite (hexagonal) structure and, less commonly, also in the zincblende (cubic) structure. Wurtzite GaN is the most commonly used compound. The growth is usually done with molecular beam epitaxy (MBE), chemical vapour deposition (CVD), or metalorganic vapour phase epitaxy (MOVPE). The latter, in particular, is important in industrial production where the higher growth rate plays a major role. Poly- and single-crystal layers of several μm on a few suitable crystalline substrate materials are accessible. The most commonly used substrate is c-plane (0001) sapphire, which induces the growth of (0001) wurtzite nitride films where the crystal/optical axis is perpendicular orientated to the surface. But the striking developments in the field of the III-nitrides growth provides now also the deposition of high quality epitaxial layers with other orientations or crystal structures.

A detailed overview about the epitaxial growth and the extraordinary physical properties of the group-III-nitrides, however, is given in a number of recent review articles and text books [1–9]. Especially, the formation of e. g. of GaN and InN epitaxial layers during MBE and MOVPE was investigated by means of in-situ optical methods in preliminary stages of this work [10–14].

Although GaN is already used in optoelectronic devices, many fundamental physical properties of the III-nitrides are still unknown. Open questions concern, for example, the bulk, surface, and interface electronic properties. A very prominent example for uncertain-

ties concerning the fundamental properties is the recent discussion about the optical band gap of InN. Up to the late 90's, InN properties were measured mostly on sputtered low quality thin films. The fundamental band gap of these samples was assumed to be around 2 eV [15, 16]. But new theoretical investigations [17], as well as experimental progress in the epitaxial growth of smooth layers by MBE [18–20] and MOVPE [21], have shown that the fundamental band gap is more likely located around 0.7 eV [22, 23].

This discussion about the optical band gap of InN emphasises, ultimately, also the uncertainties about the electronic band structure of the III-nitrides in general. The determination of optical properties and in particular of the dielectric function in the spectral range above the optical band gap (above the absorption edge) could play an essential role for a better fundamental understanding. The energy position and relative amplitudes of specific absorption structures in the dielectric function, in particular, can be used to test ab-initio band structure calculations. Together with other complementary experiments this comparison, thus, could contribute to the microscopic understanding of the electronic properties. Furthermore, the measured optical properties are also a possible criterion for the crystal quality or the surface perfection. Whereas the band structure gives rise to certain absorption structures in the dielectric function of a material, the crystal quality typically leads to a reduction in the amplitude and an overall broadening of these structures.

The optical properties of some nitride compounds have already been investigated in a large number of experimental works. But due to the limitations of conventional spectroscopic setups, these measurements were mostly restricted to the visible and near UV spectral range. Thus, the optical properties were investigated very extensively around the band gap of GaN, AlN and lastly of InN, with methods like PL but also with reflectance/transmission measurements [24–27] or ellipsometry [28–32]. In comparison, experimental results from the broad spectral range of the higher interband transitions are still rare. Most of these results have been obtained by reflectance [33, 34] or EELS [35] measurements and only a few in ellipsometric studies [10, 36].

Remarkable contributions concerning the determination of the group III-nitride dielectric function in the VUV spectral range were achieved with the same instrument that is also used in this work in an extended form [37–41]. But these measurements could not cover all open questions. Thus, the optical anisotropy of the wurtzite nitride films, for instance, was not determined and the dielectric function of InN in the VUV spectral range, e. g. , is still completely unknown. Due to these uncertainties the general understanding of the UV optical properties is low and the assignment of absorption structures to specific electronic excitations is incomplete.

In this work, therefore, we determine the unknown dielectric functions (components) and finally discuss the electronic origin of the specific structures.

For the investigation of optical properties we use the spectroscopic ellipsometry, which is a well established technique [42, 43]. This method allows a direct determination of the real- and imaginary part of the dielectric function $\varepsilon = \varepsilon_1 + i\varepsilon_2$. In reflectivity measurements, for example, the complex dielectric function or the related parameter n (refractive index) and k (absorption) has to be approximate in a subsequent Kramers-Kronig-analysis. Among many other advantages we would emphasise at this point that spectroscopic ellipsometry is a reference free, non destructive, and very accurate method. A further important point is the high surface sensitivity. This sensitivity could be utilised for characterisation of surface and surface overlayers. However, the measured bulk dielectric function could be disturbed, on

the other hand, due to a unknown surface contamination or surface morphologies. In order to identify and to account for these effects we have to investigate the surface properties as well.

The main aspect of this work concerns the installation of a suitable ellipsometer. GaN and AlN are wide band-gap semiconductors with a direct fundamental band gap at 3.4 eV (wurtzite phase). But the main electronic interband transitions occur within the spectral range of 6.5 - 15 eV and conventional ellipsometers are typically limited to photon energies below 6.5 eV. Thus, for the spectral range above 6.5 eV a dedicated setup, with a spectral range extended into the vacuum ultraviolet region, is necessary. For these measurements we use a world unique setup operating with a synchrotron light source [44]. This setup was mounted before at the Berlin synchrotron light source BESSY I. But in 1999 BESSY I was closed and replaced by a new facility BESSY II in Berlin-Adlershof. Due to several changes at the new light source several modifications were needed to reassimilate the old ellipsometer setup and a characterisation of the new light source was mandatory.

The experimental determination of the optical properties is strongly depending on the quality of the available samples. In comparison with common semiconductors like Si or GaAs the crystal quality of nitride semiconductors is still very low and comparatively high quality samples were available only for wurtzite GaN(0001) and partially AlN(0001). The determination of the full dielectric tensor in the case of the preferred wurtzite crystal structure depends on the orientation of the c-axis with respect to the surface. Indeed, wurtzite nitride samples are usually epitaxially grown on 6H-SiC or on c-Al_2O_3. These are (0001) oriented thin films, i. e. with the c axis perpendicular to the surface. Experimental data about their optical properties are, therefore, limited to the ordinary dielectric function (tensor component) $\varepsilon_\perp$ ($\vec{E} \perp c$). Data about the second independent dielectric tensor component $\varepsilon_\parallel$ ($\vec{E} \parallel c$) exist only for the transparent and near band gap region, where the dielectric components are measured by transmission, reflectance or ellipsometric measurements [31, 45]. This tensor component is also called the extraordinary dielectric function. But the recent success in depositing M-plane GaN($1\bar{1}00$) and a-plane InN($11\bar{2}0$) films now provides a way to overcome this problem. Since for these films the c-axis lies in the surface, the two independent components of the dielectric tensor can be separated by ellipsometry. The pseudodielectric (effective dielectric) function of anisotropic absorbing materials, measured by ellipsometry, depends mainly on the in-plane dielectric tensor components, while the tensor component normal to the surface is, in general, negligible [46]. Hence, depending on the orientation of light polarisation with respect to the crystal axis, the optical properties are given by a combination of the two independent tensor components in the surface. However, in order to extract these two components from ellipsometric measurements, we deduce a special optical model for the investigated anisotropic layers. This model is based on a known matrix algorithm for the plan wave propagation of light in arbitrary anisotropic layers [47].

The different experimental and theoretical aspects, as well as the results of this work are organised as follows.

- Firstly we will summarise several important properties of the III-nitride semiconductors in chapter 2.
- In chapter 3 we will introduce the experimental method, which is essentially a detailed description of the VUV-ellipsometer installation at BESSY II.

- In the following theory chapter 4 we first briefly explain the relation between the dielectric function and the electronic band structure of semiconductors and introduce a simplified model of the dielectric function, which will be used for the data evaluation. In the second part of this chapter we deduce a optical model for the treatment of anisotropic hexagonal layers in ellipsometric measurements.

- Chapter 5 includes results and a discussion concerning surface effects on ellipsometric measurements. According to these results we propose a thermal sample treatment, which is applied before ellipsometric measurements in particular for InN.

- The ellipsometric results of GaN, InN, and AlN are presented in chapter 6-8 together with a subsequent theoretical discussion of the specific features in the respective dielectric functions.

- In chapter 9 we separately discuss the contribution of semi-core d-electron excitations in the spectral range above 14 eV.

- Finally this work will be summarised in chapter 10.

2. General properties of nitrides

2.1 Crystal structure

Under ambient conditions there are two different crystal structures known for group-III-nitrides. The thermodynamically stable phase is the hexagonal wurtzite structure. But also the cubic zincblende structure has been stabilised by epitaxial growth of thin films. In both structures, the group-III atoms are coordinated by four nitrogen atoms and the other way around the nitrogen atoms are coordinated by four group-III atoms. The bonding geometry is determined by the sp^3-hybridisation of the common valence electrons. Thus, each atom is in particular also the centre of a tetrahedron (fig. 2.1). These tetrahedrons arrange in planes, which consist of two interpenetrating hexagonal closest packed superlattices. The difference between both structures corresponds to the stacking sequence of the closest packed planes. While for the wurtzite structure the stacking sequence of these planes is ABABAB, the stacking sequence of the zincblende structure is ABCABC (fig. 2.2). The formation of different structures finally originates from the two possibilities in the arrangement of the third layer. The two different stacking sequences are illustrated in figure 2.1.

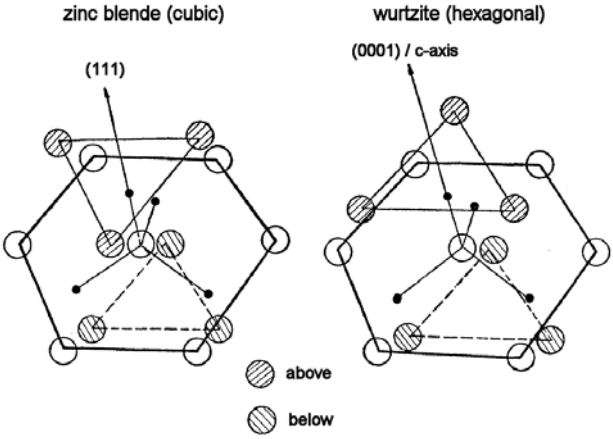

Figure 2.1: *Atomic arrangement of the first and second neighbours in the zinc blende and wurtzite crystal structure [48]. Large circles are group-III atoms and the small ones are N atoms. The two crystal structures differ in only three of the twelve second neighbour atoms and even these are just rotated symmetrically by $\pi/3$.*

The zincblende structure has a cubic unit cell containing four atoms of each element. The two different atom types arrange in this unit cell like two interpenetrating face-centred

cubic super lattices. Thereby, the (111) plane corresponds to the hexagonal closest packed planes. But the lattice constant a, of course, is defined along the [100] direction and, thus, not parallel or perpendicular to hexagonal closest packed planes. In this structure, the chemical bonds are tilted against the main crystal axis by $\approx 55^\circ$. The corresponding Brillouin zone in the reciprocal space is shown in figure 2.3. The space group for the zincblende structure is $F\bar{4}3m$ (T_d^2).

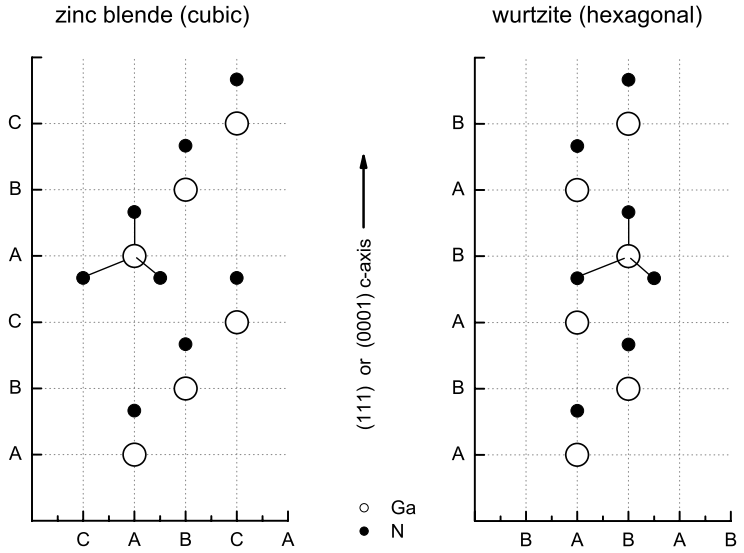

Figure 2.2: *Stacking diagram of the zincblende and wurtzite group-III-nitride crystal structure. The presented section correspond to the zincblende [110] and the wurtzite [$1\bar{1}00$] plane, respectively.*

The wurtzite structure has a hexagonal unit cell, which contains six atoms of each element. Thus, two lattice constance c and a define the Bravais lattice. "c" corresponds to the [0001] axis along the stacking direction of the hexagonal closest packed planes. "a" is defined in the (0001) hexagonal closest packed planes and, thus, perpendicular to the c axis. Due to the 60° rotation symmetry in the hexagonal planes there exist three equivalent directions. These are the [$\bar{1}\bar{1}20$], the [$\bar{1}2\bar{1}0$], and the [$2\bar{1}\bar{1}0$], which correspond to the lattice vectors $|a| \equiv |b| \equiv |c|$ (fig. 2.4). At this point we would emphasise that the Miller indices for the wurtzite structure also contain 3 entries for all these directions perpendicular to the c axis and a fourth for the direction parallel to the c axis. In order to consider the redundance in this notation, the sum over the first three numbers has to be zero. The space group for the wurtzite structure is $P6_3mc$ (C_{6v}^4). The Brillouin zone of the wurtzite structure is shown in figure 2.3.

In the wurtzite structure, the tetrahedrical chemical bonds are approximately aligned to the main crystal axis (planes). One of these four chemical bonds lies exactly parallel to the

c-axis of the crystal, where as the other three approximately arrange in the hexagonal closest packed planes. If hexagonal crystal fields (polarisation effects) are neglected, these bonds are tilted by $\approx 19^\circ$ against the hexagonal planes. In this ideal case of a undisturbed tetrahedrical chemical bond arrangement the c/a ratio of the lattice vectors should be 1.633 and all differences in the zincblende and wurtzite crystal structure are just related to the stacking order of the hexagonal closest packed planes. In real crystals the tetrahedrical chemical bond arrangement could be disturbed by hexagonal crystal fields and, thus, the c/a ratio could differ from the undisturbed value (1.633).

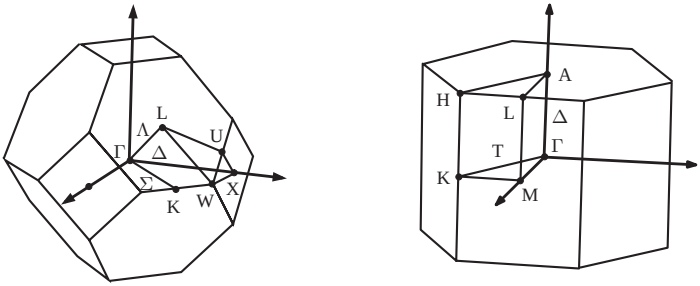

Figure 2.3: *Brillouin zones of the wurtzite [right hand side] and zincblende (left hand side) crystal structure. The labels correspond to specific high symmetry points or lines.*

Due to the fact that the hexagonal wurtzite polytype is the thermodynamically most stable structure, this wurtzite phase is also characterised as α-GaN, α-InN, and α-AlN, respectively. The cubic zincblende structure is the next metastable polytype and, thus, is called the β-phase. According to the characteristic stacking sequences the same structures are also called the 2H- and 3C-GaN (InN, AlN), respectively. The latter notation is very often used e. g. for SiC where several stable crystals are known, which relate to other stacking sequences. The 6H-SiC an 4H-SiC polytypes e. g. also correspond to hexagonal crystal structures. But these structures are periodic over 4 or 6 hexagonal planes. Nevertheless, meanwhile the formation of 6H-GaN was also observed [49]. At very high pressures, furthermore, a rocksalt or NaCl structure could be obtained. However, in this work we restrict our investigations to the wurtzite and zincblende structure. Hence, we summarise in table 2.1 only the room temperature lattice parameters for these two polytypes of GaN, InN, and AlN together with the respective fundamental band gap energy.

	α-GaN	β-GaN	α-InN	β-InN	α-AlN	β-AlN
a [Å]	3.189	4.52	3.537	4.98	3.112	4.38
c [Å]	5.185	-	5.704	-	4.982	-
E_g [eV]	3.42	3.2-3.3	0.7-0.9 ?	?	6.2	5.0-5.7 ?

Table 2.1: *Lattice constance and fundamental band gaps of group-III-nitrides at room temperatures [9, 19, 50, 51].*

2.2 Surfaces - Film orientations

A very important point for the determination of the dielectric function by means of ellipsometry is the choice of the suitable surface. In case of the anisotropic wurtzite crystal structure, first of all, this is a question of the orientation of the crystal axis in epitaxial layers. The most common samples are the so called c-plane ([0001]) films where the c axis is perpendicularly orientated to the surface. But for the determination of both the ordinary $\varepsilon_\perp$ ($\vec{E} \perp c$) and extraordinary dielectric function $\varepsilon_\parallel$ ($\vec{E} \| c$) crystal orientations are needed where the c axis is parallel to the surface. These are for instance a-plane ([$11\bar{2}0$]) and M-plane ([$1\bar{1}00$]) films. As indicated by the respective name, in a-plane films the lattice vector a is perpendicularly orientated to the surface. The "M" constitutes a high symmetry point in the Brillouin zone like shown in figure 2.3. In those films the respective high symmetry direction ($\Gamma - M$) is perpendicularly orientated to the surface. All commonly used planes and directions of wurtzite crystals are illustrated in figure 2.4.

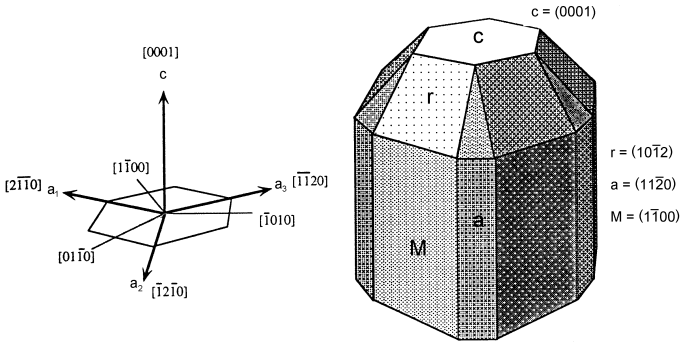

Figure 2.4: *Three-dimensional illustration of planes and directions in hexagonal crystals [9].*

Furthermore, important properties also relate to the missing inversion symmetry along the c axis. Due to energy arguments the preferred cut parallel to the hexagonal closest packed layers would follow a plane through the perpendicular single bonds in the c direction. Thus, two different c-plane surfaces are possible. The uppermost atoms are either group-III elements or nitrogen atoms. The first orientation corresponds to the (0001) surface and the second to the ($000\bar{1}$) surface. In figure 2.5 we illustrate the atomic arrangement of both surfaces for wurtzite GaN with four known surface reconstructions. Especially the Ga-rich (0001) surface (d) could have a remarkable influence on the pseudodielectric function measured with ellipsometry. As shown in figure 2.5 this surface is dominated by a Ga double layer, which could act as a metallic overlayer. But also the polarity of the crystal itself, namely whether the bonds along the c-direction are from cation sites to anion sites, ore visa versa, give rise to a spontaneous polarisation. This could lead to a remarkable polarisation charge at interfaces, which could effect ellipsometric measurements as well.

In zincblende crystals, however, the optical properties can assumed to be isotropic. Thus,

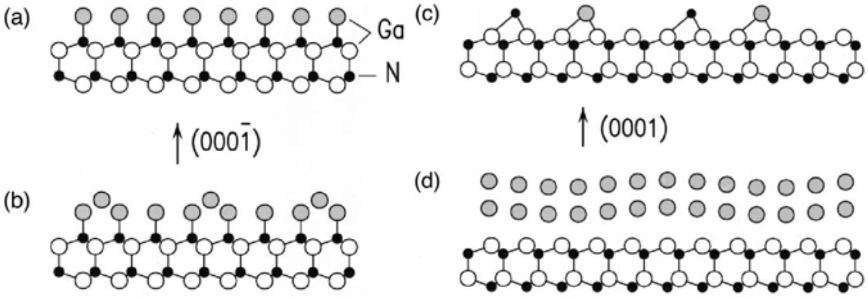

Figure 2.5: *Schematic illustration of N-face (a,b) and Ga-face (c,d) surfaces of GaN [52]. For both surfaces also the respective most N-rich (a,c) and most Ga-rich (b,d) reconstructions are presented.*

the orientation is less important for ellipsometric measurements of the bulk dielectric functions. Nevertheless, we would note that the investigated samples are [100] films, which are at the same time also the most common orientations. For this surface we further do not expect such striking surface effects like those known for the wurtzite $\pm$(0001) (zincblende $\pm$(111)) surface.

3. Experimental methods / Spectroscopic ellipsometry

The spectroscopic ellipsometry, which is used in this work for the determination of the dielectric function of III-nitrides, in general, is associated with the superordinate concept of the polarimetry. The procedure can be summarised as following: If monochromatic light with a defined polarisation is shining on a sample, the reflected light will show usually a changed polarisation depending on the sample properties e. g. the polarisability or the dielectric function and the used setup arrangement. Hence, the reflected light will be in general elliptically polarised. In the "ellipsometry", this change in the polarisation will be measured and finally is used to count back to the sample properties. The method was described already at the end of the nineteenth century in experimental and theoretical works of Drude [53, 54]. But the realisation as a standard method for the determination of optical constants was connected later in the 70'th to the development of computers for the measurement control. One of the first automated ellipsometers was introduced by Aspnes et. al. [55]. This so called rotating analyser ellipsometer (RAE) was already of the same general type like the ellipsometer we use now for our measurements in the VUV spectral range. However, the determination of changes in the polarisation instead of the absolute intensities, like reflection or absorption measurements, provides two main advantages. First, the change in the polarisation is defined by two independent parameters: the phase shift and the change in the relative amplitudes between the two electric field components parallel and perpendicular to the plain of incidence. The simultaneous measurement of these parameters enables the independent determination of both the real and imaginary part of the dielectric function (or refractive index and absorption coefficient). Second, the different polarisations only refer to the used geometry of the setup. Therefore, the ellipsometry is somehow a self calibrating method, which is independent from reference samples or data are needed.

As noted in the introduction, we use for our ellipsometric measurements in the visible and VUV spectral range a unique setup, which was mounted now for the first time on the new "second generation" synchrotron light source BESSY II. The ellipsometric setup and some general concepts, therefore, will be explained later in this chapter in more detail. However, many important general aspects of the method itself are collected for example in a recently published textbook [56]. This includes also a very short description of our BESSY-ellipsometer. The basic concepts of the BESSY-ellipsometer, in particular, were reported already in previous publications [57, 58]. Thus, we will concentrate our description to important experimental details and problems, which are connected to the new light source BESSY II and the specific requirements of our investigations.

But nevertheless, we refer in this work also to several other methods, which are used to characterise the investigated samples concerning their crystal and surface properties or for the sample preparation itself. All these methods are well established and can be repeated with similar commercially available setups. Hence, we would refer just to some selected publications and textbooks, which include a more detailed description and explanation. A very short description and the respective references are listed in the appendix C.

At the end of this chapter we will finally comment some aspects of the ellipsometric setup, which was used for in-situ measurements of the dielectric function during and after the sample preparation in MBE and MOVPE, respectively.

3.1 Principles of rotating analyser ellipsometry

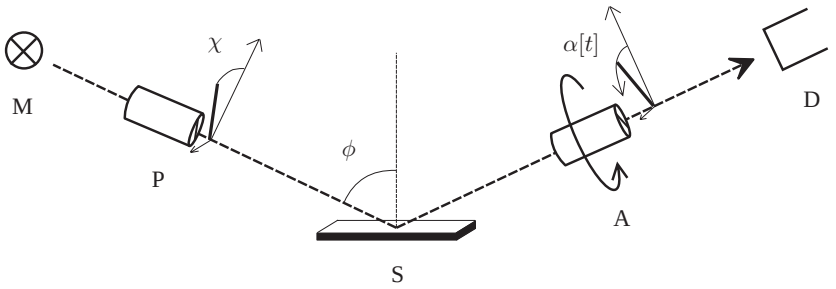

Figure 3.1: *Principle of a rotating analyser ellipsometer: First the monochromatic light from the source M is linear polarised by the polariser P with a certain angle χ to the plane of incidence. This light is reflected by the sample S under the angle of incidence ϕ and gets in general elliptical polarised. The rotating analyser A converts the "polarisation ellipse" into a modulated intensity, which is measured by the detector D.*

The essential components of a rotating analyser ellipsometer are shown in figure 3.1. In this type of ellipsometer the incoming monochromatic light gets linear polarised by a fixed polariser with a certain angle χ to the plane of incidence. The polarisation should be neither parallel nor perpendicular to the plane of incidence (usually $\chi = 45°$). The polarised light is shining on the sample under an angle of incidence ϕ different from 0°. Usually, an angle ϕ close to the (pseudo-)Brewster angle of the investigated material is the preferred value. After reflection the light is usually elliptically polarised. The rotating analyser converts the "polarisation ellipse" into a modulated intensity I, which is measured by the detector as a function of the angle $\alpha[t]$ and the time t, respectively.

$$\begin{aligned} I[\alpha[t]] &= I_0 + C_2 \cos\, 2\alpha[t] + S_2 \sin\, 2\alpha[t] \\ &= I_0(1 + c_2 \cos\, 2\alpha[t] + s_2 \sin\, 2\alpha[t]) \end{aligned} \tag{3.1}$$

The two coefficients C_2 and S_2 can be evaluated by means of a Fourier analysis. I_0 is the average intensity at the detector. The two normalised coefficients c_2 and s_2 constitute as the basic measurement result. Due to the 180° symmetry of the polarisation problem, these are the coefficients of the second harmonics. All the other harmonics should be zero except contributions of a wrong adjustment.

In a subsequent mathematical evaluation the normalised coefficient c_2 and s_2 has to be connected with the optical properties of the material given e. g. by the dielectric function.

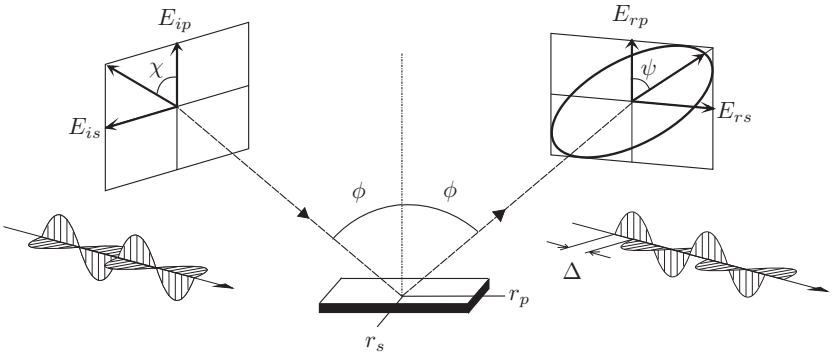

Figure 3.2: *Due to the different complex reflection coefficients parallel and perpendicular to the plane of incidence (r_p and r_s), the light is changing its state of polarisation after reflection on the sample. If the incoming light is polarised by $\chi = 45^\circ$ ($E_{ip} = E_{is}$) with respect to the plane of incidence, the ratio E_{rp}/E_{rs} is defined by the two ellipsometric angles ψ and Δ: $\frac{E_{rp}}{E_{rs}} = \frac{r_p}{r_s}\frac{E_{ip}}{E_{is}} = \tan\psi\, e^{i\Delta}$*

The simplest model assumes a half space homogeneous isotropic sample with a "perfect" planar surface. In this case the reflection of the light on the sample surface is defined by the two complex reflection coefficients r_p parallel and r_s perpendicular to the plane of incidence. The respective electric field components of the reflected light E_{rp} and E_{rs} are given by

$$E_{rp} = r_p \cdot E_{ip} = |r_p| e^{i\delta_p} \cdot E_{ip}\,, \qquad E_{rs} = r_s \cdot E_{is} = |r_s| e^{i\delta_s} \cdot E_{is}. \tag{3.2}$$

E_{ip} and E_{is} are the electric field components of the incident light. The complex reflection coefficients r_p and r_s are connected to the complex refractive index n and the complex dielectric function ε, respectively, by the known Fresnel equations.

$$\begin{gathered} r_p = \frac{n\cos\phi - n_0\cos\phi_{refr}}{n\cos\phi + n_0\cos\phi_{refr}} \qquad r_s = \frac{n_0\cos\phi - n\cos\phi_{refr}}{n_0\cos\phi + n\cos\phi_{refr}} \\ n_0 \sin\phi = n\sin\phi_{refr} \;\text{ law of refraction} \\ \sqrt{\varepsilon} = n \end{gathered} \tag{3.3}$$

n_0 denotes the ambient refractive index and can assumed to be $n_0 = 1$ for air or vacuum. However, if the complex ratio of r_p and r_s is written in the complex amplitude and phase, one gets a definition of the so called ellipsometric ratio in terms of two angles.

$$\rho := \frac{r_p}{r_s} = \frac{|r_p| e^{i\delta_p}}{|r_s| e^{i\delta_s}} = \frac{|r_p|}{|r_s|}\, e^{i(\delta_p - \delta_s)} = \frac{|r_p|}{|r_s|}\, e^{i(\Delta)} =: \tan\psi\, e^{i\Delta} \tag{3.4}$$

These two angles ψ and Δ are also called the "ellipsometric angles" and define changes in the absolute ratio and the phase shift between the electric field components parallel and

perpendicular to the plane of incidence after reflection on the sample surface (fig. 3.2). Using equation 3.4 and 3.3 ψ and Δ can be explained in terms of the dielectric function by

$$\varepsilon = \sin^2\phi\left(1+\tan^2\phi\left(\frac{1-\rho}{1+\rho}\right)^2\right). \tag{3.5}$$

But again, relations 3.2-3.5 are deduced for the simplest case of a half space homogeneous isotropic sample with a "perfect" planar surface in an air or vacuum environment. This assumption is also called the "two-phase model". The name emphasises the fact that only one reflection at a single interface between two different media is considered. In reality this idealisation is often not applicable and at least a surface roughnesses, thin overlayers, or surface contaminations have to be included. Nevertheless, the two-phase model is commonly used as a first approximation. The calculated dielectric function calculated in this manner is called the pseudodielectric (effective dielectric) function $\langle\varepsilon\rangle$, in order to point up the idealisations in the theory.

Finally, we need a connection between the measured Fourier coefficients c_2 and s_2 and the sample properties, which are translated so far only in to the ellipsometric angles ψ and Δ. A general concept to solve this problem was already betoken in equations 3.2-3.4. In the so called "Jones matrix formalism" the polarisation of the light is represented by Jones vectors, which consist of the two independent complex electric field components perpendicular to the propagation of the light [59]. In this Jones formalism, optical components are represented by a 2×2 matrix consisting of the respective reflection or transmission coefficients. If this matrix is defined in the eigensystem of an optical component or of the sample, like in equation 3.2, the mathematical representation can be simplified. A conceptual disadvantage of this formalism is the limitation to 100% polarised light. Unpolarised light can not be represented with Jones vectors. But in particular in the VUV or IR spectral range unpolarised light has to be considered.

3.2 Mueller matrix representation of the rotating analyser ellipsometer

In order to calculate the sample dielectric function from the measured Fourier coefficients c_2 and s_2 we use the so called "Mueller matrix formalism" for the mathematical representation of the ellipsometer. The particularities of the ellipsometry above 10 eV demand a formalism, which account unpolarised light related to non ideal optical components. It was shown by Stokes [60, 61] that in the plane wave approximation partially polarised light can be expressed by four quantities:

1. I_{pol}: intensity of the polarised part
2. γ: ellipticity of the polarisation ellipse
3. χ: azimuth of the polarisation ellipse)
4. I_{unpol}: intensity of the unpolarised part

Hence, the light is represented by a superposition of a totally polarised and an unpolarised part. But in order to simplify the problem, Stokes suggested a slightly different representation with four related intensities

$$\begin{aligned} S_0 &= I \\ S_1 &= I_x - I_y \\ S_2 &= I_{+\pi/4} - I_{-\pi/4} \\ S_3 &= I_l - I_r. \end{aligned} \tag{3.6}$$

$I_x, I_y, I_{+\pi/4}, I_{-\pi/4}, I_l$ and I_r are virtual intensities, which can be determined with a linear polariser if the transmission axis are chosen in the x, y, $+\pi/4$, or $-\pi/4$ direction and with a circular polariser with a transmission for left or right hand side polarised light, respectively. The cartesian coordinate system is defined with the z-axis parallel to the propagation direction of the light [61, 62]. Mueller suggested to combine these four Stokes parameters in the so called Stokes vector [63]

$$\bar{S} = \{S_0, S_1, S_2, S_3\}\,. \tag{3.7}$$

The parentheses denote here a transposed vector.

Further, he suggested real 4×4 matrices for the representation of optical components [63, 64]. The simplest representation again is given in the eigensystem of the corresponding optical component. But for this purpose, at first a transformation matrix is needed, which rotates the axis of the Stokes vector of the incoming light in the eigensystem of the optical component. The overall intensity and the intensities of the circular polarised components are not influenced by this transformation and the linear polarised components are just rotated against each other. Therefore, the transformation (rotation) matrix $\hat{M}_R$ can be written under consideration of the 180° symmetry of the problem as following:

$$\hat{M}_R = \begin{pmatrix} 1 & 0 & 0 & 0 \\ 0 & \cos 2\theta & \sin 2\theta & 0 \\ 0 & -\sin 2\theta & \cos 2\theta & 0 \\ 0 & 0 & 0 & 1 \end{pmatrix}, \tag{3.8}$$

where θ denotes the angle between the two coordinate systems. The representation of an ideal polariser in the Mueller matrix formalism is now quite simple. If the transmission axis would lie in the x-axis one gets the matrix representation

$$\hat{M}_{P_{i.}} = \frac{1}{2} \begin{pmatrix} 1 & 1 & 0 & 0 \\ 1 & 1 & 0 & 0 \\ 0 & 0 & 0 & 0 \\ 0 & 0 & 0 & 0 \end{pmatrix}. \tag{3.9}$$

A polariser with a degree of polarisation $\tilde{P}$ smaller than 1 and an additional absorption is defined by the transmission coefficients t_x and t_y parallel to the respective coordinate axis.

$$\tan\psi_P := \frac{|t_y|}{|t_x|}, \quad \tilde{P} := \frac{t_x^2 - t_y^2}{t_x^2 + t_y^2} = \cos 2\psi_P \;\equiv\; \text{degree of polarisation} \tag{3.10}$$

The corresponding Mueller matrix has the form

$$\hat{M}_P = \frac{t_x^2 + t_y^2}{2} \begin{pmatrix} 1 & \cos 2\psi_P & 0 & 0 \\ \cos 2\psi_P & 1 & 0 & 0 \\ 0 & 0 & \sin 2\psi_P & 0 \\ 0 & 0 & 0 & \sin 2\psi_P. \end{pmatrix} . \tag{3.11}$$

The representation of a polarising reflection unit is almost identical. But in this case, the transmission coefficients have to be replaced by the corresponding reflection coefficients r_x and r_y. Following the previous argumentations, it is sufficient, to define an ideal retarder or compensator, which provides a phase shift Δ_R between the x and y field components as the following:

$$\hat{M}_{Ret} = \begin{pmatrix} 1 & 0 & 0 & 0 \\ 0 & 1 & 0 & 0 \\ 0 & 0 & \cos\Delta_R & \sin\Delta_R \\ 0 & 0 & -\sin\Delta_R & \cos\Delta_R. \end{pmatrix} . \tag{3.12}$$

Finally, we have now a basic set of Mueller matrices, which can be used to represent the polarisation effect of an arbitrary (linear) optical component and in particular, for the sample under investigation, by a linear combination of those matrices. Hence, the Mueller matrix of the sample is given by

$$\hat{M}_S = \frac{{r_p}^2 + {r_s}^2}{2} \begin{pmatrix} 1 & -\cos 2\psi & 0 & 0 \\ -\cos 2\psi & 1 & 0 & 0 \\ 0 & 0 & \sin 2\psi\, \cos\Delta & \sin 2\psi\, \sin\Delta \\ 0 & 0 & -\sin 2\psi\, \sin\Delta & \sin 2\psi\, \cos\Delta \end{pmatrix} , \tag{3.13}$$

whereas a rotating "non ideal" analyser is represented by

$$\hat{M}_A = \frac{{t_p}^2 + {t_s}^2}{2} \begin{pmatrix} 1 & \cos 2\psi_A & 0 & 0 \\ \cos 2\psi_A & 1 & 0 & 0 \\ 0 & 0 & \sin 2\psi_A\, \cos\Delta_A & \sin 2\psi_A\, \sin\Delta_A \\ 0 & 0 & -\sin 2\psi_A\, \sin\Delta_A & \sin 2\psi_A\, \cos\Delta_A \end{pmatrix} . \tag{3.14}$$

In our rotating analyser ellipsometer the eigensystem of the analyser rotates around the z axis with $\alpha(t)$. However, like in the Mueller matrix of the polariser ψ_A denotes here the degree of polarisation of the analyser. At this point we should mention that the two angles ψ and Δ in the Mueller matrix of the sample are the same ellipsometric angles like those introduced in equation 3.4.

For a mathematical description of the rotating analyser ellipsometer as shown in figure 3.1, the Mueller matrices of the different optical components have to be applied in the order of the light path to the Jones vector of the incidence light. If we start the description after the fixed polariser with a defined (partly) polarisation, the Stokes vector of the incident light is defined by

$$\bar{S}_{in} = \{I_0,\, I_0 P \cos 2\gamma,\, 0,\, I_0 P \sin 2\gamma\}. \tag{3.15}$$

The quantities I_0, P, and γ denote the incoming intensity, the degree of polarisation and the ellipticity. The polarisation is chosen in the "x-axis" of the coupled eigensystem. But the reference coordinate system (laboratory system) coincides with the plane of incidence. The

x-axis is chosen parallel and the y-axis perpendicular to the plane of incidence, whereas the z-axis is taken again parallel to the propagation of the light. Thus, the Stokes vector of the incident light first has to be rotated back in the laboratory (sample) system with the matrix $\hat{M}_R[-\chi]$. χ is again the angle between the transmission axis of the polariser and the plane of incidence (q. v. fig. 3.2). The sample itself is represented by the matrix $\hat{M}_S$. After reflection at the sample, the Stokes vector has to be transferred in the rotating eigensystem of the analyser $\hat{M}_R[\alpha(t)]$, where the analyser is represented by $\hat{M}_A$. Finally, the Stokes vector has to be rotated back in the laboratory (sample) system ($\hat{M}_R[-\alpha(t)]$) and the resulting intensity will be measured by the detector. All together, one gets the following relation:

$$\bar{S}_{out} = \hat{M}_R[-\alpha(t)]\,\hat{M}_A\hat{M}_R[\alpha(t)]\,\hat{M}_S\hat{M}_R[-\chi]\,\bar{S}_{in}. \tag{3.16}$$

In general, the intensity measured by a detector should be independent from the polarisation of the light. Therefore, we can neglect the last rotation, as well as the phase shift Δ_A of the analyser. Hence, the intensity at the detector is given by the first component of $\bar{S}_{out}$:

$$\begin{aligned} I\,[\alpha(t)] = S_0 =& I_0\frac{(r_p^2+r_s^2)(t_p^2+t_s^2)}{4} \\ & \big(1 - P\cos 2\gamma\,\cos 2\psi\,\cos 2\chi \\ & - \cos 2\psi\,\cos 2\psi_A\,\cos 2\alpha(t) \\ & + P\,\cos 2\gamma\,\cos 2\psi_A\,\cos 2\chi\,\cos 2\alpha(t) \\ & + P\,\cos 2\psi_A\,\sin\Delta\,\sin 2\gamma\,\sin 2\psi\,\sin 2\alpha(t) \\ & + P\,\cos\Delta\,\cos 2\gamma\,\cos 2\psi_A\,\sin 2\psi\,\sin 2\chi\,\sin 2\alpha(t)\big) \end{aligned} \tag{3.17}$$

By a comparison of the coefficients with those in relation 3.1, one gets the relation to the Fourier coefficients measured in a rotating analyser ellipsometer [57]

$$\begin{aligned} c_2 &= \cos 2\psi_A\,\frac{P\cos 2\gamma\,\cos 2\chi - \cos 2\psi}{1 - P\cos 2\gamma\,\cos 2\psi\,\cos 2\chi} \\ s_2 &= P\cos 2\psi_A\,\sin 2\psi\,\frac{\sin\Delta\,\sin 2\gamma + \cos\Delta\,\cos 2\gamma\,\sin 2\chi}{1 - P\cos 2\gamma\,\cos 2\psi\,\cos 2\chi}. \end{aligned} \tag{3.18}$$

Thus, the latter relations connect the measured Fourier coefficients c_2 and s_2 with the unknown ellipsometric angles and the investigated sample properties, respectively. If all the setup parameters are known, we can directly determine ψ and Δ as a function of the Fourier coefficients after an inversion of the equations 3.18.

$$\begin{aligned} \tan\psi &= \sqrt{\frac{\cos 2\psi_A + c_2}{\cos 2\psi_A - c_2}}\sqrt{\frac{1 - P\cos 2\gamma\,\cos 2\chi}{1 + P\cos 2\gamma\,\cos 2\chi}} \\ \cos\Delta &= \frac{s_2\cos 2\gamma\,\sin 2\chi \pm \sin 2\gamma\,\sqrt{P^2\,\Omega^2\,\Phi - s_2^2}}{P\,\Omega\,\Phi} \\ \text{with}\qquad \Omega &= \sqrt{\frac{c_2^2 - \cos^2 2\psi_A}{P^2\cos^2 2\gamma\,\cos^2 2\chi - 1}},\quad \Phi = \cos^2 2\gamma\,\sin^2 2\chi + \sin^2 2\gamma \end{aligned} \tag{3.19}$$

The exact algebraic sign in the calculation of $\cos\Delta$ has to be determined in the experiment but is unimportant if the light shining on the sample has no circular polarised components.

If further the polariser, as well as the analyser are assumed to be ideal ($P = 1, \gamma = 0$, and $\psi_A = 0$), we achieve the known equations:

$$\tan\psi^{(id)} = \sqrt{\frac{1+c_2}{1-c_2}}\,|\tan\chi|\,, \qquad \cos\Delta^{(id)} = \frac{s_2}{\sqrt{1-c_2^2}}\,\mathrm{sgn}\,\chi. \tag{3.20}$$

We want to point out that the shown derivation does not include depolarisation effects by the sample or the analyser. We just account a possible incomplete polarisation of the incidence light by the parameter P. This value should not confuse with the degree of polarisation $\tilde{P}$ e. g. of a polariser/analyser. While the latter represents the ability to select a certain polarisation, P determines the degree of the phase correlation. If a rough sample surface or an inhomogeneous layer thickness for example is responsible for partial depolarisation (decreasing phase correlation), the Mueller matrix of the sample has to be combined with the Mueller matrix of a partial depolarisation, where $\check{P}$ denotes the degree of depolarisation

$$\hat{M}_S^{rough} = \begin{pmatrix} 1 & 0 & 0 & 0 \\ 0 & \check{P} & 0 & 0 \\ 0 & 0 & \check{P} & 0 \\ 0 & 0 & 0 & \check{P} \end{pmatrix} \hat{M}_S. \tag{3.21}$$

Finally one has to recalculate the relation between the measured Fourier coefficients and the ellipsometric angles. In case of an unknown depolarisation due to the sample, the Fourier coefficients have to be measured several times with e. g. an appropriate change in the polarisations of the incident light, to resolve the three sample parameters $\tan\psi$, $\cos\Delta$ and $\check{P}$.

3.3 BESSY ellipsometer setup

The reconstructed synchrotron ellipsometer is based, in principal, on the well known rotating analyser design. But on the other hand, not only the use of the synchrotron light source [65] turns it into a very special and unique device. As already mentioned, we use as a light source the "Berlin electron storage ring for synchrotron radiation" BESSY II and in particular, depending on the spectral range under investigation, the 3m NIM1 or the TGM4 beam lines [66]. Both are grating monochromators mounted on dipole magnets, which are the source of the intense and collimated synchrotron beam. The brilliance is much higher than that of conventional lightsources although a very broad spectral range from the infrared up to high energetic X-rays is available. The accessible photon energies essentially depend on the available dispersion elements, as well as on the geometrical design of the monochromator and the beamline. For the spectral range from 3 up to 10 eV, we use the 3m NIM1 (a 3 m normal incidence monochromator) with a $600\,l/mm$ grating (MgF_2/Al-coating) [67]. The spectral resolution of the monochromator is given by

$$\Delta E_{[\mu eV]} = 0.448 E^2_{[eV]} \sqrt{S^2_{1[\mu m]} + S^2_{2[\mu m]}}, \tag{3.22}$$

where S_1 and S_2 denote the entrance and exit slit size and E is the actual photon energy. For our experiments we use in general a slit size around 100 μm, which results in a spectral resolution of approximately 5 meV at photon energies around 8 eV.

Due to the small effective size and the respective high brilliance of the light source we receive a well collimated synchrotron beam after the last mirror of the monochromator. Therefore no additional mirror is needed in the ellipsometer setup. We placed the focus point of the beam on the sample. Thus, the spot size on the sample is about 500 μm $\times$100 μm (hor.$\times$ ver.). The divergence at focus position is only 8 mrad$\times$50 mrad.

At this beamline, unfortunately, the photon flux is too low for ellipsometric measurements at higher photon energies. And also the available "high energy" grating (2400 l/mm with a Pt-coating) does not cover the subsequent spectral range above 10 eV. Due to the increased dispersion of this grating the available intensity is finally also to low. Therefore, it was necessary to use another beamline, namely the TGM4 (toroidal grating monochromator). With a 256 l/mm grating (Au-coating), this monochromator allows us ellipsometric measurements between 7 and 32 eV. The beam divergence at focus position after the monochromator is further reduced (3 mrad$\times$6 mrad). But accordingly, the spot size of focus on the sample is larger (0.3 mm$\times$0.1 mm FWHM). The spectral resolution at 20 eV is approximately ΔE =50 meV for a typical slit size around 100 μm.

3.3.1 Ellipsometry with synchrotron radiation

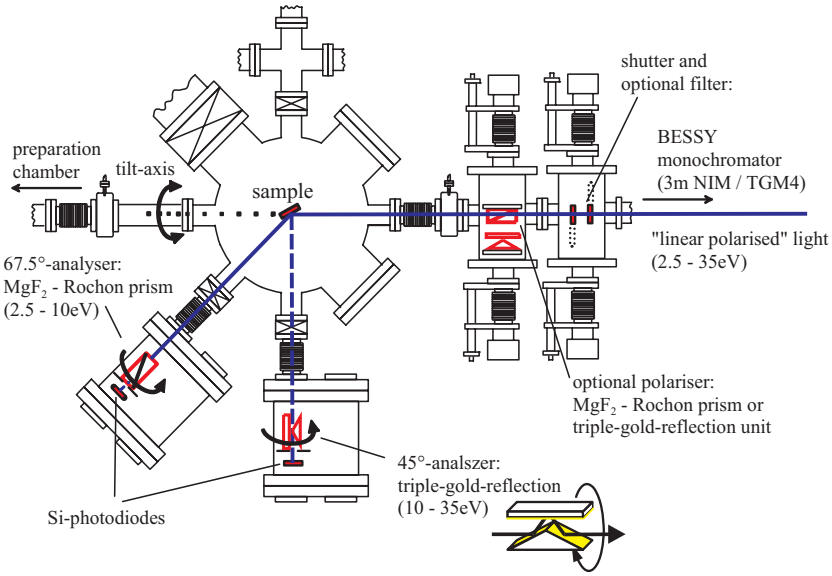

Figure 3.3: *Sketch of the UHV chamber containing the VUV-ellipsometer*

Due to the intended measurements above 10 eV all optical components have to be mounted in an UHV chamber, since air (nitrogen) absorbs light of photon energies above $\approx$6.5 eV ($\approx$9.5 eV). It exist no transparent material, which could be used for windows, above 10 eV.

Therefore, the vacuum chamber of the ellipsometer has to be connected with the UHV system of the electron storage ring. A sketch of the ellipsometer components within the UHV-vessel is shown in figure 3.3. In order to account the different vacuum requirements, the setup is separated in several differential pumped sections. These are divided by small apertures of max. 4 mm. After several modifications on the original setup, we reach now a base pressure of $2 \cdot 10^{-10}$ mbar in the main chamber, where the sample is mounted onto an UHV manipulator. Under these conditions defined/clean sample surfaces can be maintained or prepared e. g. by thermal annealing up to 1500°C (resistive heater plus direct heating). Furthermore, a cooling system allows ellipsometric measurements at liquid nitrogen temperatures. For additional preparations the sample can be also transferred under UHV conditions in a newly attached preparation chamber (not shown in fig. 3.3). This chamber could be used, for instance, for a surface cleaning by ion sputtering.

In front of the main chamber the incoming beam passes two new small chambers, which include two different polarisers, optical filter and shutters for the periodic measurement of the dark current of the electronics. Afterwards, the synchrotron beam is reflected by the sample in to one of the two different analyser chambers under a angle of incidence of either 45° or 67.5°. These chambers contain the rotating analyser and a Si-photodiode as the detector [68]. As mentioned already, the optical setup does not include any further mirror for an additional focusing. This is a major advantage of our setup. In standard rotating analyser (rotating polariser) ellipsometers, the the beam has to be refocussed after the rotating analyser by mirrors or lenses. The polarisation effect of these components lead in combination with the rotating element to an additional modulation of the intensity on the detector, which can disturb the measurement remarkable.

The preferred angle of incidence depends on the sample properties at the certain photon energies. Several competing aspects have to be taken into account. The angle of incidence should be chosen as close as possible to the (pseudo-) Brewster angle of the sample. At this angle $\cos\Delta$ is zero and the sensitivity of a rotating analyser ellipsometer is maximal. If in contrast $\cos\Delta$ is close to -1 a independent determination of the real and imaginary part of the dielectric function from the ellipsometric angles is difficult. At this point the respective equations exhibit a singularity, which cause a high signal to noise level. However, the (pseudo) Brewster angle of wurtzite GaN changes reasonably over the spectral range under investigation as shown in figure 3.4. Thus, 67.5° is an appropriate angle of incidence for the spectral range from 3-10 eV. According to the strong decrease of the Brewster angle with the increasing photon energies, 45° could be the preferred angle for higher photon energies. But a second important point is connected to the reflectivity of the sample under investigation. Following the general intention to maximise the intensity at the detector, a higher angle of incidence would be preferred in particular for higher photon energies (q. v. fig. 3.4). Otherwise the reflectivity would strongly decrease above the main interband transitions and especially at photon energies above the plasma frequency. The plasma edge of semiconductors is usually located between 10 eV and 20 eV. Thus, the feasibility of ellipsometric measurements at higher photon energies, in general, depends on the existence of further absorption structures beyond the plasma edge and the main interband transitions, which generate a sufficient reflectivity. These absorption structures above 20 eV may are created by electronic transitions from core like electrons. However, the pure intensity arguments would prefer the use of larger angles of incidence in contrast to the Brewster angle requirements. But finally the crucial factor, which favours the 45° analyser chamber for the ellipsometric measurements

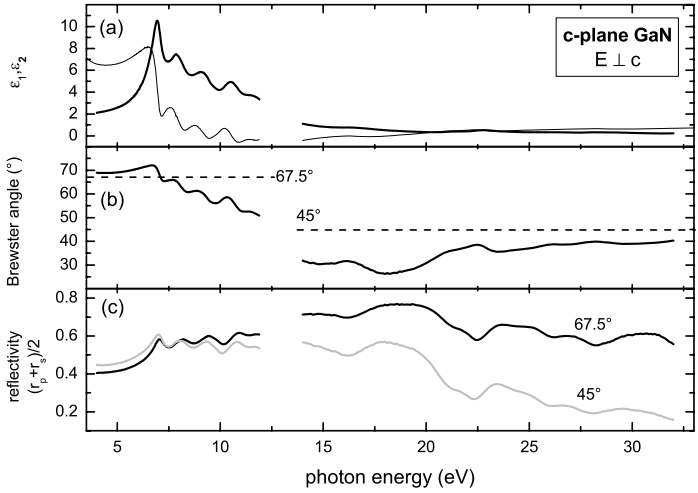

Figure 3.4: *The measured dielectric function (a) of wurtzite GaN (q. v. para. 6.1.1) is used to calculate the spectral dependence of the Brewster angle (b), as well as the reflectivity for two different angles of incidence (c). In graph (b) we marked the two available angles of incidence with dashed lines.*

on Nitride semiconductors above 10 eV, is the amount of second order light.

If a grating monochromator is used, reasonable rates of second order diffracted light with the doubled frequency could be admixed to the first order light. For a sufficient reduction we use between 3 and 5 eV and quartz glass filter. Between 5 and 10 eV the MgF_2-polariser also acts as second order filters. For a suppression between 10 and 12 eV, we use a very thin LiF filter (100 μm). However, due to the increasing absorption of LiF in this spectral region, the first order light is also reduced and ellipsometric measurements are problematic. Finally, there exist no free standing transparent materials, which can be used as filter above 12 eV. A sufficient filtering of second order light can be obtained in this spectral range by additional reflection units or gas filters (e. g. Ar). A reflection type filter based on multi reflections on Si surfaces under appropriate angles of incidence was suggest by Terminello et. al. [69]. But this kind of filter would again strongly reduce the first order light as well. The use of gas filters could prevent this general problem, but the technical implementation is very problematic due to the necessary direct connection to the vacuum system of the electron storage ring. Therefore, we could not realise these filter type in our BESSY-Ellipsometer until now.

In this situation, the reflectivity and in particular the decreasing reflectivity of the sample at higher photon energies at small angles of incidence is important again. If we choose for the higher spectral range an angle of incidence of 45°, the reflectivity of e. g. GaN at 28 eV is reduced already by a factor of 3 in comparison to the corresponding reflectivity at 14 eV (fig. 3.4). In combination with the generally decrease of the intensity at higher energies, we

can expect undisturbed ellipsometric results above 14 eV. In other words: If we use an angle of incidence of 45° the measured nitride samples also act as their one second order filter above 14 eV.

Although many was known already about ellipsometry with synchrotron radiation due to the previous experiments at BESSY I, we had to solve several unexpected experimental problems with the new light source BESSY II and the new beam lines in the beginning of this work. Big problems were related to intensity fluctuations, which possibly relate to electron beam instabilities in the storage ring. Rotating analyser ellipsometers, in principal, are very sensitive to intensity changes with time constants in the range of the analyser rotation frequency. Unfortunately, the cooling system of new insertion devices and a close loop controlling system in the electron storage ring responds to changes in the electron beam position with time constants close to our preferred analyser rotation frequency. This effect was minimised by choosing suitable apertures in the beam and a careful adjustment of the monochromator. However, the most important issue in ellipsometric measurements is the polarisation of the light, which was also effected by this time dependent changes. This problem will be discussed in more detail in the following paragraph.

3.3.2 Polarisation of the synchrotron light

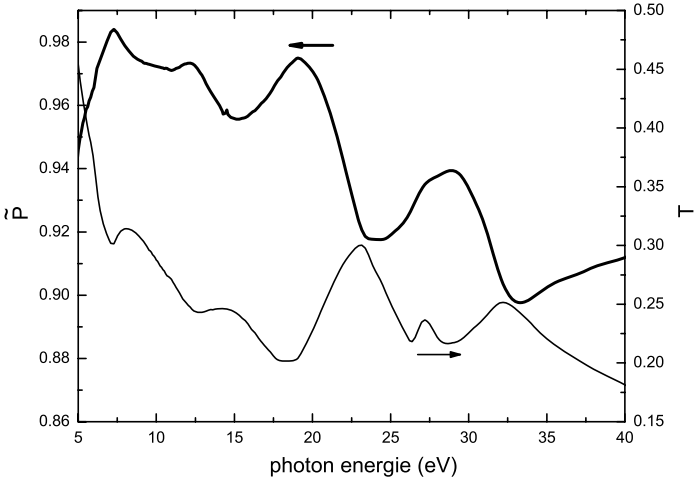

Figure 3.5: *Degree of polarisation $\tilde{P}$ [——] and the transmission T [- - -] of the reflection type polariser/analyser calculated with the optical properties of gold [70].*

Up to 10 eV we use for the polariser, as well as for the rotating analyser in the "67.5° analyser chamber" Rochon prisms made of MgF_2. With these prisms we attain a degree of polarisation of 99.998%. But above 10 eV, there exist no (birefringent) transparent materials. Accordingly, only reflection type polarisers can be used. In general, these polarisers operate

with reflections near the (pseudo) Brewster angle ϕ_B of an appropriate material. Due to the high reflectivity, usually metals are preferred. But unfortunately, the polarisation at the pseudo Brewster angel of these absorbing materials is incomplete ($|r_p[\phi_B]| > 0$). Thus, to enhance the degree of polarisation more than one reflection is needed for a sufficient solution. But this strongly reduces again the overall transmittance. However, under consideration of the transmittance, the degree of polarisation and spectral continuity of those, an optimum for the spectral range between 10 and 30 eV is found with an arrangement of three reflecting gold surfaces (fig. 3.3) [71]. The reflections are chosen as close as possible to the pseudo Brewster angle. Thus, the used gold reflection units combine three reflections under 67.5°, 45°, and again 67.5°. The degree of polarisation, as well as the transmittance is given (q. v. eq. 3.3) by:

$$t_p = r_{p_{67.5^\circ}} r_{p_{45^\circ}} r_{p_{67.5^\circ}} \ , \qquad t_s = r_{s_{67.5^\circ}} r_{s_{45^\circ}} r_{s_{67.5^\circ}} \tag{3.23}$$

$$\tilde{P} = \frac{t_p^2 - t_s^2}{t_p^2 + t_s^2} \ , \qquad T = t_p^2 + t_s^2 \tag{3.24}$$

We use the optical properties of gold from reference [70] to calculate the spectral dependence between 5 and 401 eV. As shown in figure 3.5, the polarisation of this multiple reflection unit decreases at higher energies. For a further extension of the spectral range, the metal surfaces have to be replaced by multilayer structures. Those mirrors increase the degree of polarisation significantly but are optimised just to a very narrow spectral range. A survey of methods used for the polarisation of light in the photon energy range from the visible to the X-ray regions is given by Schäfers et. al. [72].

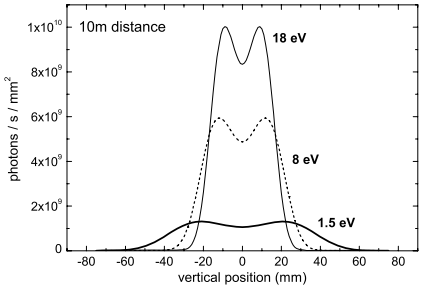

Figure 3.6:
Vertical intensity profile of the synchrotron beam at 1.5, 8, and 18 eV. This profile was calculated for a distance of 10 m to the dipole magnet

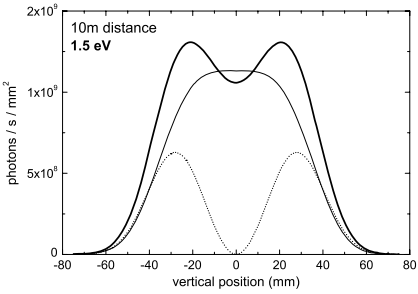

Figure 3.7:
Vertical distribution if the horizontal (thin black line) and the vertical (dotted line) polarisation to the total intensity (thick black line) in the synchrotron beam.

A major advantage of the synchrotron light, actually, is the native linear polarisation in the plane of the electron storage ring. This could be used for the ellipsometric measurements if the horizontal component is selected by appropriate apertures. In order to preserve light intensity, therefore, no (reflection type) polariser in the incidence light was used above 10 eV

within the old ellipsometer configuration at the former synchrotron light source BESSY I [57, 58]. This concept was also used at first at the new storage ring BESSY II. But we finally discovered that the native polarisation is unfortunately not sufficient at the new beam lines at BESSY II. The major problem is the different geometry of the used monochromators. At the old light source we used a 2m-Seya-Namioka monochromator. In this monochromator types all mirrors, as well as the reflection at the dispersive element are mounted in a s-geometry. Hence, the vertical polarisation components are strongly suppressed by the monochromator/beam line and the linear polarisation was finally better than 99% at BESSY I. In contrast, the monochromators at BESSY II do not provide this particular construction and the suppression of the vertical polarised light is too low. In principal, this is not problematic, if the state of the polarisation is known [73]. But a more detailed evaluation shows additional problems, which are connected to beam instabilities and small changes in the adjustment of the monochromator. Figure 3.6 and 3.7 show the vertical angular distribution of radiation emitted by the electrons moving through a bending magnet. This beam includes two different polarisation components, which are vertically and horizontally polarised [66, 74, 75]. The vertical polarised light appears only above and below the plane of the storage ring. These parts show a phase shift of +90° and -90° to the horizontal polarisation component. In the ideal case, if a symmetric section around the centre of the beam is selected, all components superpose in a focus point finally to a horizontal linear polarisation. But a small misalignment of the apertures (the beamline) or variations in the electron orbit cause a selection of different parts of the beam. In consequence also the overall polarisation of the light is strongly effected by this variations. Our test measurements show, in fact, that the polarisation often changes within several minutes at the used beam lines at BESSY II. Ellipsometric measurements were not possible under these conditions. Therefore, it is mandatory to use the triple gold reflection unit as a polariser, although the intensity is further reduced. Together with the partially polarised synchrotron light we finally reach a degree of polarisation of about 99%.

However, due to the native polarisation of the synchrotron light, we can still not change the polarisation according to the plane of incidence by a simple rotation of the polariser. In ellipsometric measurements χ should be close to 45° while for the calibration of the setup measurements at about $\chi = 0°$ are required. Thus, the intensity would be strongly reduced due to the distortion between the polarisation of the incident light and the transmission axis of the polariser in one of these cases if only the polariser is rotated. Therefore, we have to rotate (tilt) the whole vacuum chamber around the incident beam in order to change the plane of incidence according to the polarisation. Because of mechanical limitations of the setup we accomplish the ellipsometric measurements with χ =20°.

Due to the application of different polarisers, filters and the two different angles of incidence, the ellipsometric measurement of the dielectric function from 3 to 35 eV is divided in several steps. A summery of these subsequent steps and the used optical components is shown in table 3.1. Above 10 eV the assumed degree of polarisation P of the incident light, as well as the calculated polarisation of the analyser $\tilde{P}$ are used in the data evaluation according to equation 3.19.

spectral range	optical components	ϕ	P	$\tilde{P}$	notes
3.0-4.5 eV	MgF_2-polariser MgF_2-analyser quartz filter	$\approx 67.5°$	100%	100%	
4.5-10 eV	MgF_2-Polarisator MgF_2-Analysator	$\approx 67.5°$	100%	100%	
10-12 eV	reflection type polariser reflection type analyser LiF filter	$\approx 45°$	99%	fig. 3.5	very low intensities
12-14 eV	reflection type polariser reflection type analyser	$\approx 45°$	99%	fig. 3.5	disruption due to second order light
14-35 eV	reflection type polariser reflection type analyser	$\approx 45°$	99%	fig. 3.5	transparent shutter compens. straylight

Table 3.1: *Steps of the ellipsometric data acquisition: An overview of the used optical components, the polarisation parameters, and general limitations*

3.4 In-situ ellipsometry during MBE and MOVPE

In order to evaluate the effect of surface terminations and contaminations on the pseudodielectric function we compare our results also to in-situ measurements on defined GaN and InN surfaces as obtained during and after growth in a MOVPE reactor or a MBE-UHV chamber. In particular in-situ measurements during the MBE preparation allow the investigation of group-III-nitride layers under very defined conditions where also different surface reconstructions or terminations are accessible.

For those experiments we use a MBE-UHV chamber as well as a MOVPE reactor with appropriate windows. The ellipsometer setup for this in-situ studies is divided in to parts, the polarizer and the analyser arm. These arms are mounted in front of the reactor windows. This ellipsometer operates with a conventional xenon arc lamp as the light source. A sketch of the ellipsometer setup with all important components is shown in figure 3.3. The main differences of this ellipsometer construction in comparison to the BESSY ellipsometer concept are connected to the monochromator position. The monochromator is placed here after the analyser to reduce stray light effects caused by the sample heating system. Due to this modification the ellipsometer operates now with a rotating polariser and a fixed analyser. But the mathematical expressions for the calculation of the ellipsometric angles or the dielectric function are the same. This follows from the inversion symmetry of the light propagation.

According to the limitations of the used light source and the reactor windows this in-situ ellipsometer can cover only a spectral range from 1.5 to 6.6 eV. Unfortunately, the majority of the interband transition especially of GaN and AlN shows up at higher photon energies. But nevertheless, this spectral range is sufficient enough to investigate surface effects in the pseudodielectric function.

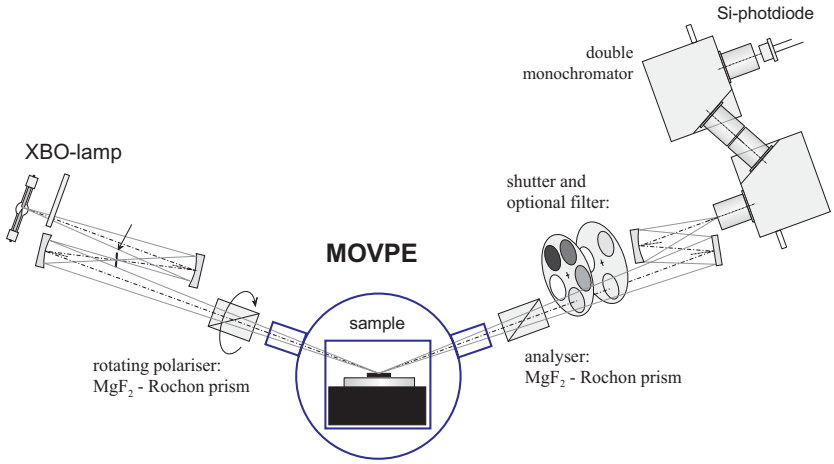

Figure 3.8: *Sketch of the in-situ-ellipsometer setup, which is used either on a MOVPE reactor (as shown here) or on an UHV-chamber with the possibility for PAMBE experiments. In this drawing the in-situ-ellipsometer is attached for example to the MOVPE reactor, which is shown here in a cross view.*

3.5 Accuracy of the ellipsometric measurements

The exact evaluation of statistical and systematic errors in the dielectric function calculated from ellipsometric measurements is difficult. As noted above the constitutional measurement result of a rotating analyser (rotating polariser) ellipsometer is given by the two normalised Fourier coefficients c_2 and s_2. According to the non linear character of the equations used for the subsequent evaluation, the statistical noise in the "measured" dielectric function depends finally on the optical properties of the sample under investigation. It is well known e. g. that statistical and systematic errors in rotating analyser ellipsometers are strongly amplified for such areas where the ellipsometric angle $\cos\Delta$ is close to 1 or -1. In a different context, this problem was actually mentioned also in paragraph 3.3. In order to minimise the effect of errors, therefore, the angle of incidence should be chosen close to the Brewster angle where $\cos\Delta$ is close to zero.

The complicated UHV housing of the ellipsometer relates to mechanical inaccuracies. Especially, the determination of the exact angle of incidence ϕ and the exact angle between the polarisation of the incidence light with respect to the plane of incidence χ is problematic. Accordingly, these values are responsible for the biggest systematic errors in our measurements. We assume that the accuracy in the spectral range below 10 eV is $\Delta\phi = \pm 0.1^\circ$ and $\Delta\chi = \pm 0.05^\circ$, respectively. Nevertheless, the related uncertainties in the determined dielectric functions are just in the range of the line width we use for the graphical representation of our results. But above 10 eV, the systematic error could be larger. In this spectral range the overall intensities are lower and additional uncertainties relate to the non ideal polarisation

of the incident light. Therefore, the pseudodielectric functions above 10 eV as presented in chapter 6, 7, and 8 could include systematic errors, which are two or five times larger than the used line width. But these systematic errors mainly result in a constant offset of the real and the imaginary part of the pseudodielectric function. For the subsequent discussion of characteristic absorption features, however, these errors (offset) are not important.

4. Models for the linear optical properties of semiconductors

In this work we use the dielectric function ε for the discussion about the linear optical properties of III-nitrides. Therefore, we will summarise in the following important definitions for this quantity and shortly introduce the optical dispersion models we will use later for the data evaluation. These are two pure classical models namely the Lorentz and Drude model. The so called JDOS model is founded on a quantum mechanical approach where the band character of electronic states in solid state materials is considered. Furthermore, we will briefly introduce an entirely theoretical approach to calculate the dielectric function of semiconductors according to ab-initio band structure calculations e. g. for group-III-nitrides. We summarise an empirical model that describes the effective dielectric function in heterogenous media. But, for a more detailed discussion about the principals of the dielectric function we would refer for example to a review about the "Optical Properties of Solids" that was published by Collins and Vedam [76] or to standard text books about this topic.

In the second part of this chapter we will introduce a mathematical method for the evaluation of the optical properties of layered sample structures. Especially for the determination of the two independent dielectric tensor components in biaxial anisotropic layers an advanced optical layer model is required. Thus, we use a known matrix formalism to deduce a special solution for the calculation of both components in our wurtzite nitride samples from appropriate ellipsometric measurements.

4.1 The dielectric function

The dielectric function is defined in the macroscopic electrodynamic model summarised in the Maxwell equations. These relations connect the electromagnetic fields $\vec{E}$ (macroscopic electric field strength), $\vec{D}$ (dielectric displacement), $\vec{B}$ (magnetic induction), $\vec{H}$ (magnetic field strength), and $\vec{J} = \sigma\vec{E}$ (current density). All higher order effects, as well as all magnetic effects can be neglected in the semiconductors under investigation. Thus, the field of the charge distribution in case of external electric fields is defined by the electric dipole concentration or the intrinsic polarisation P_e. The material equations, therefore, reduce in Fourier representation and in SI units to

$$\begin{aligned}\vec{D}[\omega] &= \varepsilon_0\vec{E}[\omega] + \vec{P}_e[\vec{E}[\omega],\omega] \\ &= \varepsilon_0(1+\chi_e[\omega])\vec{E}[\omega] = \varepsilon_0\varepsilon[\omega]\vec{E}[\omega] = \grave{\varepsilon}[\omega]\vec{E}[\omega] \\ \vec{B}[\omega] &= \mu_0\mu[\omega]\vec{H}[\omega] \approx \mu_0\vec{H}[\omega].\end{aligned} \tag{4.1}$$

Here the macroscopic electric field strength is connected with the displacement density by the free space permittivity ε_0 and the dielectric function ε. In this approximation the magnetic field strength is connected with the magnetic induction density just by the free space permeability μ_0. Hence, the permeability is assumed to be $\mu \approx 1$. The dielectric function

ε for absorbing materials is a complex quantity, which depends on angular frequency ω (the optical frequency $f = \omega/2\pi$). In case of anisotropic media this scalar dielectric function has to be replaced by a respective dielectric tensor. The related quantities $\chi_e[\omega]$ and $\sigma[\omega]$ are the electric susceptibility and the optical conductivity. But in order to regard the relation to electronic excitations in the investigated spectral range, we use in place of the angular frequency ω the photon energy $E = \hbar\omega$ in the units of electron volts (eV).

The solution of the wave equation deduced from the Maxwell relations are transversal electromagnetic (plane) waves of the form

$$\vec{E} = \vec{A}\,\mathrm{e}^{\mathrm{i}\,\omega(t-\frac{\tilde{n}}{c}r)}\,\mathrm{e}^{-\omega\frac{\kappa}{c}r} = \vec{A}\,\mathrm{e}^{\mathrm{i}\,\omega(t-\frac{n}{c}x)}, \tag{4.2}$$

where

$$\varepsilon = \varepsilon_1 - \mathrm{i}\,\varepsilon_2 = n^2 = \tilde{n}^2 - \kappa^2 - \mathrm{i}\,2\tilde{n}\kappa. \tag{4.3}$$

In this expressions n denotes the complex refractive index with $n = \tilde{n} + \mathrm{i}\,\kappa$, where $\tilde{n}$ is the (real) index of refraction and κ the (real) extinction coefficient. The complex refractive index is defined according to the ratio between v and c, which are the phase velocity in the dielectric medium and in vacuum.

$$c = 1/\sqrt{\varepsilon_0\mu_0} \tag{4.4}$$

$$v = \frac{1}{\sqrt{\varepsilon\,\varepsilon_0\mu\mu_0}} \approx \frac{1}{\sqrt{\varepsilon\,\varepsilon_0\mu_0}} = \frac{c}{\sqrt{\varepsilon}} = \frac{c}{n} \tag{4.5}$$

The Fresnel equations, as well as the law of refraction (eq. 3.3), finally, are results of the continuity condition at the boundaries of different materials.

The real and imaginary part of the optical properties, whether given by ε, n, or χ_e are not independent but connected through dispersion relations. This connection arise when e. g. the dielectric function is treated as a response function that associate the polarisation at the position r and the time t in terms of the electric field acting at all other positions and times. In the Fourier representation then the causality leads to the so called Kramers-Kronig relations [77] for the dielectric function.

$$\begin{aligned} \varepsilon_1[\omega] - 1 &= \frac{2}{\pi}\,\mathrm{P}\int_0^{+\infty} \frac{\omega'}{\omega'^2 - \omega^2}\varepsilon_2[\omega']d\omega' \\ \varepsilon_2[\omega] &= -\frac{2\omega}{\pi}\,\mathrm{P}\int_0^{+\infty} \frac{1}{\omega'^2 - \omega^2}\left(\varepsilon_1[\omega'] - 1\right)d\omega' \end{aligned} \tag{4.6}$$

P denotes in this relations the principle value of the integral.

4.1.1 Classical dispersion models

Two simple classical models can be used to describe the photon energy dependence of the complex dielectric function. These models explain already several aspects of the relationship of ε in the visible and VUV spectral range to the fundamental microscopic behaviour of electrons in solids. This is at first the Lorentz oscillator model for semiconductors and insulators. The Drude model is applicable to free electrons in metals. A superposition of different electronic states described by these models at the end is suitable to express the optical properties

of solids and metals. Both models base on the classical equation for the motion of an electron with the charge $-e$ and the mass m_e (a spherical charge distribution) bounded to a fixed nucleus in the solid with the charge $+e$. Under assumption of a time dependent external electric field $E[t] = E_0 e^{i\omega t}$ Newton's second law leads to the equation of a harmonic oscillator

$$m\frac{d^2\vec{r}}{dt^2} = eE[\omega] - m\omega_0^2\vec{r} - m\gamma\frac{d\vec{r}}{dt}, \tag{4.7}$$

where $\vec{r}$ is the displacement of the electron. The first term on the right hand side is the driving force generated by the external field. The second is the Hook's law restoring force with the force constant $m_e\omega_0^2$ and the third is a damping of the motion of the electron cloud given by a frictional constant γ. The displacement of electrons against the positive charged ions represents now a dipole moment, which can be translated in the macroscopic polarisation $P_e[\omega]$ by assuming N_e identical electrons per unit volume. With equation 4.1 and 4.7, thus, we receive the Lorentz model for the dielectric function of a single electronic state

$$\varepsilon[\omega] = 1 + \frac{\omega_p^2}{\omega_0^2 - \omega^2 - i\gamma\omega}. \tag{4.8}$$

$\omega_p^2 := (N_e e^2)/(m_e\varepsilon_0)$ is called the plasma frequency, which correspond to longitudinal collective oscillations in the charge density (plasmons) at this frequency. If an electronic system contains different electronic states, this model can be applied in a linear combination of the form

$$\varepsilon[\omega] = 1 + \omega_p^2 \sum_j f_j \frac{1}{\omega_j^2 - \omega^2 - i\gamma_j\omega}. \tag{4.9}$$

The oscillator strength f_i, of course, has to fulfil the sum rule

$$\sum_j f_j = N_e, \tag{4.10}$$

where N_e is the total number of electrons per unit volume. The Drude model for optically isotropic and nonmagnetic metals (free electrons) can be extracted by setting the restoring force in equation 4.7 equal to zero ($\omega_0 = 0$). Relation 4.8, thus, reduces to

$$\varepsilon[\omega] = 1 + \frac{i\omega_p^2}{\gamma\omega - i\omega^2}. \tag{4.11}$$

The respective characteristic photon energy dependence of the dielectric function ε and the reflectance R in case of the Lorentz, as well as the Drude like excitation is shown in figure 4.1 and 4.2. As demonstrated in the two examples the imaginary part of the dielectric function can assumed to be zero in both models at sufficiently high frequencies where all electrons behave like free electrons with $\varepsilon_1(\omega) = 1 - \omega_p^2/\omega 2$. This agreement together with the Kramers-Kronig relations [77] can be used to relate the optical properties to the concentration of electrons N_e that participate on transitions induced by the external electric field:

$$\int_0^\infty \omega'\varepsilon_2(\omega')d\omega' = \frac{\pi}{2}\omega_p^2 = \frac{\pi N_e e^2}{2\varepsilon_0 m_e}. \tag{4.12}$$

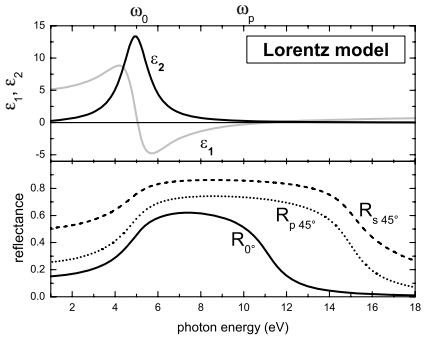

Figure 4.1:

Real (ε_1) and imaginary (ε_1) part of the dielectric function, as well as the absolute reflectance (R) at 0° and 45° for a single Lorentz oscillator with the resonance energy $\hbar\omega_0 = 5\,eV$, the broadening $\hbar\gamma = 1.5\,eV$, and the strength $\hbar\omega_p = 10\,eV$.

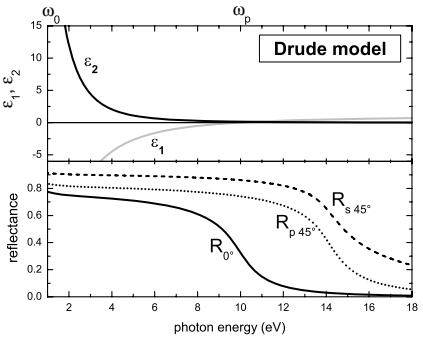

Figure 4.2:

Real (ε_1) and imaginary (ε_1) part of the dielectric function, as well as the absolute reflectance (R) at 0° and 45° for free electrons, according to the Drude model Again, the broadening $\hbar\gamma = 1.5\,eV$, and the strength $\hbar\omega_p = 10\,eV$ is assumed.

For practical use the infinite frequency could be replaced by finite value, which leads to cumulative integral for the effective number of electrons contributing to the optical properties in the investigated spectral:

$$N_{eff} = \frac{2V\varepsilon_0 m_e}{\pi e^2} \int_{\omega_b}^{\omega_e} \omega' \varepsilon_2(\omega') d\omega'. \tag{4.13}$$

In the latter relation V denotes the volume of the unit cell.

4.1.2 Electronic transitions in semiconductors

In the last paragraph the photon energy dependance of the dielectric function was explained in a classical approach for independent point charges (electrons) in the potential of a single nucleus. But in a real semiconductor, the potential of the single nucleus has to be replaced by a periodic potential of the ions in the crystal. The overlapping valence electrons delocalise and can be represented in a quantum mechanically approach by one electron Bloch waves with a defined wave vector $\vec{k}$ in the respective Brillouin zone. The energy dispersion of the corresponding bond energies of the occupied valence states and of the unoccupied conduction band states is shown e. g. for GaAs in figure 4.4. The dielectric function can be calculated in this model by quantum mechanical expressions for the complex polarisation in the presents of an electric field. In the electric dipole approximation the dielectric function, thus, is treated as a sum over absorptions due to transitions from valence bands to conduction bands at different

points of the Brillouin zone [78]:

$$\varepsilon[\omega] = 1 + \frac{1}{4\pi^3}\frac{e^2}{\varepsilon_0 m_e^2 \hbar^2}\sum_{c,v}\int_{B.Z.} \mathrm{d}^3\, k\ \frac{P_{cv}[\vec{k}]}{E_{cv}^2[\vec{k}]}\left(\frac{1}{\hbar\omega + E_{cv}[\vec{k}] + \mathrm{i}\,\Gamma} - \frac{1}{\hbar\omega - E_{cv}[\vec{k}] + \mathrm{i}\,\Gamma}\right). \tag{4.14}$$

$P_{cv}[\vec{k}]$ are the dipole transition matrix elements, which are defined by the respective dipole operator $e \cdot \vec{\mathbf{p}}$:

$$P_{cv}[\vec{k}] = \left| < \varphi_v[\vec{k}]|e \cdot \vec{\mathbf{p}}|\varphi_c[\vec{k}] > \right|^2. \tag{4.15}$$

This approximation considers already the fact that the $\vec{k}$ vector of the electromagnetic wave is very small in comparison to the size of the Brillouin zone, and thus, direct transition are only allowed between states with almost the same $\vec{k}$ vector. $\varphi_c[\vec{k}]$ and $\varphi_v[\vec{k}]$ are the electron wave functions with the respective energy difference $E_{cv}[\vec{k}]$. Γ denotes a broadening parameter, which relates to the life time broadening of the exited states ($\Gamma \sim \Delta E \sim \hbar/\Delta t$) plus various other independent broadening processes e. g. temperature effects due to the electron phonon coupling [79, 80]. The life time broadening could be also enlarged due to a small grain size in the material. The scattering at the grain boundaries leads to a reduced lifetime. However, since $\vec{k}$ is conserved in electronic transitions, the integration over the Brillouin zone can be convert to an integration over a surface S of a constant energy E_{cv} and an integration over all these energies E_{cv} [81]:

$$\varepsilon[\omega] = 1 + \frac{1}{4\pi^3}\frac{e^2}{\varepsilon_0 m_e^2 \hbar^2}\sum_{c,v}\int_0^\infty \mathrm{d}\, E_{cv}\ \ \frac{P_{cv}}{E_{cv}^2} J[E_{cv}]\left(\frac{1}{\hbar\omega + E_{cv} + \mathrm{i}\,\Gamma} - \frac{1}{\hbar\omega - E_{cv} + \mathrm{i}\,\Gamma}\right). \tag{4.16}$$

$J[E_{cv}]$ is the so called joint density of states (JDOS) between the valence and conduction bands

$$J[E_{cv}] = \int_{S_{E_{cv}}} \frac{\mathrm{d}\, k_1\, \mathrm{d}\, k_2}{\nabla_{\vec{k}} E_{cv}[\vec{k}]}\ . \tag{4.17}$$

Here, the dipole transition matrix element $P_{cv}[\vec{k}]$ of certain band pairs was assumed k- independent in a first approximation. According to relation 4.17 large contributions to the dielectric function are only expected for energies where $\nabla_{\vec{k}} E_{vc}[\vec{k}]$ is small or zero. Hence, absorption structures in the dielectric function are connected with areas or points in the band structure where the valence and conduction band pairs are parallel. These points are the so called critical points (CP) or van-Hove-singularities [82] and occur usually in the vicinity of high symmetry points in the Brillouin zone. Due to this finding the (measured) dielectric function can be analysed in terms of an association of absorption structure to specific band pairs at certain points or lines in the Brillouin zone. But for this kind of analysis usually at least the calculated/measured band structure [83] is needed. More detailed results are obtained from ab-initio calculations with subsequent band-to-band analysis where only single pairs of valence and conduction bands are used for the summation in equation 4.16 [84].

In this context it has to be noted that all measurements, which will presented in this work, are recorded at room temperature, and therefore, temperature effects have to be considered. This is of importance, in particular, within a comparison to results of band structure calculations, where the temperature is usually assumed to be zero and the electron phonon coupling

is neglected. The room temperature during the measurements, in general, leads to a red shift of transition energies and a broadening of the corresponding transitions [79, 80].

In the last two decades one of the most intensively investigated cubic materials, is the cubic GaAs. For this material the origin of structures in the dielectric function is well known already from various theoretical and experimental investigations. This correlation with distinct interband transitions is shown in figure 4.3 and 4.4. The labels E_0, E_0', E_1, E_1', and E_2 for the characteristic absorption structures correspond in the isoelectronic sequence scheme to peaks observed in earlier studies on Si, diamond or other zincblende materials [85, 86]. In these labels, the subscripts stand for transition points in specific k space directions. The 0 correspond to transitions at the Γ-point, the 1 to transitions at points along the [111] direction, and the 2 for those in the [100] direction of the zincblende k space. Within this notation the GaAs "E_1" transitions, e. g. are observed and well understood in terms of critical points or lines along the $[111]$ directions of the zincblende Brillouin zone. Whereas the "$E_1 + \Delta_1$" correspond to the dispartment of the same transition due to the spin-orbit splitting of the valence band.

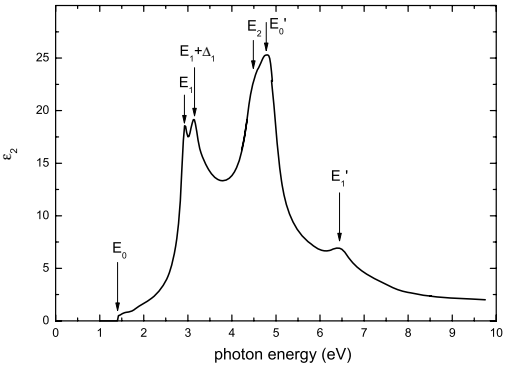

Figure 4.3:

Measured imaginary part of the dielectric function of GaAs [40, 87]. The labels refer to the interband transitions shown in Fig. 4.4.

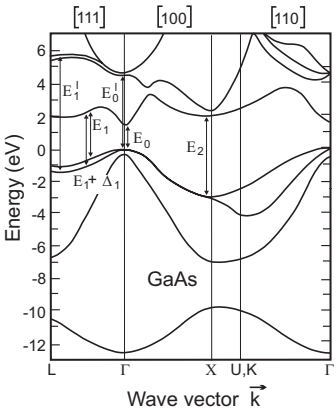

Figure 4.4:

Band structure of GaAs [83]. The transition at critical points, where pairs of valence and conduction bands are approximately parallel are indicated.

JDOS model

The JDOS model [81, 88] considers the dielectric function as a sum of contributions from allowed interband transitions at CP's. Therefore, only transitions at k-vectors close to CP's with $\nabla_{\vec{k}} E_{cv}[\vec{k}] = 0$ significantly contribute to the dielectric function. Under these circumstances it is sufficient to further approximate a parabolic dependency of $E_{cv}(\vec{k})$ if we neglect

higher terms in the series expansion:

$$E_{cv}[\vec{k}] = E_{CP} + \frac{\hbar}{2}\left(\frac{k_x^2}{\mu_{cv_x}} + \frac{k_y^2}{\mu_{cv_y}} + \frac{k_z^2}{\mu_{cv_z}}\right), \tag{4.18}$$

where

$$\mu_{cv}^{-1} = m_e^{-1} + m_h^{-1}. \tag{4.19}$$

Here μ_{cv}, m_e, and m_h are the reduced effective mass and the electron and hole effective mass, respectively. Hence, a CP can be classified with respect to the number of negative or positive reduced effective masses μ_{cv}. Totally negative reduced effective masses corresponds to a energy difference $E_{cv}[k]$ at a CP, which increases in all k directions. The other way round the band distance would decreases in all k directions if all components are positive. These two CP's are called M_0 and M_3. A combination of negative and positive reduced effective masses relates to saddle points. These CP's are called M_1 and M_2, respectively. The dimension of a CP is defined by the number of finite reduced effective masses α. An infinite mass component correlates with parallel bands in the respective direction.

The parabolic band approximation in equation 4.18 can be substituted into the integral of relation 4.14. Thus, we can deduce a simple analytical expression for the line shape of the dielectric function at a CP by neglecting the non resonant term and assuming a vanishing $\vec{k}$ dependence of the transition matrix element in the vicinity of the CP:

$$\varepsilon[\omega] = -Ae^{\mathrm{i}\,\varphi[s]}(\hbar\omega - E_{cv} + i\Gamma)^{\alpha/2-1}. \tag{4.20}$$

A is an amplitude factor proportional to the dipole transition matrix element:

$$A \sim \frac{P_{cv}}{E_{cv}^2} T_x T_y T_z\ , \qquad T_l = \begin{cases} \hbar^{-1}\sqrt{2|\mu_l|} \\ K_l \quad \text{for} \quad \mu_l^{-1} \equiv 0 \end{cases},$$

and $\varphi[s]$ is a phase factor with

$$\varphi[s] = \begin{cases} \frac{1}{2}(s-1)\pi + \varphi_E & \text{for} \quad \alpha = 1,3 \\ \frac{1}{2}\,s\,\pi + \varphi_E & \text{for} \quad \alpha = 0,2 \end{cases}.$$

In the case $\alpha/2 - 1 = 0$ the polynomial function has to be replaced by the natural logarithm of $(\hbar\omega - E_{cv} + i\Gamma)$. The characteristic line shapes of possible CP resonances in the dielectric function are shown in figure 4.5. Each of these CP's shows a specific photon energy dependency. For the upper most 0 dimensional CP all reduced effective masses are infinity, and thus, this corresponds to localised excitonic transitions. In fact, the deduced line shape of this CP is identical to those of the Lorentz oscillator model calculated with the classical description of a bounded electron in the potential of a nucleus. However, the line shape of all possible CP resonances in the JDOS model is defined now by six parameters:

α**:** dimension of the CP (number of finite reduced effective masses)

s**:** behaviour of the CP (M_s, number of negative reduced effective masses)

E_{cv}**:** resonance energy of the CP

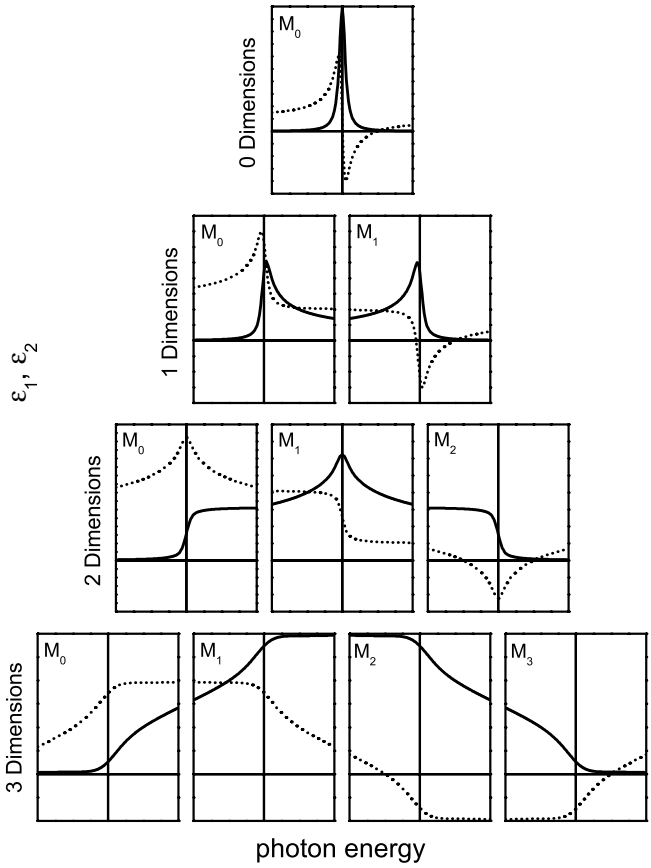

Figure 4.5: *Schematic dependence of the dielectric function in the vicinity of Van Hove singularities (i. e. interband critical points) for the real [dotted lines] and imaginary [full lines] part.*

Γ**:** broadening parameter

A**:** amplitude of the CP

φ_E**:** phase factor which describes the transformation in the behaviour of the CP' due to excitonic influences [89]

For the representation of e. g. the GaAs dielectric function a superposition of at least six CP's are necessary in order to represent the transitions at the Γ, X, L, and $\Gamma - L$ high symmetry points or lines. But even if the band structure of GaAs unambiguously claims a 3-dimensional

CP for the E_0 transition at the Γ point and a 2-dimensional CP for the E_1 transition at the L point, the measured dielectric function line shapes requires lower dimensional CP's. These differences are connected with excitonic effects and, thus, with the electron-hole coupling, which is not considered in a ground state band structure. The excitonic effects lead for instance to an intermixture of the line shapes of the M_0 and M_1 CP in the case of the E_0 3-dimensional CP. This results finally in a line shape similar to the 2-dimensional M_0 CP. Therefore, a determination of the undisturbed dimension by means of a CP analysis of the dielectric function is problematic. Furthermore, it is important that the given model does not consider constant offsets by neglecting the non nonresonant term in equation 4.14. Thus, we apply the JDOS model only to the third derivative of $\varepsilon_1(\omega)$ and $\varepsilon_2(\omega)$. In the third derivative spectra the constant, linear, as well as the quadratic terms are removed and features in the dielectric function appear more distinct than in the undifferentiated spectra. The line shapes of the third derivative of the CP's is demonstrated in figure 4.6. These line shapes, in fact, are also directly obtained in electro(photo)-reflectance experiments [88, 90], where a periodic variation of an external field leads to a modulation of the reflectivity, which can be detected e. g. with a lock-in amplifier.

We use the JDOS model for a detailed line shape evaluation of the measured dielectric functions in the third derivative of the spectra. Therefore, a numerical fit will applied where the number of CP's contributing to the spectrum, as well as the respective energy positions of those can be determined. The numerical fit will be started at first with a minimal number of CP's, which obviously included. These CP's are assumed in the beginning as 0 dimensional. The values for E_{CP}, Γ, A, and $\varphi(s)$ will be determined in a LevenbergMarquardt fit algorithm [91]. In following cycles we stepwise increase the dimension of CP's if the value for the phase factor $\varphi(s)$ is not in a physically meaningful range. By this approach we finally determine the minimal dimension of the CP. This is the minimum number of directions, where the used effective mass of the electrons/holes is finite at the respective CP´s. However, the chosen dimension does change significantly the determined energy positions of the CP. Basically only the oscillator strength and the broadening parameter are influenced if an admixed CP of a higher dimension is chose. In consideration of the uncertainties in the CP fit and due to the typical broadening of transition structures in the measured dielectric functions, we would estimate the error in the determined CP energies below ± 0.05 eV.

The chosen dimension does also not affect at the end the number of CP's needed for a good agreement between the JDOS model and the experiment. This number will be determined in a third step, where we compare the calculated and the measured dielectric function. If undetermined structures remain in the measured dielectric function additional CP's has to be included in the model.

For the analysis within the JDOS model we use a meanwhile commercially available software for the evaluation of optical multi layer systems [92].

4.1.3 Band structure calculations (for III-nitrides)

In paragraph 4.1.2 we attributed the dielectric function of semiconductors to transitions between certain bands at specific points of the Brillouin zone in the empirical JDOS model. Ab-initio band structure calculations and the respective calculated dielectric functions can provide a very fundamental understanding of electronic transitions in a comparison with the experimental results.

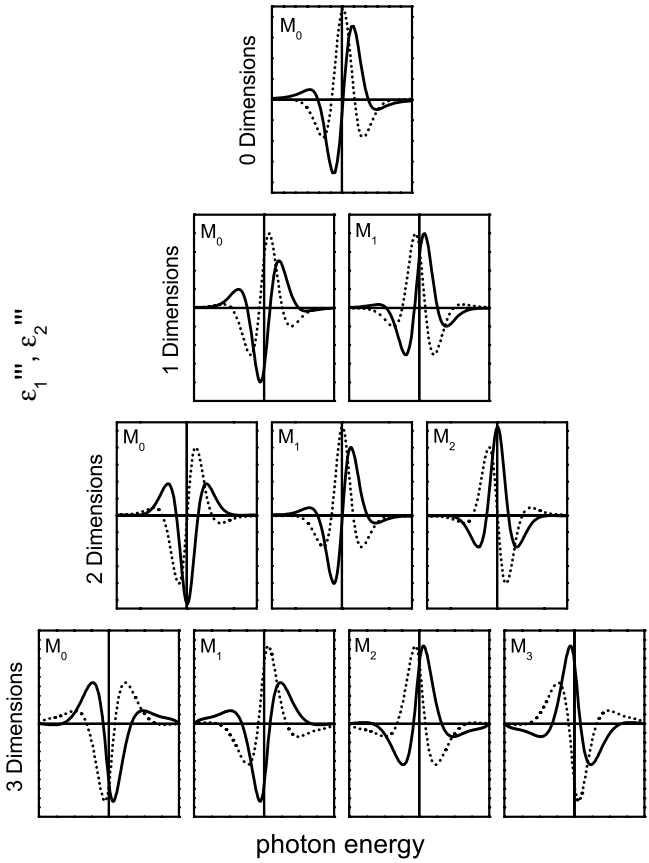

Figure 4.6: *Schematic dependence of the third derivatives of the dielectric functions in the vicinity of Van Hove singularities (i. e. interband critical points) for the real [dotted lines] and imaginary [full lines] part.*

A very successful method for the ab-intio calculation of the band structure is the density functional theory (DFT) [93]. All band structure calculation presented in this work are based on this method. In the density functional theory the system of N interacting electrons in the semiconductor is described by an effective single particle equation, the Kohn Sham equation. The effective potential in this specific Schrödinger equation includes the external potential of the ions (atomic core + core electrons) and two further contributions that account the interaction of the electrons. The first is the Hartree potential and the second is the so called exchange and correlation potential, which is in general unknown but often approximated in the so called local density approximation (LDA) [93]. Within this theory ground state

properties (equilibrium properties) are exactly determined. These are for example the atomic structure, lattice parameters, total energy, and the ground state band structure.

But for the calculation of the dielectric function, several further effects have to be taken into account, which are not included in the pure ground state electronic band structure. In the investigated spectral range the dielectric function is defined by electronic transitions. Therewith, correlated excited states are involved and quasi particle effects have to be considered. This includes a self energy, which is attributed to single particle excitations (additional electrons or holes) and to excitonic effects, which are attributed to two particle excitations (to the electron-hole pair interaction). The effect on the CP transitions and, thus, the optical properties are remarkable. The energetic position, as well as the oscillator strength could be strongly influenced. Therefore, these quasi particle effects have to be subsequently considered in the theory as correction terms. An exact common solution of the whole problem was not possible until now. But in contrast to the experiment, it is possible to separate the band-to-band and the corresponding CP contributions in the overall dielectric function. Therefore, we use later in this work the comparison of theoretical and our experimental results to evaluate the origin of specific structures in the measured dielectric function.

The calculated ground state electronic band structure of all three investigated III-nitrides in the wurtzite and in the zincblende crystal structure is shown in figure 4.7. These calculations of Christensen et. al. [94] were made by means of DFT-LDA with the so called "linear muffin-tin-orbital (LMTO) method in the atomic-sphere approximation (ASA)". The Ga3d states and In4d states, respectively, were included as additional band states to account the influence of those semi-core electrons. Unfortunately, they are not drawn in the original published band structure. Therefore, we subsequently add these states to the diagrams with respect to recent results of Bechstedt et. al. [97] in order to illustrate the character and the energy position. The calculation for the hexagonal structure was performed under the assumption that the crystal has a perfect wurtzite structure. The c/a ratio in this crystals is equal to 1.633 . The calculated wurtzite band structures clearly demonstrate already the increased number of electronic states and, thus, the increased number of possible electronic transitions. The additional states and transitions in the wurtzite crystal relate to the reduced symmetry and to the larger unit cell (larger Brillouin zone) of wurtzite polytypes. On the other hand the number of allowed transitions reduces, if we consider that the optical properties are dominated by dipole transitions with the electric field vector either parallel or perpendicular to the c axis. This selection relates to the symmetry of the involved valence and conduction bands and respective selection rules. The symmetry of the electronic states can be represented by certain numbers, which indicate the irreducible representations at the respective symmetry points [84, 97]. In figure 4.7 this labels are shown e. g. for GaN. The corresponding band structures of InN and AlN are in principal quite similar and the symmetry character of the bands is therefore the same. The allowed transitions according to dipole selection rules are summarised in table 4.1 [84, 98] for the two different polarisations of the light. Further restrictions (attenuations) for expected interband transitions can be explained, if the underlaying atomic orbital character is considered. The influence of the angular momentum is still present in the corresponding interband transition matrix elements although these former atomic orbitals are strongly perturbed in a crystal. In figure 4.7, we show the main contributions of the former atomic orbitals to the valence bands (bonding orbitals) and conduction bands (antibonding orbitals) at the right hand side of each calculated band structure. This assignment is supposed to illustrate the p- and s-character of the upper most valence bands

and the lowest conduction bands, respectively [99–101]. According to the atomic dipole selection rule $l = \pm 1$ for the angular momentum, transitions between those bands are favoured whereas transitions to higher conduction bands with a more p-like character are suppressed.

	$E \perp c$	$E \parallel c$
Γ and $\Delta \equiv \Gamma - A$	1-6, 2-6, 3-5, 4-5, 5-6	1-1, 2-2, 3-3, 4-4, 5-5, 6-6
M and $U \equiv M - L$	1-2, 1-3, 2-4, 3-4	1-1, 2-2, 3-3, 4-4
K, $T \equiv \Gamma - K$, and $P \equiv K - H$	1-3, 2-3, 3-3	1-1, 2-2, 3-3
$\Sigma \equiv \Gamma - M$	1-2, 1-1, 2-2	1-1, 2-2, 3-3

Table 4.1: *Allowed transitions in the wurtzite band structure [84, 98]. The numbers indicate the irreducible representations at the respective symmetry points in the band structure [78, 97].*

As mentioned already in paragraph 4.1.2 characteristic structures in the dielectric function above the fundamental band gap energy basically correlate with electronic transitions at high symmetry lines or points in the Brillouin zone. But a clear assignment is problematic especially for complicated band structures. The particular position of the transition in the Brillouin zone is not accessible by optical experiments like the spectroscopic ellipsometry. Whereas the exact energy position could be inaccurate in the band structure calculations due to the quasi particle effects. However, the agreement of the already measured $\varepsilon_\perp$ dielectric tensor component ($\vec{E} \perp c$) of wurtzite GaN with corresponding results of band structure calculations is very good [38] (fig. 4.8) and was used already for an assignment of CP to high symmetry points in the Brillouin zone. But the general relation of the respective CP in $\varepsilon_\parallel$ ($\vec{E} \parallel c$) (known only from theory so far) or in the zincblende dielectric function was unknown until now. Therefore, the labels for the main features in the dielectric function were commonly chosen simple in an ascending order (E_0, E_1, E_2, ...). In this work, however, we introduce a different notation, which correspond to the symmetry of the CP's.

4.1.4 Effective medium dielectric function

In the preceding paragraphs of this chapter we assume homogeneous bulk materials for the discussion of the optical properties. But in reality, the optical properties often originate from heterogenous or composite systems, which are more accurately described as a mixture of separated regions of at least two different materials. If the characteristic dimensions of the microstructure are on the one hand large enough ($\gtrsim 10\text{Å}$) so that the individual dielectric properties are preserved and on the other hand small compared with the wavelength ($\lesssim 0.1\lambda$), the optical properties of those materials can be calculated within the so called effective medium theory. Due to screening effects (local field effects), the resulting dielectric function is not simply the average of the dielectric functions of the constituting materials. But depending on the certain microstructure, some simple representation can be obtained from a generic formula proposed by Aspnes [42, 102]:

$$\frac{\varepsilon - \varepsilon_h}{\varepsilon + 2\varepsilon_h} = f_a \frac{\varepsilon_a - \varepsilon}{\varepsilon_a + 2\varepsilon} + f_b \frac{\varepsilon_b - \varepsilon}{\varepsilon_b + 2\varepsilon} \ldots \tag{4.21}$$

where ε_a, ε_b and f_a, f_b are the dielectric function and volume fractions of the inclusions a and b in a host material with the dielectric function ε_h. The Maxwell-Garnet expression ($\varepsilon_h = \varepsilon_a$ or ε_b), for instance, describes the averaged electrostatic solution of dielectric spheres in a dielectric host. In the effective medium theory according to Bruggeman [103] (EMA, Effective Medium Approximation) a self-consistent solution with $< \varepsilon >= \varepsilon_h$ leads to an expression suitable for random configurations:

$$0 = f_a \frac{\varepsilon_a - \varepsilon}{\varepsilon_a + 2\varepsilon} + f_b \frac{\varepsilon_b - \varepsilon}{\varepsilon_b + 2\varepsilon} \tag{4.22}$$

This is a complex quadratic relation, which we can rewrite in the form [61, 104]

$$\begin{gathered} \varepsilon^2 + z\,\varepsilon - \frac{\varepsilon_a \varepsilon_b}{2} = 0 \\ z = \frac{(f-2)\varepsilon_b + (1-2f)\varepsilon_a}{2(f+1)}, \qquad f = \frac{f_a}{f_b}, \end{gathered} \tag{4.23}$$

where the positive root relates to the physical solution.

$$\begin{aligned} \mathrm{Re}[\varepsilon] &= \frac{1}{2}\left(-\mathrm{Re}[z] + \mathrm{Re}\left[\sqrt{z^2 + 2\varepsilon_a\varepsilon_b}\right]\right) \\ \mathrm{Im}[\varepsilon] &= \frac{1}{2}\left(-\mathrm{Im}[z] + \mathrm{Re}\left[\sqrt{z^2 + 2\varepsilon_a\varepsilon_b}\right]\right) \end{aligned} \tag{4.24}$$

4.2 Layered sample structures

4.2.1 Isotropic layers

A general problem in the determination of optical properties e. g. by ellipsometry is the fact that the samples under investigation usually can not be assumed as half infinite materials with a "perfect" surface. Quite in contrary, the samples consist very often of at least one finite layer. Thus, the measured optical properties are not only determined by the dielectric function of one material. As mentioned already in paragraph 3.1 the deduced optical properties are rather effective optical properties (pseudodielectric functions) and would also include the respective geometry of the layered structure.

In particular the III-nitrides investigated in this work are only thin films from several 100 nm up to a couple of μm on a certain substrate. But not only the film structure requires a layer model. Furthermore, unintentional surface contaminations or at least a surface roughness [105] must be considered. These surface contributions lead to a broadening and damping of absorption structures in the measured pseudodielectric function in case of very thin overlayers [106, 107].

This problem can be addressed in a simple algebraic expression, if only one (over-)layer on a half infinite substrate is assumed and if the layer, as well as the substrate are optically isotropic. In this case the so called 3-phase model can be used in order to calculate the ellipsometric ratio as defined already in the respective 2-phase model in paragraph 3.1 [13, 59]:

$$\rho := \frac{r_{01_p} + r_{12_p} e^{i\,2\beta}}{1 + r_{01_p}\, r_{12_p} e^{i\,2\beta}} \frac{1 + r_{01_s}\, r_{12_s} e^{i\,2\beta}}{r_{01_s} + r_{12_s} e^{i\,2\beta}} \tag{4.25}$$

The reflection coefficients $r_{01_{p/s}}$ and $r_{12_{p/s}}$ of the corresponding reflections on the ambient layer boundary and the layer substrate boundary are defined by the Fresnel equations (equ. 3.3). The including phase shift β is given by:

$$\beta = 2\pi \frac{d_{layer}}{\lambda} \sqrt{\varepsilon_{layer} - \varepsilon_{ambient} \sin^2 \phi} \,. \tag{4.26}$$

λ is the wave length of the light in vacuum, d_{layer} the layer thickness, and ϕ the angle of incidence. But nevertheless, in this approach, additional ellipsometric measurements are necessary to determine the extra parameters.

For the description of multilayer systems or for anisotropic layers, however, a more general formalism based on an matrix representation of each boundary reflection is necessary [59, 61, 108].

4.2.2 Surface roughness

As noted above, a unintentional surface roughness effects the optical properties measured by ellipsometry. In a commonly used approximation this surface roughness is treated as a surface heterogenous layer. In this layer the substrate material and the ambient (air or vacuum) contribute in a random distribution to an effective medium dielectric function according to the EMA of Bruggeman (para. 4.1.4) [102]. The volume fraction in this model is usually assumed with 50%. Under these conditions the effective medium dielectric function of the introduced surface layer simplifies to

$$\begin{aligned} \mathrm{Re}[\varepsilon] &= \frac{1}{8}\left(1 + \mathrm{Re}[\varepsilon_s] + \mathrm{Re}\left[\sqrt{1 + 34\varepsilon_s + \varepsilon_s^2}\right]\right) \\ \mathrm{Im}[\varepsilon] &= \frac{1}{8}\left(\mathrm{Im}[\varepsilon_s] + \mathrm{Re}\left[\sqrt{1 + 34\varepsilon_s + \varepsilon_s^2}\right]\right) \end{aligned} \tag{4.27}$$

The relation comprise only the dielectric function of the underlying substrate material ε_s, whereas the ambient dielectric function was assumed with $\varepsilon_{ambient} = 1$. This surface layer dielectric function can be substituted in equation 4.25 of the 3-phase model. Apart from the wanted dielectric function of the substrate, these equations include the layer thickness and the measured ellipsometric ratio. For the layer thickness we can use the root mean square roughness (RMS-roughness) value as calculated e. g. from AFM scans of the sample surface [102]. By determination of this last unknown value, finally, the dielectric function of the substrate material can directly calculated from the ellipsometric measurement.

But the application of the RMS-roughness measured by AFM as a thickness of a model EMA-layer is connected to some general assumptions. The size of the effective surface microstructure has to be small in comparison to the wavelength ($\lesssim 0.1\lambda$). This requirement was demanded already for application of effective medium models. A sufficient limitation to appropriate microstructure in a AFM determination of the RMS-roughness can be achieved by a limitation of the scan areas. The scan area, which shall be used for the RMS-roughness calculation, must by smaller than $1\times1\,\mu$m in case of the visible and VUV spectral range. In combination with the commonly applied quadratic line by line smoothing of the AFM images, hence, we achieve the RMS value for microstructures smaller than $\lambda/10$ but with an acceptable averaging over the scan range. In order to achieve appropriate mean value, however, we determine and calculate the RMS-roughness for a couple of AFM scans on different surface regions.

4.2.3 Anisotropic layers

For the mathematical description of arbitrarily anisotropic materials we assume a stack of homogeneous anisotropic layers with plane parallel interfaces. A incident light beam is assumed as a monochromatic plane wave coming from an isotropic ambient medium at a given angle of incidence. The z-axis of the reference cartesian coordinate system is chosen normal to the interfaces. The x-axis is chosen parallel to the interfaces and the plane of incidence (see fig. 4.9). According to Berreman, the propagation of light in each arbitrarily anisotropic homogeneous layer can be described in terms of 4×4 matrix formalism [47, 59, 109–111]. Within this model, plane parallel electromagnetic waves with a time dependence represented by $\exp[\mathrm{i}(kx - \omega t)]$ are assumed. Therefore, the two Maxwell's "curl" equations reduce to

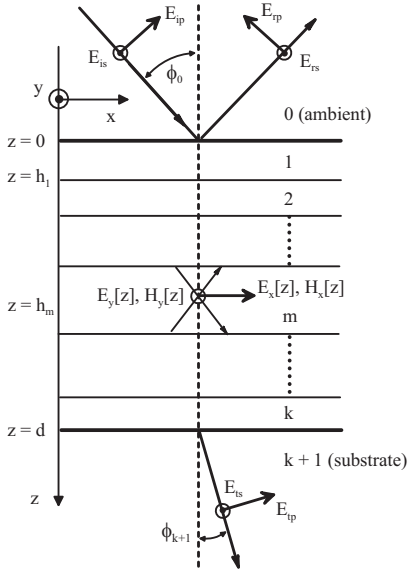

Figure 4.9:
Plane wave components in a stack of homogeneous anisotropic layers with plane parallel interfaces.

$$\nabla \times \vec{E} = -\frac{\mathrm{i}\,\omega}{c}\vec{B}\,, \qquad \nabla \times \vec{H} = \frac{\mathrm{i}\,\omega}{c}\vec{D}\,, \tag{4.28}$$

where $\vec{E}$, $\vec{D}$, $\vec{H}$, and $\vec{B}$ denote the electromagnetic field vectors. In agreement with the deviation of Berreman and for simplification of the following expressions, the Maxwell equations are written in Gaussian units in this paragraph. In cartesian coordinates the two Maxwell equations can be combined in a matrix form

$$\begin{pmatrix} 0 & 0 & 0 & 0 & -\frac{\partial}{\partial z} & \frac{\partial}{\partial y} \\ 0 & 0 & 0 & \frac{\partial}{\partial z} & 0 & -\frac{\partial}{\partial x} \\ 0 & 0 & 0 & -\frac{\partial}{\partial y} & \frac{\partial}{\partial x} & 0 \\ 0 & \frac{\partial}{\partial z} & -\frac{\partial}{\partial y} & 0 & 0 & 0 \\ -\frac{\partial}{\partial z} & 0 & \frac{\partial}{\partial x} & 0 & 0 & 0 \\ \frac{\partial}{\partial y} & -\frac{\partial}{\partial x} & 0 & 0 & 0 & 0 \end{pmatrix} \begin{pmatrix} E_x \\ E_y \\ E_z \\ H_x \\ H_y \\ H_z \end{pmatrix} \mathrm{e}^{\mathrm{i}\,\omega t} = \frac{\mathrm{i}\,\omega}{c} \begin{pmatrix} D_x \\ D_y \\ D_z \\ B_x \\ B_y \\ B_z \end{pmatrix} \mathrm{e}^{\mathrm{i}\,\omega t}\,. \tag{4.29}$$

This relation can be rewritten as

$$\bar{O}\vec{G} = \frac{\mathrm{i}\,\omega}{c}\vec{C}\,, \tag{4.30}$$

by definition of a 6×6 matrix operator $\bar{O}$ and the two column vectors $\vec{G}$, $\vec{C}$, whose elements are the time independent cartesian field components. The connection of the two vectors $\vec{G}$ and $\vec{C}$ is given by the Maxwell relations. Neglecting nonlinear optical effects, these equations

can also be combined in a 6×6 matrix form:

$$\bar{M} = \begin{pmatrix} \bar{\varepsilon} & \bar{\rho} \\ \bar{\rho}' & \bar{\mu} \end{pmatrix} \text{ and} \tag{4.31}$$

$$\vec{C} = \bar{M}\vec{G}\,. \tag{4.32}$$

The sub-matrices $\bar{\varepsilon}$ and $\bar{\mu}$ of the matrix $\bar{M}$ are the dielectric and magnetic tensors, respectively. $\bar{\rho}$ and $\bar{\rho}'$ denote optical rotation tensors. If eq. 4.32 is substituted into eq. 4.30, the resulting relation represent the spatial wave equation for the frequency ω.

$$\bar{O}\vec{G} = \frac{\mathrm{i}\,\omega}{c}\bar{M}\vec{G} \tag{4.33}$$

According to the symmetry of the investigated problem, it is sufficient to assume that there is no alteration of the time independent field components along the y direction and $\partial/\partial y = 0$. For a certain angle of incidence, the x components of the field are found with spatial variation given by $\exp[-\mathrm{i}\,\xi x]$ so that $\partial/\partial x = -\mathrm{i}\,\xi$. ξ is the x component of the wave vector defined by the refractive index of the ambient n_0 and the angle of incidence ϕ_0.

$$\xi = \frac{\omega}{c} n_0 \sin\phi_0 = k \sin\phi_0 \tag{4.34}$$

With these simplifications the six independent differential equations of relation 4.33 reduce to four linear homogeneous first-order differential equations, which can be combined in a 4×4 matrix form

$$\frac{\partial}{\partial z}\begin{pmatrix} E_x \\ E_y \\ H_x \\ H_y \end{pmatrix} = \frac{\mathrm{i}\,\omega}{c}\begin{pmatrix} \Delta_{11} & \Delta_{12} & \Delta_{13} & \Delta_{14} \\ \Delta_{21} & \Delta_{22} & \Delta_{23} & \Delta_{24} \\ \Delta_{31} & \Delta_{32} & \Delta_{33} & \Delta_{34} \\ \Delta_{41} & \Delta_{42} & \Delta_{43} & \Delta_{44} \end{pmatrix}\begin{pmatrix} E_x \\ E_y \\ H_x \\ H_y \end{pmatrix} \text{ or shortened} \tag{4.35}$$

$$\frac{\partial}{\partial z}\vec{\psi} = \frac{\mathrm{i}\,\omega}{c}\bar{\Delta}\vec{\psi} \tag{4.36}$$

The field components parallel to the z axis are not longer independent and can be calculated as a function of the four field components E_x, E_y, H_x, and H_y solved in the generalised field vector $\vec{\psi}$. Equation 4.36 is a wave equation representing the variation of the generalised field vector in the z direction. The included 4×4 propagation matrix of the medium $\bar{\Delta}$ is determined by the elements of the 6×6 optical matrix $\bar{M}$ (eq. 4.31). For a homogeneous non magnetic material ($\bar{\mu} = \bar{E}$) without an optical rotation ($\bar{\rho} = 0$), the matrix components of $\bar{\Delta}$ are assigned as following [111]:

$$\bar{\Delta} = \begin{pmatrix} -\eta\frac{\varepsilon_{31}}{\varepsilon_{33}} & -\eta\frac{\varepsilon_{32}}{\varepsilon_{33}} & 0 & 1-\frac{\eta^2}{\varepsilon_{33}} \\ 0 & 0 & -1 & 0 \\ \varepsilon_{23}\frac{\varepsilon_{31}}{\varepsilon_{33}} - \varepsilon_{21} & \eta^2 - \varepsilon_{22} + \varepsilon_{23}\frac{\varepsilon_{32}}{\varepsilon_{33}} & 0 & \eta\frac{\varepsilon_{23}}{\varepsilon_{33}} \\ \varepsilon_{11} - \varepsilon_{13}\frac{31}{33} & \varepsilon_{12} - \varepsilon_{13}\frac{\varepsilon_{32}}{\varepsilon_{33}} & 0 & -\eta\frac{\varepsilon_{13}}{\varepsilon_{33}} \end{pmatrix} \tag{4.37}$$

$$\eta = \frac{c}{\omega}\xi = n_0 \sin\phi_0$$

The components of the orientation dependent dielectric tensor used in equation 4.31 and 4.37 are chosen in a cartesian coordinate system introduced above. This coordinate system is not necessarily the intrinsic eigensystem of the anisotropic material. The matrix transformation between a cartesian crystal coordinate system and the used laboratory coordinate system is given by an orthogonal rotation matrix defined by the three Euler angles. In the special case, where the crystal axes are parallel to the chosen laboratory coordinate axis the non diagonal dielectric tensor components disappear and $\bar{\Delta}$ can be further simplified. However, if $\bar{M}$ and $\bar{\Delta}$, respectively, are constant over an interval along z, equation 4.36 is directly integrable and yields to

$$\vec{\psi}[z+h] = \bar{L}\vec{\psi}[z], \tag{4.38}$$

where

$$\bar{L} = \mathrm{e}^{\frac{\mathrm{i}\omega}{c}h\bar{\Delta}} = \left(\bar{E} + \frac{\mathrm{i}\,\omega}{c}h\bar{\Delta} - \frac{1}{2!}\left(\frac{\omega h}{c}\right)^2\bar{\Delta}^2 - \frac{1}{3!}\left(\frac{\omega h}{c}\right)^3\bar{\Delta}^3 + \ldots\right) \tag{4.39}$$

is defined as the partial transfer matrix of the layer. In case of a multi layer system the connection of electric and magnetic fields between the two surfaces at $z = 0$ and $z = d$ is obtained by a recursive application of the partial transfer matrix corresponding to each layer.

$$\bar{\mathcal{L}} = \prod_i \bar{L}_i. \tag{4.40}$$

The generalised field vector for the two surfaces at $z = 0$ and $z = d$ are, therefore, connected by a total transfer matrix $\bar{\mathcal{L}}$ given as a product of the partial transfer matrices $\bar{L}_i$ for each layer.

$$\vec{\psi}[d] = \bar{\mathcal{L}}\vec{\psi}[0]. \tag{4.41}$$

The incident, reflected and transmitted plane electromagnetic waves in an isotropic ambient or substrate, respectively, are commonly described by the two electric field components parallel and perpendicular to the plane of incidence. In addition, the angle of incidence or the angle of refraction, respectively, are used as a third parameter to verify the direction of propagation in the three dimensional space. Both field components are independent, perpendicular to the wave vector and can be combined in the so called Jones vector. This representation is finally used for the calculation of the pseudodielectric function from an ellipsometric measurement according to equation 3.4. The related coordinate system is coupled to the direction of propagation and changes in each layer, according to the angle of refraction given by the Snell's law (eq. 3.3). By the definition of the generalised field vector $\vec{\psi}$ (eq. 4.36), this representation is transferred into a fixed coordinate system coupled to the boundaries of the sample and the plane of incidence. Instead of the three parameters consisting of the transversal electric field components and the angle of incidence, the plane electromagnetic wave is represented by two electric field components and two magnetic field components parallel to the sample boundaries. It should be noticed that in non magnetic materials the forth parameter is redundant. This is also seen in the related propagation matrix $\bar{\Delta}$ (eq. 4.37). The "direction of propagation" in each layer again depends on the optical properties of the layer.

For the computation of the optical properties measured by ellipsometry, reflectance or transmission measurements, it is convenient to translate the generalised field vectors $\vec{\psi}$ at the two surfaces at $z = 0$ and $z = d$ in the associated Jones vectors or the related field

components. Due to the continuity of the tangential field components at an interface, the generalised field vector $\vec{\psi}$ is constant across the boundary and can be divided in an incident and reflected part.

$$\vec{\psi}[0^+] = \vec{\psi}[0^-] = \vec{\psi}_i[0^-] + \vec{\psi}_r[0^-] \tag{4.42}$$

The $-$ and $+$ superscripts distinguish the ambient and the layer side of the boundary. Accepting that there exists no incident wave in the substrate, the generalised field vector on the substrate boundary is given by

$$\vec{\psi}[d^-] = \vec{\psi}_t[d^+] \tag{4.43}$$

The components of the Jones vectors associated to the incident, reflected and transmitted waves, are assumed to be (E_{ip}, E_{is}), (E_{rp}, E_{rs}), and (E_{tp}, E_{ts}), as shown in figure 4.9. In non magnetic optically isotropic materials, the magnetic field components are related to the electric field components through the index of refraction n

$$\frac{H_p}{E_s} = \frac{H_s}{E_p} = n. \tag{4.44}$$

Using equation 4.44, the projection of these field components in the generalised field vectors $\vec{\psi}_i$, $\vec{\psi}_r$, and $\vec{\psi}_t$ leads to

$$\vec{\psi}_i = \begin{pmatrix} E_{ip}\cos\phi_0 \\ E_{is} \\ -n_a E_{is}\cos\phi_0 \\ n_a E_{ip} \end{pmatrix}, \quad \vec{\psi}_r = \begin{pmatrix} -E_{rp}\cos\phi_0 \\ E_{rs} \\ n_a E_{rs}\cos\phi_0 \\ n_a E_{rp} \end{pmatrix}, \text{ and } \quad \vec{\psi}_t = \begin{pmatrix} E_{tp}\cos\phi_0 \\ E_{ts} \\ -n_s E_{ts}\cos\phi_0 \\ n_s E_{tp} \end{pmatrix} \tag{4.45}$$

n_a and n_s denote the index of refraction in the isotropic ambient and substrate, respectively. The algebraic signs are defined by the definition of the parallel and perpendicular directions as shown in figure 4.9. This definition is based on the convention that $\vec{E} \times \vec{H}$, is showing in the direction of the propagation. According to equations 4.42 and 4.43, the substitution of equations 4.45 into equations 4.41 presents the connection of the electric field component in the ambient and the substrate.

$$\begin{pmatrix} E_{tp}\cos\phi_0 \\ E_{ts} \\ -n_s E_{ts}\cos\phi_0 \\ n_s E_{tp} \end{pmatrix} = \begin{pmatrix} \mathcal{L}_{11} & \mathcal{L}_{12} & \mathcal{L}_{13} & \mathcal{L}_{14} \\ \mathcal{L}_{21} & \mathcal{L}_{22} & \mathcal{L}_{23} & \mathcal{L}_{24} \\ \mathcal{L}_{31} & \mathcal{L}_{32} & \mathcal{L}_{33} & \mathcal{L}_{34} \\ \mathcal{L}_{41} & \mathcal{L}_{42} & \mathcal{L}_{43} & \mathcal{L}_{44} \end{pmatrix} \begin{pmatrix} (E_{ip} - E_{rp})\cos\phi_0 \\ E_{is} + E_{rs} \\ (E_{rs} - E_{is}) n_a \cos\phi_0 \\ (E_{ip} + E_{rp}) n_a \end{pmatrix} \tag{4.46}$$

Relation 4.46 represents a set of four linear equations. The electric field components of the transmitted wave can be easily eliminated by the combination of the first with the third, and the second with the last equation, deduced from relation 4.46. Therefore, the field components of the incident and the reflected wave are connected by two linear equations:

$$\begin{aligned} 0 &= a_{ip}E_{ip} + a_{is}E_{is} + a_{rp}E_{rp} + a_{rs}E_{rs}, \\ 0 &= b_{ip}E_{ip} + b_{is}E_{is} + b_{rp}E_{rp} + b_{rs}E_{rs}, \end{aligned} \quad \text{where} \tag{4.47}$$

$$
\begin{aligned}
a_{ip} &= \mathcal{L}_{14} n_a n_s - \mathcal{L}_{44} n_a \cos\phi_0 + \mathcal{L}_{11} n_s \cos\phi_0 - \mathcal{L}_{41} \cos\phi_0^2, \\
a_{is} &= \mathcal{L}_{12} n_s - \mathcal{L}_{42} \cos\phi_0 - \mathcal{L}_{13} n_a n_s \cos\phi_0 + \mathcal{L}_{43} n_a \cos\phi_0^2, \\
a_{rp} &= \mathcal{L}_{14} n_a n_s - \mathcal{L}_{44} n_a \cos\phi_0 - \mathcal{L}_{11} n_s \cos\phi_0 + \mathcal{L}_{41} \cos\phi_0^2, \\
a_{rs} &= \mathcal{L}_{12} n_s - \mathcal{L}_{42} \cos\phi_0 + \mathcal{L}_{13} n_a n_s \cos\phi_0 - \mathcal{L}_{43} n_a \cos\phi_0^2, \\
b_{ip} &= -\mathcal{L}_{34} n_a - \mathcal{L}_{31} \cos\phi_0 - \mathcal{L}_{24} n_a n_s \cos\phi_0 - \mathcal{L}_{21} n_s \cos\phi_0^2, \\
b_{is} &= -\mathcal{L}_{32} + \mathcal{L}_{33} n_a \cos\phi_0 - \mathcal{L}_{22} n_s \cos\phi_0 + \mathcal{L}_{23} n_a n_s \cos\phi_0^2, \\
b_{rp} &= -\mathcal{L}_{34} n_a + \mathcal{L}_{31} \cos\phi_0 - \mathcal{L}_{24} n_a n_s \cos\phi_0 + \mathcal{L}_{21} n_s \cos\phi_0^2, \\
b_{rs} &= -\mathcal{L}_{32} - \mathcal{L}_{33} n_a \cos\phi_0 - \mathcal{L}_{22} n_s \cos\phi_0 - \mathcal{L}_{23} n_a n_s \cos\phi_0^2.
\end{aligned}
\tag{4.48}
$$

These relations can be resolved in a form, in which the Jones vectors of the incident and reflected wave are connected by a complex reflection matrix $\bar{r}$, the so called Jones matrix of the layered system (sample).

$$
\begin{pmatrix} E_{rp} \\ E_{rs} \end{pmatrix} = \bar{r} \begin{pmatrix} E_{ip} \\ E_{is} \end{pmatrix} = \begin{pmatrix} r_{pp} & r_{ps} \\ r_{sp} & r_{ss} \end{pmatrix} \begin{pmatrix} E_{ip} \\ E_{is} \end{pmatrix} \tag{4.49}
$$

The reflection matrix is defined by the total transfer matrix $\bar{\mathcal{L}}$ of the anisotropic layers, the index of refraction of the isotropic ambient n_a, the index of refraction of the isotropic substrate n_s and the angle of incidence ϕ_0. Using the abbreviation of equation 4.48, the matrix is given by

$$
\bar{r} = \frac{1}{a_{rs} b_{rp} - a_{rp} b_{rs}} \begin{pmatrix} (a_{ip} b_{rs} - a_{rs} b_{ip}) & (a_{is} b_{rs} - a_{rs} b_{is}) \\ (a_{rp} b_{ip} - a_{ip} b_{rp}) & (a_{rp} b_{is} - a_{is} b_{rp}) \end{pmatrix}. \tag{4.50}
$$

With the latter reflection (Jones) matrix, the polarisation properties of a sample as measured in a reflection experiment are connected to the internal sample structure and the respective layer dielectric tensor components. The associated Jones matrix for transmitted light can be derived from eq. 4.46 in a similar manner as shown here for the reflection matrix. After an algebraic or numerical inversion, this matrix expression can be used for the evaluation of the sample properties from a reflection and transmission experiment, respectively.

The given description does not include depolarisation effects or incoherent wave correlations. In particular rough surfaces or very thick layers would result in a partly depolarisation and a disappearance of interference effects [112]. Depending on the wavelength λ_0 and the spectral resolution (line width) $\Delta\lambda$, the coherence length is approximately $l = \lambda_0^2/\Delta\lambda$. If the layer thickness and the penetration depth of the light are larger than the coherence length of the light, the phase correlation in the reflected beam is lowered, and therefore, the polarisation of the light is decreased. Furthermore, we assume plane electromagnetic waves, which include the assumption of an infinite lateral distribution of the waves. In thick layers this approximation does not fit anymore, if the light separation due the birefringence is bigger than the lateral coherence length in the beam or bigger than the beam size itself.

Generalised ellipsometry

In a single ellipsometric measurement using a rotating analyser setup as described above (para. 3.1), the result is usually expressed in terms of the ellipsometric angles ψ and Δ defined

through the amplitude ratios of the incident and reflected waves (cp. eq. 3.3).

$$\tan\psi\, e^{i\Delta} := \frac{E_{rp}}{E_{ip}} \left(\frac{E_{rs}}{E_{is}}\right)^{-1} = \frac{r_p}{r_s} =: \rho \tag{4.51}$$

For an anisotropic sample, the same definition relates the measured ellipsometric angles and the four Jones reflection coefficients in the form

$$\tan\psi\, e^{i\Delta} = \rho = \left(\frac{r_{pp}}{r_{ss}} + \frac{r_{sp}}{r_{ss}}\tan\chi\right)\left(1 + \frac{r_{pp}}{r_{ss}}\frac{r_{ps}}{r_{pp}}\tan\chi^{-1}\right)^{-1}, \text{ where} \tag{4.52}$$

$$\tan\chi := \frac{E_{is}}{E_{ip}}. \tag{4.53}$$

and χ refer to the angle between the polarisation of the incident wave and the plane of incidence. In contrast to the isotropic case, the ellipsometric angles ψ and Δ are not necessarily independent of the chosen polarisation of the incident light.

In the concept of the so called "generalised ellipsometry" an anisotropic sample has to be measured several times with different angles of incidence, polarisations of the incident light, or sample orientations to determine the independent reflection matrix elements. The particular measurement configurations depend on the specific problem. All unknown parameters have to contribute independent to the different measurements so that finally a clear separation is ensured within the given signal to noise ratio.

Calculation of the partial transfer matrix

The partial transfer matrix of each layer in an anisotropic sample is determined by a summation of exponential series as shown in relation 4.39. However, the calculation of this matrix in an analytical or numerical form could be complicated. Wöhler et. al. [110] use the Caley-Hamilton theorem to find a close algebraic expression. This theorem is based on the finding of the eigenvalues $q_l, (l = 1, 2, 3, 4)$ of the propagation matrix $\bar{\Delta}$ (4.36). An algebraic representation of eigenvalues for the special case of a homogeneous, non magnetic material without any optical rotation ($\varepsilon_{ij} = \varepsilon_{ji}$, eq. 4.37) was given by Schubert [111]. A more general treatment of this problem was shown by Azzam and Bashara in reference [59]. For this solution we have to determine the eigenvectors of the propagation matrix. Equation 4.36 has four particular plan-wave solutions, namely for the eigenvectors $\vec{\psi}_l[0]$ of the propagation matrix $\bar{\Delta}$ of the form

$$\vec{\psi}[z] = \vec{\psi}_l[0]\, \mathrm{e}^{\mathrm{i}\,\frac{\omega}{c} q_l h}\ ,\ l = 1, 2, 3, 4\ . \tag{4.54}$$

It is shown in reference [59] that the partial transfer matrix for a layer with a thickness h can be written in the form

$$\bar{L} = \bar{\psi}\bar{K}[h]\bar{\psi}^{-1}, \tag{4.55}$$

where the 4×4 matrix $\bar{\psi} = (\vec{\psi}_{kl}[0])$ is constructed from the four eigenvectors as columns. The diagonal matrix $\bar{K}[h]$ is determined by the eigenvalues q_l and the layer thickness h with

$$K_{ll}[h] = \mathrm{e}^{\mathrm{i}\,\frac{\omega}{c} q_l h} \text{ for } l = 1, 2, 3, 4 \text{ and } K_{ij}[h] = 0 \text{ for } i \neq j\ . \tag{4.56}$$

However, the algebraic determination of eigenvalues and the corresponding eigenvectors is still a problem and perhaps just possible for some special cases. Anyhow, for the most general

treatment, a number of commercial or free available algorithms can be used for a numerical determination of the eigensystem. For the finale calculation of dielectric functions a algebraic solution is not necessary.

Semi-infinite anisotropic substrates

In all previous derivations, the Jones reflection coefficients were determined for the special case of an isotropic substrate. This derivation was based on the definition of a Jones vector for the two independent waves parallel and perpendicular to the plane of incidence in the semi-infinite substrate. In contrast, these waves are coupled in arbitrarily anisotropic substrates and the given description would fail. However, as discussed in the previous paragraph, a set of four eigenvectors (generalised field vectors) $\vec{\psi}_l[0]$ of the substrate propagation matrix $\bar{\Delta}$ can be found. Every wave in the homogeneous substrate, therefore, can be expressed in a linear combination of these linear independent vectors. As mentioned in reference [59], only two of them could be exited in a semi-infinite substrate. These are the two plane waves propagating in the positive z-direction and they are related to the eigenvalues with a positive real part. If these two eigenvectors are labeled $\vec{\psi}_1$ and $\vec{\psi}_2$, the generalised field vector on the substrate boundary can be expressed by a linear combination of these two vectors

$$\vec{\psi}[d^-] = C_1\vec{\psi}_1[d^+] + C_2\vec{\psi}_2[d^+]. \tag{4.57}$$

C_1 and C_2 are constant but unknown amplitude factors. With the substitution of the left side of equation 4.46 by the right side of the equation 4.57, the electric field components in the ambient are connected now to the two generalised field vectors, namely the eigenvectors, in an anisotropic substrate.

$$C_1\begin{pmatrix}\psi_{11}\\ \psi_{21}\\ \psi_{31}\\ \psi_{41}\end{pmatrix} + C_2\begin{pmatrix}\psi_{12}\\ \psi_{22}\\ \psi_{32}\\ \psi_{42}\end{pmatrix} = \begin{pmatrix}\mathcal{L}_{11} & \mathcal{L}_{12} & \mathcal{L}_{13} & \mathcal{L}_{14}\\ \mathcal{L}_{21} & \mathcal{L}_{22} & \mathcal{L}_{23} & \mathcal{L}_{24}\\ \mathcal{L}_{31} & \mathcal{L}_{32} & \mathcal{L}_{33} & \mathcal{L}_{34}\\ \mathcal{L}_{41} & \mathcal{L}_{42} & \mathcal{L}_{43} & \mathcal{L}_{44}\end{pmatrix}\begin{pmatrix}(E_{ip}-E_{rp})\cos\phi_0\\ E_{is}+E_{rs}\\ (E_{rs}-E_{is})n_a\cos\phi_0\\ (E_{ip}+E_{rp})n_a\end{pmatrix} \tag{4.58}$$

Similar to the treatment of equation 4.46, the two unknown parameters C_1 and C_2 on the left hand side of relation 4.58 can be eliminated and the set of four equations is reduced to a set of two equations, which relate the incident and the reflected waves. Finally, these two equations can be resolved again in a form, where the Jones vectors of the incident and reflected waves are connected by a complex reflection Jones matrix $\bar{r}$. The coefficients of this Jones matrix are

$$\bar{r} = \frac{1}{b_{1rp}a_{rs} - a_{rp}b_{1rs}}\begin{pmatrix}(a_{ip}b_{rs} - a_{rs}b_{ip}) & (a_{is}b_{rs} - a_{rs}b_{is})\\ (a_{rp}b_{ip} - a_{ip}b_{rp}) & (a_{rp}b_{is} - a_{is}b_{rp})\end{pmatrix}, \text{ where} \tag{4.59}$$

$$
\begin{aligned}
a_{ip} &= \frac{c_{2ip}\,\psi_{11} - c_{1ip}\,\psi_{21}}{\psi_{11}\,\psi_{22} - \psi_{12}\,\psi_{21}} + \frac{c_{3ip}\,\psi_{41} - c_{4ip}\,\psi_{31}}{\psi_{31}\,\psi_{42} - \psi_{32}\,\psi_{41}}\,, \\
a_{is} &= \frac{c_{2is}\,\psi_{11} - c_{1is}\,\psi_{21}}{\psi_{11}\,\psi_{22} - \psi_{12}\,\psi_{21}} + \frac{c_{3is}\,\psi_{41} - c_{4is}\,\psi_{31}}{\psi_{31}\,\psi_{42} - \psi_{32}\,\psi_{41}}\,, \\
a_{rp} &= \frac{c_{2rp}\,\psi_{11} - c_{1rp}\,\psi_{21}}{\psi_{11}\,\psi_{22} - \psi_{12}\,\psi_{21}} + \frac{c_{3rp}\,\psi_{41} - c_{4rp}\,\psi_{31}}{\psi_{31}\,\psi_{42} - \psi_{32}\,\psi_{41}}\,, \\
a_{rs} &= \frac{c_{2rs}\,\psi_{11} - c_{1rs}\,\psi_{21}}{\psi_{11}\,\psi_{22} - \psi_{12}\,\psi_{21}} + \frac{c_{3rs}\,\psi_{41} - c_{4rs}\,\psi_{31}}{\psi_{31}\,\psi_{42} - \psi_{32}\,\psi_{41}}\,, \\
b_{ip} &= \frac{c_{1ip}\,\psi_{22} - c_{2ip}\,\psi_{12}}{\psi_{11}\,\psi_{22} - \psi_{12}\,\psi_{21}} - \frac{c_{4ip}\,\psi_{32} + c_{3ip}\,\psi_{42}}{\psi_{31}\,\psi_{42} - \psi_{32}\,\psi_{41}}\,, \\
b_{is} &= \frac{c_{1is}\,\psi_{22} - c_{2is}\,\psi_{12}}{\psi_{11}\,\psi_{22} - \psi_{12}\,\psi_{21}} - \frac{c_{4is}\,\psi_{32} + c_{3is}\,\psi_{42}}{\psi_{31}\,\psi_{42} - \psi_{32}\,\psi_{41}}\,, \\
b_{rp} &= \frac{c_{1rp}\,\psi_{22} - c_{2rp}\,\psi_{12}}{\psi_{11}\,\psi_{22} - \psi_{12}\,\psi_{21}} - \frac{c_{4rp}\,\psi_{32} + c_{3rp}\,\psi_{42}}{\psi_{31}\,\psi_{42} - \psi_{32}\,\psi_{41}}\,, \\
b_{rs} &= \frac{c_{1rs}\,\psi_{22} - c_{2rs}\,\psi_{12}}{\psi_{11}\,\psi_{22} - \psi_{12}\,\psi_{21}} - \frac{c_{4rs}\,\psi_{32} + c_{3rs}\,\psi_{42}}{\psi_{31}\,\psi_{42} - \psi_{32}\,\psi_{41}}\,, \text{ and}
\end{aligned}
\tag{4.60}
$$

$$
\begin{aligned}
c_{1ip} &= \mathcal{L}_{14} n_a + \mathcal{L}_{11}\cos\phi_0\,, & c_{1is} &= \mathcal{L}_{12} - \mathcal{L}_{13} n_a \cos\phi_0\,, \\
c_{1rp} &= \mathcal{L}_{14} n_a - \mathcal{L}_{11}\cos\phi_0\,, & c_{1rs} &= \mathcal{L}_{12} + \mathcal{L}_{13} n_a \cos\phi_0\,, \\
c_{2ip} &= \mathcal{L}_{24} n_a + \mathcal{L}_{21}\cos\phi_0\,, & c_{2is} &= \mathcal{L}_{22} - \mathcal{L}_{23} n_a \cos\phi_0\,, \\
c_{2rp} &= \mathcal{L}_{24} n_a - \mathcal{L}_{21}\cos\phi_0\,, & c_{2rs} &= \mathcal{L}_{22} + \mathcal{L}_{23} n_a \cos\phi_0\,, \\
c_{3ip} &= \mathcal{L}_{34} n_a + \mathcal{L}_{31}\cos\phi_0\,, & c_{3is} &= \mathcal{L}_{32} - \mathcal{L}_{33} n_a \cos\phi_0\,, \\
c_{3rp} &= \mathcal{L}_{34} n_a - \mathcal{L}_{31}\cos\phi_0\,, & c_{3rs} &= \mathcal{L}_{32} + \mathcal{L}_{33} n_a \cos\phi_0\,, \\
c_{4ip} &= \mathcal{L}_{44} n_a + \mathcal{L}_{41}\cos\phi_0\,, & c_{4is} &= \mathcal{L}_{42} - \mathcal{L}_{43} n_a \cos\phi_0\,, \\
c_{4rp} &= \mathcal{L}_{44} n_a - \mathcal{L}_{41}\cos\phi_0\,, & c_{4rs} &= \mathcal{L}_{42} + \mathcal{L}_{43} n_a \cos\phi_0\,.
\end{aligned}
\tag{4.61}
$$

The linear optical response of every stack of optically anisotropic layers can be calculated by this Jones matrix if the dielectric tensor and the orientation of the optical axis of each layer and the substrate are known.

Isotropic ambient and a biaxial layer on biaxial substrate

The orientation of an epitaxial grown layer is usually coupled to the crystal symmetry of the substrate. Thus, the optical axes of the layer is aligned to the axis of the substrate in the nitride samples under investigation and also in the majority of other semiconductors. Furthermore, the optical axes are very often either parallel or perpendicular to sample edges and the film boundaries. If the optical axes of the sample are arranged in a cartesian coordinate system, these axis can be also aligned either parallel or perpendicular to the plane of incidence. Therewith the calculation of the Jones matrix $\bar{r}$, given by relation 4.59, can be fairly simplified.

We consider now a biaxial layer on a biaxial substrate, where the optical axes are aligned to the plane of incidence and the layer boundaries. The diagonal elements of the dielectric tensor are defined by $\varepsilon_x, \varepsilon_y, \varepsilon_z$ for the substrate and by $\tilde{\varepsilon}_x, \tilde{\varepsilon}_y, \tilde{\varepsilon}_z$ for the layer. The labels of

the different axes correspond to the definitions presented in figure 4.9. With this definition the propagation matrix 4.37 reduces for a biaxial substrate to

$$\bar{\Delta} = \begin{pmatrix} 0 & 0 & 0 & 1 - \frac{n_a^2 \sin\phi_0^2}{\varepsilon_z} \\ 0 & 0 & -1 & 0 \\ 0 & n_a^2 \sin\phi_0^2 - \varepsilon_y & 0 & 0 \\ \varepsilon_x & 0 & 0 & 0 \end{pmatrix} . \tag{4.62}$$

The respective propagation matrix of the layer has the same form. The eigenvalues of this matrix are

$$\begin{aligned} q_1 &= -\sqrt{\varepsilon_y - n_a^2 \sin\phi_0^2} = -n_y \sqrt{1 - \frac{n_a^2}{n_y^2} \sin\phi_0^2} \,, \\ q_2 &= \sqrt{\varepsilon_y - n_a^2 \sin\phi_0^2} = n_y \sqrt{1 - \frac{n_a^2}{n_y^2} \sin\phi_0^2} \,, \\ q_3 &= -\sqrt{\varepsilon_x \left(1 - \frac{n_a^2}{\varepsilon_z} \sin\phi_0^2\right)} = -n_x \sqrt{1 - \frac{n_a^2}{n_z^2} \sin\phi_0^2} \,, \\ q_4 &= \sqrt{\varepsilon_x \left(1 - \frac{n_a^2}{\varepsilon_z} \sin\phi_0^2\right)} = n_x \sqrt{1 - \frac{n_a^2}{n_z^2} \sin\phi_0^2} \,. \end{aligned} \tag{4.63}$$

For a further simplification Schubert suggest the following abbreviation [111]:

$$N_{ij} = n_i \sqrt{1 - \frac{n_a^2}{n_j^2} \sin\phi_0^2} \,. \tag{4.64}$$

With this definitions the eigenvalues are given by

$$q_1 = -N_{yy} \,, \quad q_2 = N_{yy} \,, \quad q_3 = -N_{xz} \,, \quad q_4 = N_{xz} \,. \tag{4.65}$$

The associated eigenvectors are

$$\vec{\psi}_1 = \begin{pmatrix} 0 \\ \frac{1}{N_{yy}} \\ 0 \\ 0 \end{pmatrix} , \quad \vec{\psi}_2 = \begin{pmatrix} 0 \\ -\frac{1}{N_{yy}} \\ 0 \\ 0 \end{pmatrix} , \quad \vec{\psi}_3 = \begin{pmatrix} -\frac{N_{xz}}{n_x^2} \\ 0 \\ 0 \\ 0 \end{pmatrix} , \quad \vec{\psi}_4 = \begin{pmatrix} \frac{N_{xz}}{n_x^2} \\ 0 \\ 0 \\ 0 \end{pmatrix} . \tag{4.66}$$

Again, the eigenvectors for the layer can deduced in the same form. By substituting this eigensystem of the layer propagation matrix in equation 4.55, the partial transfer matrix of this biaxial layer is obtained as

$$\bar{L}_{bi} = \begin{pmatrix} \cos\beta_p & 0 & 0 & \mathrm{i}\, \frac{N_{\tilde{x}\tilde{z}}}{n_x^2} \sin\beta_p \\ 0 & \cos\beta_s & -\mathrm{i}\, \frac{1}{N_{\tilde{y}\tilde{y}}} \sin\beta_s & 0 \\ 0 & -\mathrm{i}\, N_{\tilde{y}\tilde{y}} \sin\beta_s & \cos\beta_s & 0 \\ \mathrm{i}\, \frac{\tilde{n}_x^2}{N_{\tilde{x}\tilde{z}}} \sin\beta_p & 0 & 0 & \cos\beta_p \end{pmatrix} , \quad \text{where} \tag{4.67}$$

$$\beta_p = \frac{\omega}{c} N_{\tilde{x}\tilde{z}} h \,, \quad \beta_s = \frac{\omega}{c} N_{\tilde{y}\tilde{y}} h \,. \tag{4.68}$$

The Jones matrix $\bar{r}$ of the biaxial system can be calculated now with relation 4.59 by substituting the two eigenvectors $\vec{\psi}_2$ and $\vec{\psi}_4$ of the substrate and the partial transfer matrix of the biaxial layer $\bar{L}_{bi}$. The two eigenvectors $\vec{\psi}_2$ and $\vec{\psi}_4$ relate to the positive eigenvalues q_2 and q_4 of the substrate. However, as discussed in paragraph 4.2.3, ellipsometric measurements are usually evaluated in terms of the ellipsometric angles ψ and Δ or the ellipsometric ratio ρ (q. v. eq. 4.51). Due to the symmetry of the problem, the non diagonal elements of the Jones matrix are found to be zero. Thus, the ellipsometric ratio can be calculated in the form $\rho = r_{pp}/r_{ss}$, like in the isotropic case. If the result is rearranged in a form similar to the well known formula for the isotropic three phase model (q. v. eq. 4.25), the ellipsometric ratio measured with a biaxial layer on a biaxial substrate is found to be

$$\rho = \frac{r_{pp}}{r_{ss}} = \frac{r_{01_p} + r_{12_p} e^{i\,2\beta_p}}{1 + r_{01_p}\, r_{12_p} e^{i\,2\beta_p}} \, \frac{1 + r_{01_s}\, r_{12_s} e^{i\,2\beta_s}}{r_{01_s} + r_{12_s} e^{i\,2\beta_s}}, \text{ where} \tag{4.69}$$

$$\begin{aligned} r_{01_p} &= \frac{N_{\tilde{x}a} - N_{a\tilde{z}}}{N_{\tilde{x}a} + N_{a\tilde{z}}}\,, \qquad r_{01_s} = \frac{N_{aa} - N_{\tilde{y}\tilde{y}}}{N_{aa} + N_{\tilde{y}\tilde{y}}}\,, \\ r_{12_p} &= \frac{N_{x\tilde{z}} - N_{\tilde{x}z}}{N_{\tilde{x}a} + N_{a\tilde{z}}}\,, \qquad r_{12_s} = \frac{N_{\tilde{y}\tilde{y}} - N_{yy}}{N_{\tilde{y}\tilde{y}} + N_{yy}}\,. \end{aligned} \tag{4.70}$$

The values N_{ij} are defined according to equation 4.64. The labels i, j and $\tilde{i}, \tilde{j}$, respectively, refer to the respective complex refraction tensor components n_x, n_y, n_z for the substrate and $\tilde{n}_x, \tilde{n}_y, \tilde{n}_z$ for the layer as defined above.

The relation 4.69 is suitable for every biaxial three phase system, where the optical axes are defined in a cartesian coordinate system and are aligned to the plane of incidence and the boundaries of the layer. This also includes the special case of an uniaxial three phase system.

We should mentioned at this point that relation 4.69 is basically identical to the result of Schubert [111] although the more general method as suggested in reference [59] was used. Only the sign of the exponential factor is different to the result of Schubert [111]. But this difference quite obvious relates to a misprint in his publication. However, according to our calculations and those of Schubert we conclude, that the solution presented by Azzam and Bashara [59] is wrong.

Wurtzite nitride samples

In this work the investigated III-nitride films, as well as the used substrates have a hexagonal (wurtzite) or cubic (zincblende) crystal structure. Furthermore, the crystal axis of the epitaxial grown films are parallel to the axis of the substrate. In the hexagonal crystal symmetry the samples are uniaxial anisotropic with a optical axis parallel to the c-axis of the crystal. The dielectric function connected to the optical axis ($\vec{E} \| c$) is often called the extraordinary dielectric function and corresponds to the $\varepsilon_{\|}$ component of the dielectric tensor. The two identical perpendicular components in the hexagonal crystal planes ($\vec{E} \perp c$) are often called the ordinary dielectric function and correspond to the $\varepsilon_{\perp}$ component of the dielectric tensor. If the x-axis of a Cartesian coordinate system is chosen parallel to the c-axis of the wurtzite crystal, thus, the dielectric tensor is given by:

$$\bar{\varepsilon} = \begin{pmatrix} \varepsilon_x & 0 & 0 \\ 0 & \varepsilon_y & 0 \\ 0 & 0 & \varepsilon_z \end{pmatrix} = \begin{pmatrix} \varepsilon_{\|} & 0 & 0 \\ 0 & \varepsilon_{\perp} & 0 \\ 0 & 0 & \varepsilon_{\perp} \end{pmatrix}. \tag{4.71}$$

Apart from strain or morphological effects the zincblende samples are assumed to be isotropic. Therefore, the optical properties are given by the scalar complex dielectric function. This can be calculated from an ellipsometric measurement within the isotropic two phase model (para. 4.1), or, if a surface layer should be considered, in an isotropic three phase model (para. 4.1.4). Usually, the same models are used for the wurtzite samples, if the c-axis is perpendicular to the sample surface. Under these conditions the effect of $\varepsilon_{\parallel}$ to the measured pseudodielectric function is very small. Aspnes describes a approximate solution for the pseudodielectric function measured on a biaxial crystal, based on a first-order expansion which assumes that the anisotropies are small corrections to an isotropic mean value [46].

$$< \varepsilon >= \varepsilon + \frac{\varepsilon - \sin^2\phi_0}{(\varepsilon - 1)\sin^2\phi_0}\Delta\varepsilon_x - \frac{\varepsilon\cos^2\phi_0 - \sin^2\phi_0}{(\varepsilon - 1)\sin^2\phi_0}\Delta\varepsilon_y - \frac{1}{\varepsilon - 1}\Delta\varepsilon_z, \text{ where} \quad (4.72)$$

$$\varepsilon_x = \varepsilon + \Delta\varepsilon_x\ ,\ \ \varepsilon_y = \varepsilon + \Delta\varepsilon_y\ ,\ \text{and}\ \ \varepsilon_z = \varepsilon + \Delta\varepsilon_z\ . \quad (4.73)$$

This relation is not exact, but reveals the very small influence of the ε_z component normal to the surface, if $|\varepsilon|$ is moderately large. The physical reason is simple. If the material is optically thick ($n_0 \ll n_1$), the incoming light is refracted in the direction of the surface normal and the electric and magnetic field vectors are mostly parallel to the surface. Therefore, the z-component can be neglected. On the other hand, it is usually not possible to measure $\varepsilon_{\parallel}$ if the optical axis (c axis) is perpendicular to the sample surface.

Thus, the determination of the two independent dielectric function components $\varepsilon_{\perp}$ and $\varepsilon_{\parallel}$ of a biaxial (hexagonal) material is usually dependent on the accessibility of a sample, where the optical axis is aligned in the surface. According to the optical setup two high-symmetry orientations are possible: The c axis of the sample can be oriented either parallel ($\alpha = 0$) or perpendicular ($\alpha = \pi/2$) to the plane of incidence. In both cases a diagonal reflection matrix with independent reflection coefficients for s- and p-polarised light is obtained. Like mentioned in reference [46] and [113], the measured pseudodielectric function is mainly influenced by the optical axis parallel to the plane of incidence and the sample surface, respectively. This is also seen in equation 4.72, where the influence of ε_y is strongly reduced for typical angles of incidence about $70°$. For this reason, the pseudodielectric functions measured in the two orientations with $\alpha = 0$ or $\alpha = \pi/2$ are already roughly the $\varepsilon_{\parallel}$ and $\varepsilon_{\perp}$ dielectric tensor component, respectively. The accurate values can easily separated from these pseudodielectric functions with the methods introduced above.

The main focus of this work is attended to the spectral range above the band gap. In this region, the investigated nitride films are assumed to be opaque. Thus, the layer system can be described simply by an uniaxial bulk sample with the optical axis parallel to the surface plane. Therefore, the measured ellipsometric ratio ρ as defined in relation 4.69 reduces to

[114]

$$\rho_0 = \frac{r_{1pp}}{r_{1ss}} = \left(\frac{\sqrt{\varepsilon_\perp \varepsilon_\parallel}\cos\phi_0 - \sqrt{\varepsilon_\perp - \sin^2\phi_0}}{\sqrt{\varepsilon_\perp \varepsilon_\parallel}\cos\phi_0 + \sqrt{\varepsilon_\perp - \sin^2\phi_0}} \right) \left(\frac{\cos\phi_0 - \sqrt{\varepsilon_\perp - \sin^2\phi_0}}{\cos\phi_0 + \sqrt{\varepsilon_\perp - \sin^2\phi_0}} \right)^{-1} \quad (\alpha = 0) \tag{4.74}$$

or

$$\rho_{\pi/2} = \frac{r_{2pp}}{r_{2ss}} = \left(\frac{\varepsilon_\perp \cos\phi_0 - \sqrt{\varepsilon_\perp - \sin^2\phi_0}}{\varepsilon_\perp \cos\phi_0 + \sqrt{\varepsilon_\perp - \sin^2\phi_0}} \right) \left(\frac{\cos\phi_0 - \sqrt{\varepsilon_\parallel - \sin^2\phi_0}}{\cos\phi_0 + \sqrt{\varepsilon_\parallel - \sin^2\phi_0}} \right)^{-1} \quad (\alpha = \pi/2). \tag{4.75}$$

$\alpha = 0$ and $\alpha = \pi/2$ are azimuthal rotation angles, which correspond to the two high-symmetry orientations. The ambient refractive index n_a is assumed to be $n_a = 1$. For the determination of the two independent dielectric tensor components $\varepsilon_\perp$ and $\varepsilon_\parallel$, the pseudodielectric function $< \varepsilon >=< \varepsilon_1 > + \mathrm{i} < \varepsilon_2 >$ derived from the measured complex ellipsometric ratio ρ has to be measured in both orientations. The two components $\varepsilon_\perp = \varepsilon_{1\perp} + \mathrm{i}\,\varepsilon_{2\perp}$ and $\varepsilon_\parallel = \varepsilon_{1\parallel} + \mathrm{i}\,\varepsilon_{2\parallel}$ can be calculated from these two ellipsometric measurements by a numerically solving of the four coupled nonlinear equations obtained from eq. (4.75):

$$\begin{aligned} < \varepsilon_1 >_0 &= f_1[\varepsilon_{1\perp}, \varepsilon_{2\perp}, \varepsilon_{1\parallel}, \varepsilon_{2\parallel}] \qquad (\alpha = 0), \\ < \varepsilon_2 >_0 &= f_2[\varepsilon_{1\perp}, \varepsilon_{2\perp}, \varepsilon_{1\parallel}, \varepsilon_{2\parallel}] \qquad (\alpha = 0), \\ < \varepsilon_1 >_{\pi/2} &= f_3[\varepsilon_{1\perp}, \varepsilon_{2\perp}, \varepsilon_{1\parallel}, \varepsilon_{2\parallel}] \qquad (\alpha = \pi/2), \\ < \varepsilon_2 >_{\pi/2} &= f_4[\varepsilon_{1\perp}, \varepsilon_{2\perp}, \varepsilon_{1\parallel}, \varepsilon_{2\parallel}] \qquad (\alpha = \pi/2). \end{aligned} \tag{4.76}$$

If the inescapable surface roughness should be considered, we use relation 4.69 for the biaxial three phase system in combination with the effective medium approach for the surface roughness. As discussed above, the reflection coefficient r_{ss} is defined only by the y-components of the layer dielectric functions, whereas r_{pp} is especially in thin layers [113] basically determined by the x-components. Therefore, it is sufficient to approximate the rough surface by a layer with a biaxial effective medium dielectric function. The two in-plane components can be separately calculated from the respective substrate dielectric function components. As mentioned in paragraph 4.2.2, the roughness is fairly good approximated by the effective medium theory according to Bruggeman [103] using a mixture of 50% voids (ambient) and 50% substrate. The ambient dielectric function is assumed to be $\varepsilon_a = 1$. Thus, both layer dielectric function components can be calculated from "substrate" effective medium dielectric functions according to

$$\begin{aligned} \varepsilon_{layer\ \perp} &= \frac{1}{8}\left(1 + \varepsilon_\perp + \sqrt{1 + 34\varepsilon_\perp + \varepsilon_\perp^2}\right) \\ \varepsilon_{layer\ \parallel} &= \frac{1}{8}\left(1 + \varepsilon_\parallel + \sqrt{1 + 34\varepsilon_\parallel + \varepsilon_\parallel^2}\right). \end{aligned} \tag{4.77}$$

If the refractive index deduced from these EMA dielectric functions is used as a layer dielectric function in equation 4.64 and 4.69, we obtain again a set of four coupled nonlinear

equations. This system of equations has the same general form as the relations 4.76. $\varepsilon_{\perp}$, as well as $\varepsilon_{\parallel}$ can be calculated from the two ellipsometric measurements within a numerically solution. For this calculation we use the commercial program ”Mathematica”. The implementation of the calculation is documented in the appendix A.

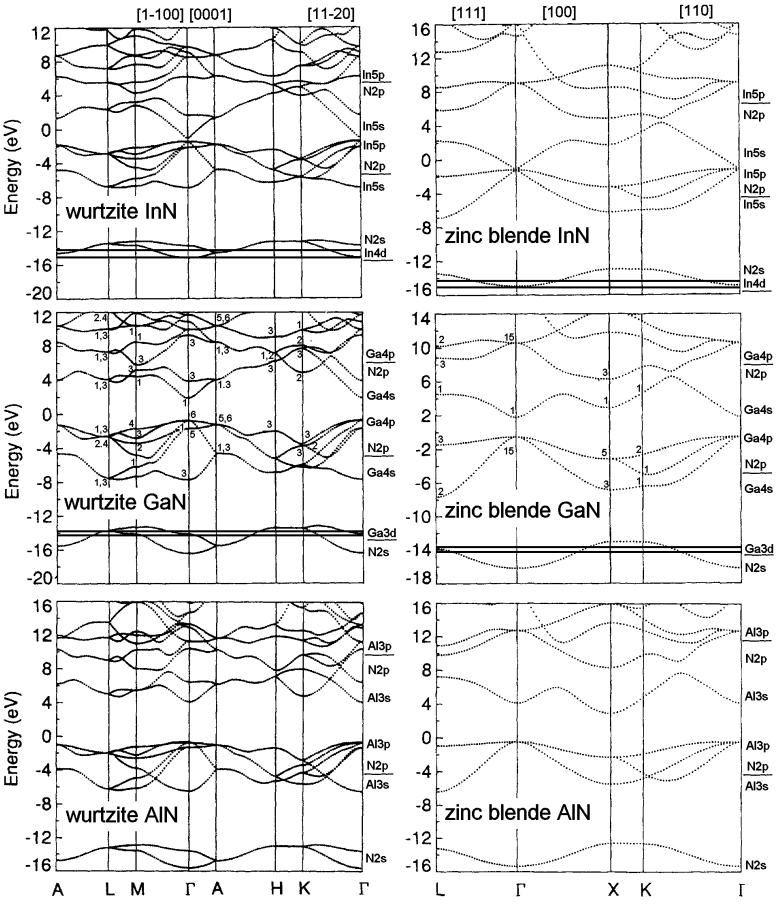

Figure 4.7: *Electronic band structure of InN, GaN, and AlN calculated by means of DFT-LDA [94]. On the right hand side of each band structure plot we also denote the main characteristic atomic orbital contributions to the electronic bands at the respective energy [95, 96]. This is of course only a rough estimation in particular for the higher valence and conduction bands. The semi-core Ga3d and In4d states are added by horizontal lines in order to illustrate the energy position. Furthermore we label the different electronic bands e. g. for GaN with numbers indicating the irreducible representations at the respective symmetry points [84, 97] in order to illustrate the symmetry.*

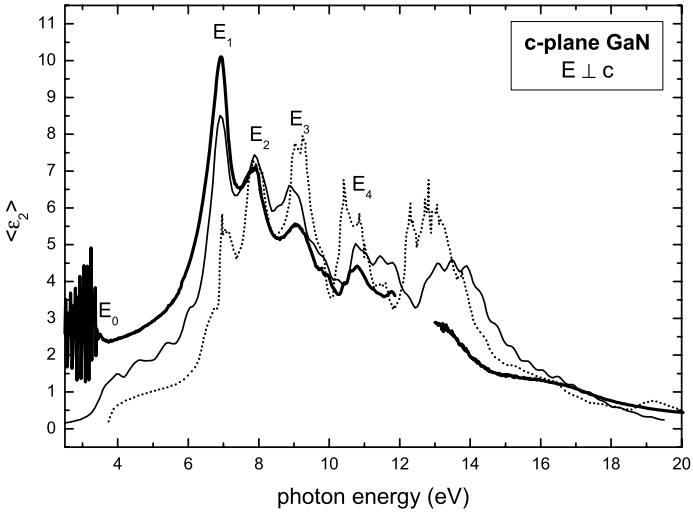

Figure 4.8: *Imaginary part of the GaN $< \varepsilon_{\perp} >$ [thick line] [38] in comparison to $\varepsilon_{2\perp}$ calculated by Benedict et al. [41] [thin line] and Lambrecht et al. [84] [dotted line]. Below the band gap (E_0) at about 3.5 eV Fabry-Perot oscillations dominate the measured pseudodielectric function.*

5. Surface effects and sample preparation

The aim of our ellipsometric investigations is the determination of the ”pure” bulk dielectric function of the different nitride semiconductors. But on the other hand, the ellipsometric measurements are based on the reflection of the light on the sample surface and interfaces. The contribution of layers beyond the surface region depend finally on the optical properties of the investigated sample. We concentrate our discussion in this work to the spectral range above the optical band gap, where the nitride layers can assumed to be opaque. The residual penetration depth of the probing light is shown e. g. for wurtzite GaN in figure 5.1. Depending on the respective photon energy this value is between 50 and 6 nm. Thus only the uppermost 10-100 monolayers contribute to the measured spectra. However, the theoretical treatment of the ellipsometric measurements considers a ideal case of half space ”perfect” homogeneous crystals with a perfect smooth surface. The investigated samples, therefore, should fulfil this requirements as good as possible in the surface region according to the penetration depth of the light.

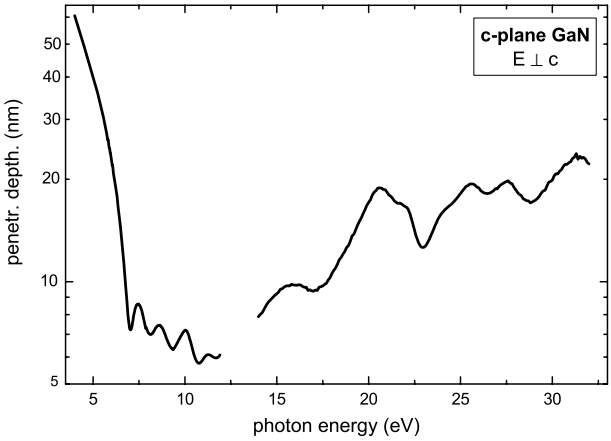

Figure 5.1: *Penetration depth of the probing light in wurtzite GaN calculated from $\varepsilon_\perp$ as presented in figure 4.8.*

In this connection, the treatment of the sample after the growth could be very important. Wethkamp shows already in previous ellipsometric investigations on GaN that exposure to air produce remarkable changes in the measured dielectric function [38]. These changes were attributed to a surface oxidation. It was also shown that annealing in UHV leads to a reduction of this surface contamination.

We observed these changes after exposure to air rather increased also for InN. The dielectric function of uncontaminated InN(0001) films is known up to about 6 eV from in-situ ellipsometric studies during(after) growth in the MOVPE-reactor. Afterwards, the samples

were transported on air to our synchrotron ellipsometer at BESSY for extended measurements. But these measurements reveal already remarkable differences in comparison to the in-situ measured dielectric function. The dominating absorption structures are changed in the relative peak amplitudes. But the imaginary part of the dielectric function was also reduced in the overall amplitude. These differences were found independent from the area of the investigated sample surface and are typical for surface overlayers or changes of the crystalline quality of the whole layer. Due to these findings about a possible film degeneration on air a more detailed investigation of the surface contamination and possible cleaning methods was recommended at first.

Nevertheless, we should mention again that spectroscopic ellipsometry is based on the reflection of the probing light at the sample surface. Due to the broken symmetry at the sample boundaries, surface effects have to be taken into account even if the sample would provide a "perfect" surface. In the strict sense the electronic states and, thus, the optical properties of a bulk semiconductor are only well defined in an infinite crystal. In some additional experiments, which are not shown in this work, we could determine the pseudodielectric function measured by ellipsometry on different surface reconstructions and termination, respectively [115, 116]. These differences, on the one hand, can be used for a detailed analysis of the respective surface properties e. g. during the growth of III-nitride layers. But on the other hand, if the bulk optical properties are investigated by means of spectroscopic ellipsometry, these effects has to be considered in the evaluation of the measurements. However, the biggest changes in the measured pseudodielectric function are obtained for the very special situation of a very Ga rich surface, where Ga double layer constitutes the special surface properties. But also for N-rich surfaces smaller differences depending on the exact surface stoichiometry (on the specific surface reconstruction) are found. Finally we conclude from these measurements that the GaN spectra measured on samples stored in air (e. g. fig. 6.2) are very close to the results obtained on very defined N-rich surfaces.

5.1 Film degeneration/contamination on air

5.1.1 GaN/AlN

In order to remove (organic) surface contaminations we have cleaned all samples measured in this work successively with acetone, H_2O, isopropyl alcohol and finally again with H_2O. After the transfer in the BESSY ellipsometer the samples were annealed in the UHV enviroment (p <1E-9 mbar) in order to remove residual surface contaminations. At temperatures between 100 and 200°C at first we notice a desorption of water and other volatile contaminations. But for the GaN samples a characteristic desorption of a thin surface overlayer (≈ 1 nm) is observed depending on the sample history at ≈ 500°C. This was interpreted already in previous measurements [38] as the desorption of a native oxide. It was also found that a further increased temperature under normal UHV conditions would result in an irreversible roughening of the surface.

A rapid formation of a native oxide is well known for lower band gap III-V materials. Like on the GaAs(100) surface several group III and group V oxides such as Ga_2O_3, As_2O_3, or As_2O_5 are determined with XPS [117]. GaN and AlN are much more stable in contrast to the low band gap III-V materials. In a RHEED study of Gupta et. al. [118] no surface oxidation was detected after one day exposure to air. In contrast, XPS and AES studies reveal

the formation of native oxides, particular Ga_2O_3 and Al_2O_3, respectively, on the surface [119, 120]. But a desorption of these native oxides by means of sample heating was either not observed [119] or only at more elevated temperatures (600-800°C) [121]. Hence, it is not clear if the oxide is removed completely or what kind of overlayer is actually desorbed by annealing at ≈ 500°C. Therefore, a remaining surface contamination with oxides and carbon should be considered.

For AlN in contrast, an annealing up to 900°C does not show any change in the pseudodielectric function, which could be attributed to a reduction of overlayers. This was somehow expected, if we assume Al_xO_y:N with compositions close to the very stable Al_2O_3 with just small amount of incorporated N as possible oxides [122].

5.1.2 InN

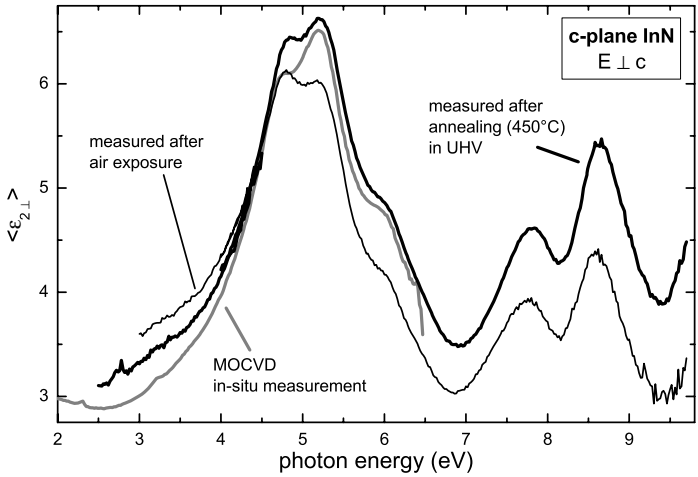

Figure 5.2: *InN film degeneration on air shown on the imaginary part of the pseudodielectric function measured on wurtzite c-plane InN. The grey line was measured in-situ directly after growth in a nitrogen atmosphere [11, 123]. The thin line was obtained on the as-grown sample transferred to BESSY in air. After ≈15min annealing at 450°C in UHV (≈5E-9mbar) the imaginary part of the pseudodielectric function recovers the former overall amplitudes, but is still showing remarkable differences in the relative peak amplitudes.*

Especially for the InN layers a degeneration while exposure to air was clearly observed by comparing the dielectric functions measured in-situ directly after growth in the MOVPE reactor, with those spectra measured subsequently in the BESSY-Ellipsometer (fig. 5.2). Between both measurements the sample was stored approximately two weeks under normal air conditions. The in-situ measurement was recorded at room temperature in a nitrogen atmosphere, where a contamination of the film can be excluded [123]. The comparison of the spectra shows remarkable differences in the overall amplitude and especially in the relative

amplitudes of the two interband transitions at about 4.8 and 5.2 eV. This kind of changes are well known in connection with additional thin amorphous surface layers like native oxides, surface roughening or a degeneration of the whole film. According to the results on GaN, we, therefore, annealed the sample in the ellipsometer chamber under UHV-conditions (5E-9 mbar) at 450°C (±20°C) for 15min, in order to recover the "clean" InN film. After cooling down to room temperature, in fact, a partial recovery of the in-situ results is observed as shown in figure 5.2. In comparison to the previous spectra the alteration of the sample is considerable reduced and the relative peak amplitudes at 4.8 and 5.2eV are reversed again. However, remarkable differences in comparison to the in-situ measurements remain. In particular, the relative amplitudes of the two interband transitions around 5 eV are still modified. These remaining differences could not be attributed anymore to a simple amorphous overlayer. Furthermore, a longer treatment of the sample does not change the ellipsometric results while an increased temperature, especially above 500°C, lead to a subsequent decrease of the amplitude. This indicates a roughening of the surface or deterioration of the whole layer. Similar results are also found by in-situ studies in the MOVPE reactor, where annealing in both, ammonia and hydrogen ambient, generally results in a deterioration of the layers, leaving indium droplets on the surface [12].

In a second approach to restore a clean InN film we tried to remove the uppermost monolayers of the oxidised or contaminated film by argon ion sputtering. But in contrast to the thermal treatment, the ion sputtering does not recover the former dielectric function at all and finally just results in a roughening of the surface. We conclude from this experience that the change while exposure to air, does not originate just from a thin closed overlayer, but is related to changes in the InN layer.

In order to verify possible surface contaminations, Auger Electron Spectroscopy (AES) was applied before and after annealing in UHV. As seen in the upper part of figure 5.3, various elements apart from the expected indium and nitrogen contribute to the spectrum. We found in particular among other not explicitly identified species, a distinct amount of carbon and oxygen. While the carbon can be assigned to contamination during the growth of the InN layer or during the AES measurement itself, the oxygen could originate from a native InN-oxide formation. Furthermore, the AES investigation of the InN surface before and after the annealing process shows an oxide peak reduction of 75% in comparison to the nitrogen peak (fig. 5.3). This result would seem to suggest, that the native oxides on the surface is reduced.

For a further investigation of this "oxidation" effect, we have annealed a MOVPE grown InN layer at 400°C in an oxygen enriched atmosphere for one hour [123]. After this treatment all characteristic absorption features in the InN dielectric function are disappeared or appear spectrally broadened (fig. 5.4 dash-dotted line). But the most prominent difference is the appearance of a distinct Fabry-Perot interference structure below 3.3 eV indicating a formation of a layer of at least hundred nm thickness with a new fundamental band gap of approx. 3.5 eV. This layer can only explained by a partly transformation of the former InN layer if we consider that the original InN layer was not thicker than 400 nm. Furthermore, it is very remarkable that the previously found characteristic absorption features in the higher photon energy range at about 7.9 eV and 8.7 eV partly remain. Therefore, the formation of a closed "oxide layer" can be excluded. The penetration depth in a assumed closed pure "oxide" layer would strongly decrease above the absorption edge at approximately 3.5 eV. Accordingly, the contribution of a remaining InN underneath should decrease very rapidly in the higher spectral region of the measured pseudodielectric function. Furthermore, we

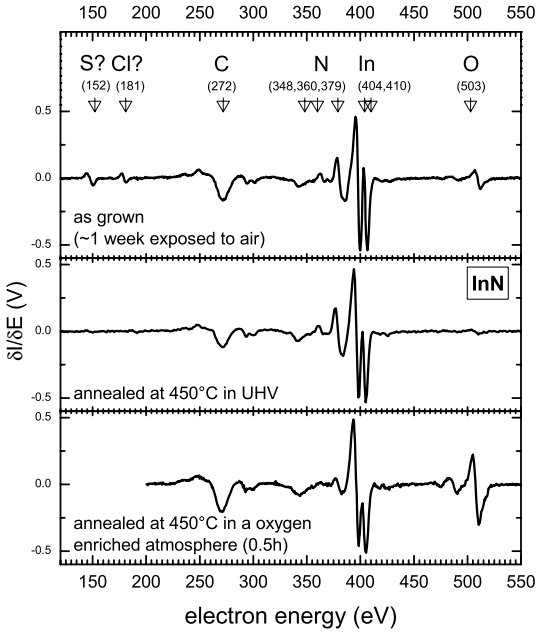

Figure 5.3:

AES results on InN grown by MOVPE. The upper graph is showing the sample after approximately one month in air. The spectrum in the middle was measured after ≈15min annealing at 450°C in UHV (≈5E-9mbar) while the spectrum in the lower part was measured at a sample that was half an hour annealed in an oxygen enriched atmosphere.

observe very inhomogeneous optical properties at the ”oxidised” InN film. Over the sample surface of approximately 7×7 mm the onset of the Fabry-Perot interference structures shift several 100 meV, indicating different layer thicknesses or a variation of the energy position of the absorption edge. The distinct reproduction of the interferences in our ellipsometric measurements as shown in figure 5.4 was possible, because of the very small spot diameter of less than one millimeter of the probing light on the sample surface. Corresponding AES measurements for these layers show a strongly increased oxide peak in comparison to the nitrogen peak (fig. 5.3). This further supports the formation of a native oxide.

In figure 5.4 the imaginary part of the dielectric function is plotted for the as-grown InN as previously shown together with the ”oxidised” InN film. Furthermore, we present the dielectric function of a sputtered InN film, as well as a sputtered InO film. The absorption edge of the sputtered amorphous InO film is found here in the same spectral region between 3 and 4 eV like that one of the annealed InN film. Below 3.5 eV the spectrum is also dominated by strong Fabry-Perot interference structures while the higher photon energy range is showing no distinct absorption structures. In comparison, the dielectric function measured on the sputtered polycrystalline InN film shows already a weak and broad absorption structure around 5 eV, as known from epitaxial InN layers. The band gap of this layer is found fairly above 1 eV and lies between the absorption edge of the epitaxial InN layer and the sputtered InO.

We tried also to reproduce the InN oxidation performed so far by annealing at 400°C in an oxygen enriched atmosphere, under more defined conditions in the UHV ellipsometer chamber. For this experiment we used a sample, which was annealed in UHV as the sample shown in figure 5.2. After this treatment we exposed the sample for 30-60 min to pure oxygen (par-

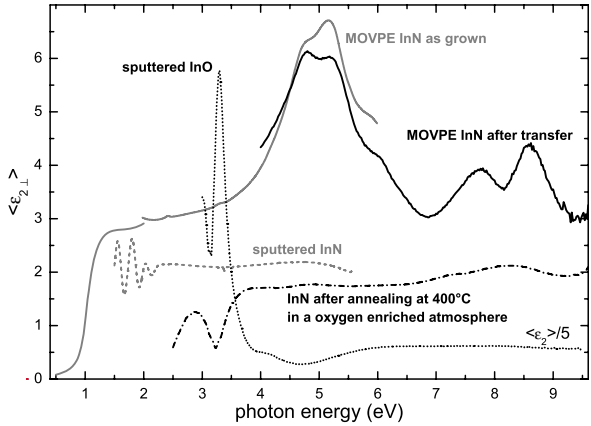

Figure 5.4: *Imaginary part of the pseudodielectric function of various InN and InO films. The grey line is representing the dielectric function as measured in-situ directly after growth in the MOVPE-reactor [123]. Below 2 eV, this spectrum was evaluated in a layer model to determine the bulk dielectric function [124]. The same sample was measured after approximately one week exposure to air with the synchrotron ellipsometer at BESSY (black line). The grey and black dashed lines show the pseudodielectric function of a sputtered InN and a sputtered InO film, respectively. Finally, the black dotted line is found for the MOVPE-grown sample after 1 h annealing at 400° C in an oxygen enriched atmosphere [123].*

tial pressure: 10^{-2} mbar, sample temperatures: 400-200°C decreasing). But this treatment did not change the measured pseudodielectric function and the formation of one monolayer or more InO can be excluded. According to this result, the oxidation seems to be linked to catalytic effects. Especially the influences of water or hydrogen has to be considered. The impact of this two on the oxidation process of other semiconductors is well known. Encouraged by this result, the degeneration/oxidation of InN films was finally investigated in a water enriched atmosphere. These experiments show that the imaginary part of the measured pseudodielectric function is strongly broadened after exposure of the InN films to water enriched atmospheres even at room temperature [125]. Surprisingly, this treatment seems to shift also the transparent spectral range to higher energies. We find new Fabry-Perot interference up to 3 eV, similar to the previous experiments. These changes are relative stable up to sample temperatures of about 130°C but are fully reversible by a further annealing at higher temperatures in a dry atmosphere. According to these results, a remarkable water assimilation on the InN surface or in the whole InN film has to be considered. Thus, a annealing of the InN films above 150°C seems to be recommended for a subsequent reliable determination of the InN optical properties by spectroscopic ellipsometry.

5.1.3 Discussion

The comparison of all results concerning the degeneration of nitrides and especially of InN while storing on air demonstrates the strong influence a of sample oxidation or of other contaminations on the measured optical properties in the range of the interband transitions and especially on the energetic position of the observed optical band gap. The physical background is still under discussion and the results presented in this work do not indicate an unambiguous explanation.

However, for the interpretation of the different results it is important that all available InN films reveal a very poor crystalline quality in comparison to the investigated GaN films and in particular in comparison to other semiconductors like GaAs or Si. Even if no unambiguous proof can be provided, it is most likely that a partial oxidation of InN layers is responsible for the distinct changes in the measured pseudodielectric function after exposure to air. A simple explanation for the different results could be a preferred oxidation on defects, holes, dislocations or crystallite boundaries while the oxidation of the smooth surface is very weak. This localised oxidation is known already from GaN films, where the preferred oxidation on holes and dislocations is used to reduce the leakage current at these imperfections in GaAlN devices. The localisation of the native oxide at dislocations and grain boundaries would also explain the discrepancy between RHEED or PL and AES or XPS measurements [118–120]. Thus, the measured dielectric function has to be interpreted as an effective medium dielectric function that is formed by a mixture of the InN and InO or other components like water. In this model it is also conceivable that InN films show a more and more oxide like optical properties and finally get transparent below 3.5 eV although typical InN absorption structures remain especially in the higher energy with the increasing amount of InO. These assumptions are also supported by the fact that MBE grown InN films with a slightly better overall crystal quality and less defects show a smaller film degeneration in comparison to the MOVPE films. After annealing under UHV-conditions we determined a partial deoxidation of oxidised InN films. But recent MOVPE in-situ experiments show also a positive effect of an annealing procedure between 520°C and 550°C in a nitrogen ambient on the crystal quality (crystallite etching, grooves closing) [12]. A similar effect is also conceivable in connection with an annealing under UHV conditions. However, all these results maybe demonstrate finally, why the InN fundamental band gap was assumed above 2 eV in the past and explain the persistent discussions about the optical properties.

6. Gallium Nitride

Although, different GaN samples of each material were measured, only a selected number is presented in this work. The ordinary dielectric tensor component $\varepsilon_\perp$ of wurtzite GaN(0001), as well as zincblende GaN dielectric function was measured and discussed already in previous publications [37–41]. These measurements were also performed with the BESSY-ellipsometer setup. A major issue in the investigations of Wethkamp [38] was a detailed study of possible characteristic differences between samples grown by MBE and MOCVD on various substrates. But finally, no principal differences were found. Therefore, we measure the dielectric function just once again at at a zincblende GaN sample with a slightly "better" crystal quality, while for a more precise determination of $\varepsilon_\perp$ the same wurtzite GaN(0001) sample was used like in the work of Wethkamp [38]. The higher accuracy in these measurements was obtained by some improvements on the ellipsometric setup at BESSY II. Thus, several new features could be resolved, finally, in particular in the spectral range above 10 eV.

A measurement of the extraordinary dielectric tensor component $\varepsilon_\parallel$ was not possible in the previous works due to the orientation of the available wurtzite GaN samples. The first determination of both dielectric tensor components $\varepsilon_\perp$ and $\varepsilon_\parallel$ above the band gap is provided now by the recent success of the Berlin Paul-Drude-Institut für Festkörperelektronik in depositing wurtzite M-plane GaN $(1\bar{1}00)$ on γ-$LiAlO_2$ by MBE. These results can be used now for a detailed discussion of the contribution of specific interband transitions to the different dielectric tensor components.

6.1 Results

6.1.1 Wurtzite GaN(0001)

Sample characterisation

The investigated wurtzite c-plane GaN(0001) sample is a thin film grown by MOVPE (Cree Research Inc.) on wurtzite c-plane Al_2O_3. This layer has a thickness of 1.78 μm and an unintentional n-type doping level of $5 \cdot 10^{-15}\,\mathrm{cm}^{-3}$. From AFM measurements in $1\times1\,\mu$m scan areas a RMS-roughness of 0.87 nm was determined. In order to remove (organic) surface contaminations the sample was successively cleaned with acetone, H_2O, isopropyl alcohol and finally again with H_2O. Furthermore, the sample was annealed at $\approx 500°$C in the UHV-environment of the ellipsometer chamber as discussed in chapter 5.

Dielectric function

Figure 6.1 shows the real and imaginary part of the dielectric function measured at room temperature from 2.5 to 33 eV. This spectrum was recorded in several steps at two different beamlines as discussed in paragraph 3.3. Up to 9.5 eV the pseudodielectric function was measured under an angle of incidence of 68°. For the spectral range above 9.5 eV an angle of incidence of 45° was used.

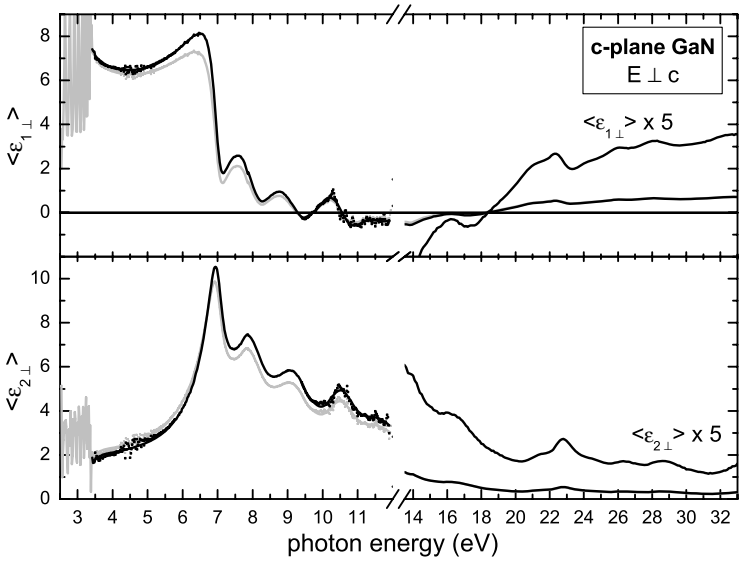

Figure 6.1: *Dielectric tensor component $< \varepsilon_\perp >$ of wurtzite GaN (c-plane) [black line]. The surface roughness of the sample was corrected within the EMA-Model shown in para. 4.2.2. The grey line represents the uncorrected pseudodielectric function as measured by ellipsometry. In order to emphasise the general line shape of the spectra we apply a spline smoothing algorithm between 4.5 and 5.5 eV as well as between 9.5 and 12 eV. The raw data are shown with gray and black dots, respectively.*

The measured pseudodielectric function $< \varepsilon_\perp >$ is shown by grey lines in figure 6.1. For the correction of surface roughness effects we used the RMS-roughness value determined by AFM as a thickness of a effective medium film on the GaN surface. The GaN-bulk dielectric tensor component $\varepsilon_\perp$ was calculated then within the three phase model as described in paragraph 4.2.2 (fig. 6.1 black line). The penetration depth in GaN is less than 10 nm in the spectral range above 5 eV (fig. 5.1). This value is in particular sufficiently below the layer thickness. Thus, an opaque GaN can assumed in the spectral range, which is mainly discussed in this work. Consequently, the deeper layers and finally the substrate does not influence the measured GaN pseudodielectric function. But residual thin surface contaminations (< 1 nm) still effect the measurement and can lead to broadening of structures accompanied by a decrease of the absolute value of $< \varepsilon_\perp >$ in the vicinity of interband transitions (s. a. para. 4.2.2). Anyhow, as discussed in paragraph 5, this effects are small and the shown pseudodielectric function $< \varepsilon_\perp >$ can be interpreted above 5 eV as a bulk dielectric tensor component $\varepsilon_\perp$ of the wurtzite GaN layer.

Below the optical band gap at 3.4 eV, referred to E_0, the spectrum is dominated by Fabry-Perot oscillations in the transparent GaN layer. Between 6 and 10 eV three peak like struc-

tures dominate the imaginary part of the dielectric function $< \varepsilon_2 >$. These refer to known interband transitions usually labeled with E_1, E_2 and E_3. However, to prevent misunderstandings in the following discussion, we temporarily use a modified notation, where e. g. the wurtzite E_1 structure in $\varepsilon_\perp$ is called $A_\perp$ (fig. 6.2). The letter denote just in ascending order the identified absorption structures whereas the subscripts distinguish the wurtzite dielectric tensor components $\varepsilon_\perp$ or $\varepsilon_\parallel$ and the zincblende dielectric function ε_c. The absolute value of $< \varepsilon_{2\perp} >$ at the $A_\perp$ critical point around 7 eV, is found to be 10.6 and at least 9.9 in the uncorrected pseudodielectric function. In comparison with previous publications [10, 37], this reveals the high quality of the sample. In particular the in situ ellipsometric study of Peters et. al. [10] on GaN layers during and after growth of GaN in a MOVPE reactor reveals very similar values. The published spectrum shows an uncorrected absolute amplitude in $< \varepsilon_2 >$ of about 10.5 for a sample with 0.3 nm RMS-roughness and a FWHM of 432 arcsec derived from a X-ray $\omega - 2\Theta$ scan. This sample was not exposed to air and can be, therefore, assumed as oxide/contamination free.

CP analysis

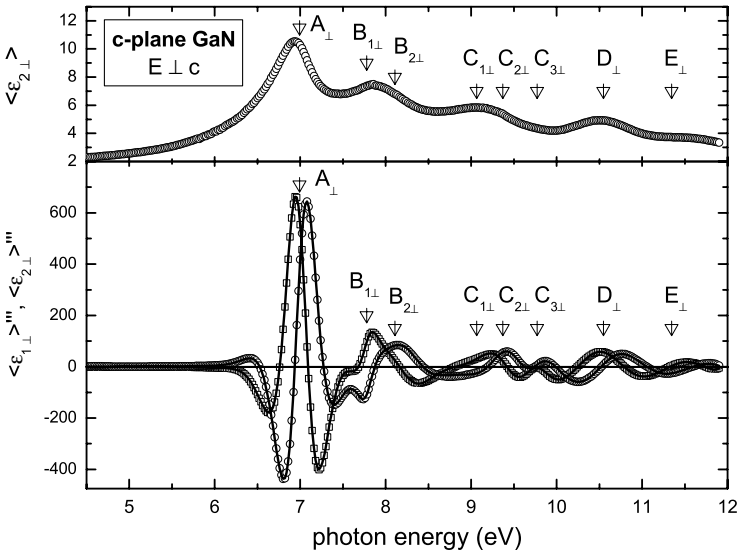

Figure 6.2: *Third derivative of the wurtzite GaN $\varepsilon_\perp$ tensor component. $< \varepsilon_{1\perp} >'''$ [squares] and $< \varepsilon_{2\perp} >'''$ [circles] are calculated from the spectra measured on c-plane GaN as shown in figure 6.1 below 12 eV. The full lines are obtained by fitting the third derivative spectra within the JDOS model. The found critical points are marked with triangles and ascending alphanumeric labels.*

In order to analyse the line shape in more detail, the third derivative of the dielectric function $d^3\varepsilon/d\omega^3$ was calculated above 4.5 eV (fig. 6.2 and 6.3). The measured characteristic

line shape was subsequently analyzed within the JDOS model by performing a numerical fit according to equation 4.20. In the lower photon energy range this fit was started with four critical points dedicated to the four pronounced peak like structures between 6 eV and 12 eV in the imaginary part of the dielectric function $< \varepsilon_2 >$. But this assumption was not reproducing all structures found in the experimental results. Finally, eight CP's were needed to reproduce the measured spectrum in the model. In figure 6.2 the fit result is plotted together with the measured derivative spectrum and all found CP energies are marked with arrows. By this fit, the known $B_\perp$ and $C_\perp$ CP's split in several transitions. One additional CP with a low relative amplitude was found below 8 eV, which belongs to the main $B_{1\perp}$ absorption feature and three CP's around 9 eV contribute to the associated $C_\perp$ peak. A first indication for a further structure below 8 eV was found already by Logothetidis et. al. [37] in low temperature measurements (83K). But the crystal quality of the sample in this investigation was much lower in comparison to our sample. Hence, the maximum peak amplitude in the imaginary part of the dielectric function at the $A_\perp$ CP was below 5.5 (room temperature) and a discovery of smaller structures was difficult. According to the old notation, we label the various additional transition structures $B_{1\perp}$, $B_{2\perp}$, $C_{1\perp}$, etc..

Due to the excitonic influence on the line shape of CP's and due to the general similarity of CP's of a low dimensionality with those showing a saddle point character, the real dimension of the CP's is not fully determined by the investigated dielectric function. Therefore, we choose in our model fit the dimension as small as possible as described in paragraph 4.1.2. However, the whole set of parameters obtained by the model fit is collected in table B.1.

In the spectral range between 14 and 33 eV we found that at least nine CP's contribute to the dielectric function. Due to the experimental limitations unfortunately no reliable data are obtained between 12 and 14 eV. Nevertheless, the line shape of the derivative spectra between 14 eV and 15 eV gives clear indications for at least one major additional CP between 12 and 14 eV. This would also agree with earlier reflectance [34] and EELS [35] measurements, where also a strong absorption structure was found between 12 and 13 eV. Correspondingly, within the CP-fit an additional transition below 14 eV was needed to achieve a good overall agreement. But the calculated values for the exact energy position and the character of this transition are ambiguous. Therefore, the data are not be presented here. As discussed later in more detail, all absorption structures above 20 eV originate from transitions between Ga3d core levels and conduction bands. According to the strong excitonic character of these transitions, all structures were assumed as zero dimensional CP's in the fit. The phase factor was fixed at $\varphi = 0°$. This excitonic character is related to the weak dispersion and, thus, to the localisation of the 3d-electron states.

6.1.2 Wurtzite GaN($1\bar{1}00$)

Sample characterisation

The wurtzite M-plane GaN($1\bar{1}00$) sample was grown in the Paul-Drude-Institut für Festkörperelektronik by PAMBE on the (001) face of γ-$LiAlO_2$ [127, 128]. For the determination of the layer properties we used a M-plane GaN sample, which was grown under almost the same conditions. We apply Raman spectroscopy in the backscattering geometry with the 514.5 nm line of an Ar^+ ion laser [126, 127] and X-ray diffraction measurement in a triple-crystal $\omega - 2\Theta$ scan [127]. Figure 6.4 shows the Raman spectra for the M-plane GaN in three different scattering configurations. In the upper spectrum a polarisation along the [$11\bar{2}0$] direction

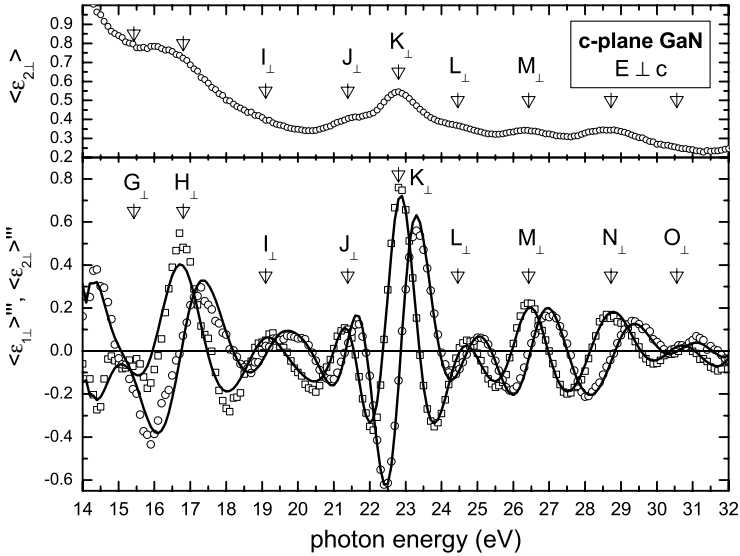

Figure 6.3: *Third derivative of the wurtzite GaN $\varepsilon_\perp$ tensor component. $< \varepsilon_{1\perp} >'''$ [squares] and $< \varepsilon_{2\perp} >'''$ [circles] are calculated from the spectra measured on c-plane GaN as shown in figure 6.1 above 14 eV. The full lines are obtained by fitting the third derivative spectra within the JDOS model. The found critical points are marked with triangles and ascending alphanumeric labels.*

(perpendicular to the c-axis) was selected in the incoming laser light, as well as in the scattered light. In the middle spectrum the polarisations were chosen parallel to the c-axis along the [0001] direction. Finally in the lower spectrum a crossed polarisation was used. These three results are consistent with the selection rules expected for $[1\bar{1}00]$ oriented films. In particular, the complete absence of the E_2 phonon in $y(z,z)\bar{y}$ geometry with polarisation along the c-axis evidences that the sample under investigation is indeed single-domain M-plane. It also reveals the in-plane orientation of the GaN [0001] axis with respect to the surface and the sample edges. The related X-ray diffraction $\omega - 2\Theta$ scan is shown in Figure 6.5. Here, a sharp peak at 16.15° is obtained beside the substrate peak of $LiAlO_2$. This peak originates from the M-plane GaN $(1\bar{1}00)$. But in particular, there is no noticeable signal in the vicinity of the assumed GaN (0002) reflection. This emphasizes again that the fraction of possible c-plane GaN is very small. From the line width of the substrate peaks taken from X-ray diffraction scans with different azimuth angles Waltereit et. al. [127] deduces an in-plane stress along the [0001] and the $[11\bar{2}0]$ directions of about 0.3 GPa and 0.8 GPa, respectively. Furthermore, he found, depending on the azimuth angle, a peak with of the M-plane GaN (0002) reflex between 12arcmin and 51arcmin (FWHM). The surface of the sample under investigation was finally characterized by AFM. In contrast to the previous investigations, [127, 129] this sample is showing an isotropic surface morphology. The RMS roughness over an area of $1 \times 1\ \mu$m

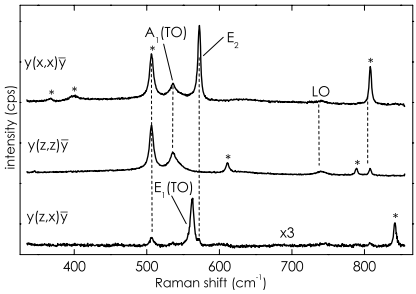

Figure 6.4:

Raman spectra of M-plane wurtzite GaN ($1\bar{1}00$) grown on γ-$LiAlO_2$ (100) [126, 127]. The cartesian axes x, y and z correspond to the [$11\bar{2}0$], [$1\bar{1}00$] and [0001] directions. An asterisk refers to a peak originating from the substrate. The absence of the E_2 phonon under y(z,z)$\bar{y}$ geometry evidences the in-plane orientation of the GaN [0001] axis.

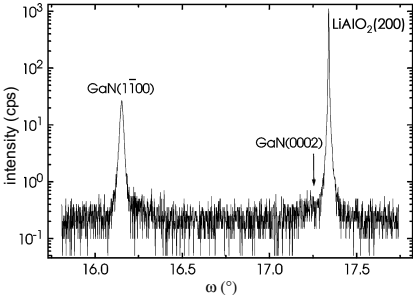

Figure 6.5:

X-ray $\omega - 2\Theta$ scan of M-plane wurtzite GaN ($1\bar{1}00$) grown on γ-$LiAlO_2$ (100) [127]. The reflex of M-plane wurtzite GaN, as well as the $LiAlO_2$ substrate peak is presented. There was no detectable signal found of c-plane wurtzite GaN (0002)

amounts to 3 nm.

Dielectric function

The ellipsometric determination of both independent dielectric tensor components $\varepsilon_\perp$ and $\varepsilon_\parallel$ was separated in several steps. In the spectral range from 2.5 to 9.5 eV the sample was measured in the two azimuthal orientation $\alpha = 0$ and $\alpha = \pi/2$ under an angle of incidence of 68°. In the higher energy range above 10 eV again these two measurements were performed under an angle of incidence of 45°. The azimuthal orientation was accomplished by a different mounting of the sample on the UHV-manipulator with respect to the sample edges. According to this adjustment, the mistake in the orientation is assumed to by less than $\pm 1°$. The measured pseudodielectric functions for the two high-symmetry orientations $\alpha = 0$ and $\alpha = \pi/2$ are presented in figure 6.6 and 6.7, respectively. These spectra are calculated within the simple isotropic two phase model. Above the optical band gap at 3.4 eV both spectra show remarkable differences in the amplitudes and the overall line shape. As expected, the pseudodielectric function is very similar to the results obtained on the c-plane GaN sample if the c axis lies parallel to the plane of incidence ($\alpha = \pi/2$). But unfortunately, the noise level in the spectral range between 10 and 12 eV is rather increased. In addition to the low photon flux from the monochromator, also a higher amount of light get lost due to the scattering of the light on the rough sample surface. However, the step in the absolute values of the pseudodielectric functions around 9.5 eV does not originate from a bad accuracy. This step has to be attributed to the different angle of incidence.

Above 4 eV, where the GaN is assumed to be opaque, the two independent dielectric

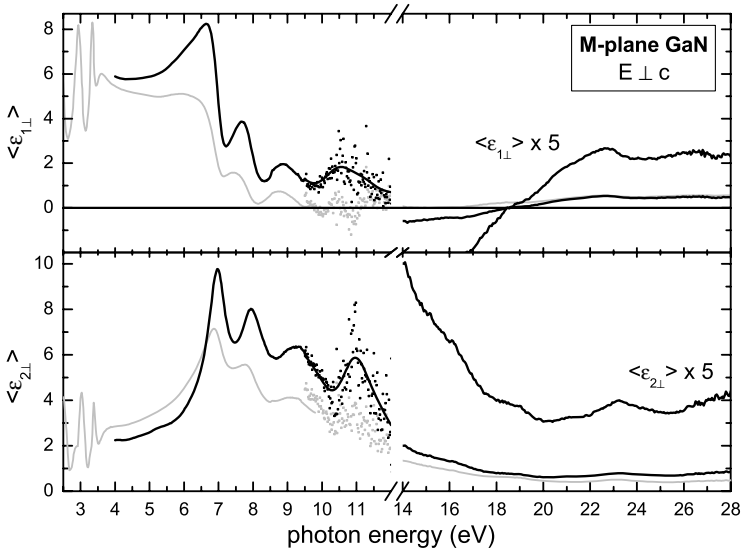

Figure 6.6: *Dielectric tensor component $< \varepsilon_\perp >$ of wurtzite GaN (M-plane) [black line]. The spectrum was calculated from the pseudodielectric functions measured in the two high symmetric sample orientations $\alpha = 0$ [gray line] and $\alpha = \pi/2$ [gray line, fig. 6.7]. Within this calculation a surface RMS-roughness of 3 nm was assumed. In order to emphasise the general line shape of the spectra we apply a spline smoothing algorithm between 9.5 and 12 eV. The raw data are shown with gray and black dots, respectively.*

tensor components $\varepsilon_\perp$ and $\varepsilon_\parallel$ were calculated with the numerical procedure as discussed in paragraph 4.2.3. For this purpose, the four coupled nonlinear equations 4.76 including the correction of the surface roughness were solved. The dielectric functions are shown in figure 6.6 and 6.7 with black lines. As expected, the principal line shapes of the two dielectric tensor components $\varepsilon_\perp$ and $\varepsilon_\parallel$ are similar to the pseudodielectric functions as measured in the two high-symmetry orientations $\alpha = 0$ and $\alpha = \pi/2$, respectively. The increased amplitudes are mainly attributed to the corrected effect of the rather high surface roughness. These similarities are in agreement with our previous assumption that both tensor components are reasonably separated already in the two particular measurement geometries. Thus, the obtained fit results are reliable. Furthermore, the deviations in the pseudodielectric functions measured around 9.5 eV are almost disappeared in the calculated dielectric tensor components. The respective pseudodielectric functions below and above 9.5 eV were measured with different angles of incidence. But the effect of surface roughness and anisotropy depends on the chosen angle of incidence. Thus, a continuous line shape is given only in the calculated dielectric tensor components.

$\varepsilon_\perp$ is basically determined by four absorption structures between 4 and 12 eV. This is

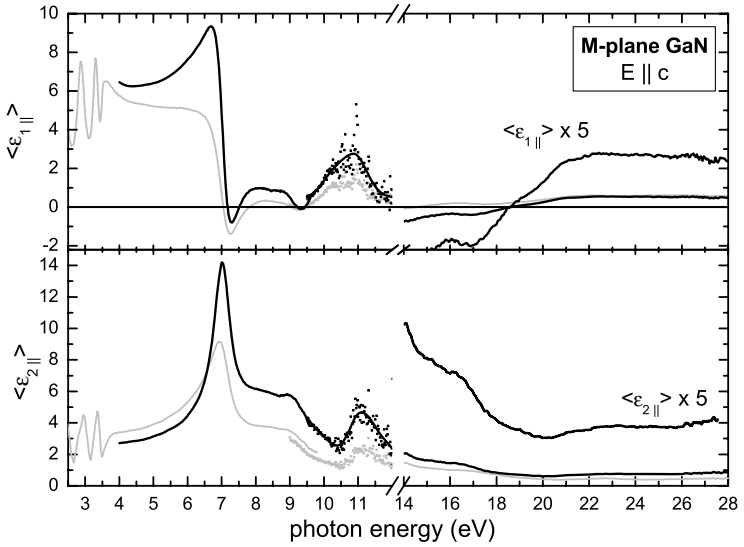

Figure 6.7: *Dielectric tensor component $< \varepsilon_{\parallel} >$ of wurtzite GaN (M-plane) [black line]. The spectrum was calculated from the pseudodielectric functions measured in the two high symmetric sample orientations $\alpha = \pi/2$ [gray line] and $\alpha = 0$ [gray line, fig. 6.6]. Within this calculation a surface RMS-roughness of 3 nm was assumed. In order to emphasise the general line shape of the spectra we apply a spline smoothing algorithm between 9.5 and 12 eV. The raw data are shown with gray and black dots, respectively.*

in agreement with the measurements on the c-plane GaN sample. But the absolute value in the imaginary part of $\varepsilon_{\perp}$ at the $A_{\perp}$ critical point around 7 eV are somewhat smaller. We determine 9.8 for the M-plane sample in comparison to 10.6 for the c-plane sample. Such a reduced amplitude can be explained by the lower crystal quality and the effect of residual surface contaminations or native oxides. In contrast to the c-plane GaN, this sample was not cleaned by annealing in UHV. It was just successively treated with acetone, H_2O, isopropyl alcohol and finally again with H_2O. Therefore, this differences can be mainly attributed to residual surface overlayers. Nevertheless, the overall line shape of $\varepsilon_{\perp}$ is in good agreement with the respective dielectric tensor component measured on the c-plane sample. Only above 14 eV considerable larger differences are found concerning the observed amplitudes and the widths of the structures. These differences probably result from the higher surface roughness of the M-plane sample. The surface roughness was actually addressed in the calculation of the "layer" (bulk) dielectric function as an additional surface layer, where the morphology of the surface was replaced by effective medium dielectric function. Nevertheless, depolarisation effects are completely neglected in this model. But especially at shorter wavelengths, this effect becomes more important. The wavelength for instance at 30 eV is already one order of

magnitude smaller than in the visible spectral range. Therefore, the phase polarisation in the polarised light could be disturbed already.

However, the extraordinary dielectric tensor component $\varepsilon_{\parallel}$ shows remarkable differences in the overall line shape in comparison to $\varepsilon_{\perp}$. The most prominent differences appear in the spectral region of the former $B_{\perp}$ critical points around 8 eV, where the amplitude of the dielectric function is fairly reduced. The $A_{||}$ ($A_{\perp}$) critical point at about 7 eV, on the other hand, is increased. The imaginary part of the dielectric function shows a absolute value of 14 at this transition energy. This strong anisotropic behaviour also proceeds in the higher photon energy range, where the various absorption structures contribute with clearly different amplitudes.

CP analysis

The measured spectra were analysed again in the third derivative of the dielectric function by means of a JDOS model fit. Figure 6.8 shows the result for $\varepsilon_{\perp}$, as well as for $\varepsilon_{\parallel}$ in the photon energy range between 4.5 and 9.6 eV.

For $\varepsilon_{\perp}'''$, the analysis in the JDOS model was started with the CP parameters obtained with the c-plane sample. But with this set of CP's clear deviation remain near the onset of the most dominant $A_{\perp}$ absorption structure at 7 eV in comparison to the measurement. However, this slope deviation is Kramers-Kronig consistent (not shown here) and, thus, denotes a further absorption structure below 7 eV. Further indications for this additional absorption structure are visible already in $\varepsilon_{\perp}$ (fig. 6.6). A shoulder at 6 eV alters the expected line shape of the real part and, thus, evidences the additional absorption structure below 7 eV. This shoulder was also observed in the dielectric functions of other c-plane GaN samples, which are not shown here. Consequently, the optical model was expanded by a further CP, which finally converges at 6.36 eV. As assumed before, the line shape above 7 eV is almost identical and the three following CP's are roughly at the same photon energies like in the c-plane GaN sample (tab. B.2).

The third derivative of $\varepsilon_{\parallel}$ clearly evidences the complete absence of the $B_{\perp}$ absorptions structures between 4.5eV and 9.6eV. But like in $\varepsilon_{\perp}$, the CP fit shows remaining deviations around 7 eV. In contrast to this fit of $\varepsilon_{\perp}'''$, the deviations are much smaller now and no unambiguous fit is achieved. Two solutions containing an additional CP somewhat below or above the $A_{||}$ CP at 7.0 eV are possible. Both would enhance the overall agreement. But the solution with an additional CP at 7.3 eV above $A_{||}$ was finally slightly better in the overall agreement. This solution is shown in figure 6.8 and listed in table B.3.

Unfortunately, the noise level in the measured dielectric tensor components is very high between 9.7 and 12 eV. As a consequence the analysis in the third derivative was not possible in this spectral range. The CP parameters as presented in table B.2 and B.3 are, therefore, calculated in the less sensitive first derivative and the values of the oscillator strength and the attenuation parameter are not comparable with the other results.

Above 14 eV the third derivative spectra reveal in principal the same absorption structures in both dielectric tensor components (fig. 6.9). Nevertheless, some smaller differences can be noticed. First of all the absorption structures above 20 eV appear strongly broadened in $\varepsilon_{\parallel}$ in comparison to the $\varepsilon_{\perp}$ absorption structures. Second, the energetically positions of several CP's are shifted against each other. But furthermore, the position of CP's in $\varepsilon_{\perp}$ are also slightly changed in comparison with the CP energies in $\varepsilon_{\perp}$ measured on the c-plane sample. In connection with these energy shifts, it has to be noted that the index of refraction

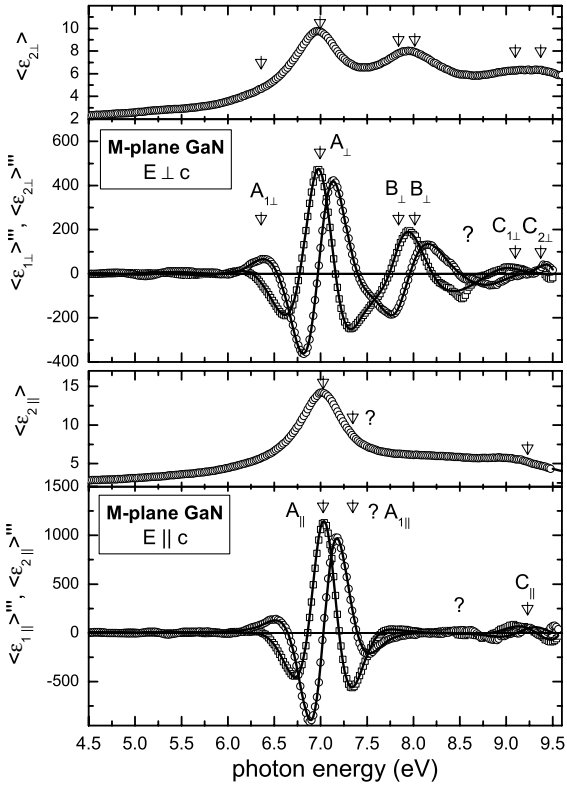

Figure 6.8: *Third derivative of the wurtzite GaN $\varepsilon_\perp$ and $\varepsilon_\parallel$ tensor component. $<\varepsilon_{1\perp}>'''$ [squares] and $<\varepsilon_{2\perp}>'''$ [circles], as well as $<\varepsilon_{1\parallel}>'''$ and $<\varepsilon_{2\parallel}>'''$ are calculated from the spectra measured on M-plane GaN as shown in figure 6.6 and 6.7 below 12 eV. The full lines are obtained by fitting the third derivative spectra within the JDOS model. The critical points are marked with triangles and ascending alphanumeric labels.*

generally decreases above 10 eV in both optical axis of GaN. In the region above 14 eV we calculate finally absolute values around the vacuum refractive index of $n = 1$. Therefore, the assumption about the negligible contribution of the $\varepsilon_\parallel$ component to pseudodielectric function measured on c-plane GaN samples is not longer valid. Moreover, the spectral range above 10 eV was measured under an angle of incidence of 45°. Under these conditions, the pseudodielectric function determined on c-plane GaN above 10 eV has to be interpreted as a superposition of both independent dielectric tensor component. The two dielectric tensor components calculated from the measurements on the M-plane sample, in contrast, should represent $\varepsilon_\perp$ and $\varepsilon_\parallel$ well separated. But the lower overall sample quality and a possible small

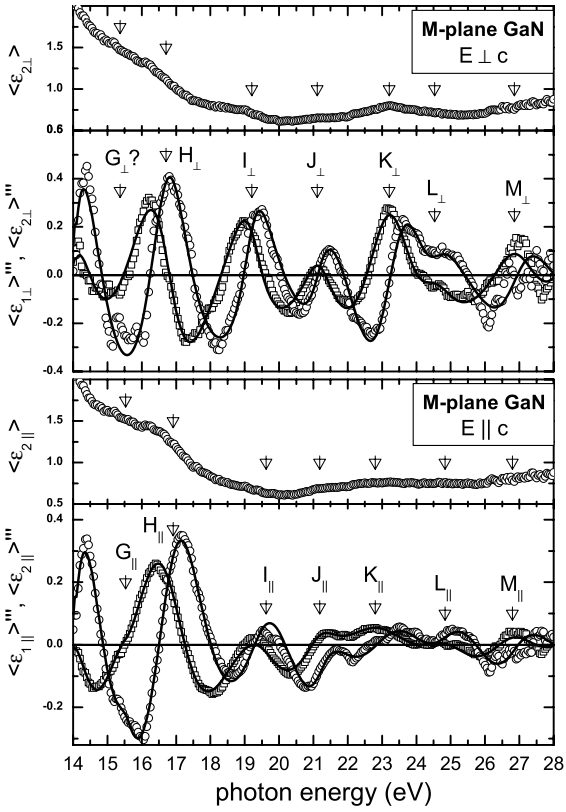

Figure 6.9: *Third derivative of the wurtzite GaN $\varepsilon_\perp$ and $\varepsilon_\parallel$ tensor component. $<\varepsilon_{1\perp}>'''$ [squares] and $<\varepsilon_{2\perp}>'''$ [circles], as well as $<\varepsilon_{1\parallel}>'''$ and $<\varepsilon_{2\parallel}>'''$ are calculated from the spectra measured on M-plane GaN as shown in figure 6.6 and 6.7 above 14 eV. The full lines are obtained by fitting the third derivative spectra within the JDOS model. The found critical points are marked with triangles and ascending alphanumeric labels.*

anisotropy in the surface roughness maybe constrains here a higher accuracy especially above 20 eV. Nevertheless, at the end we can conclude a notable shift of -0.2 eV and -0.4 eV for the two absorption structures $H_\perp$ and $I_\perp$ in $\varepsilon_\perp$ with respect to those in the $\varepsilon_\parallel$, which is not an artifact of measurement broblems.

6.1.3 Zincblende GaN

Sample characterisation

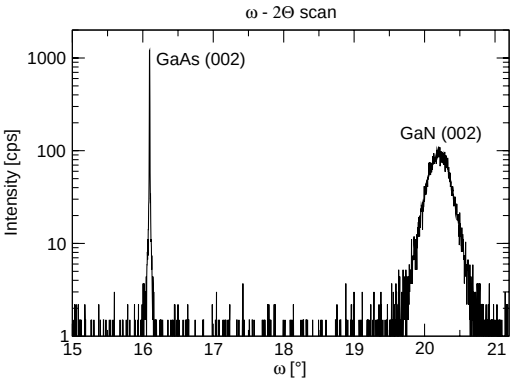

Figure 6.10:
X-ray $\omega - 2\Theta$ scan of the zincblende GaN sample. The reflex of the zincblende GaN at about 20.2°, as well as the GaAs substrate peak at about 16° is presented [130].

The presented optical properties of zincblende GaN are obtained on a GaN(001) layer grown by MBE on a GaAs(001) substrate at the University of Paderborn [131, 132]. The layer with a thickness of about 400 nm is assumed to be pure zincblende phase with a fraction of wurtzite inclusions less than 1%. This assumption is supported by X-ray $\omega-2\Theta$ diffraction scan, which shows only two sharp peaks. These are the GaAs(002) and the GaN(002) reflex (fig. 6.10). But in particular, there is no side band visible below the GaN(002) reflex at 20.2°. Wurtzite inclusions would result in an additional peak 1.5° below the zincblende (002) reflex as shown in more detailed by Sun et. al. [133]. The peak width of the GaN(002) reflex is calculated to 40.9 arcmin (FWHM). If this value is used as a scale for the crystal quality, the zincblende GaN layer is showing like the M-plane GaN film also a much lower quality than the wurtzite c-plane sample. This is also emphasised by the high surface RMS-roughness of 5nm, which was calculated from 1×1 μm AFM scans. For a reduction of surface contaminations, the sample was again subsequently cleaned with acetone, H_2O and isopropyl alcohol and finally annealed at ≈450°C in the UHV-environment of the ellipsometer chamber.

Dielectric function

The dielectric function was measured in the same manner like this of the c- and M-plane wurtzite GaN samples. The grey line in figure 6.11 indicates the pseudodielectric function, whereas the black line shows the spectrum corrected according to the surface roughness. For this correction an EMA layer of 3 nm, somewhat lower than the RMS roughness of 5.4 nm determined by AFM, was assumed. The approximate consideration of surface roughnesses within an EMA approximation is established in the visible spectral range for RMS-roughnesses of only a few nm. But the approximation is problematic for RMS values higher than 5 nm. Therefore, a lower value was finally used in order to avoid a wrong (over-) correction. However, the imaginary part of the dielectric function was also calculated with the true value of 5.4 nm for comparison (dashed line in fig. 6.11). Due to the zincblende symmetry the sample is optically isotropic and the orientation of the layer, with respect to

the measurement geometry, is not relevant. Furthermore, the layer is optically opaque above the band gap. Therefore, the effective values as shown in figure 6.11 with black lines can be assumed already as the bulk dielectric function of the zincblende GaN layer if residual surface contaminations are neglected.

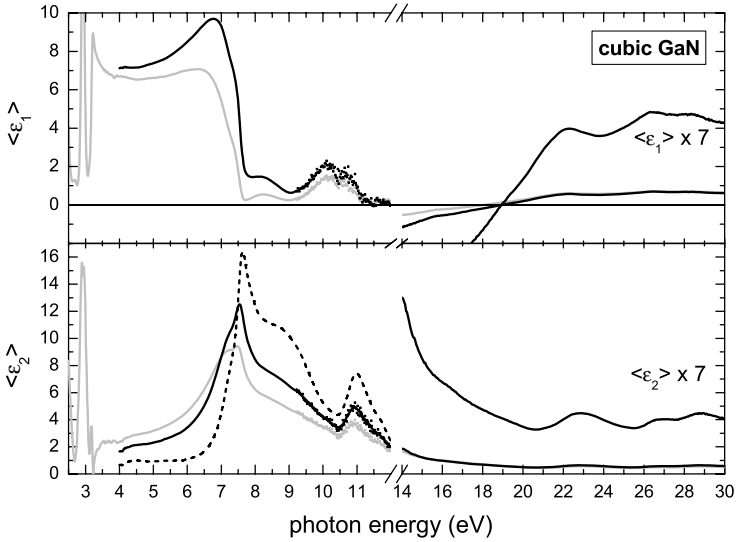

Figure 6.11: *Pseudodielectric function of the zincblende GaN sample [grey line]. The surface roughness of the sample was corrected within the EMA-model for different RMS-roughnesses values of 3 nm [black line)] and 5.4 nm [dashed line]. In order to emphasise the general line shape of the spectra we apply a spline smoothing algorithm between 9.5 and 12 eV. The raw data are shown with gray and black dots, respectively.*

According to these ellipsometric measurements, the dielectric function of zincblende GaN shows only two absorption structures in the spectral range between the band gap and 10 eV. The corresponding peaks in the imaginary part of the dielectric function lie at approximately 7.2 eV and 7.5 eV. Furthermore, the second structure at about 7.5 eV is much sharper and more dominant than the first. The amplitude of this peak is deduced depending on the surface roughness correction between 16.3 and 12. In both cases this is particularly higher than the $A_\perp$ absorption peaks that was found in $\varepsilon_\perp$ of wurtzite GaN and probably also higher than the peak amplitude in the corresponding $\varepsilon_\parallel$ dielectric tensor component. This finding is in agreement with the stronger degeneration of electronic states in the zincblende phase due to the higher crystal symmetry. Above 10 eV, the general line shape of the zincblende dielectric function is very similar to the dielectric function measured on the wurtzite samples. In particular between 10 and 12 eV the dielectric function is dominated again by at least one major absorption structure. However, the continuously increasing overall amplitude of the

imaginary part of the dielectric function above 25 eV (fig. 6.11) has to be attributed to an increasing influence of scattered light from the monochromator. Thus, it is not correlated with the real sample properties.

CP analysis

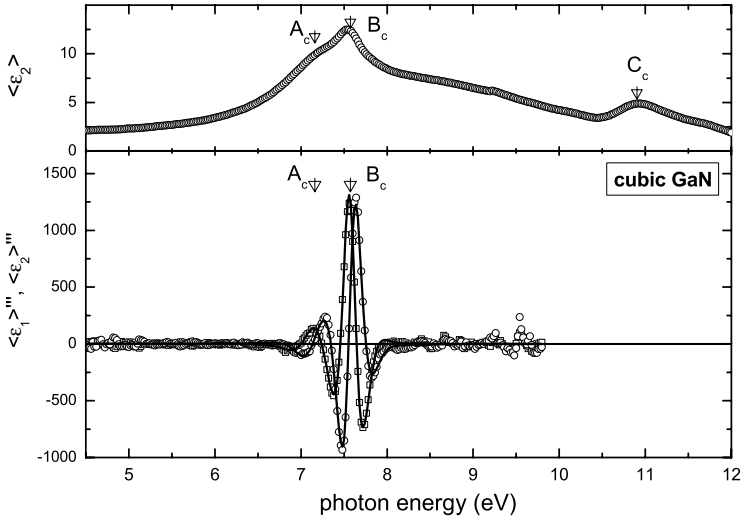

Figure 6.12: *Third derivative of the zincblende GaN dielectric function.* $< \varepsilon_1 >'''$ *[squares] and* $< \varepsilon_2 >'''$ *[circles] are calculated from the spectra as shown in figure 6.11 below 12 eV. The full lines are obtained by fitting the third derivative spectra within the JDOS model. The found critical points are marked with triangles and ascending alphanumeric labels.*

The previous assumption that only two neighbouring absorption structures close to 7 eV contribute to the dielectric function below 10 eV, is strongly supported also by the general line shape of the third derivative spectra (fig. 6.12). The CP-fit reveals these two structures, which are labeled with A_c and B_c, at 7.16 and 7.57 eV, respectively. Both structures can be reproduced very well under the assumption of one dimensional CP's. It is remarkable that both components of the double absorption peak appear shifted to higher photon energies in comparison with the $A_\perp$ absorption structure in $\varepsilon_\perp$ (6.99 eV), or the $A_{||}$ in $\varepsilon_\parallel$ (7.03 eV) of wurtzite GaN. The evaluation of the following C_c CP between 10 and 12 eV was again only possible in the first derivative spectrum due to the increased noise level in this region. The transition energy of the CP in this photon energy range is determined to 10.5 eV.

Above 14 eV the principal line shape of dielectric function is rather similar to the wurtzite GaN results. However, the third derivative spectra (figure 6.13) reveal several differences. At first, the various absorption structures appear more indistinct in comparison to the wurtzite GaN dielectric function. But moreover, we need also additional CP's to achieve a good

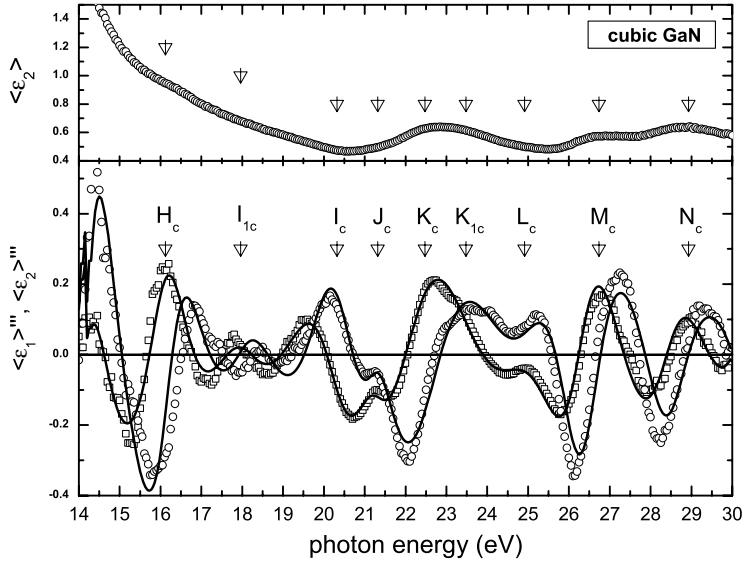

Figure 6.13: *Third derivative of the zincblende GaN dielectric function.* $< \varepsilon_1 >'''$ *[squares] and* $< \varepsilon_2 >'''$ *[circles] are calculated from the spectra as shown in figure 6.11 above 14 eV. The full lines are obtained by fitting the third derivative spectra within the JDOS model. The found critical points are marked with triangles and ascending alphanumeric labels.*

representation of the experimental results in JDOS model. The labels used for the CP's are chosen with respect to results for wurtzite GaN. In particular above 21 eV, the allocation to CP in the wurtzite dielectric function is quite obvious. A remarkable difference appears only around 23 eV. Two CP's (K_c and K_{1c}) seem to contribute to the dielectric function in this energy region. However, these findings have to be interpreted with care due to the relatively low quality of the ellipsometric results. This applies in particular to the spectral range from 14 to 21 eV. The problems are partly related to the strong surface roughness. A RMS roughness of 5.4 nm also indicates already a polycrystalline character of the layer. But nevertheless, we can conclude from these measurements that above 19 eV almost the same absorption structures contribute to the dielectric function like in the wurtzite phase. This transitions are just slightly shifted to higher photon energies.

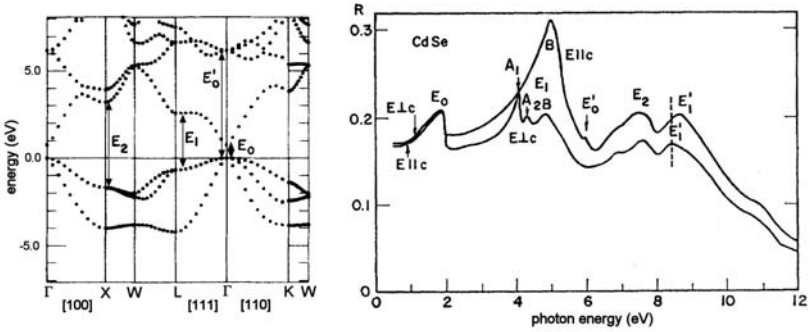

Figure 6.14: *Reflectivity for $\vec{E}\perp c$ and $\vec{E}\| c$ of wurtzite CdSe measured at room temperatures [134] [right hand side]. The given labels for the transition structures correspond to the respective transitions in the zincblende structure. On the left hand side the calculated LDA band structure of zincblende CdSe [135] is shown with arrows at the proposed CP transitions.*

6.2 Discussion of GaN interband transitions below 12 eV

6.2.1 Heuristic assignment of CP's

A heuristic assignment of various structures in the wurtzite-type CdS and $CdSe$ reflectivity was presented by Cardona et. al. in ref. [134, 136, 137]. His assignment is based on a general comparison with zincblende spectra and a comprehensive discussion of characteristic differences in the respective crystal structures [48, 138, 139]. Figure 6.14 shows, e. g. the ordinary ($\vec{E}\perp c$) and extraordinary ($\vec{E}\| c$) reflectivity spectra for wurtzite CdSe in relation to the zincblende band structure. The proposed labels E_0, E_0', E_1, E_1', and E_2 for the characteristic reflection (absorption) structures relate to the corresponding peaks observed in other zincblende materials such as GaAs as shown in figure. 4.3 and 4.4. However, in general the eightfold degeneracy of the corresponding cubic states is disturbed in the hexagonal structure. On the other hand, the symmetry of the zincblende $\pm[111]$ directions is very similar to that of the corresponding $\pm[0001]$ c axis of wurtzite crystals. Therefore, a direct correlation can be found between the zincblende E_1 and the so called "E_1" structures in wurtzite CdSe. The other six cubic directions ($\pm[1\bar{1}1]$, $\pm[\bar{1}1\bar{1}]$, $\pm[\bar{1}\bar{1}1]$) split in wurtzite structures from the $\pm[111]$. But these directions remain basically degenerate with each other due to the sixfold symmetry around the c axis. Together, this leads to the splitting of the E_1 related reflection structure for $\vec{E}\perp c$ in CdSe (fig. 6.14).

In order to understand the differences in the symmetry and, thus, in the electronic structure, it is helpful to compare the Brillouin zones of the wurtzite and the zincblende structure in more detail. Figure 6.15 shows both Brillouin zones, the truncated octahedron of the zincblende and the hexagon of the wurtzite structure. For this comparison it is important that the wurtzite primitive unit cell contains twice as many atoms as the zincblende primitive unit cell. Thus, the Brillouin zone of the wurtzite has actually only one half of the volume of the

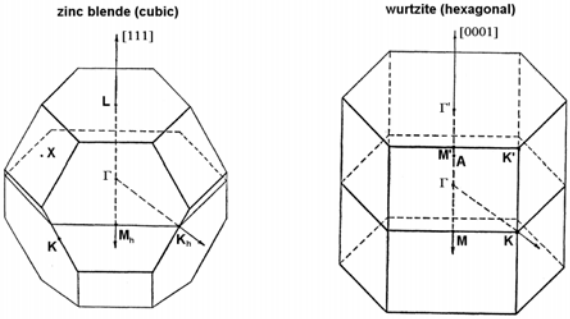

Figure 6.15: *Brillouin zone of zincblende (cubic) and double Brillouin zone of wurtzite (hexagonal) materials [48]. By this definition, both zones are equal in volume and* $|\Gamma - L| = |\Gamma - \Gamma'| = |\vec{k}|_{max}$ *is the common maximum wave vector. But we should note that the hexagon perpendicular to the [111] ([0001]) direction is somewhat larger in the zincblende Brillouin zone than in the wurtzite Brillouin zone.*

zincblende zone. In consideration of this fact Birman [48] introduced a doubled zone scheme for the wurtzite structure as shown in figure 6.15. In this doubled zone scheme the wurtzite electronic states along the Γ-Γ′ ("c" direction) can by obtained as disturbed zincblende states of the $\Gamma - L$ direction ([111]). The perturbation of the cubic states could be related to differences in the crystal potential of both crystal types and leads to an anergy shift, as well as a splitting of corresponding states (Γ_{15}(ZB)↔ Γ_1, Γ_5(Wur)) (q. v. fig. 4.7). The similarity of electronic states in this direction can easily be demonstrated in the plane wave representation. Except the different stacking order of the hexagonal close packed nets both crystal types are very similar. Thus, also the periodic potentials along the zincblende $\Gamma - L$ and the wurtzite Γ-Γ′ direction are almost the same. Therefore, the related energy of each wave function with a $|\vec{k}|$ along the $\Gamma - L$ direction is also almost identical with the energy of those with the same $|\vec{k}|$ but along Γ-Γ′ direction in the wurtzite double zone. This principal agreement is demonstrated for the shortest wavelength with $\vec{k} = \Gamma - L = \vec{k} = \Gamma - \Gamma'$ in figure 6.16. The corresponding waves are shown there in relation to the hexagonal close packed nets. The phase of both waves is shifted by π on progressing from one plane to the next identical one, in either structure. But, whereas the wavelength of the shortest plane wave in the doubled Brillouin zone is identical with the periodicity of hexagonal close packed nets (ABAB...) in the wurtzite structure, this wavelength is still smaller and asymmetric in comparison to the (ABCABC...) periodicity of the zincblende structure. This behaviour can be explained by the different orientation of the main crystal axis. In fact, the zincblende unit cell is defined in a (cartesian) coordinate in which the main axis are not parallel or perpendicular to the [0001] direction of the wurtzite structure.

However, in contrast to the good correlation of the wurtzite [0001] (c-axis) and the zincblende [111] axis, there is no direct representation in the zincblende Brillouin zone for the

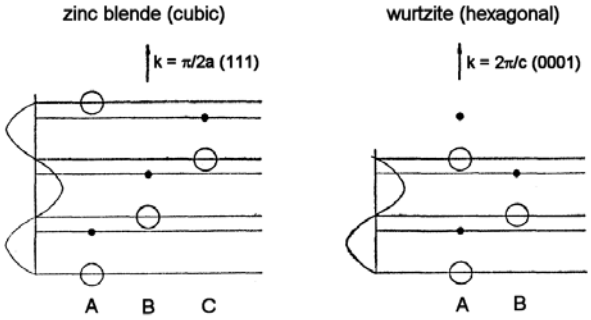

Figure 6.16: *Plane wave propagation at the edge of the zincblende and doubled wurtzite Brillouin zone in the* $\Gamma - L$ *and* $(\Gamma - \Gamma')$ *direction, respectively [48].*

wurtzite high symmetry lines Γ-K and Γ-M perpendicular to the c-axis. Therefore, wurtzite electronic states along this symmetry lines possibly are represented by a composition of certain zincblende states. These states can include, in particular, a significant contribution from zincblende states along the [100] axis, which are very dominant in the zincblende optical spectra.

In consideration of these symmetry arguments, the E_1 absorption peaks of zincblende materials should split into at least two peaks in the corresponding wurtzite structure. A simple symmetry consideration indicates now that the [111]([0001])-like singlet with $\vec{k} \| c$ appears only for $\varepsilon_\perp$ where the electric field vector lies perpendicularly to the $[111]$-like c-axis ($\vec{k_E} \| c$). While the $\pm[1\overline{1}\overline{1}]$ triplet should appear for both polarisations. This behaviour is, in fact, observed in our ellipsometry spectra on the M-plane GaN samples in the first major absorption structures (fig. 6.17). But a comparison of the dielectric tensor components $\varepsilon_\perp$ and $\varepsilon_\parallel$ measured on GaN with the results obtained for CdS and CdSe shows that the singlet and triplet peaks seem to be reversed in energy with respect to those in CdS and CdSe (fig. 6.14). It could be possible that the effect of the hexagonal field has the opposite sign in GaN. But on the other hand, we found in $\varepsilon_\perp$ measured on M-plane GaN clear indications for a third structure below 7 eV flanking the $A_\perp$ CP. This appears much more pronounced also in InN, as we will show in the following chapter. But also in CdSe a splitting in three CP's is imaginable. The two A_1 and A_2 features in the CdSe reflectivity spectra in principal relates to only one spin-orbit splitted peak A. But we think that the so called "E_0'" structure actually correlates also with a further E_1-correlated absorption. This is strongly supported also by the newer band structure calculation (fig. 6.14). According to these similarities we attribute the first "three" absorption structures in $\varepsilon_\perp$ of hex. GaN also to the perturbed zincblende E_1 CP. Hence, the $E_1(A)$ ($A_{1\perp}$) should correspond to [111] like states in the [0001] direction, while the $E_1(B)$ ($A_\perp$) and the $E_1(C)$ ($B_\perp$) CP's correspond to the $\pm[1\overline{1}\overline{1}]$-like triplet.

In order to emphasise the correlation of zincblende and wurtzite CP's, we have renamed the three structures in $\varepsilon_\perp$ to $E_1(A)$, $E_1(B)$, and $E_1(C)$ while the single peak in $\varepsilon_\parallel$ is called just E_1. These labels correspond to the isoelectronic sequence scheme used for zincblende materials (fig. 6.17 and 7.10). It should be mentioned that these labels are different to the

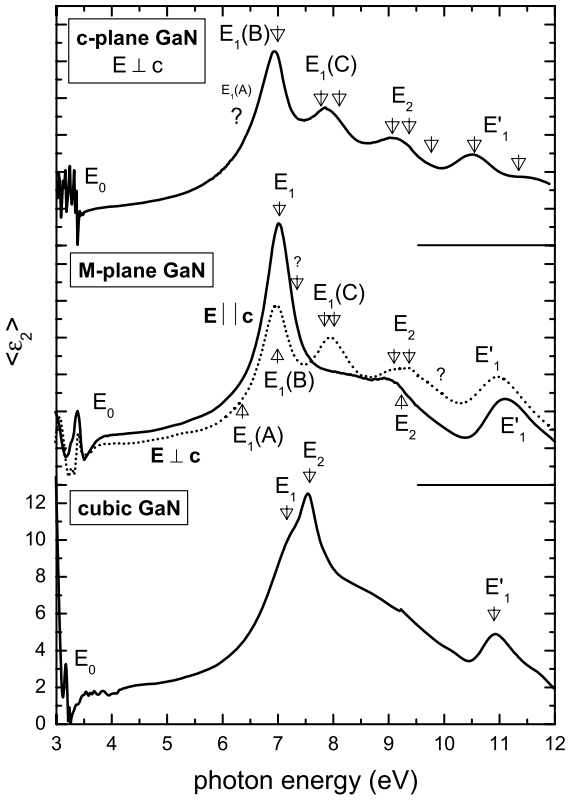

Figure 6.17: *Comparison of the imaginary part of different dielectric functions measured on zincblende and wurtzite GaN. The labels E_0, E_1, E_1', and E_2 for the characteristic absorption structures correspond, in the isoelectronic sequence scheme, to peaks observed in various zincblende materials [85, 86].*

commonly used labels for wurtzite GaN (fig. 4.8). But the suggested new labels account the correlation of transitions in the wurtzite and zincblende structure and further allow a better discussion of similarities and differences in the respective spectra. This would be not possible with the old commonly used labels.

According to the argumentation of Cardona et. al., the following two major absorptions structures $C_\perp$ and $D_\perp$ in the wurtzite GaN $\varepsilon_\perp$ are attributed to the perturbed zincblende E_2 and E_1' transitions, respectively. Both are expected in $\varepsilon_\perp$, as well as in $\varepsilon_\parallel$ (fig. 6.2 and 6.17) and can be also observed in the CdS and CdSe dielectric tensor components. The assumption is supported by the fact that the E_1' ($D_\perp$) absorption structure in $\varepsilon_\perp$ is located at a somewhat lower photon energy ($\approx$0.5 eV) than the corresponding E_1' in $\varepsilon_\parallel$. Furthermore, this is also

in a good agreement with the experimental findings on the CdS and CdSe (fig. 6.14). But in general, a similar splitting as those of the E_1 transitions in $\varepsilon_\perp$ is also expected for the E_1' peak. We discover a first indication for this splitting in $\varepsilon_\perp$ measured on the c-plane (0001) sample. The two CP's $D_\perp$ and $E_\perp$ jointly contribute to the broad absorption structure between 10 and 12 eV (fig. 6.2). Unfortunately, this double structure is not resolved in the measurements on M-plane GaN. Thus, the expected disappearance of a second structure in the respective $\varepsilon_\parallel$ can not taken as a proof of this interpretation.

The zincblende GaN dielectric function reveals in agreement with the previous interpretations two CP's A_c and C_c at almost identical photon energies like the wurtzite E_1 and E_1' CP's. Consequently, we attribute these directly to the known zincblende E_1 and E_1' transitions (fig. 6.12 and fig. 6.17). But surprisingly, there is no indication for a CP at photon energies close to the so called E_2 CP in the wurtzite dielectric function. Furthermore, the zincblende E_1 seems to split up in two structures namely the A_c and the B_c (fig. 6.12). A comparison with the zincblende GaAs dielectric function shown in figure 4.3 supports the explanation of the double structure by a spin-orbit splitting of the E_1 transition. This would correspond to a splitting of the top zincblende valence band along the Δ_1 line ($[111]$). The splitting has been observed also for the E_2 peaks of $CdSe$ ($\approx$0.3 eV), but not for CdS,[137], where it in deed should be much smaller. Recent LMTO-ASA calculations including the effect of the core-like Ga3d-levels show that the Δ_1 splitting in the zincblende, as well as in the wurtzite phase of GaN is Δ_1 $\approx$0.032 eV [140]. Against expectations, this is larger than the splitting Δ_0 $\approx$0.020 eV at the centre of the Brillouin zone (experimental Δ_0 $\approx$0.017 eV, Ref. [25]). But the predicted value is still much smaller than the width of the peaks in our measured dielectric functions (Γ $\approx$0.2 eV) and in particular smaller than the observed double structure ($E_{B_c} - E_{A_c}$ $\approx$400 meV). Therefore, the spin-orbit splitting of the E_1 transition can be excluded. Accordingly, it seems to be likely that either the E_2 or E_0' structure is shifted to lower energies in the vicinity of the E_1 peak. However, due to the very good agreement of E_0, E_1, and the E_1', we also expect only a small perturbation for the E_0' transition, which also belongs to the well defined [111]([0001])-axis. Therefore, a shifted E_0' peak is also excluded and it is more likely that B_c structure in the zincblende dielectric function is in fact associated with the E_2 transition at the X point in the respective Brillouin zone. It was mentioned already, also by Birman [48] that in contrast to the E_1 CP's the assignment of E_2 like transitions in the wurtzite structure is problematic. There exist no corresponding high symmetry axis in the wurtzite Brillouin zone for the zincblende $[100]$ axis. Therefore, a correlation within a simple perturbation theory should fail. Due to this reason, it seems to be more likely that the B_c peak in the zincblende GaN dielectric function corresponds to the E_2 transition.

6.2.2 Comparison with ab-initio calculations

We compare in figure 6.18 the imaginary part of both the wurtzite, as well as the zincblende GaN dielectric functions with the recent theoretical results of Benedict et al. and Lambrecht et al. [84, 98, 141]. The authors of the first work use a pseudopotential band-structure calculations including the electron-hole interaction in the determination of the optical properties. These calculations have already been presented in reference [41]. In the latter publication the authors use the LMTO (ASA) method very similar to the band structure calculation of Christensen et. al. [94]. This calculation, in contrast, does not include the influence of the electron-hole interaction. Hence, the presented spectra are shifted already by the authors ap-

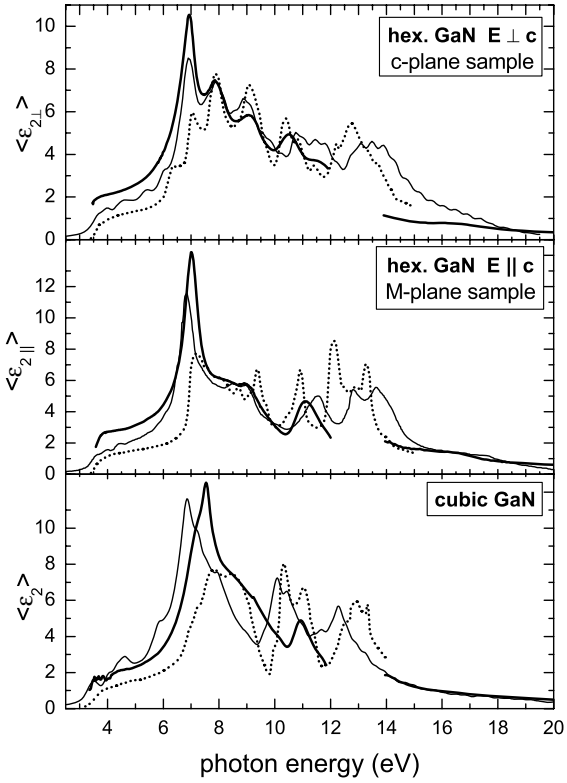

Figure 6.18: *Measured imaginary parts of the dielectric function (tensor components)* $<\varepsilon_2>$ *[thick line] compared to* ε_2 *calculated by Benedict et al. [41] [thin line] and Lambrecht et al. [84, 98, 141] [dotted line].*

proximately 1 eV to higher energies in order to address the well known "band gap problem" of this kind of calculations and to fit the fundamental band gap to the experimental value. Especially for the two dielectric function components $\varepsilon_\perp$ and $\varepsilon_\parallel$ of the wurtzite crystal type, the inclusion of the electron-hole interaction in the calculation of Benedict et. al. leads to a dramatically improved overall agreement of the theory in comparison to the experimental results. The line shape of theory and experiment is just about the same. In the calculation of Christensen et. al., in contrast, the $E_1(B)$ structure is reduced in comparison to the $E_1(C)$ structure. It is also well known that excitonic effects (direct coulomb and exchange interactions) shift oscillator strengths from higher to lower energy transitions. Accordingly, the general line shape of both calculations are in good agreement with the experimental results. All major structures are reproduced by both theories also in the zincblende dielectric function. But obviously, the excellent agreement is somehow reduced for the zincblende crystal

structure. In the calculations of Benedict et al. the excitonic effects seem to be somehow overcompensated. Notable is also the small shoulder at about 6.4 eV calculated by Lambrecht et. al. in the wurtzite $\varepsilon_\perp$ dielectric tensor component. This absorption structure coincide with the $E_1(A)$ ($A_{1\perp}$) CP found in $\varepsilon_\perp$ measured on the M-plane GaN sample.

In particular, we would like to emphasise again the good agreement of both calculated $\varepsilon_\parallel$ to the measured spectrum presented here. The calculated $\varepsilon_\parallel$ also shows only one dominating CP up to 9 eV. This E_1 peak arise at about 7 eV as well. But the weak second small structure predicted by the theories at around 8.5 eV, is not resolved in the experiment. At this point we have to note that in the calculated dielectric function (tensors) the electron-phonon-interaction is neglected [79, 80, 142]. Thus, temperature effects, which leads to a broadening of structures, are not included. For the comparison, therefore, experiments at low temperatures would be desirable and would help to resolve weaker structures in the measured dielectric function.

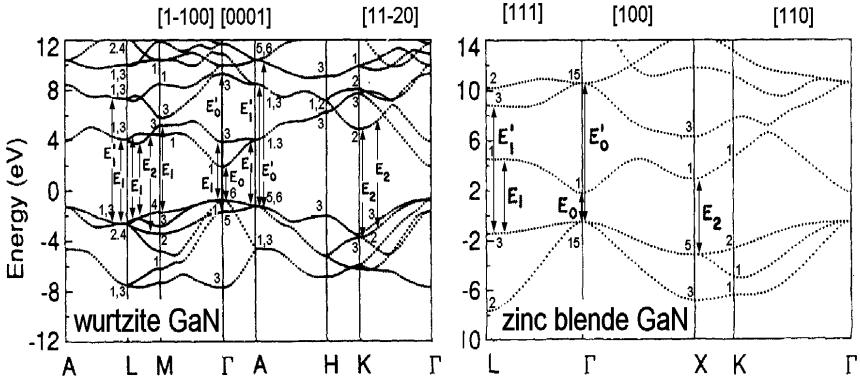

Figure 6.19: *GaN band structure calculated by Christensen et. al. [94] as already shown in paragraph 4.1.3 figure 4.7. The arrows correspond to interband transitions, which are related to specific absorption structures in the dielectric functions of wurtzite and zincblende GaN (fig. 6.17).*

In order to elucidate the origin of absorption structures in the dielectric function Lambrecht et. al. [84, 98, 141] also present a detailed theoretical analysis by means of a separation of the different band-to-band contributions to the calculated CP's. According to this analysis Lambrecht et. al. also resolve a first weak absorption structure close to the $E_1(A)$, which we can determine in $\varepsilon_\perp$ measured on M-plane GaN. He attributes this to $\Gamma_5^v \rightarrow \Gamma_3^c$ and $A_{5,6}^v \rightarrow A_{1,3}^c$ transitions (fig. 6.19). This feature is, in fact, much weaker (not detectable) in our GaN spectra and also does not appear in the exciton calculation of Benedict et. al.. Two tentative explanations are offered by Lambrecht et. al. for this problem. First, the band difference curvature at the minimum $\Gamma_5^v \rightarrow \Gamma_3^c$ is stronger for GaN relative to the size of the Brillouin zone. Thus, the contribution of this transition is relatively weaker already in the approximated one electron spectrum. Secondly, this structure is very close to the $E_1(B)$ peak in energy. The excitonic effects on the $E_1(B)$ peaks are much stronger in GaN than in CdSe

or InN and the small $E_1(A)$ feature could be essentially hidden under the low energy tail of the $E_1(B)$ structure due to the lifetime broadening. In fact, the calculation of Benedict et. al. , which include excitonic effects, uses imaginary contribution that leading to a broadening of the structures similar to the broadening in experimental spectra. However, the $\Gamma_5^v \rightarrow \Gamma_3^c$ transition is only allowed for $\vec{E} \perp c$ and corresponds to the folded $L_\parallel$ point of the zincblende Brillouin zone. According to this assignment of Lambrecht et. al. the $E_1(A)$ absorption is only seen for $\vec{E} \perp c$. This is in agreement with our measurements on M-plane GaN. The assignment supports, in particular, our previous expectation that the [111]([0001])-like singlet appears at lower energies than the E_1 $\pm[1\overline{1}\overline{1}]$ triplet as known from CdSe. Furthermore, this assignment agrees with the expected correlation of the E_1 singlet in the wurtzite structure with the E_1 transition ($L_3^v \rightarrow L_1^c$) in the zincblende structure. Both are determined close in energy. This is also in agreement to the theoretical predictions of Lambrecht et. al. (fig. 6.18 thin lines).

The following $E_1(B)$ or (E_1) wurtzite peak detectable in both components is attributed by Lambrecht et. al. to a strong saddlepoint transition along the U direction. They correspond in particular to $U_4^v \rightarrow U_3^c$ for $\vec{E} \perp c$ and $U_3^v \rightarrow U_3^c$ for $\vec{E} \| c$, respectively. These transitions occur along the M_L line very close to the prominent point at $2/3M - L$ where the folded $L_\perp$ of the zincblende Brillouin zone would lie. This interpretation is in very good agreement with the previous assumption where these structures correlated with the E_1-like $\pm[1\overline{1}\overline{1}]$ triplet.

The third wurtzite absorption feature $E_1(C)$ is only seen in $\varepsilon_\perp$. According to Lambrecht et. al., this absorption is mainly correlated to transitions at the M point between $M_4^v \rightarrow M_3^c$, which are in fact, only allowed for $\vec{E} \perp c$. Thus, the $E_1(C)$ transition also correlates somehow to electronic states perpendicular to the $L_\parallel$ states in zincblende. This explanation is in contrast to a previous assumption, which we suggest in reference [126]. In this publication we assumed a correlation of the strong $E_1(C)$ peak with the folded $L_\parallel$ states of zincblende. But in this publication we have also discussed already the problem that $E_1(B)$ and $E_1(C)$ are reversed in energy with respect to those in CdS and $CdSe$. However, finally the new interpretation for the E_1 related structures in GaN fits very well now with the pure symmetry arguments of the previous paragraph and the old results on CdS and $CdSe$ given by Cardona et. al. [134, 136, 137].

The interpretation of the wurtzite GaN "E_2" peak at about 9 eV is now more complex. This structure does not energetically agree with the E_2 in the zincblende dielectric function and also Lambrecht et. al. noticed in his recent publication [98] that these structures might not correlate. But his theoretical assumption that the transition in the wurtzite dielectric function primarily corresponds to transitions at the M point between M_2-M_1 can be disproved by our measurements. These transitions are forbidden in $\varepsilon_\parallel$. But according to the experimental results, at least one major absorption structure also appears in $\varepsilon_\parallel$ around 9 eV. However, Lambrecht et. al. suggests already in the same publication, as well as in a previous work, that transitions at the L- and the A-point occur at same energy. These kind of transitions are also allowed in $\varepsilon_\parallel$. On the other hand, it was mentioned already that in contrast to the E_1 CP's the assignment of E_2 like transitions in the wurtzite structure is in principal more problematic. Thus, the adoption of the cubic E_2 label perhaps is not adequate. Nevertheless, we will use in the following the E_2-label for these transitions to address the similar energetic coordination and the good agreement with the results on CdS, $CdSe$, and ZnS [138]. But the question remains, whether the B_c peak determined in in the zincblende crystals is really the expected E_2 transitions. A first indication for this correlation appears in the electronic band structure.

In comparison to GaAs (fig. 4.4), the $X_5^v \rightarrow X_1^c$ gap is reduced in relation to e. g. the L and K gap in all three nitrides. Thus, a relative shift of the E_2 seems to be possible. The band-to-band analysis of Lambrecht et. al. further emphasises this assumption. In his calculation he predicts also a double peak structure in the zincblende dielectric function at about 7 eV (fig. 6.18) and attribute this to the $L_3^v \rightarrow L_1^c$ closely followed by the $X_5^v \rightarrow X_1^c$ transition.

Between 10 and 12 eV we find a joint absorption peak in both dielectric tensor components of wurtzite GaN. But we could confirm this absorption peak in particular also for zincblende GaN. In earlier publications this absorption structure was under discussion [141, 143] due to the unknown contribution of second order light in the measurement [143]. In our ellipsometric measurements an influence of second order light can be excluded in this spectral region.

However, with respect to the overall agreement in the different GaN spectra between 10 and 12 eV and due to the agreements with the CdS and CdSe spectra, we already allocated these features to the zincblende E_1' transition. The analysis of Lambrecht et. al. further supports now this assignment. In this work the structure(s) between 10 and 12 eV are associated in the wurtzite crystal to transitions at the A point between $A_{5,6}$-$A_{1,3}$ and at the L point between $L_{1,3}$-$L_{1,3}$. This assignment actually nicely agrees with the interpretation that the transition correlates with perturbed cubic transitions along the $\pm[111]$ direction. The expected splitting of the E_1' structure is unfortunately only measured in $\varepsilon_\perp$ measured on the c-plane GaN sample. But the ab-initio calculations of Benedict et. al. clearly show at least two structures in the $\varepsilon_\perp$ tensor component between 10 and 12 eV, whereas only one structure seems to contribute in $\varepsilon_\parallel$.

The last major absorption structure that relates to interband transitions, is consistently predicted in all theoretical works between 12 and 14 eV in the two wurtzite dielectric function components, as well as in the zincblende GaN dielectric function. In the band-to-band analysis of Lambrecht et. al. , this absorption is associated in the wurtzite crystal to a couple of different interband transitions including the $\Gamma_5^v \rightarrow \Gamma_3^c$, $\Gamma_6^v \rightarrow \Gamma_1^c$, and the $A_{5,6}^v \rightarrow A_{5,6}^c$. All these transitions correlate with the zincblende E_0' CP at the Γ point between $\Gamma_{15}^v \rightarrow \Gamma_{15}^c$. The relatively high energy position of E_0' in GaN is astonishing. The E_0' ($\Gamma_{15}^v \rightarrow \Gamma_{15}^c$) transition is located e. g. in the zincblende GaAs between E_1 and E_1'. But a comparison of the respective zincblende band structures of the III-nitrides and GaAs (fig. 4.7 and 4.4) also indicates a strong shift of the unoccupied Γ_{15}^c states to much higher energies in the nitride band structures. Consequently, we would attribute this highest absorption peak in the zincblende, as well as in the wurtzite dielectric function to the E_0' transition. Unfortunately, we are not able to determine reliable data for this spectral range, but the very good agreement between the theory and our measurements at lower and higher photon energies emphasise the plausibility of the ab-initio calculations also for this intermediate spectral range.

A summary of the measured CP's and the correlation to specific interband transitions is shown in table 6.1. In this overview we also attribute the main absorption structures in the wurtzite GaN dielectric function to respective CP's in the zincblende GaN dielectric function.

GaN	CP's wurtzite $E \perp c$		CP's wurtzite $E \| c$		CP's zincblende	
	Theory	Exp.(eV)	Theory	Exp.(eV)	Theory	Exp.(eV)
E_0	$\Gamma_6^v \rightarrow \Gamma_1^c$	3.42[1)]	$\Gamma_1^v \rightarrow \Gamma_1^c$	3.46[1,2)]	$\Gamma_{15}^v \rightarrow \Gamma_1^c$	3.2-3.3[1)]
$E_1(A)$	$\Gamma_5^v \rightarrow \Gamma_3^c$ $A_{5,6}^v \rightarrow A_{1,3}^c$	6.36($A_{1\perp}$)	forbidden		$L_3^v \rightarrow L_1^c$	7.16(A_c)
$E_1(B)$	$U_4^v \rightarrow U_3^c$	6.99($A_\perp$)	$U_3^v \rightarrow U_3^c$	7.03($A_{\|\|}$)	-	-
$E_1(C)$	$M_4^v \rightarrow M_3^c$ $L_{2,4}^v \rightarrow L_{1,3}^c$ $L_{1,3}^v \rightarrow L_{1,3}^c$	7.78($B_{1\perp}$) 8.11($B_{2\perp}$)	forbidden $L_{1,3}^v \rightarrow L_{1,3}^c$	?	-	-
E_2	$U_2^v \rightarrow U_1^c$ $T_2^v \rightarrow T_2^c$ $K_3^v \rightarrow K_2^c$	9.06($C_{1\perp}$) 9.37($C_{2\perp}$)	$T_2^v \rightarrow T_2^c$	9.23($C_{\|\|}$)	$X_5^v \rightarrow X_1^c$	7.57(B_c)
E_1'	$A_{5,6}^v \rightarrow A_{1,3}^c$ $L_{1,3}^v \rightarrow L_{1,3}^c$ ...	9.77($C_{3\perp}$) 10.55($D_\perp$) 11.35($E_\perp$)	$L_{1,3}^v \rightarrow L_{1,3}^c$	10.8($D_{\|\|}$)	$L_3^v \rightarrow L_3^c$	10.52(C_c)
E_0'	$\Gamma_5^v \rightarrow \Gamma_3^c$ $\Gamma_6^v \rightarrow \Gamma_1^c$ $A_{5,6}^v \rightarrow A_{5,6}^c$ ...		$\Gamma_6^v \rightarrow \Gamma_6^c$ $A_{5,6}^v \rightarrow A_{5,6}^c$ ...		$\Gamma_{15}^v \rightarrow \Gamma_{15}^c$	

Table 6.1: *Assignment of absorption structures in wurtzite and zincblende GaN. The CP's determined in the ellipsometric measurements are compared with specific interband transitions deduced in an ab-initio band-to-band analysis of Lambrecht et. al. [84, 98, 141]. The zincblende, as well as the wurtzite CP's, are correlated to characteristic zincblende transitions, which are called E_0, E_0', E_1, E_1', and E_2 in the isoelectronic sequence scheme of zincblende materials.*
([1)] ref. [9], [2)] ref. [144])

7. Indium Nitride

The crystal quality of wurtzite InN samples was very pure so far in comparison to GaN. However, a significant enhancement in the quality was obtained in the last five years with improvements in the MBE and MOVPE growth technique of thin films. With the new sample quality a ongoing discussion about the InN fundamental band gap was initiated. But furthermore, these samples allow now for the first time also a investigation of higher interband transitions. Therefore, we determined at first the optical properties of InN above the band gap on MBE and MOVPE deposited wurtzite (0001). But the recent success in MBE deposition of wurtzite a-plane InN ($11\bar{2}0$) films on r-plane ($1\bar{1}02$) Al_2O_3 permits also an independent determination of the two dielectric tensor components $\varepsilon_\perp$ and $\varepsilon_\parallel$. These measurements were done in a collaboration with R. Goldhahn of the Technische Universität Ilmenau.

The first high quality InN layers with polycrystalline or mono-crystalline (optical) properties were grown by MBE. Encouraged through these developments the MOVPE system at the Technische Universität Berlin was used to study and develop the growth of InN layers also in a MOVPE reactor. Of major importance in this connection was the possibility of in-situ ellipsometric growth control. Thus, in a short time high quality InN layers where grown by M. Drago and T. Schmidling et. al. in this system. These samples are used in this work for a comprehensive study of the optical properties and the influence of surface degradations as shown in chapter 5.

7.1 Results

Due to the high number of uncertainties concerning the general properties of InN the results of three different c-plane wurtzite InN films will be presented. All three samples are grown on a Al_2O_3 (0001) substrate. Two of them are deposited by MOVPE in the Technical University of Berlin with slightly different growth parameters. The film thickness was specified with 300 nm and 400 nm, respectively. These samples will be called in the following sample A and B, respectively. The third InN sample was grown by MBE in the University of Cornell and has a film thickness of approximately 1070 nm.

7.1.1 Wurtzite InN(0001) - MOVPE

Sample characterisation

Sample A was one of the best InN samples concerning crystalline quality and measured optical properties grown by Drago and Schmidtling et. al. [12, 145] in the Technical University of Berlin. This ≈300 nm thick wurtzite InN film was presented already in chapter 5 (fig. 5.2). XRD measurements reveal in $\omega - 2\Theta$ scans a peak width of 43.3 arcmin (FWHM) for the InN (0002) reflex (figure 7.2). In comparison to other wurtzite nitrides this value is still rather poor, but it has to be mentioned again that the quality of the available InN samples is in general very low due to the special difficulties of the growth procedure. This problem is also

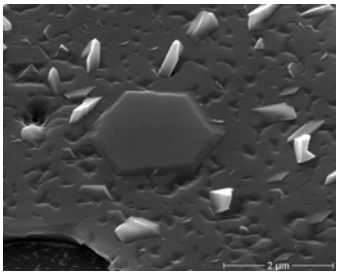

Figure 7.1:
SEM image of the ≈300 nm thick c-plane wurtzite InN film grown by MOVPE [123] (sample A).

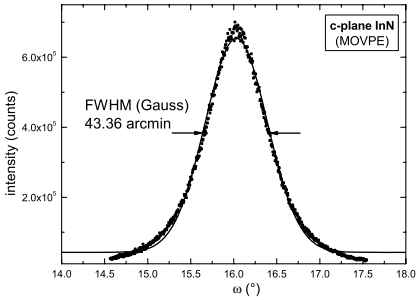

Figure 7.2:
X-ray $\omega - 2\Theta$ scan of the (0002) reflex from the ≈300 nm thick c-plane wurtzite InN film grown by MOVPE [123] (sample A). The FWHM of 43.3 arcmin was determined with a Gauss fit of the measured peak [black line].

seen in a SEM image of the sample A (figure 7.1). The surface is covered with a lot of holes and small randomly oriented crystallites. But fortunately, these localised crystallites do not essentially contribute to the measured dielectric function. The light shining on these crystallites will be mostly scattered and reflected in other directions and do not reach the detector. In between these well-localised crystallites, the sample has segments with a very smooth surface, where SEM shows nicely orientated (0001) single crystalline areas. Therefore, the effect on the ellipsometric results can be neglected. AFM scans in these areas ($1\times1\,\mu$m scan range) reveal a RMS roughness of about 2.7 nm. In the lower left corner of the SEM image 7.1 one can see a larger hole in the layer. These kind of holes appear in areas where the film was partly peeled off during the growth. This problem becomes critical for further increased film thicknesses and is attributed to the relaxation of strain in the InN layer. However, the layer peeling starts already at film thickness of about 100 nm. But the uncovered substrate material was overgrown with InN again. Therefore, only a few small areas of the surface are finally not covered by InN and the layer can assumed to be closed. The resulting differences in the layer thickness do not influence the measured dielectric function in the spectral range of the discussed interband transition. In this spectral range above 4 eV the penetration depth is smaller than 40 nm. The thin InN layers can assumed to be opaque (q. v. GaN penetration depth of light fig. 5.1).

As noted above, the second MOVPE InN layer (sample B) was deposited under very similar growth conditions. But the InN layer thickness of ≈400 nm is somewhat higher than in sample A. Anyhow, the very localised crystallites with a random orientation are disappeared in sample B. But the well orientated (0001) single crystalline areas are much smaller (around 250 nm diameter). The Consequently, the RMS roughness of the sample surface, deduced from $1\times1\,\mu$m scan areas, is higher. Values above 6.5 nm depending on the surface region have to be considered.

Dielectric function

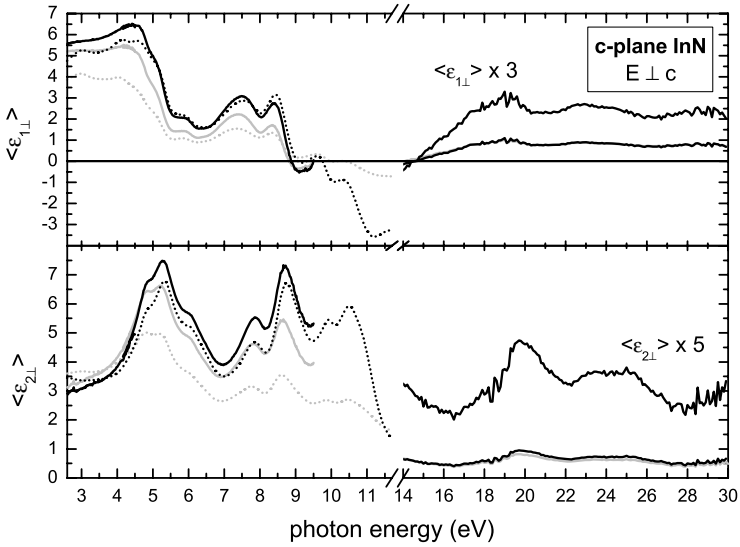

Figure 7.3: *Dielectric tensor component $< \varepsilon_\perp >$ of wurtzite InN (c-plane) grown by MOVPE. The full black line shows the result for sample A and the dotted black line for sample B. The surface roughness of the samples were corrected within the EMA-model as shown in para. 4.2.2. The grey lines represent the uncorrected pseudodielectric functions as measured by ellipsometry.*

For both MOVPE grown InN films the dielectric function was subsequently measured at the two appropriate BESSY monochromators (fig. 7.3). Preliminary to each measurement, the samples were heated in UHV up to 400°C to remove possible overlayers, as discussed in chapter 5. The angle of incidence was 67.5° and 45°, respectively, according to the different spectral regions below and above 10 eV. Thus, the measured pseudodielectric functions represent almost the ordinary component of the dielectric tensor $\varepsilon_\perp$ due to the (0001) orientation of the films. But experimental problems unfortunately constrain a measurement of the entire spectral range for both samples. Consequently, the dielectric function of sample A is not available between 10 eV and 12 eV, while sample B was not measured above 14 eV. However, the general line shape of the dielectric functions is almost identical in the overlapping regions. Therefore, we can assumed also a quite similar behaviour in the missing intermediate areas. But in contrast to the agreements in the general line shape, the imaginary part of the dielectric function of sample B is found to be smaller in the overall amplitudes even after correction of the surface roughness effects. This could be correlated with the lower overall crystal quality of sample B. The higher number of defects and more polycrystalline character of the film leads to overall damping of the measured dielectric function.

The InN dielectric function $< \varepsilon_\perp >$ shows huge contributions of higher interband transitions between 7 eV and 12 eV in comparison to GaN (fig. 7.3). Whereas in GaN a large amount of the oscillator strength seems to be concentrated in the $A_\perp$ (fig. 6.2) absorption peak, we observe for InN a distribution similar to the Si or GaAs dielectric function. After correction of roughness effects, the absorption structure at ≈8.7 eV shows approximately the same amplitude like the main absorption peak at ≈5.3 eV (sample A: $\varepsilon_2[5.3eV] = 7.6$). Above 11 eV, the imaginary part of the dielectric function decreases strongly. If we imply a Kramers-Kronig consistent line shape, also no noticeable absorption structures are expected between 12 and 14 eV. Even though measurements are not possible in this range, further additional interband transitions can be excluded because of the measurements belove and above this break. In comparison to GaN, the whole bunch of higher interband transitions seems to be shifted to lower photon energies. This is also in agreement with the much lower band gap of InN. For example, the first strong absorption peak comparable to the $A_\perp$ structure of GaN is located already around 5 eV. However, in contrast to GaN, at least two distinct CP's contribute now in this energy region to the InN $\varepsilon_\perp$. But also the following features in the InN spectra are considerably changed.

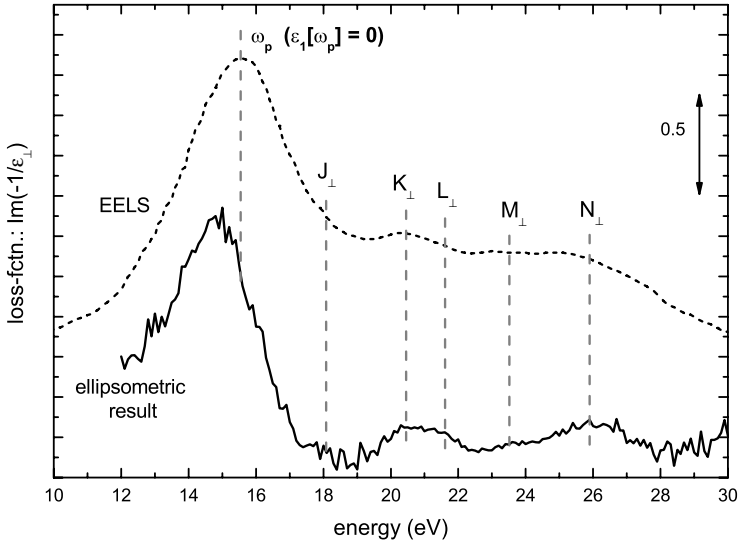

Figure 7.4: *Calculate InN loss function* $\mathrm{Im}[-1/\varepsilon]$ *from the ellipsometric measurements [full line] in comparison with EELS results [dotted line] [146]*

The situation above 15 eV is rather different. The general line shapes of the measured InN dielectric functions $\varepsilon_\perp$ look very similar to GaN. The main absorption structures are just shifted approximately 3 eV to lower photon energies (fig. 7.3 and 6.1). This value is clearly higher than the ≈2 eV red shift of the comparable absorption structures below 12 eV. Unfortunately, it was not possible to reduce the rather high noise level in the measurements above

14 eV. The reflectivity of the InN samples is much lower in this spectral range in comparison to the c-plane GaN sample and in consequence the intensities were reduced on the detector by nearly one order of magnitude. This reduced reflectivity is partly attributed to increased light scattering on the rough surface of the sample and the lower overall crystal quality. But it should be noticed as well that the plasma edge ($\varepsilon_1 = 0$) of InN is located at ≈14.5 eV (GaN: ≈18.5 eV) according to our measurement. Because of this lower position of the plasma edge, the overall reflectivity of InN strongly decreases already at 17 eV for the used angle of incidence of 45°. Therefore, even for "perfect" samples the mean intensity on the detector would lower in this spectral range than for GaN. Nevertheless, we can identify four distinct absorption peaks at 18.1, 19.8, 23.4, and 25.2 eV in the imaginary part of the dielectric function. A more detailed evaluation in a derivative spectrum was not possible due to the high noise level. But a recently published EELS measurement also reveals these absorption structures at the same energies [146]. Figure 7.4 shows the comparison of our ellipsometric results with the data obtained by EELS. For this comparison, we calculated the loss function $\mathrm{Im}[-1/\varepsilon]$ from the ellipsometric results. Both spectra show a strong peak at the plasmon energy of about 15 eV ($\varepsilon_1 = 0$, $\varepsilon_2 < 1$). The differences in the exact peak position may originate from small deviations in the ellipsometric results, where the plasmon peak corresponds to a singularity in the calculation of the loss function at $\varepsilon_1 = 0$. Hence, small uncertainties in the absolute value of ε_1 could result already in considerable deviations of the exact zero position due to the weak slope of ε_1 in this area. EELS measurements, in contrast, directly detect the plasmon excitation. This direct excitation of longitudinal plasmons is forbidden in ellipsometric (optical) measurements due to the transversal character of the light. However, above 17 eV the EELS data reasonably reproduce our ellipsometric results and the energetic positions of the main absorption features show a very good agreement. All these absorption structures above 15 eV are caused by transitions between atomic core levels and conduction bands. For GaN we attribute these transitions already to the excitation of the Ga3d electrons. Under consideration of the higher atomic number of the In atom, therefore, the In4d electronic states should be considered in InN. However, a more detailed discussion about the origin of the different absorption structures will follow later in chapter 9.

CP analysis

Below 12 eV, the analysis of the third derivative spectra reveals at least ten separated absorption structures within the JDOS model. Moreover, up to 10 eV both samples show an identical line shape in the third derivative spectra with almost identical CP's at the same photon energies. Therefore, only the fit results of sample B are presented in figure 7.5 and table B.5.

But nevertheless, we should comment some deviations at about 9.4 eV and the edges of the spectrum. In these areas the real and imaginary part of the (derivative) dielectric function does not fulfil the Kramers-Kronig relation (eq.. 4.6). Consequently, no exact solution is found in the optical model at this energies. The deviations at 9.4 eV and at the higher energy edge of the spectrum are quite small. In particular, at 9.4 eV the problems correlate with the junction of the two subsequent measurements taken with 65° and 45° angle of incidence, respectively. Very small differences between both measurements can generate already inconsistent line shapes in the corresponding derivative spectra. Nevertheless, a further CP in this region should be also taken into consideration. Additionally deviations at the high energy edge can be simply related to the increasing noise level in the measurement. However,

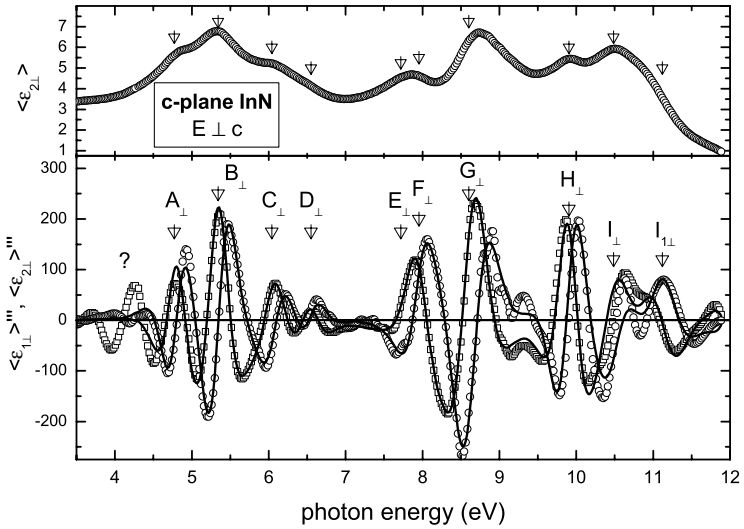

Figure 7.5: *Third derivative of the wurtzite InN $\varepsilon_\perp$ tensor component. $< \varepsilon_{1\perp} >'''$ [squares] and $< \varepsilon_{2\perp} >'''$ [circles] are calculated from the spectra measured on c-plane InN (sample B) as shown in figure 7.3. The full lines are obtained by fitting the third derivative spectra within the JDOS model. The found critical points are marked with triangles and ascending alphanumeric labels.*

the non Kramers-Kronig consistent structure below 4.5 eV is quite large for both samples in comparison to the the problems at 9.5 eV. In connection with these structures we have to mention that the investigated InN layers are just a few 100 nm thick and that the penetration depth is rapidly increasing below 4.5 eV (q. v. GaN penetration depth of light fig. 5.1). Anyhow, the calculated penetration depth at 4 eV is estimated to be smaller than 50 nm. A direct interpretation of the non Kramers-Kronig consistent behaviour by layer interference effects is therefore not stringent. One explanation could be the influence of areas on the sample, where the InN film was peeled off during the growth. The subsequent overgrowth generates regions with a much lower film thickness in comparison to the rest of the sample. In fact, a complicated layer structure could lead to non Kramers-Kronig consistenst line shapes in the real and imaginary part of the dielectric function.

Unfortunately, a CP analysis was not possible in the spectral range above 14 eV. Due to the high noise level in this spectral range the indispensable smoothing has to be increased a lot in order to achieve reasonable derivative spectra. Thus, the derivative spectra would provide finally no further information.

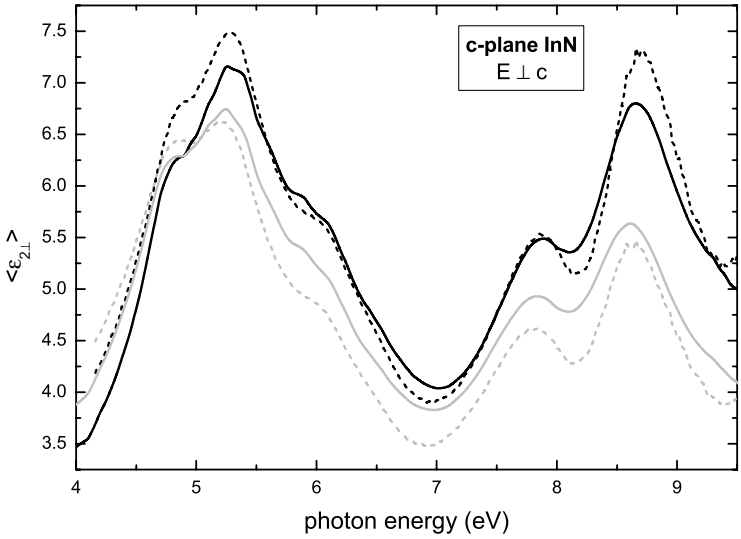

Figure 7.6: *Imaginary part of the dielectric tensor component $< \varepsilon_{\perp} >$ of wurtzite InN (c-plane) grown by MBE [black line]. The dashed black line corresponds to the result obtained for the MOVPE grown sample A. Both spectra are corrected concerning surface roughness effects while the grey curves show the related uncorrected pseudodielectric function.*

7.1.2 Wurtzite InN(0001) - MBE

Most recently, we determined the dielectric function of a relative thick MBE grown c-plane InN film of very high quality. This single-crystalline InN film was grown in the Cornell University. They use a (0001) sapphire substrate followed by a 10 nm AlN nucleation layer and 195 nm GaN buffer layer. A more detailed description of the growth procedure is presented by Lu et. al. [147]. The RMS surface roughness was determined by AFM to δ = 1.9 nm. Hall measurements at room temperature evidenced electron densities (mobilities) of $\approx 1.5 \times 10^{18}\, cm^{-3}$ ($\approx 1200\, cm^2/Vs$) [23]. The comparison of the imaginary parts of the dielectric functions of the MOVPE grown sample A and the MBE sample is presented in figure 7.6. Both samples show very similar optical properties. The specific absorption structures appear almost at the same photon energies and the overall amplitudes in the imaginary part of the dielectric function are comparable. Small differences in the amplitude can be related to uncertainties in the surface roughness determination or in the correction method. Whereas the weak difference in the line shape around 5.7 eV could be related to a small additional structure in the dielectric function of the MBE sample. But a detailed evaluation of the spectrum in the third derivative reveals a Kramers-Kronig inconsistent behaviour. Thus, we have to address this difference to uncertainties during the measurement of the MBE sample dielectric function. But at the end we can conclude from the very good agreement that the investigated InN layers, in fact, do not depend on the preparation method. They most likely represent the

optical properties, which are material related and not growth related.

7.1.3 Wurtzite InN ($11\bar{2}0$)

Sample characterisation

For the ellipsometric investigation of the extraordinary dielectric tensor component $\varepsilon_{\parallel}$ of wurtzite InN, samples were required, which have the c-axis in the surface plane, like in the M-plane GaN ($1\bar{1}00$). As recently published Lu et. al. succeeded in depositing high quality a-plane InN ($11\bar{2}0$) on a r-plane sapphire using a plasma assisted MBE [147]. At first they have deposited a 12 nm thick AlN nucleation layer at 850°C followed by a 300 nm thick GaN buffer layer grown at 820°C. This GaN buffer layer was determined to be a-plane using in-situ reflection high-energy electron diffraction (RHEED) and ex-situ by using XRD measurements. On top of this buffer a 670 nm thick InN layer was grown at around 470°C. The layer orientation follows the orientation of the GaN buffer layer. Again, in situ RHEED measurements and detailed XRD studies reveal a highly a-axis-oriented InN film. In the XRD scans only the wurtzite-type InN ($11\bar{2}0$) peak is clearly observed. According to a reciprocal space map the a-plane InN film is fully relaxed. It was also demonstrated that a-plane InN films show a strong photoluminescence around 0.7 eV at low temperatures similar to the usually investigated (0001) c-plane layers. Room temperature Hall measurements yield an electron concentration of 6×10^{18} cm^{-3} and a mobility of 250 cm^2/Vs. AFM measurements revealed a RMS surface roughness of 6 nm for the investigated sample. In addition to the characterisation by Lu et. al. we have used Raman spectroscopy to verify the crystal orientation of the film (fig. 7.7). Therefore, we chose again three different scattering configurations.

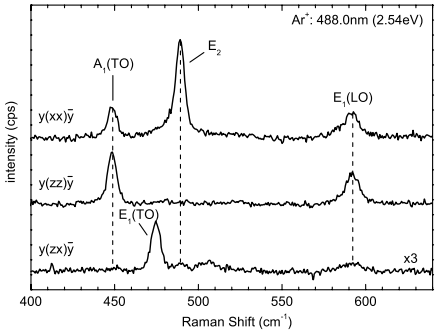

Figure 7.7:

Raman spectra of the a-plane wurtzite InN ($11\bar{2}0$) grown on r-plane Al_2O_3 ($1\bar{1}02$). The cartesian axes x, y and z correspond to the [$1\bar{1}00$], [$11\bar{2}0$] and [0001] directions. The absence of the E_2 phonon under y(z,z)$\bar{y}$ geometry evidences the in-plane orientation of the InN [0001] axis.

In the upper spectrum a polarisation along the [$1\bar{1}00$] direction (perpendicular to the c-axis) was selected for both the incoming laser light and the the scattered light. The middle and the lower spectrum correspond to polarisations parallel to the c-axis along the [0001] direction and a crossing polarisation. In these spectra we observe the same Raman modes and the same selection rules like in GaN. The symmetry properties are identical for M-plane GaN and for a-plane InN. But according to the higher weight of the In atoms, the phonon modes are shifted now to lower frequencies. The complete absence of the E_2 phonon in y(z,z)$\bar{y}$ geometry with

polarisation along the c-axis reveals again the highly accurate in-plane orientation of the InN [0001] axis with respect to the surface and the sample edges. These Raman measurements are in good agreement with results published by Davydov et. al. [148]. In this work a more detailed discussion is presented about the different Raman and infrared active phonon modes in InN.

Dielectric function

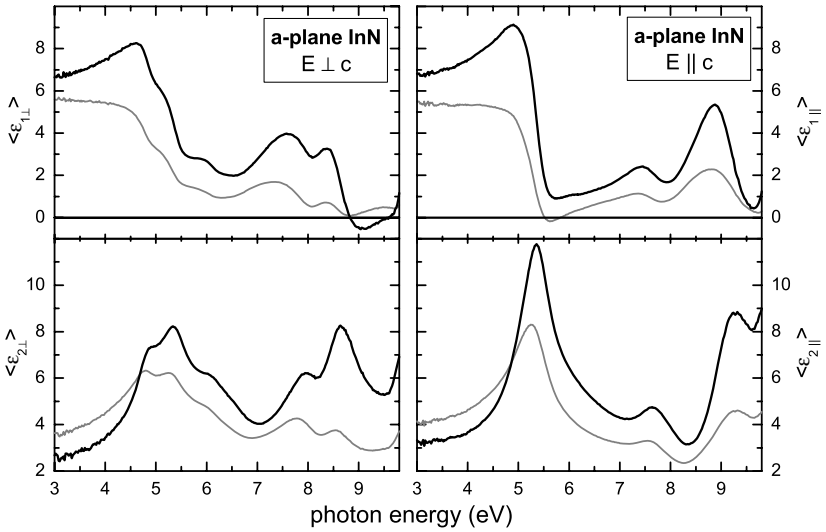

Figure 7.8: *$\varepsilon_\perp$ and $\varepsilon_\parallel$ measured on the a-plane wurtzite InN sample (black line). The spectra were calculated from the pseudodielectric functions measured in the two high symmetry sample orientations $\alpha = \pi/2$ and $\alpha = 0$ (grey lines). Within this calculation, the surface RMS-roughness of 6 nm was considered as a surface overlayer in the optical model.*

By use of this a-plane InN sample, a ellipsometric measurement of both independent dielectric tensor components were realised by rotating the sample in the two high symmetry orientations, where the optical axis is either parallel $\alpha = 0$ or perpendicular $\alpha = \pi/2$ to the plane of incidence. The results of these two measurements, taken under an angle of incidence of 68.7°, are shown in figure 7.8. The grey lines indicate the pseudodielectric function calculated with the simple isotropic two phase model. Whereas the black lines show the independent dielectric tensor components calculated under consideration of the surface roughness by the numerical procedure as discussed in paragraph 4.2.3. The InN layer was assumed to be opaque above 3 eV for both calculations. Unfortunately, these measurements are restricted so far to the spectral range below 10 eV. The corresponding measurements above 10 eV are not finished yet. A first discussion of the anisotropic optical properties below 10 eV

was already published in collaboration with Goldhahn et. al. [32] where also results for the dielectric function in the band gap region below 3 eV are presented.

Above the optical band gap, both spectra again show remarkable differences in the amplitudes as well as the overall line shape. As expected, the results for $\varepsilon_\perp$ are almost identical to the previously measured pseudodielectric function $< \varepsilon_\perp >$ of the c-plane films. While at least seven absorption structures contribute to this tensor component, only three seem to remain up to 10 eV in $< \varepsilon_\parallel >$. It is conspicuous that the absorbtion peaks in both tensor components deviate much more in the magnitude and photon energy position than in GaN. Especially photon energy positions of common peaks in both tensor components are very similar for GaN.

CP analysis

By fitting the third derivative spectra in the JDOS model, the observed seven absorption structures (CP's) in $\varepsilon_\perp$ can be located at 4.82, 5.38, 6.18, 6.54, 7.66, 7.94 and 8.54 eV($\pm$0.05 eV) (fig. 7.9 and tab. B.6). The respective fit clearly evidences also the three CP's at 5.40, 7.61 and 9.16 eV in $\varepsilon_\parallel$ up to 10 eV. But small remaining differences in the slope indicate a further contribution below 5.40 eV (not shown here). This fourth CP structure could be located at 4.90 eV, according to our model calculation. Only with this additional structure, finally, a very good agreement could be obtained between the JDOS model and the measured spectra (fig. 7.9). Anyhow, with respect to the results determined on GaN, we think that the required additional absorption structure in $\varepsilon_\parallel$ actually originates from the ordinary tensor component $\varepsilon_\perp$. Due to the low refractive index in this spectral range or due to a small amount of misaligned crystallites in the InN film this feature could be also emerge here in $\varepsilon_\parallel$.

7.2 Discussion of InN interband transitions below 12 eV

7.2.1 Heuristic assignment of CP's in comparison to GaN

Wurtzite InN shows much larger differences between both dielectric tensor components than GaN. In particular the photon energy positions of CP's in the two tensor components above 7 eV are very different. Therefore a unambiguous assignment of appropriate CP's in two components is difficult. These differences can be explained by a closer look on the wurtzite InN crystal parameters. If the difference between the wurtzite and the zincblende phase is just related to the different stacking sequence of the hexagonal close packed nets, the c/a ratio of the wurtzite lattice vectors should be 1.633. Indeed, this ratio is found in many materials within 1% of the expected value and also GaN (1.627) fits rather good in this rule. In such materials the arrangement of the first and the second neighbour atoms is nearly the same in both crystal structures. Therefore, transitions, which related to states along the [111] direction, can easily correlate in both structures according to the perturbation approach suggested by Birman [48]. This approach was successively applied already to GaN in paragraph 6.2.1. For InN, however, the c/a ratio is 1.613. This is appreciably different from the ideal value 1.633 [149]. A general problem in theoretical treatments of group-III-nitrides is related to extreme differences between the cation and nitrogen anion. These are, in particular, the very different atomic size and the large differences in the electronegativities, which cause a considerable charge transfer between cations and anions (strongly ionic bonds). Hence, a considerable

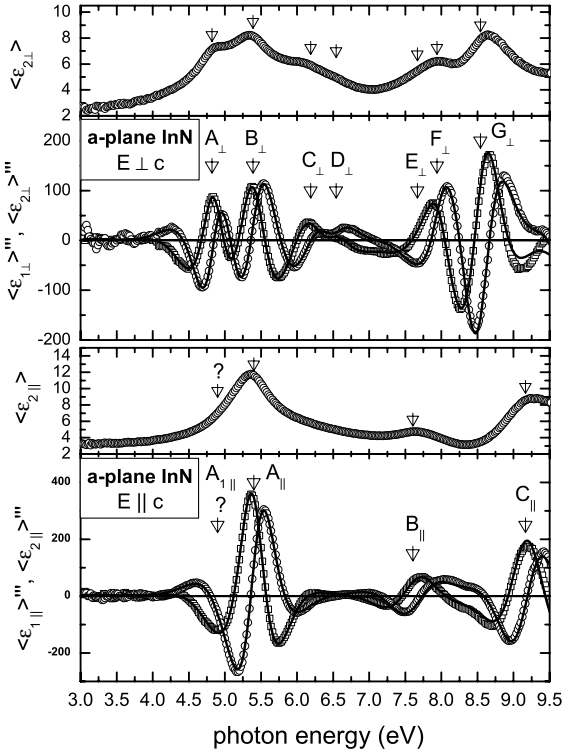

Figure 7.9: *Third derivative of the wurtzite InN $\varepsilon_\perp$ and $\varepsilon_\parallel$ tensor component. $<\varepsilon_{1\perp}>'''$ [squares] and $<\varepsilon_{2\perp}>'''$ [circles], as well as $<\varepsilon_{1\parallel}>'''$ and $<\varepsilon_{2\parallel}>'''$ are calculated from the spectra measured on a-plane InN as shown in figure 7.8. The full lines are obtained by fitting the third derivative spectra within the JDOS model. The found critical points are marked with triangles and ascending alphanumeric labels.*

charge transfer arise in the hexagonal close packed nets along the $[0001]$ axis in the wurtzite structure. This leads to an anisotropy of the chemical bonds, which are either perpendicular or almost parallel to the hexagonal packed nets. These charge asymmetries [150] are further increased in InN compared to GaN. Together with the deviations from the ideal c/a ratio, it may explain the increased differences between both dielectric tensor components. For GaN the "pure" symmetry argumentations, based on the perturbation approach of Birman, perfectly explains the differences between $\varepsilon_\perp$ and $\varepsilon_\parallel$. Obviously connected absorption structures in the two GaN dielectric tensor components are almost at the same photon energies. But this approach partially fails for InN. Possibly connected absorption structures for InN occur now at different positions in the two tensor components with very different amplitudes.

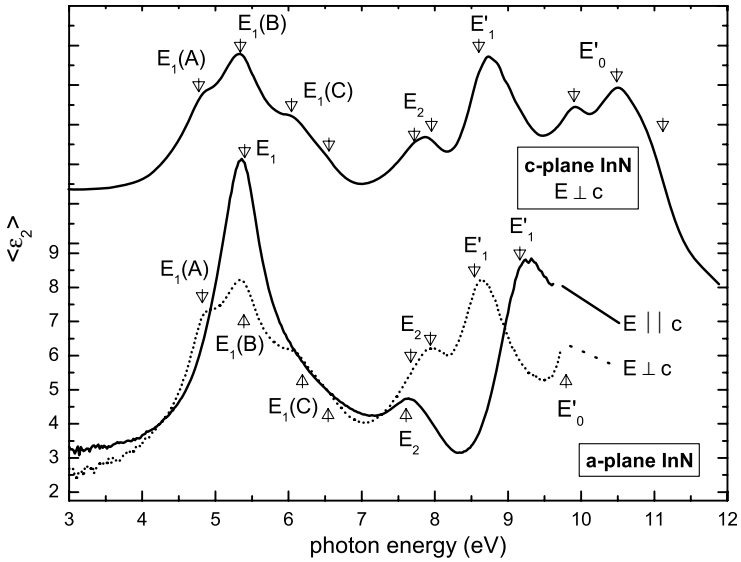

Figure 7.10: *Comparison of the imaginary part of the two independent dielectric tensor components measured on wurtzite InN (c-plane InN (sample B) and a-plane InN). The labels E_0, E_0', E_1, E_1', and E_2 for the characteristic absorption structures correspond, in the isoelectronic sequence scheme, to peaks observed in various zincblende materials [85, 86]*

Unfortunately, zincblende type InN films are not available until now. Therefore, a verification of the CP assignment in the wurtzite InN dielectric functions by a comparison with zincblende CP's was not possible yet. Nevertheless, we can suggest an assignment of CP's in the dielectric tensor components of wurtzite InN in comparison with the related GaN results as shown in figure 7.10. But we point out that this has to be proven with further investigations especially on zincblende InN films.

In comparison to GaN it is quite obvious, however, that the first three or four absorption structures in $\varepsilon_\perp$ of wurtzite InN ($A_\perp$-$D_\perp$) correlate with the zincblende E_1 CP. In $\varepsilon_\parallel$ only one of these remains but shows much higher oscillator strength. Consequently, these CP's $B_\perp$ and $A_{||}$) must attribute to the zincblende $\pm[1\overline{1}1]$-like triplet $E_1(B)$ as in GaN. This should appear, in fact, for both components. In contrast to GaN, the measurements on InN reveal now a very clear splitting of this CP into at least three major absorption structures in $\varepsilon_\perp$. One of these, the $A_\perp$, appears at lower photon energies. Therefore, it can be correlated with the $[111]$-like states in the $[0001]$ direction. This $E_1(A)$ InN structure further evidences also the assumed low energy $E_1(A)$ CP in GaN, where it is partially hidden in the low energy tail of the $E_1(B)$ structure.

The similarities to the GaN results further encourage a association of the following major structure between 7 and 8 eV to the zincblende E_2 CP. These are the $E_\perp$ and $F_\perp$ in $\varepsilon_\perp$ and

$B_{||}$ in $\varepsilon_{||}$ dielectric tensor component. As mentioned above, in InN these structures in the two tensor components are slightly shifted against each other in their photon energy position. However, the strong differences concerning line shape and energy positions are further increased in the spectral range between 8 and 9 eV, where E_1' related CP's are expected. For a unambiguous assignment, further measurements e. g. on a-plane InN in the extended spectral range and on zincblende InN are needed.

Finally, there are three groups of connected CP's in $\varepsilon_\perp$ of wurtzite InN below 10 eV (fig. 7.10). The first is assigned to the zincblende E_1, the second to the E_2, and the third to the E_1'. In agreement with the previous discussion on GaN, the subsequent fourth absorption structure in $\varepsilon_\perp$ above 10 eV, is most likely the predicted E_0' CP. Unfortunately, for GaN this structure is assumed in a spectral region between 12 and 14 eV where we could not obtain reliable experimental results. But this can be verified now in the InN dielectric function, because all structures are generally shifted to lower energies.

7.2.2 Comparison with ab-initio calculations

The very good agreements of the different theoretical approaches with our results measured by ellipsometry are very helpful to reach a plausible interpretation of specific features in the GaN dielectric function. But there exist no comparably detailed band-to-band analysis yet for InN. But on the other hand, the band ordering in InN should be essentially the same like in GaN. This is nicely demonstrated e. g. in the band structure calculation of of Christensen et. al. [94] as shown in figure 6.15 and 7.12. According to this calculation, the principal dispersion of the electronic bands and their relative positions, in fact, are almost the same. This general conformity in the electronic structure also corresponds to the overall agreements in the general line shape of the dielectric functions in InN and GaN. In figure 7.11 e. g. we show the imaginary part of the measured InN dielectric function together with the results of two ab-initio calculations. The thin solid lines show the results of Persson et. al. [151], which base on a DFT-LDA(GGA) calculation with a relativistic, full-potential linearised augmented plane wave (FPLAPW) method. The authors have chosen experimental values for the lattice constants and the internal lattice parameter. The second calculation of Bechstedt et. al. [17] (dotted line) is also done in a DFT-LDA, but takes quasiparticle effects into account and includes In4d electrons as valence electrons. In the latter work the authors calculated only the ordinary dielectric tensor component $\varepsilon_\perp$ of wurtzite InN, while Persson et. al. presents results for all three dielectric functions of interest. Surprisingly, the inclusion of quasiparticle effects does not lead to a better reproduction of the experimental line shapes as in the GaN case. Quite the contrary, the calculation of Persson et. al. shows already a very good agreement with the experimental results for both independent dielectric tensor components without that corrections. In figure 7.11 we shifted the calculated spectra of Persson et. al. by -0.75 eV to lower energies. In order to address the known band gap problem of pure DFT-LDA calculations the authors have introduced a subsequent quasi-particle correction to increase the band gap and to achieve an agreement with the experimental gap. Unfortunately, they use the wrong old references before 2002, where too large band gaps are reported and obviously overcorrect the dielectric function. On the other hand, the very good agreement, which we achieve after the subsequent reversal energy shift, confirms the new experimental band gap of less than 1 eV.

Furthermore, the good agreement of theoretical and experimental wurtzite InN spectra

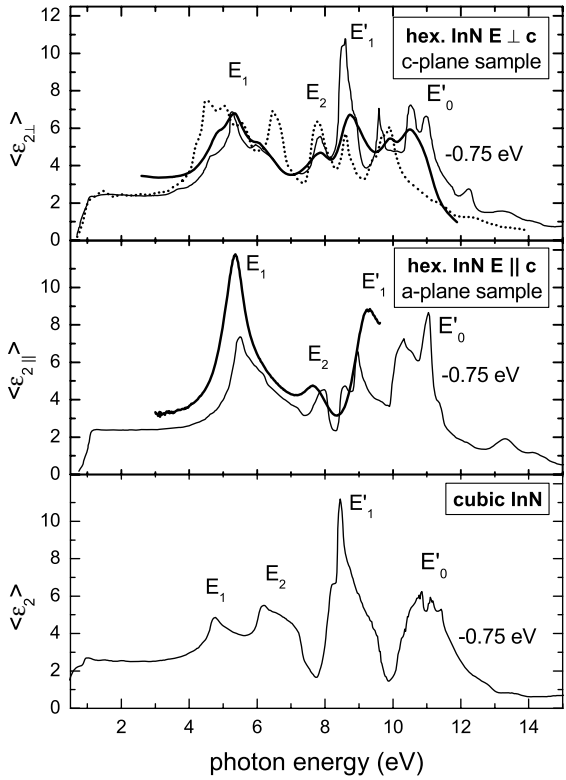

Figure 7.11: *Measured imaginary parts of the dielectric function (tensor components)* $< \varepsilon_2 >$ *[thick line] compared to* ε_2 *calculated by Bechstedt et al. [17] [dotted line] and Persson [151] [thin line].*

also evidences the reliability of the respective theoretical result for zincblende InN. If we further compare the experimental, as well as the calculated dielectric functions for GaN with those of InN, the general agreement of the line shape is obvious. In both materials, the dielectric functions of the zincblende crystal structures are dominated by four major absorption peaks. The biggest difference is observed in the spectral range around 6 eV. The ab-initio calculation of Persson et al. [151] predicts here for InN a much better separation of the E_1 and the E_2 CP than for GaN (fig. 7.11).

Finally, we think that the very good agreement between theory and experiment, as well as the huge number of similarities between GaN and InN is sufficient enough to assume the same interband transition as allocated for GaN in table 6.1 also for InN. This assumption is also confirmed by recent band structure calculations of Fritsch et. al. [152], where the

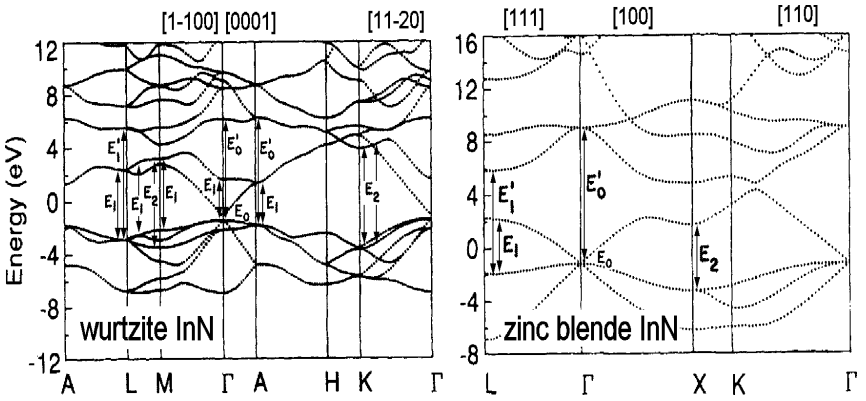

Figure 7.12: *InN band structure calculated by Christensen et. al. [94] as already shown in paragraph 4.1.3 figure 4.7. The arrows correspond to interband transitions, which we attribute to specific absorption structures in the dielectric functions of wurtzite InN (fig. 7.10).*

authors predict almost the same CP transitions for the first three absorption structures in $\varepsilon_\perp$ of wurtzite InN like Lambrecht et. al. for GaN.

8. Aluminium Nitride

AlN has the widest band gap among the nitrides. For the wurtzite crystal coordination e. g. this is located at ≈6.2eV. Thus, the whole bunch of interband transitions is also shifted to higher photon energies, where conventional ellipsometers or other spectroscopic methods with conventional light sources are usually not applicable. Data about the optical properties even of the band gap area, therefore, are still rare. A comprehensive study of the ordinary dielectric tensor component $\varepsilon_\perp$ of wurtzite c-plane AlN(0001) and in particular a discussion of the excitonic contribution to the dielectric function around the band gap was presented by Wethkamp et. al. [38, 39]. The measurements in this work were realised with the BESSY ellipsometer at the former synchrotron storage ring BESSY I. However these measurements were restricted to the determination of $\varepsilon_\perp$ due to the crystal orientation of the investigated thin films. Zincblende crystals were also not available, and therefore, only $\varepsilon_\perp$ of wurtzite AlN is known until now. Meanwhile it was shown that on Si(111) either wurtzite or zincblende AlN films can be deposited by use of plasma-induced MBE, depending on the carbonisation prior to growth [153]. But unfortunately, wurtzite AlN samples with a in plane orientation of the c-axis are still not available. For a comparison of the principal character of the dielectric function above the band gap, therefore, the previous results measured on a c-plane AlN sample will be presented together with new measurements on a zincblende sample. Finally, the comparison with the zincblende and wurtzite GaN dielectric functions admit also some predictions for the extraordinary dielectric tensor component $\varepsilon_\parallel$ of wurtzite AlN. But in general, we notice a much lower crystal quality of the AlN samples and in particular for the zincblende sample in comparison to GaN. Those, the presented data are still no ”reference” data and have to be used under reserve due to the uncertainties concerning the crystal quality (purity) especially for zincblende AlN.

8.1 Results

8.1.1 Wurtzite AlN(0001)

Sample characterisation

The ordinary component of the wurtzite AlN dielectric tensor $\varepsilon_\perp$ was measured on a 1.0 μm thick film grown by plasma-induced MBE in the Walter-Schottky-Institute Munich. The film was deposited on Al_2O_3 (0001). High resolution XRD scans reveal a FWHM value of 0.11° deduced from the (0002) rocking curve and 10×10 μm AFM scans indicate a 3 nm RMS roughness of the surface. The unintentional doping level of n: 6×10^{15} cm^{-3} shown by Hall measurements is very low. A surface cleaning by annealing in UHV was not applied. For the AlN samples, it was shown in contrast to GaN and InN that an annealing up to 900°C does not change the ellipsometric results.

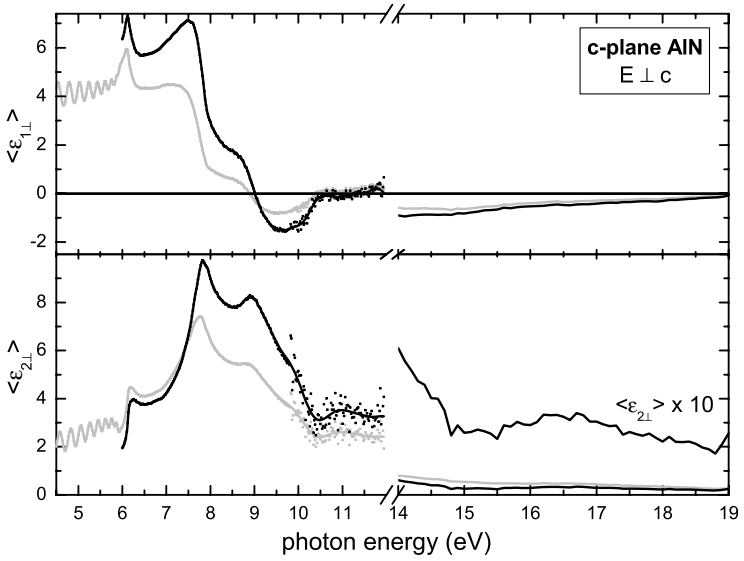

Figure 8.1: *Dielectric tensor component $< \varepsilon_{\perp} >$ of wurtzite AlN (c-plane)[black line]. The surface roughness of the sample was corrected within the EMA-model shown in para. 4.2.2. The grey line represents the uncorrected pseudodielectric function as measured by ellipsometry. [38, 39]. In order to emphasise the general line shape of the spectra we apply a spline smoothing algorithm between 9.5 and 12 eV. The raw data are shown with gray and black dots, respectively.*

Dielectric function

The pseudodielectric function of AlN was determined in two steps, with an angle of incidence of 68° below 10 eV and afterwards with 45° above 10 eV. But in contrast to the procedure used at the new synchrotron storage ring BESSY II, these spectra were measured back-to-back on a single monochromator [38, 39]. The results of these measurements are shown in figure 8.1 (grey line). Below the fundamental band gap at 6.13 eV, the spectrum is dominated by interference structures, which are related to multiple reflections at the ambient/AlN and the AlN/Al_2O_3 interface. At the fundamental band gap the effective masses of the electrons (holes) are strongly increased due to very strong excitonic effects. Thus, a peak like absorption structure dominates the imaginary part of the dielectric function $\varepsilon_{\perp}$ near the absorption edge. As confirmed at lower temperatures, this absorption peak splits in three distinct features, which can be attributed to a spin-orbit- and a crystal-field induced splitting of the valence band maximum [38, 39]. Above the band gap, the penetration depth of light decreases rapidly and the AlN layer can assumed to be opaque (q. v. GaN penetration depth of light fig. 5.1). In this spectral region the surface roughness was corrected within the simple three phase model using the Bruggemann-EMA approach for the rough surface. The black line in

figure 8.1, finally, represents the corrected $\varepsilon_\perp$.

This dielectric tensor component of AlN shows very similar to the GaN spectrum four localised absorption structures above the band gap (below 12 eV). In agreement with the higher band gap of AlN, these four structures are also shifted to higher energies. But the amplitudes of the third and fourth feature is clearly reduced in comparison and also the principal line shape differs from the GaN dielectric tensor component.

CP analysis

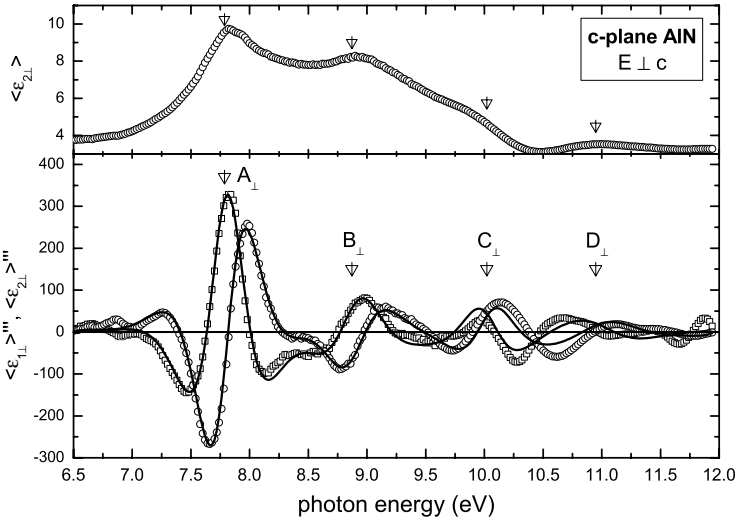

Figure 8.2: *Third derivative of the wurtzite AlN $\varepsilon_\perp$ tensor component. $< \varepsilon_{1\perp} >'''$ [squares] and $< \varepsilon_{2\perp} >'''$ [circles] are calculated from the spectra measured on c-plane AlN as shown in figure 8.1. The full lines are obtained by fitting the third derivative spectra within the JDOS model. The found critical points are marked with triangles and ascending alphanumeric labels.*

The evaluation of the spectra in the third derivative further verifies the obvious absorption structures and the assumption of only four CP's in the optical model reproduces the line shape of the third derivative spectrum below 12 eV. In contrast to GaN or InN results, no further CP's are required, which could possibly contribute also to the major absorption structures. All CP transitions are seen directly in the measured dielectric function (fig. 8.2). In general, we would expect a very similar splitting of the main peaks like in GaN. But this "fine structure" is possibly not resolved due to a lower sample quality. On the other hand, the analysis within the JDOS model reveals some discrepancies between the real and imaginary part of the dielectric function between 10 and 11 eV. The line shape of both is not Kramers-Kronig inconsistent here. Indeed, this spectral range is the most problematic region in the presented measurements. Above 10 eV the triple gold reflection polarisers have to be used

and a significant fraction of second order light from the monochromator would influence the ellipsometric results up to about 14 eV. As mentioned in chapter 3 we use therefore a very thin LiF filter between 10 and 12 eV in order to suppress this second order light. But due to the notable absorption of LiF in this spectral region, the first order light is also reduced. Additionally, precise ellipsometric measurements strongly depend on the reflectivity of the sample. In particular, rough surfaces, as found for the investigated AlN sample, could further reduce the intensity and disturb the measurement. However, in agreement with the reliable line shapes below 9.5 eV the third prominent absorption feature can be located at about 10 eV and the fourth at about 11 eV. For a sufficient adaptation of the spectra we introduce these two CP's in the fit but use constant phase factors to eliminate divergent results. The determined transition energy of both are, therefore, just approximations whereas the first to CP's can clearly located at 7.8 eV and 8.9 eV, respectively.

8.1.2 Zincblende AlN

Sample characterisation

The zincblende AlN films were deposited by a plasma-induced MBE in the Technical University of Ilmenau. As mentioned above, Cimalla et. al. [153] succeed now to grow either wurtzite or zincblende AlN films depending on the carbonisation conditions prior to growth. This procedure includes the preparation of an approximately 3 nm thick 3C-SiC film on the Si substrate before the ultimate deposition of about 200 nm AlN was started. The polytype of the AlN layers was confirmed by XRD experiments, which demonstrate a fraction of wurtzite inclusions of about 20% [153].

The total energy of the zincblende crystal phase is much higher than in the preferred wurtzite phase. Therefore, the growth of zincblende crystals has to be accomplished far away from the thermodynamical equilibrium conditions. Thus, very clean zincblende phase layers are still not available and also the knowledge about the optical properties is very poor. However, according to ab-initio band structure calculations, zincblende AlN is the only nitride compound with an indirect band gap. The theories predict this indirect gap at about 4.9 eV [97, 154]. But experiments show still controversial results concerning the direct or indirect character of zincblende AlN [155, 156].

Dielectric function and CP analysis

Together with Goldhahn et. a. [157] we could determine now the zincblende AlN dielectric function for the first time up to 9.5 eV (fig. 8.3). According to this measurements on the MBE sample from Ilmenau, zincblende AlN is transparent up to ≈5.7 eV. This value is approximately 700 meV higher than the experimental value reported in Ref. [51]. Below 5.7 eV the measured pseudodielectric function is dominated by strong interference structures in the layer (fig. 8.3, grey line). But due to the small layer thickness, it was not possible to resolve an indirect band gap of zincblende AlN in an optical model calculation. Well above the first undisputable direct band gap at 5.7 eV the layer can assumed to be opaque. Thus, the dielectric function as shown by black lines in figure 8.3 can be interpreted as the bulk dielectric function after correction of surface roughness effects. But the maximum amplitudes in this corrected dielectric function are still low in comparison to e. g. GaN and all structures arise spectrally broadened due to the relative low crystal quality.

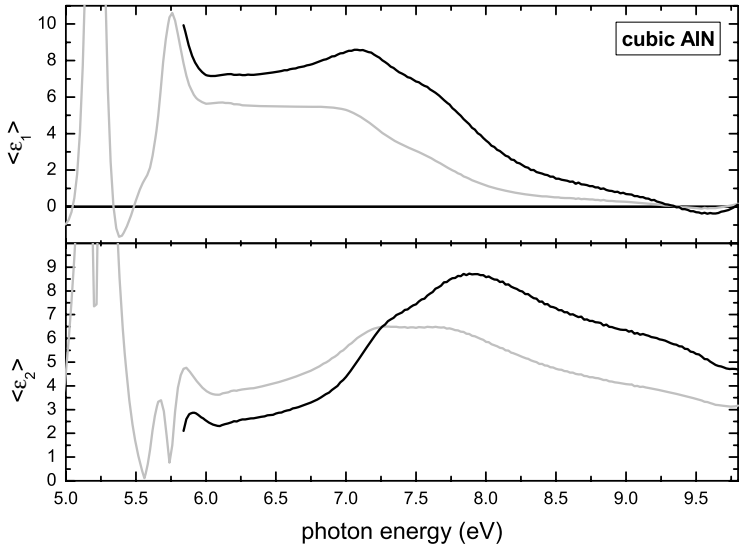

Figure 8.3: *Dielectric function of zincblende AlN [black line]. The surface roughness of the sample was corrected within the EMA-model shown in para. 4.2.2. The grey line represents the uncorrected pseudodielectric functions as measured by ellipsometry.*

A CP analysis, finally, reveal at least three CP in the dielectric of the zincblende AlN sample at 7.2, 7.7, and 9.6 eV. But beside these well reproduced structures, two further points in the dielectric function at about 6.2 and 8.7 eV remain, which could not addressed in the JDOS model due to a non Kramers-Kronig consistent line shape of ε_1 and ε_2. Nevertheless, we refer these features to absorption structures. But we should mention again that the film under investigation is very thin and contains a rather high fraction of wurtzite inclusions. Hence, the controversial feature at ≈6.2 eV could either be related to the strongly excitonic enhanced band gap transition of wurtzite AlN or to a strong absorption structure in the thin cubic 3C-SiC buffer layer [129]. The small shoulder at ≈8.7 eV, however, appears at almost the same photon energy like the $B_\perp$ peak in the wurtzite dielectric function.

8.2 Discussion of AlN interband transitions below 12 eV

8.2.1 Heuristic assignment of CP's in comparison to GaN

In the case of AlN, decent optical data are unfortunately only available for $\varepsilon_\perp$ of the wurtzite crystal type. The extraordinary dielectric tensor component $\varepsilon_\parallel$ is still unknown and the measurements on zincblende AlN has to be evaluated with care, due to the relative high fraction of wurtzite inclusions. Thus, a direct relation of CP's is even more problematic than for InN.

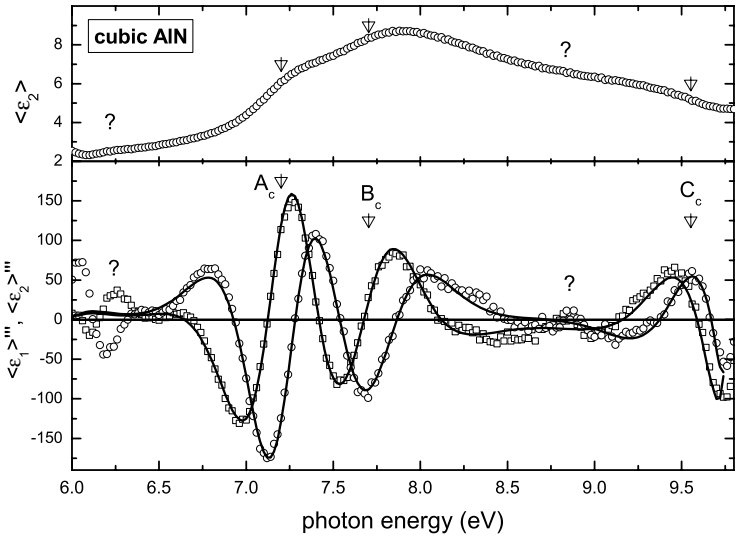

Figure 8.4: *Third derivative of the zincblende AlN dielectric function.* $< \varepsilon_1 >'''$ *[squares] and* $< \varepsilon_2 >'''$ *[circles] are calculated from the spectra as shown in figure figure 8.3. The full lines are obtained by fitting the third derivative spectra within the JDOS model. The found critical points are marked with triangles and ascending alphanumeric labels.*

In addition, the general line shape of the measured wurtzite $\varepsilon_\perp$ also reasonably differs from respective GaN and InN dielectric tensor components. These differences are somehow expected. The wurtzite InN $\varepsilon_\perp$ was already clearly modified in comparison to GaN. But the difference in the electronegativity value of Nitogen and the group III component is now further increased in AlN ($EN_N - EN_{Al} = 1.54$) compared to GaN ($EN_N - EN_{Ga} = 1.23$) or InN ($EN_N - EN_{In} = 1.20$). This increased ionic character of the chemical bonds may also cause a further increased charge asymmetry, as well as a bigger deflection of the c/a ratio (AlN: 1.600) from the ideal value (1.627) [149]. In comparison, the c/a ratio of InN (1.613) and especially of GaN (1.627) is much closer to the ideal value and, thus, the distortion of the ideal tetrahedrical chemical bond arrangement is weaker. Under these conditions, finally, the optical anisotropy should be further increased and also the differences between the zincblende and the wurtzite phase dielectric functions are expected much larger than for GaN.

Anyhow, the first dominant peak in the wurtzite $\varepsilon_\perp$ of GaN and InN is clearly connected to the zincblende E_1 transition. Consequently we attribute this first major peak of AlN ($A_\perp$, fig. 8.2) also to the $E_1(B)$ CP. This assumption is further supported by the fact that the zincblende dielectric function also contains a strong absorption structure at a similar photon energy (B_c, fig. 8.4). The following absorption peak in the wurtzite AlN $\varepsilon_\perp$, in contrast,

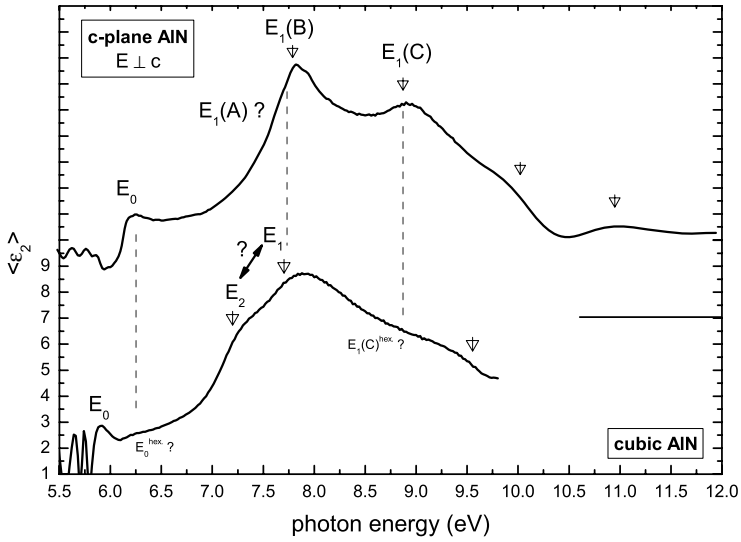

Figure 8.5: *Comparison of the imaginary part of different dielectric functions measured on zincblende and wurtzite AlN. The labels E_0, E_0', E_1, E_1', and E_2 for the characteristic absorption structures correspond, in the isoelectronic sequence scheme, to peaks observed in various zincblende materials [85, 86]*

has no relation in the zincblende dielectric function. Therefore, it is most likely the expected $E_1(C)$ CP. This behaviour is very similar to that of GaN. A further proof for our assignment of the $E_1(B)$ and $E_1(c)$ peak is given by the measurements of Wethkamp et. al. [40]. In this earlier work at BESSY I, he determined the pseudodielectric function of $Al_xGa_{x-1}N$ with different compositions up to 9 eV. All samples are grown by MBE on a sapphire substrate. As shown in figure 8.6 the E_0, $E_1(B)$, and $E_1(C)$ transition structures of GaN continuously shift to higher photon energies with the increasing fraction of Al. Finally even if the $E_1(C)$ moves out of the investigated spectral range these measurements give a clear evidence for the assignment of both the $E_1(B)$ and $E_1(C)$ structure in wurtzite AlN.

Surprisingly, we observe a further distinct absorption structure A_c for zincblende AlN somewhat below the "E_1" (B_c) peak. A similar behaviour is known already from the zincblende GaN dielectric function, where the E_1 is accompanied by a second CP. But this appears at higher photon energies with respect to the E_1. This second feature close to the E_1 transition was attributed for GaN to the E_2 transition. It appears at a relative low energy in comparison to the E_2 peak e. g. in GaAs. AlN has a further increased ionic character of the chemical bonds between the group III and group V component, which maybe increase this shift. Therefore, we would attribute this low energy A_c peak in AlN also to a E_2 transition.

In general, all major structures in the zincblende AlN are spectrally broadened in comparison to the structures of the wurtzite sample. Furthermore, some weaker structures seem

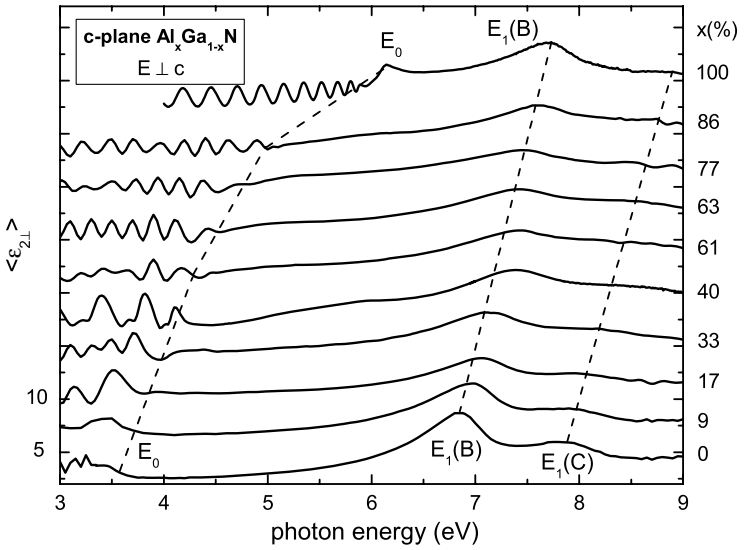

Figure 8.6: *Imaginary part of the dielectric tensor component $< \varepsilon_\perp >$ of wurtzite $Al_xGa_{x-1}N$ ($0 \leq x \leq 1$; c-plane) [40].*

to correlate with major transitions in the wurtzite dielectric function. The broadening of CP's and the additional structures in the zincblende AlN dielectric function are probably correlated with defects in the stacking order along the (111)-direction. Especially the common small structures at 6.25 and 9.0 eV, thus, could be related to wurtzite inclusions. Beside the zincblende-3C and the wurtzite-2H phase, also a number of further arrangements of the hexagonal AlN (0001) layers are conceivable. Other possible stacking structures like the hexagonal 4H- and 6H-phase have only slightly increased total energies [49] in comparison to the pure wurtzite or zincblende phase. This crystal diversity is well known from the SiC-system.

For the CP's above 9 eV ($C_\perp$,$D_\perp$, and C_c) we can not propose an unambiguous explanation until now. For these features we find no correlation to structures in the respective GaN and InN dielectric functions, and also the helpful comparison with the wurtzite $\varepsilon_\parallel$ is not available. However, it was shown in a recent publication that a growth of wurtzite a-plane AlN can be realised by PAMBE on r-plane sapphire [158]. With these samples we could determine also the $\varepsilon_\parallel$ dielectric tensor component. The comparison with the $\varepsilon_\perp$ component under consideration of the selection rules for dipole transitions could finally provide important information for the unambiguous assignment of CP. Furthermore, especially for AlN, it would be essential to extend the spectral range above 10 eV in order to obtain an overview about the whole bunch of interband critical points.

8.2.2 Comparison with ab-initio calculations

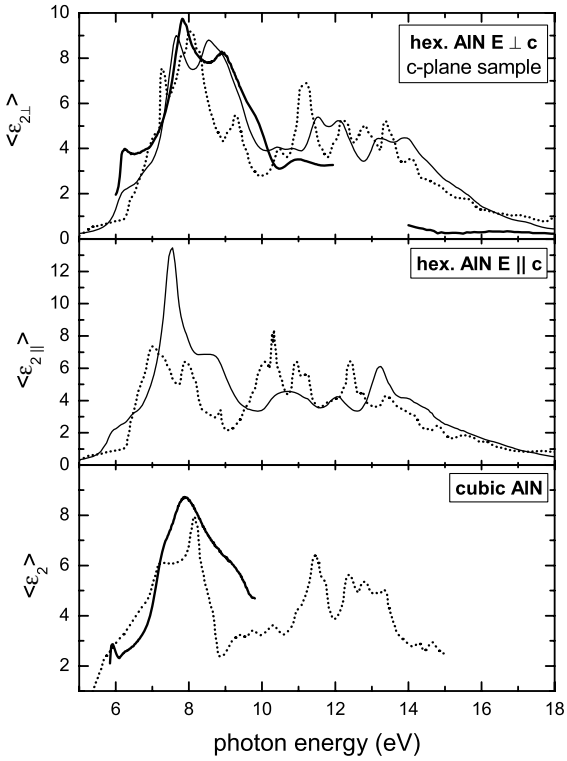

Figure 8.7: *Measured imaginary parts of the dielectric function (tensor components)* $< \varepsilon_2 >$ *[thick line] compared to* ε_2 *calculated by Benedict et al. [41] [thin line] and Christensen et. al. [94] [dotted line].*

In figure 8.7 we compare our measured dielectric functions for AlN with ab-initio calculations of Benedict et. al. [41] (thin solid line) and Christensen et. al. [94] (dotted line). As discussed already in paragraph 6.2.2, the first was calculated including quasi-particle effects and the latter one without. The inclusion of quasi-particle and excitonic effects, respectively, leads here again to a better agreement in the general line shape of the measured and calculated $\varepsilon_\perp$ as shown in figure 8.7 (thin line). But the calculated absorption structures seem to be slightly shifted to lower energies in comparison to the experiment. The calculation of Christensen et. al. [94] do not consider quasi-particle effects and the calculated dielectric function differs remarkably from the experimental results concerning the general line shape. Nevertheless, it generates also the same absorption structures like the experiment. Furthermore, this calculation confirms our experimentally found CP's especially for zincblende AlN,

where other theoretical results are not available.

It was mentioned earlier in this chapter that zincblende AlN has an indirect band gap ($\Gamma_{15}^v \rightarrow X_1^c$) according to several band structure calculations (fig. 8.8). This indirect gap is generated by the very low energy of the lowest conduction band stats near the X_1^c point. In this connection it is also conceivable that the relative position of the E_2 gap ($X_5^v \rightarrow X_1^c$) is further shifted to lower photon energies. The band structure calculation of Christensen et. al. [94] clearly indicate that the E_2 gap is smaller than the E_1 gap, whereas in GaN the E_2 transition is still expected above the E_1 transition ($L_3^v \rightarrow L_1^c$).

The respective calculated dielectric function for zincblende AlN [94] shows the expected line shape with four major absorption structures. The third and fourth dominant feature is unfortunately predicted for photon energies above 11 eV where the mentioned experimental problems prevent reliable results. Nevertheless, these structures has to be attributed to the E_1' ($L_3^v \rightarrow L_3^c$) and the E_0' ($\Gamma_{15}^v \rightarrow \Gamma_{15}^c$), respectively. Hence, we can assume the related transition of the wurtzite crystal structure in the same photon energy range. But a further improvement of the experimental setup in order to reach reliable values for the wurtzite and zincblende dielectric functions also in the spectral range above 10 eV would be strongly recommended to clarify this point.

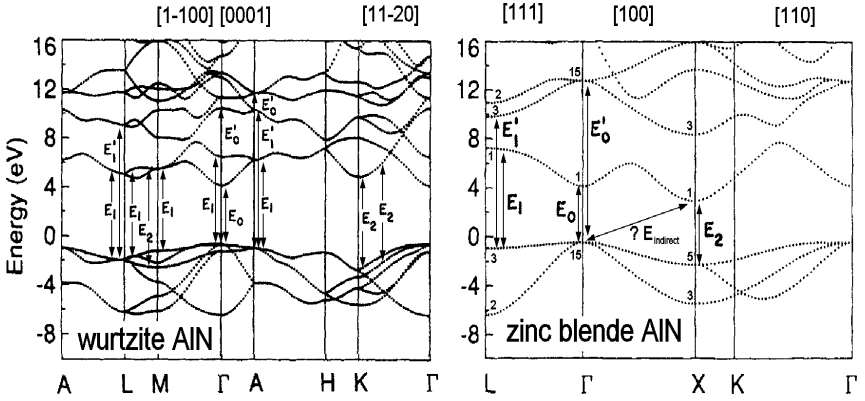

Figure 8.8: *AlN band structure calculated by Christensen et. al. [94] as already shown in paragraph 4.1.3 figure 4.7. The arrows correspond to interband transitions, which we attribute to specific absorption structures in the dielectric functions of wurtzite AlN (fig. 8.5).*

9. Core level excitations

In following we finally discuss the dielectric functions measured above 14 eV. The main contributions to the dielectric function below 14 eV originate from transitions of the 6 uppermost valence states to the lowest conduction bands. This fact is also confirmed by the "incomplete" sum rule for the number of excited electrons per unit cell (eq. 4.13). Figure 9.1 shows for wurtzite GaN (InN) that this sum flattens out above 14 eV (12 eV). 12 electrons finally contribute to the dielectric function up to 21 eV (18 eV). These 12 electrons correspond at the same time to the 6 bonding p-valence states. A further remarkable step like increase in the effective number of electrons at 23 eV (20 eV) indicates the additional contribution of core state excitations. However, the effective number of electrons continuously raises slowly also after this step. In particular for InN, N_{eff} does not saturate at 16 electrons, which would correspond to the maximum number of available valence electrons. The further increase clearly indicates here the contribution of core states. The additional transitions are, in particular, transitions from Ga3d (In4d) core states to conduction bands above 23 eV (18 eV) (fig. 4.7). Unfortunately we could not calculate reliable values for the effective number of electrons in AlN. For AlN we have to take into account remarkable contributions to the effective number of electrons from the unknown spectral range between 12 and 14 eV, which probably influence the final number of electrons conspicuously.

Al is the smallest group III element with the atomic number 7. Thus, Al has no d electrons and we do not expect characteristic transitions for AlN above 20 eV. But as we noticed already in paragraph 3.3 the absence of this transition leads also to a strongly reduced reflectivity above 20 eV. The intensity of the light after reflection on the sample was finally strongly reduced. Ellipsometric measurements above 19 eV, therefore, were also not possible. On the other hand this intensity problem above 19 eV illustrates indirectly the influence of d electrons to the dielectric function and those also to the reflectivity of InN and GaN.

In LDA calculations it was shown, however, that the Ga3d (In4d) core states overlap with N2s valence band electrons and partly hybridise [84, 97] (fig. 4.7 on page 56). Therefore, the Ga3d (In4d) states are often described as semi-core states. The general role of the cation semi-core d states in the determination of group-III-nitride properties has been discussed by several authors [84, 97, 159, 160] and are still not completely solved. But the hybridisation of N2s and Ga3d (In4d) is assumed to be rather weak, and therefore, the dispersion of these localised semi-core d-states is insignificant. Thus, there are 10 Ga3d electrons concentrated in a very narrow peak in the density of states [159, 160] and it seems to be sufficient to ignore the transitions originating from N2s bands in the following. The Ga3d or In4d electrons are located between 13-15 eV below the valence band maximum of the GaN or InN according to the different band structure calculations [84, 97, 159, 160]. Hence, the excitation of these semi-core states into the conduction band could be expected for transition energies at about 18 eV for GaN and 16 eV for InN. We found, indeed, at $\approx$2 eV higher energies the onset of further significant absorption structures in our measured dielectric functions on GaN and InN (fig. 9.2). This is in agreement with the predicted strong excitonic effects that increases these transition energies. The interpretation of these structures as semi-core d state transition is

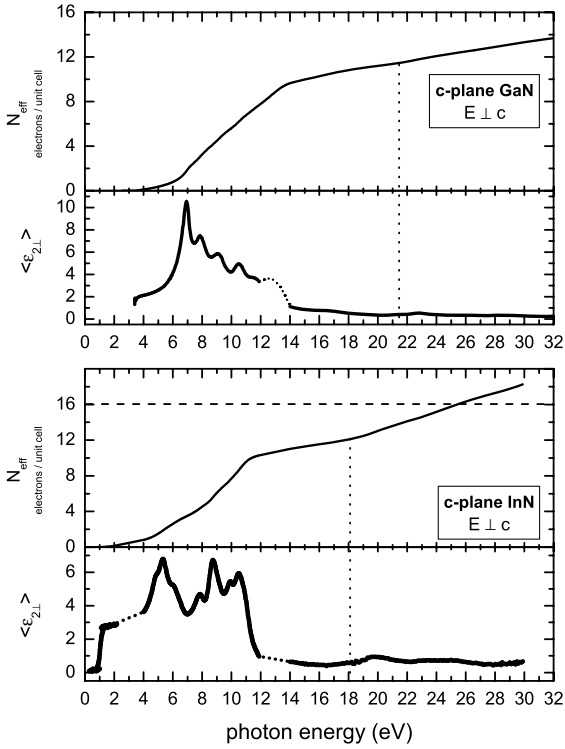

Figure 9.1: *The effective number of electrons per unit cell N_{eff} calculated from the imaginary part of the wurtzite GaN and InN dielectric tensor component $\varepsilon_{\perp}$ (q. v. equ. 4.13). The vertical dotted lines indicate the photon energy where both N_{eff} integrals accumulates to 12 electrons, which corresponds to the top 6 p-like valence states (q. v. fig. 4.7). The horizontal dashed line indicate the maximum number of 16 valence electrons.*

also in agreement with various previous works on GaAs [90, 161], InP [162], as well as on wurtzite GaN [34, 84] based on reflectance measurements, where these absorption structures are attributed to Ga3d or In4d excitations as well.

The Ga3d (In4d) core levels are only slightly disturbed due to the weak hybridisation with the N2s valence states. Therefore, the quantisation of the angular momentum and especially the d character of these semi-core electrons is well preserved. Furthermore, these states are still strongly localised around the Ga (In) atoms. The dispersion in the reciprocal space, therefore, is insignificant. In consideration of these two arguments, the measured absorption peaks should correlate with transitions to p-like and f-like conduction bands at points with small band dispersion. Or in other words, the measured absorption structures above 20 eV

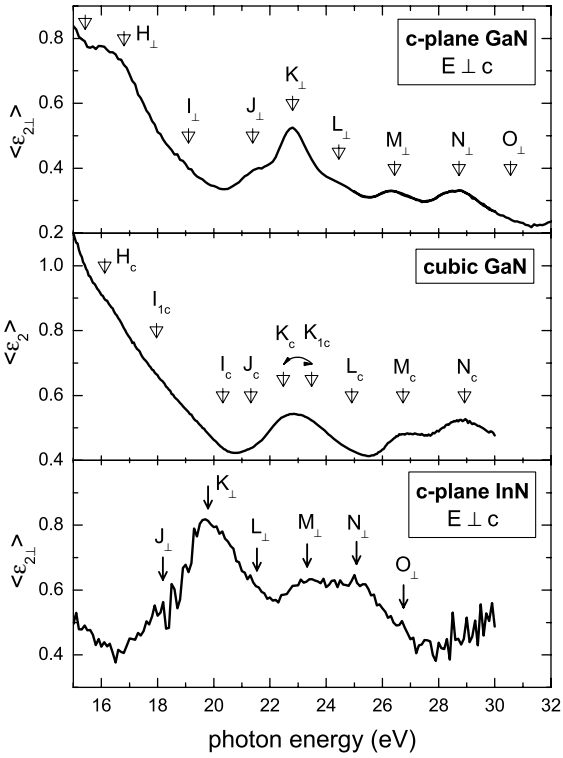

Figure 9.2: *Imaginary part of the dielectric function of wurtzite GaN and InN ($\vec{E} \perp c$), as well as zincblende GaN above 14 eV. The dielectric function reveal also in this higher spectral range several distinct absorption structures, which are marked by arrows according to the analysis shown in paragraph 6.1.2, 6.1.3, and 7.1.3. Above 20 eV and 17 eV these structures originate from semi-core d state excitation of Ga3d and In4d, respectively.*

(17 eV) should correlate with the partial density of states (PDOS) of p- or f-like conduction bands. But in GaN (InN) the lower conduction bands are actually dominated by the antibonding Ga4p (In5p) states. In a further approximation, therefore, the absorption structures are also correlated to the overall DOS of the conduction bands. The zincblende Ga4p PDOS calculated in a DFT-LDA [96], indeed, is quite similar to the imaginary part of the measured zincblende GaN dielectric function above 20 eV (fig. 9.3). For this comparison the PDOS was at first shifted to the appropriate energies according to the assumed energy of the Ga3d level. At second the PDOS was multiplied by $1/E^2$ to consider the prefactor $1/E_{CV}^2$ in relation 4.16. The latter relation represents the connection of the joint density of states with the dielectric function. The line shape of the three dielectric functions generally shows remark-

able similarities above 15 eV. This applies, in particular, also for the InN dielectric function, where the distinct absorption structures appear just shifted by about 2 eV to lower energies.

These results emphasises again the overall similarity of the corresponding GaN and InN band structures and in particular emphasises the agreements of the wurtzite and zincblende projected DOS. Unfortunately, the various absorption structures occur somehow reduced or broadened in the measured zincblende GaN dielectric function. This is probably just a consequence of the poor surface morphology of the sample. In this shorter wavelength region the influence of surface roughnesses or surface distortion on the ellipsometric measurements is very important. The penetration depth of the light is low, which leads to an increased surface sensitivity (fig. 5.1). Furthermore, the influence of scattering and depolarisation should also increase if the wavelength becomes smaller in relation to the surface morphology.

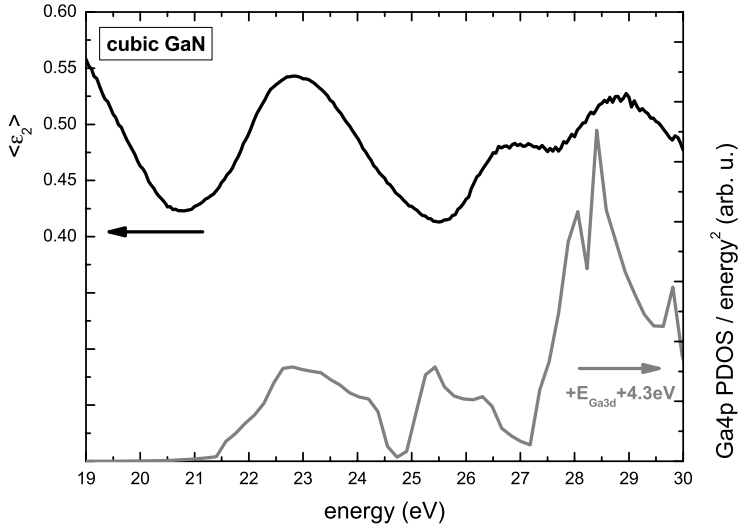

Figure 9.3: *Imaginary part of the zincblende GaN dielectric function in comparison to the valence band PDOS with a dominant p-character. The PDOS was calculated within a DFT-LDA by Schmidt et. al. [96]. For the comparison with the dielectric function we choose the energy position of the PDOS in relationship to Ga3d-core states. Finally the PDOS was additionally shifted by +3 eV.*

Fortunately, Lambrecht et. al. [84] extended the band-to-band evaluation of the dielectric function of wurtzite GaN also to higher energies up to 35 eV. The authors decompose in this calculation the joint contributions from the upper six N2p bands and the joint contributions from the lower 12 bands associated with the Ga3d and N2s bands in the region 18-35 eV. This procedure is similar to the separation of the different interband transitions in the lower spectral range. We show these two calculated components of the dielectric function together with our ellipsometric results and a dielectric function deduced from reflection measurements by Kramers-Kronig analysis [84] in figure 9.4. In this comparison one can clearly see the

good agreement of the measured absorption structures with structures calculated for the two components and that the peaks between 20 and 28 eV are only related to transitions from the Ga3d states. On the other hand, the N2p contribution provides the gradually decreasing background and respond to peaks at about 16 eV (not shown here), 19 eV, and 30 eV. The absorption feature at about 16 eV is nicely seen in our measurements shown in figure 9.2 and was ascribed by Lambrecht et. al. to transitions on the L point ($L^v_{2,4} \rightarrow L^c_{2,4}$). The calculated Ga4p PDOS is quite similar to the "Ga3d" contribution in the dielectric function as demonstrated also in figure 9.4. The reduced oscillator strength at higher energies possibly relates to effect of the transition matrix elements.

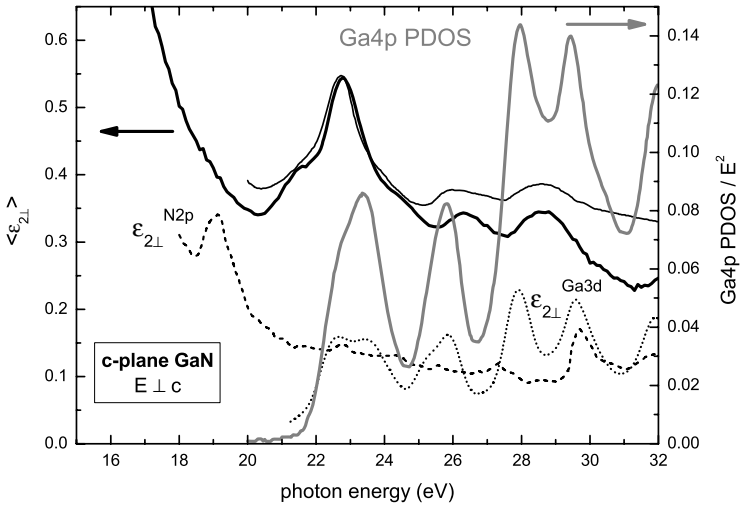

Figure 9.4: *Imaginary part of the wurtzite GaN dielectric tensor component $\varepsilon_\perp$ above 14 eV (black line) in comparison to the valence band PDOS with a dominant p-character (gray line) as calculated within DFT-LDA [84]. The dotted and dashed lines correspond to the calculated $\varepsilon_2(E)$, where only transitions from the Ga3d and N2p states, respectively, are taken into account [84]. The thin solid line shows the $\varepsilon_2(E)$ deduced from reflectivity measurements of Lambrecht et. al. [84] by a Kramers-Kronig analysis.*

In reference [84] the authors have shifted the Ga3d contribution to the dielectric function of GaN by 4.5 eV to higher energies in order to fit the theoretical results to the experiment. The Ga4p partial density of states in the conduction band was shifted by the same amount in addition to the binding energy difference between the Ga4p conduction band and Ga3d semi-core states. This additional shift of 4.5 eV was explained by large self-energy effects on the narrow semi-core like Ga3d band, which are not included in the LDA calculation. We applied the same shift already to the calculated Ga4p PDOS of zincblende GaN, in order to achieve an agreement of all four distinct absorption peaks (fig. 9.3). But not only self-energy effects have to be considered. As mentioned already, we also neglect the effects of

the respective transition matrix elements, as well as quasi particle effect (excitonic effects). These additional effects can change the line shape of the resulting dielectric function a lot. The given comparison, therefore, can only highlight the general agreement but differences are very likely.

Thus, an unambiguous correlation to conduction band regions with a flat dispersion is problematic. This assignment is further complicated due to the complex band structure of the wurtzite crystal structure. But in the zincblende crystal structure the assignment is easier. For example in InAs [162] flat regions in the lowest conduction bands are mainly located in the vicinity of the X and L points (q. v. fig. 4.4). But the reduced energy of the lowest conduction band near the X point leads to an increased dispersion of the respective bands in the investigated nitrides. Thus, we would attribute the first Ga3d peak at ≈23 eV mainly to transition at the L_1 point (fig. 4.7). The second valence band has a similar flat region near the X_3 point, which possibly relate to the next major peak in the dielectric function at ≈26.5 eV.

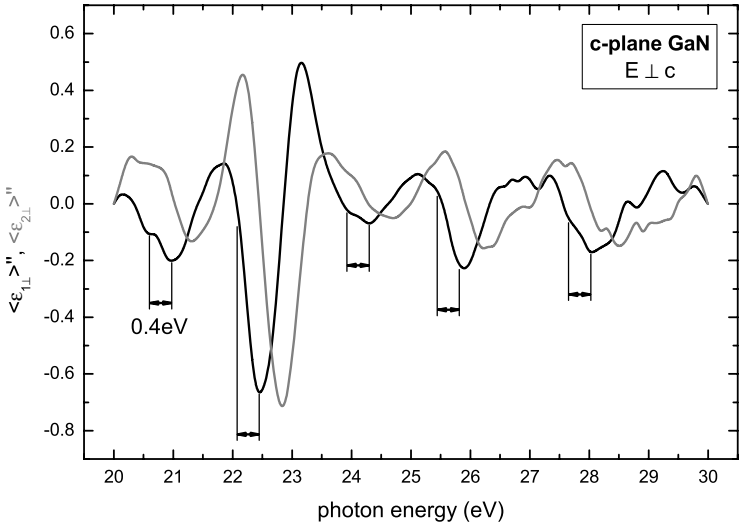

Figure 9.5: *Spin-orbit splitting of semi-core d states in GaN*

In the discussion of core level excitations we neglect until now the known spin-orbit splitting of semi-core d states in GaN and InN. The spin-orbit interaction should lead to a gaugeable splitting of the semi-core d states in to levels namely the Ga3(In4)$d_{5/2}$ and Ga3(In4)$d_{3/2}$ states. According to soft-x-ray photoemission spectroscopy (SXPS) experiments e. g. on InGaP [163] this splitting amounts to ≈0.4 eV for GaN and ≈0.8 eV for InN. Olson et. al. [34], indeed, saw already indications for the Ga3d spin-orbit splitting of 0.4 eV in wurtzite c-plane GaN at the $K_\perp$ absorption structure around 23 eV. They have used reflection measurements under an angle of incidence between 30-60°. Unfortunately, we did not found the expected splitting even on the best spectra measured on c-plane GaN. But in our CP fit as present in paragraph 6.1.1 it is conspicuous that all the CP above 20 eV show a rather increased broad-

ening in comparison to the interband CP (tab. B.1). This CP's should actually relate to very defined d state excitations. Thus, we assumed that the spin-orbit splitting is possibly hidden in the broadened structures. This broadening of absorption structures could relate to crystal(surface) defects or to temperature effects due to the electron phonon interaction.

Encouraged by this noticeable broadening we evaluate the c-plane GaN spectrum again but in the second derivative using a smaller averaging parameter for the calculation. In this somehow more sensitive treatment, we can, finally, also find indications for the expected spin-orbit splitting in our measurements. As shown in figure 9.5 all the known absorption features above 20 eV seem to be superimposed by a double structure with a ≈0.4 eV energy distance. Unfortunately, such an analysis in a derivative dielectric function was not possible for the c-pane InN spectrum, which has a much higher noise level. But nevertheless, indications for the ilspin-orbit splitting of ≈0.8 eV are also seen already in the directly measured pseudodielectric function. For the investigated zincblende GaN, at the end, an identification of the spin-orbit splitting was not possible at all. The broadening of the semi-core level excitation due to the lower overall crystal (surface) quality is fairly to large in this sample in comparison with the expected spin-orbit splitting. Just the unexpected additional structure K_{1c} at 23.5 eV could be related somehow to the unresolved splitting of the d states. Due to uncertainties in the phase factor, an overestimation of the energy gap in the CP fit is conceivable if the absorption structures are very close to each other.

The cited pure DFT-LDA calculations, in general, do not include the spin-orbit interaction. Therefore, the calculated spectra should just show a single peak for CP's, which split or broaden in our experimental results.

Finally, the investigation of excitations between (semi-)core states and the conduction band should allow a further evaluation of the electronic structure and/or chemical bonds. Similar to inverse photo emission experiments, ellipsometric measurements can help to elucidate the conduction band structures in semiconductors. In particular by taking advantage of the polarisation of the light one can obtain information about the anisotropy of the chemical bonds and the bond length in e. g. hexagonal crystals. Wurtzite GaN is assumed rather isotropic concerning the bond lengths and charge asymmetry parallel and perpendicular to the c-axis, respectively. This agreement is nicely reproduced in our experiments (parg. 6.1.2, fig. 6.9). We determine a high overall agreement in the dielectric tensor components $\varepsilon_{\perp}$ and $\varepsilon_{\parallel}$, as well as the zincblende dielectric function in the spectral range of core level excitations. For InN and more pronounced for AlN much higher differences in the chemical bonds are predicted. Thus, we would expect remarkable differences also in the "high energy" dielectric function. Furthermore, the measurements of (semi-)core level excitations with ellipsometry can be used to investigate the distortion of the conduction band e. g. in superlattice structures like shown in reference [164]. The defined energy of the (semi-)core Ga3d in a GaAs/AlAs superlattice structures were used in this work as reference energy in the ellipsometric evaluation of quantum-size effects in the conduction bands. But for all these experiments it would be very helpful to accomplish the ellipsometric measurements at low temperatures in order to reduce the temperature broadening. If the spin-orbit splitting is resolved in such measurements the assignment of transitions would be easier and a further evaluation could be possible.

10. Summary

This work presents a study of the optical properties of group-III nitride semiconductors between 3 and 30 eV. These are in particular GaN, InN, and AlN in the stable wurtzite and zincblende crystal structure. Our investigation focuses on the dielectric function in the spectral region above the E_0 fundamental band gap, where the most significant structures of the dielectric function are located. In a comprehensive discussion we assign most of these absorption structures to specific interband transitions at high symmetry points in the Brillouin zone and to transitions from semi-core d states to the conduction band, respectively. For this purpose it was essential to measure both wurtzite dielectric tensor components $\varepsilon_\perp$ and $\varepsilon_\parallel$, as well as the zincblende dielectric function.

The group-III nitride semiconductors attracted an enormous amount of scientific and commercial attention in recent years as a potential material class for the development of (opto-)electronic devices. However, many fundamental properties are still unknown. Although GaN is already successfully used in optoelectronic devices, the extraordinary dielectric tensor component $\varepsilon_\parallel$ is unknown above the band gap. The ongoing discussion about the exact band gap of InN also illustrates the uncertainties concerning fundamental properties.

The recent progress in epitaxial growth of smooth group-III nitride layers by MBE and MOVPE also provides new experimental ways to study fundamental properties. The quality of the epitaxial layers is improved, especially for InN, and zincblende or wurtzite crystal structures with different crystal orientations are available now. With these new samples it was possible to measure for the first time both independent dielectric tensor components $\varepsilon_\perp$ and $\varepsilon_\parallel$ of wurtzite GaN and InN above the band gap. For AlN, on the other hand, some initial experimental data have been obtained for the cubic polytype. But the growth of pure cubic crystals is still difficult.

For the determination of the dielectric function in the broad spectral range of interband transitions up to the excitation of semi-core d-electrons, we use a unique ellipsometer setup at the synchrotron light source BESSY II. On the basis of an existing setup, which was used at the former storage ring BESSY I, we rebuilt the necessary UHV system and optimised the optical design according to the new requirements. With this setup ellipsometric measurements are possible between 3 and 35 eV. Ellipsometer setups with conventional light sources, in contrast, are usually restricted to the spectral range below 6 eV.

The determination of both dielectric tensor components of wurtzite crystals was realised on M- and a-plane samples, respectively. In these samples the optical axis lies parallel to the surface. The ellipsometric measurements, however, were performed in two steps with the optical axis parallel and perpendicular to the plane of incidence. The two dielectric tensor components were subsequently calculated from the measured pseudodielectric functions according to an optical model for anisotropic layers. We present, in this connection, a special solution for biaxial samples with an unintentional surface roughness.

The dielectric tensor components of wurtzite GaN and InN show huge anisotropies in the spectral range of interband transitions. The two components differ according to the amplitude, the photon energy position, and the number of absorption structures. We basically

attribute this anisotropy to the different selection rules for dipole transitions between specific electronic states [138]. These states are related to respective zincblende electronic states, but split in the wurtzite structure due to the reduced symmetry [48]. The dipole selection rules depend on the polarisation of the incident light and the orientation of electric field vector, respectively. Thus, several transitions are forbidden if the electric field vector is chosen parallel to the c-axis. This leads, in fact, to a reduced number of absorption structures in $\varepsilon_{\parallel}$.

According to these symmetry arguments we introduce a comprehensive assignment of the specific transitions in the wurtzite and zincblende crystal structure of GaN. Unfortunately, a complete unambiguous assignment was not possible for InN and AlN. Strong variations concerning the photon energy position of correlated transition features in InN indicates an additional charge anisotropy and, thus, an anisotropy of the chemical bonds parallel and perpendicular to the hexagonal closest packed planes. Finally, the comparison of the GaN, InN, and AlN dielectric functions enables the assignment of the major absorption structures in all three materials.

Furthermore, a comparison with the dielectric function derived from DFT-LDA band structure calculations shows very good agreement concerning the principal line shapes and partially also concerning peak positions. But surprisingly, the inclusion of quasiparticle effects in the theory does not improve the overall agreement to the measured dielectric functions in all investigated materials. For zincblende GaN and the ordinary dielectric tensor component $\varepsilon_{\perp}$ of wurtzite InN, the respective calculations without quasiparticle corrections essentially show better agreement than the advanced theories.

According to the detailed theoretical band-to-band analysis for wurtzite and zincblende GaN of Lambrecht et. al. [84, 98, 141] we can attribute the dielectric function features to transitions between certain bands at specific high symmetry points or lines in the Brillouin zone (tab. 6.1). This assignment can also be adopted to InN and AlN due to the general agreements in the calculated band structure and the similarities in the measured dielectric function of GaN, InN, and AlN.

Above 14 eV we found, in the measured dielectric functions of GaN and InN, very characteristic absorption features, which can be related to transitions from the Ga3d and In4d electronic states, respectively, to p-like conduction bands. The characteristic features in the dielectric function roughly refer to the partial density of states (PDOS) of the p-like conduction bands due to the strong localisation of the semi-core d states. Therefore, the measured dielectric function of wurtzite and zincblende GaN above 20 eV, in fact, agree somehow with the general line shape of the respective calculated PDOS. Furthermore, we measure only a weak anisotropy in the dielectric function region of the Ga3d transitions. This small optical anisotropy, thus, indicates an isotropic PDOS and represent a small isotropy of the tetrahedral hybridisation in the GaN wurtzite crystal. Unfortunately we could not determine both dielectric tensor components for wurtzite InN in the range of In4d excitations. We would expect much bigger anisotropies for InN due to the increased charge anisotropy in the chemical bonds. AlN, however, has no semi-core d electrons. Therefore, the imaginary part of the dielectric function, as well as the reflectivity vanishes above the main interband transitions.

In addition to the determination of bulk dielectric functions, we have further investigated the influence of surface contamination, oxide layers, and different surface terminations on ellipsometric results. We found a stronger surface/film degeneration of InN during exposure to air. This degeneration is also measured on GaN surface but is much weaker. In both cases the dielectric function of the uncontaminated sample can be partially restored by thermal an-

nealing up to 400°C and 500°C, respectively. The characteristic changes were attributed to surface oxidation and a contamination with water or other hydroxides. But in several literature results on GaN (XPS) a reduction of the respective Ga_xO_y by annealing is unlikely. This assumption is also confirmed for InN in a very recent SXPS experiment of Vogt et. al. [165], where a strong reduction of hydroxides was determined in connection with this annealing procedure. Nevertheless, the results concerning the strong surface degradation of InN may explain, at the end, the wrong conclusions drawn about the fundamental band gap of InN until now.

A. Software modules

The two independent dielectric tensor components $\varepsilon_{\perp}$ and $\varepsilon_{\parallel}$ of the biaxial anisotropic samples were numerically calculated according to the theory introduced in paragraph4.2.3 equation. 4.76. We realise these calculations in the commercial software for numerical and algebraic mathematics "Mathematica". The implementation is shown in the following.

In a first step we define the ellipsometric ratio ρ and the pseudodielectric for the two high-symmetry orientations, where the c axis of the sample is either parallel ($\alpha = 0$) or perpendicular ($\alpha = \pi/2$) orientated to the plane of incidence.

```
<< Algebra`ReIm`

Off[General::spell1]
```

Effective medium approximation of the rough surface (EMA / Bruggeman)

```
EMA dielectric function of the rough surface (ϵx, ϵy, ϵz) :

ϵx̂[ex_] := 1/8 (1 + ex + √(1 + 34 ex + ex^2))

ϵŷ[ey_] := 1/8 (1 + ey + √(1 + 34 ey + ey^2))

ϵẑ[ez_] := 1/8 (1 + ez + √(1 + 34 ez + ez^2))

EMA refractive index of the rough surface (ϵx, ϵy, ϵz) :

nx̂[ex_] := √(ϵx̂[ex])

nŷ[ey_] := √(ϵŷ[ey])

nẑ[ez_] := √(ϵẑ[ez])
```

Ellipsometric ratio / Pseudodielectric Funktion

```
refractive index of the substrate (ϵx, ϵy, ϵz) :

nx[ex_] := √ex

ny[ey_] := √ey

nz[ez_] := √ez
```

ellipsometric ratio (ϵ_x, ϵ_y, ϵ_z, ϕ, d, E):

$$N_{\hat{x}a}[ex\_, \phi\_] := n_{\hat{x}}[ex]\,\mathrm{Cos}[\phi]$$

$$N_{a\hat{z}}[ez\_, \phi\_] := \sqrt{1 - \left(\frac{1}{n_{\hat{z}}[ez]}\,\mathrm{Sin}[\phi]\right)^2}$$

$$N_{aa}[\phi\_] := \mathrm{Cos}[\phi]$$

$$N_{\hat{y}\hat{y}}[ey\_, \phi\_] := n_{\hat{y}}[ey]\sqrt{1 - \left(\frac{1}{n_{\hat{y}}[ey]}\,\mathrm{Sin}[\phi]\right)^2}$$

$$N_{x\hat{z}}[ex\_, ez\_, \phi\_] := n_x[ex]\sqrt{1 - \left(\frac{1}{n_{\hat{z}}[ez]}\,\mathrm{Sin}[\phi]\right)^2}$$

$$N_{\hat{x}z}[ex\_, ez\_, \phi\_] := n_{\hat{x}}[ex]\sqrt{1 - \left(\frac{1}{n_z[ez]}\,\mathrm{Sin}[\phi]\right)^2}$$

$$N_{yy}[ey\_, \phi\_] := n_y[ey]\sqrt{1 - \left(\frac{1}{n_y[ey]}\,\mathrm{Sin}[\phi]\right)^2}$$

$$N_{\hat{x}\hat{z}}[ex\_, ez\_, \phi\_] := n_{\hat{x}}[ex]\sqrt{1 - \left(\frac{1}{n_{\hat{z}}[ez]}\,\mathrm{Sin}[\phi]\right)^2}$$

$$r_{01pp}[ex\_, ez\_, \phi\_] := \frac{N_{\hat{x}a}[ex, \phi] - N_{a\hat{z}}[ez, \phi]}{N_{\hat{x}a}[ex, \phi] + N_{a\hat{z}}[ez, \phi]}$$

$$r_{01ss}[ey\_, \phi\_] := \frac{N_{aa}[\phi] - N_{\hat{y}\hat{y}}[ey, \phi]}{N_{aa}[\phi] + N_{\hat{y}\hat{y}}[ey, \phi]}$$

$$r_{12pp}[ex\_, ey\_, ez\_, \phi\_] := \frac{N_{x\hat{z}}[ex, ey, \phi] - N_{\hat{x}z}[ex, ez, \phi]}{N_{x\hat{z}}[ex, ey, \phi] + N_{\hat{x}z}[ex, ez, \phi]}$$

$$r_{12ss}[ey\_, \phi\_] := \frac{N_{\hat{y}\hat{y}}[ey, \phi] - N_{yy}[ey, \phi]}{N_{\hat{y}\hat{y}}[ey, \phi] + N_{yy}[ey, \phi]}$$

$$k_0[E\_] := \frac{2\pi E}{1239.852}$$

$$\kappa_p[ex\_, ez\_, \phi\_, d\_, E\_] := k_0[E]\,d\,N_{\hat{x}\hat{z}}[ex, ez, \phi]$$

$$\kappa_s[ey\_, \phi\_, d\_, E\_] := k_0[E]\,d\,N_{\hat{y}\hat{y}}[ey, \phi]$$

$$\rho[ex\_, ey\_, ez\_, \phi\_, d\_, E\_] := \left(\frac{r_{01pp}[ex, ez, \phi] + r_{12pp}[ex, ey, ez, \phi]\,\mathrm{Exp}[I\,2\,\kappa_p[ex, ez, \phi, d, E]]}{1 + r_{01pp}[ex, ez, \phi]\,r_{12pp}[ex, ey, ez, \phi]\,\mathrm{Exp}[I\,2\,\kappa_p[ex, ez, \phi, d, E]]}\right)\left(\frac{1 + r_{01ss}[ey, \phi]\,r_{12ss}[ey, \phi]\,\mathrm{Exp}[I\,2\,\kappa_s[ey, \phi, d, E]]}{r_{01ss}[ey, \phi] + r_{12ss}[ey, \phi]\,\mathrm{Exp}[I\,2\,\kappa_s[ey, \phi, d, E]]}\right)$$

ellipsometric ratio for c parallel to the plane of incidence ($\epsilon_x = \epsilon_e$, $\epsilon_y = \epsilon_z = \epsilon_o$):

```
ρp = ρ[ee, eo, eo, ϕ, d, PE]

ellipsometric ratio for c perpendicular to the plane of incidence
(εy = εe, εx = εz = εo):

ρs = ρ[eo, ee, eo, ϕ, d, PE]

effective dielectric function  (ρ, ϕ):

ε[ρ_, ϕ_] := Sin[ϕ]^2 (1 + Tan[ϕ]^2 ((1 - ρ)/(1 + ρ))^2)
```

With these definitions we create a new function ”epssolve”, which has 8 input values (lists). These are the RMS roughness ”d”, the angle of incidence ”ϕ”, the number of spectral points ”imax”, a list(vector) with the respective photon energies ”Energy”, as well as 4 lists(vectors) with the real and imaginary parts of the measured ellipsometric ratios ”ReRhoP, ImRhoP, ReRhoS, ImRhoS”. The result of the function will be provided as list(matrix) ”epseo” with 4 columns, which contain the real and imaginary part of the two dielectric tensor components.

```
<< Algebra`ReIm`

Off[General::spell1]

epssolve = Compile[
  {
   {d, _Real},
   {ϕ, _Real},
   {imax, _Integer},
   {ReRhoP, _Real, 2},
   {ImRhoP, _Real, 2},
   {ReRhoS, _Real, 2},
   {ImRhoS, _Real, 2},
   {Energy, _Real, 2}
  },
  (
   epseo = Table[i, {i, imax}];
   For[i = 1, i < imax + 1,
    (
     epsp = ε[ReRhoP[[i, 1]] + i ImRhoP[[i, 1]], ϕ];
     epss = ε[ReRhoS[[i, 1]] + i ImRhoS[[i, 1]], ϕ];
     PE = Energy[[i, 1]];
     tmp = FindRoot[{ReRhoP[[i, 1]] + i ImRhoP[[i, 1]] == ρp[ee, eo, ϕ, d, PE],
        ReRhoS[[i, 1]] + i ImRhoS[[i, 1]] == ρs[ee, eo, ϕ, d, PE]},
       {eo, epss, epsp}, {ee, epsp, epss}];
     epseo[[i]] = {Re[eo], Im[eo], Re[ee], Im[ee]} /. tmp
    );
    i++]
  );
 ];
```

In the next step, the 3 required scalar values are directly defined in Mathematica. The 5 vectors has to be imported from 5 ASCII files. Each file should include only one column with the photon energies and the ellipsometric ratio components, respectively.

```
number of spectral points:

imax = 491;

angle of incidence:

ϕ = 68.1 Pi / 180;

RMS-thicknes of the rough surface in nm:

d = 2.4;

Energy = ReadList["e:/temp/Energy.dat", Number, RecordLists -> True];

Reρp = ReadList["e:/temp/ReRhoP.dat", Number, RecordLists -> True];
ListPlot[Table[{Energy[[i, 1]], Reρp[[i, 1]]}, {i, imax}]];

Imρp = ReadList["e:/temp/ImRhoP.dat", Number, RecordLists -> True];
ListPlot[Table[{Energy[[i, 1]], Imρp[[i, 1]]}, {i, imax}]];

Reρs = ReadList["e:/temp/ReRhoS.dat", Number, RecordLists -> True];
ListPlot[Table[{Energy[[i, 1]], Reρs[[i, 1]]}, {i, imax}]];

Imρs = ReadList["e:/temp/ImRhoS.dat", Number, RecordLists -> True];
ListPlot[Table[{Energy[[i, 1]], Imρs[[i, 1]]}, {i, imax}]];
```

Finally the calculation can be started. The results are saved in an ASCII file ”eps_eo_ee.dat” with 4 columns. This file includes the real and imaginary part of the dielectric tensor components $\varepsilon_\perp$ and $\varepsilon_\parallel$. The last four lines produce just a graphical presentation of the result.

```
epssolve[d, ϕ, imax, Reρp, Imρp, Reρs, Imρs, Energy];

Export["e:/temp/eps_eo_ee_68.dat", epseo];

ListPlot[Table[{Energy[[i, 1]], epseo[[i, 1]]}, {i, imax}], PlotJoined -> True];
ListPlot[Table[{Energy[[i, 1]], epseo[[i, 2]]}, {i, imax}], PlotJoined -> True];
ListPlot[Table[{Energy[[i, 1]], epseo[[i, 3]]}, {i, imax}], PlotJoined -> True];
ListPlot[Table[{Energy[[i, 1]], epseo[[i, 4]]}, {i, imax}], PlotJoined -> True];
```

B. Parameter of the JDOS model fits

In the following we summaries the parameters obtained within the line shape analysis according to the JDOS model (eq. 4.20) in a tabulated form. These parameters are obtained in the third derivative spectra of the respective dielectric functions measured for GaN, InN, and AlN. All values marked with "*" correspond to fixed parameters while the numerical adaptation of the optical model. "$^+$" correspond to CP parameters obtained in the respective second derivative spectra.

B.1 GaN

CP	E(eV)	α	$\varphi[s](^\circ)$	A	Γ(eV)
$A_\perp$	6.99	1	-6.0	4.131	0.208
$B_{1\perp}$	7.78	1	-90.0	0.123	0.096
$B_{2\perp}$	8.11	2	155.1	3.558	0.403
$C_{1\perp}$	9.06	1	-8.8	2.781	0.553
$C_{2\perp}$	9.37	1	-6.2	1.813	0.383
$C_{3\perp}$	9.77	1	-22.7	0.505	0.259
$D_\perp$	10.55	0	11.1	3.184	0.728
$E_\perp$	11.35	1	-90.0	4.254	0.701
$G_\perp$	15.43	3	180.0*	0.049	0.316
$H_\perp$	16.81	1	-22.5	0.722	1.225
$I_\perp$	19.10	1	-25.9	0.052	0.746
$J_\perp$	21.39	0	0*	0.059	0.675
$K_\perp$	22.81	0	0*	0.209	0.785
$L_\perp$	24.45	0	0*	0.128	1.220
$M_\perp$	26.43	0	0*	0.130	1.027
$N_\perp$	28.72	0	0*	0.450	1.696
$O_\perp$	30.56	0	0*	0.131	1.448

Table B.1: *Critical point parameters of $\varepsilon_\perp$ measured on c-plane hexagonal GaN (fig. 6.2 and 6.3).*

CP	E(eV)	α	$\varphi[s](^\circ)$	A	Γ(eV)
$A_{1\perp}$	6.36	3	120.9	4.660	0.278
$A_{\perp}$	6.99	1	-29.6	6.707	0.291
$B_{1\perp}$	7.84	1	-90.0	0.427	0.197
$B_{2\perp}$	8.01	2	106.5	6.250	0.418
$C_{1\perp}$	9.10	1	0^*	7.832	0.568
$C_{2\perp}$	9.37^*	1	-87.2	9.637	0.597
$D_{\perp}$	10.7^+	1	-90.0^+	0.677^+	0.093^+
$G_{\perp}$	15.4?	-	-	-	-
$H_{\perp}$	16.70	2	166.5	0.179	0.511
$I_{\perp}$	19.21	2	142.2	0.070	0.321
$J_{\perp}$	21.10	0	0^*	0.170	0.414
$K_{\perp}$	23.21	0	0^*	0.198	0.976
$L_{\perp}$	24.54	0	0^*	0.026	0.606
$M_{\perp}$	26.85	0	0^*	0.064	0.918

Table B.2: *Critical point parameters of $\varepsilon_\perp$) measured on M-plane hexagonal GaN (fig. 6.8 and 6.9).*

CP	E(eV)	α	$\varphi[s](^\circ)$	A	Γ(eV)
$A_{\|\|}$	7.03	1	-43.7	10.067	0.247
$A_{1\|\|}$	7.34	3	-90.0	17.803	0.291
$C_{\|\|}$	9.23	1	0.0	2.968	0.455
$D_{\|\|}$	10.8^+	1	-90.0^+	0.682^+	0.376^+
$G_{\|\|}$	15.53	3	155.0	0.274	0.094
$H_{\|\|}$	16.92	2	163.6	0.426	0.748
$I_{\|\|}$	19.62	2	170.1	0.072	0.496
$J_{\|\|}$	21.19	0	0^*	0.035	0.531
$K_{\|\|}$	22.80	0	0^*	0.487	1.931
$L_{\|\|}$	24.83	0	0^*	0.074	0.994
$M_{\|\|}$	26.80	0	0^*	0.069	0.931

Table B.3: *Critical point parameters of $\varepsilon_\parallel$ measured on M-plane hexagonal GaN (fig. 6.8 and 6.9).*

CP	E(eV)	α	$\varphi[s](^\circ)$	A	Γ(eV)
A_c	7.16	1	-39.4	1.488	0.301
B_c	7.57	1	-15.9	1.269	0.121
C_c	10.52^+	0	0^{*+}	4.561^+	0.783^+
H_c	16.12	0	0^*	0.132	1.008
I_{1c}	17.96	1	-1.8	0.040	0.607
I_c	20.32	2	155.4	0.047	0.694
J_c	21.32	0	0^*	0.006	0.599
K_c	22.47	0	0^*	0.115	0.946
K_{1c}	23.48	0	0^*	0.286	1.376
L_c	24.91	0	0^*	0.081	1.098
M_c	26.74	0	0^*	0.171	1.117
N_c	28.93	0	0^*	0.686	2.168

Table B.4: *Critical point parameters of the cubic GaN dielectric function (fig. 6.12).*

B.2 InN

CP	E(eV)	α	$\varphi[s](^\circ)$	A	Γ(eV)
$A_\perp$	4.81	2	-18.6	0.516	0.236
$B_\perp$	5.36	1	-10.1	1.276	0.300
$C_\perp$	6.19	1	0.0	0.853	0.351
$D_\perp$	6.52	1	-37.7	0.333	0.274
$E_\perp$	7.66	1	-89.3	3.823	1.041
$F_\perp$	8.01	2	159.7	0.629	0.259
$G_\perp$	8.54	1	-90.0	1.990	0.382
$H_\perp$	9.94	1	-30.2	0.612	0.290
$I_\perp$	10.55	1	-57.6	0.849	0.425
$I_{1\perp}$	11.09	1	-29.9	0.606	0.458
$J_\perp$	18.1	-	-	-	-
$K_\perp$	19.8	-	-	-	-
$M_\perp$	23.4	-	-	-	-
$N_\perp$	25.2	-	-	-	-

Table B.5: *Critical point parameters of $\varepsilon_\perp$ measured on c-plane hexagonal InN (fig. 7.5). The parameters are obtained by fitting the third derivative spectra of the MOVPE grown sample B. Due to the high noise level it was not possible to evaluate the third derivative dielectric function in the spectral range above 14 eV. Hence, the given CP energies are determined as peak positions in the imaginary part of the dielectric function.*

CP$_{\vec{E}\perp c}$	E(eV)	α	$\varphi[s](^\circ)$	A	Γ(eV)
$A_\perp$	4.82	1	-50.9	1.253	0.175
$B_\perp$	5.39	1	-27.3	2.656	0.255
$C_\perp$	6.19	1	-17.5	2.471	0.401
$D_\perp$	6.54	1	-58.8	0.445	0.225
$E_\perp$	7.67	1	-89.4	2.637	0.537
$F_\perp$	7.94	2	93.6	0.841	0.164
$G_\perp$	8.54	1	-90.0	3.617	0.259
CP$_{\vec{E}\parallel c}$	E(eV)	α	$\varphi[s](^\circ)$	A	Γ(eV)
$A_{1\vert\vert}$	4.90	3	-88.4	1.053	0.316
$A_{\vert\vert}$	5.40	1	-21.1	4.950	0.240
$B_{\vert\vert}$	7.61	1	-85.9	4.304	0.468
$C_{\vert\vert}$	9.16	1	-51.5	8.060	0.397

Table B.6: *Critical point parameters of $\varepsilon_\perp$ and $\varepsilon_\parallel$ measured on a-plane hexagonal InN (fig. 7.9).*

B.3 AlN

CP$_{hexagonal}$	E(eV)	α	$\varphi[s](^\circ)$	A	Γ(eV)
$A_\perp$	7.79	1	-55.5	2.656	0.200
$B_\perp$	8.87	1	-89.3	1.459	0.292
$C_\perp$	(10.02)	1	0.0*	0.666	0.231
$D_\perp$	(10.50)	1	-90.0*	1.905	0.518
CP$_{cubic}$	E(eV)	α	$\varphi[s](^\circ)$	A	Γ(eV)
A_c	7.20	1	-85.5	1.852	0.236
B_c	7.70	2	38.3	3.453	0.340
C_c	9.55	1	-10.4	2.492	0.516

Table B.7: *Critical point parameters of $\varepsilon_\perp$ and ε measured on c-plane hexagonal and cubic AlN (fig. 8.2 and 8.4).*

C. Experimental methods

In this work we refer to several well known methods for the characterisation of the samples and for the sample preparation itself, which are not explained in detail. This methods, therefore, are listed with a very short description and literature references in the following.

Auger Electron Spectroscopy (AES): Detection of chemical elements in the surface region of a sample according to emitted secondary electrons [166].

Atomic Force Microscopy (AFM): Mapping of the surface morphology in e. g. $1\times1\,\mu$m scan fields with sub-nm resolution [167].

Low Energy Electron Diffraction (LEED): Determination of surface reconstructions according to the diffraction image of low energy electrons [166]. The resulting image shows a fourier transformed picture of the scattering centres near the sample surface.

Scanning Electron Microscopy (SEM): Mapping of the surface morphology in scan fields of e. g. $5\times5\,\mu$m by means of the scattering of a focused electron beam [168].

X-Ray Diffraction (XRD): Characterisation of the crystal structure, orientation, and quality according to angle scans over X-ray diffraction peaks [169].

Metalorganic Vapour Phase Epitaxy (MOVPE): Deposition of epitaxial layers at low pressures [170, 171]. The required elements are provided by a gas flow over the sample surface.

Molecular Beam Epitaxy (MBE): Deposition of epitaxial layers in UHV [170, 172]. The required elements are provided by molecular(atom) beams, which merge on the sample(substrate) surface.

Raman Spectroscopy: Structural and symmetry characterisation according to the lattice dynamics measured by inelastic scattered light in the visible and near UV spectral range [173].

Argon Ion Sputtering: Cleaning of the sample surface by a ion bombardment in an UHV environment [166].

Bibliography

[1] S. Strite and H. Morkoc, *GaN, AlN, and InN: A review*, *J. Vac. Sci. Technol. B* **10**, 1237 (1992).

[2] F. A. Ponce and D. P. Bour, *Nitride-based semiconductors for blue and green light-emitting devices*, *Nature* **386**, 351 (1997).

[3] S. Nakamura and G. Fasol, *The Blue Laser Diode*, Springer-Verlag, Berlin, Heidelberg, New York, 1997.

[4] S. J. Pearton, J. C. Zolper, R. J. Shul, and F. Ren, *GaN: Processing, defects, and devices*, *J. Appl. Phys.* **86**, 1 (1999).

[5] S. C. Jain, M. Willander, J. Narayan, and R. V. Overstraeten, *III-nitrides: Growth, characterization, and properties*, *J. Appl. Phys.* **87**, 965 (2000).

[6] I. Vurgaftman and J. R. Meyer, *Band parameters for nitrogen-containing semiconductors*, *J. Appl. Phys.* **94**, 3675 (2003).

[7] A. G. Bhuiyan, A. Hashimoto, and A. Yamamotoa, *Indium nitride (InN): A review on growth, characterization, and properties*, *J. Appl. Phys.* **94**, 2779 (2003).

[8] V. Y. Davydov and A. A. Klochikhin, *Electronic and Vibrational States in InN and $In_xGa_{1-x}N$ Solid Solutions*, *Semiconductors* **38**, 861 (2004).

[9] H. Morkoc, *Nitride Semiconductors and Devices*, Springer-Verlag, Berlin, 1999.

[10] S. Peters, T. Schmidtling, T. Trepk, U. W. Pohl, J.-T. Zettler, and W. Richter, *In situ monitoring of GaN metal-organic vapor phase epitaxy by spectroscopic ellipsometry*, *J. Appl. Phys.* **88**, 4085 (2000).

[11] T. Schmidtling, M. Drago, U. W. Pohl, and W. Richter, *Spectroscopic ellipsometry during metalorganic vapor phase epitaxy of InN*, *J. Cryst. Growth* **248**, 523 (2003).

[12] M. Drago, T. Schmidtling, C. Werner, M. Pristovsek, U. W. Pohl, and W. Richter, *InN growth and annealing investigations using in-situ spectroscopic ellipsometry*, *J. Cryst. Growth* **272**, 87 (2004).

[13] G. Bauer and W. Richter, *Optical characterization of epitaxial semiconductor layers*, Springer-Verlag, Berlin, 1996.

[14] W. Richter, *In-situ observation of MOCVD epitaxial growth*, *Appl. Phys. A* **75**, 129 (2002).

[15] T. L. Tansley and C. P. Foley, *Optical band gap of indium nitride*, *J. Appl. Phys.* **59**, 3241 (1986).

[16] K. Ikuta, Y. Inoue, and O. Takai, *Optical and electrical properties of InN thin films grown on $ZnO/\alpha - Al_2O_3$ by RF reactive magnetron sputtering*, *Thin Solid Films* **334**, 49 (1998).

[17] F. Bechstedt, J. Furthmüller, M. Ferhat, L. K. Teles, L. M. R. Scolfaro, J. R. Leite, V. Y. Davydov, O. Ambacher, and R. Goldhahn, *Energy gap and optical properties of $In_xGa_{1-x}N$*, *Phys. Stat. Sol. (a)* **195**, 628 (2003).

[18] T. Inushima, V. V. Mamutin, V. A. Vekshin, S. V. Ivanov, T. Sakon, M. Motokawa, and S. Ohoya, *Physical properties of InN with the band gap energy of 1.1 eV*, *J. Cryst. Growth* **227-228**, 481 (2001).

[19] V. Y. Davydov, A. A. Klochikhin, R. P. Seisyan, V. V. Emtsev, S. V. Ivanov, F. Bechstedt, J. Furthmüller, H. Harima, A. V. Mudryi, J. Aderhold, O. Semchinova, and J. Graul, *Absorption and Emission of Hexagonal InN. Evidence of Narrow Fundamental Band Gap*, *Phys. Stat. Sol. (b)* **229**, r1 (2002).

[20] J. Wu, W. Walukiewicz, K. M. Yu, J. W. Ager, E. E. Haller, H. Lu, W. J. Schaff, Y. Saito, and Y. Nanishi, *Unusual properties of the fundamental band gap of InN*, *Appl. Phys. Lett.* **80**, 3967 (2002).

[21] T. Matsuoka, H. Okamoto, M. Nakao, H. Harima, and E. Kurimoto, *Optical bandgap energy of wurtzite InN*, *Appl. Phys. Lett.* **81**, 1246 (2002).

[22] Q. Guo, , O. Kato, M. Fujisawa, and A. Yoshida, *Optical constants of indium nitride*, *Solid State Commun.* **83**, 721 (1992).

[23] R. Goldhahn, *Dielectric function of nitride semiconductors: recent experimental results*, *ACTA PHYSICA POLONICA A* **104**, 123 (2003).

[24] S. Shokhovets, R. Goldhahn, V. Cimalla, T. S. Cheng, and C. T. Foxon, *Reflectivity study of hexagonal GaN films grown on $GaAs$: Surface roughness, interface layer, and refractive index*, *J. Appl. Phys.* **84**, 1561 (1998).

[25] N. V. Edwards, S. D. Yoo, M. D. Bremser, J. T. W. Weeks, O. H. Nam, R. F. Davis, H. Liu, R. A. Stall, M. N. Horton, N. R. Perkins, T. F. Kuech, and D. E. Aspnes, *Variation of GaN valence bands with biaxial stress and quantification of residual stress*, *Appl. Phys. Lett.* **70**, 2001 (1997).

[26] N. V. Edwards, M. D. Bremser, A. D. Batchelor, I. A. Buyanova, L. D. Madsen, S. D. Yoo, T. Wethkamp, K. Wilmers, C. Cobet, N. Esser, R. F. Davis, D. E. Aspnes, and B. Monemar, *Optical characterization of wide bandgap semiconductors*, *Thin Solid Films* **364**, 98 (2000).

[27] D. Brunner, H. Angerer, E. Bustarret, F. Freudenberg, R. Höpler, R. Dimitrov, O. Ambacher, and M. Stutzmann, *Optical constants of epitaxial $AlGaN$ films and their temperature dependence*, *J. Appl. Phys.* **82**, 5090 (1997).

[28] J. Petalas, S. Logothetidis, S. Boultadakis, M. Alouani, and J. M. Wills, *Optical and electronic-structure study of cubic and hexagonal GAN thin-films*, *Phys. Rev. B* **52**, 8082 (1995).

[29] U. Köhler, D. J. As, B. Schöttker, T. Frey, K. Lischka, J. Scheiner, S. Shokhovets, and R. Goldhahn, *Optical constants of cubic GaN in the energy range of 1.5-3.7 eV*, *J. Appl. Phys.* **85**, 404 (1999).

[30] N. V. Edwards, M. D. Bremser, T. W. Weeks, R. S. Kern, R. F. Davis, and D. E. Aspnes, *Real-time assessment of overlayer removal on GaN, AlN, and $AlGaN$ surfaces using spectroscopic ellipsometry*, *Appl. Phys. Lett.* **69**, 2065 (1996).

[31] G. Yu, G. Wang, H. Ishikawa, M. Umeno, T. Soga, T. Egawa, J. Watanabe, and T. Jimbo, *Optical properties of wurtzite structure GaN on sapphire around fundamental absorption edge (0.78-4.77 eV) by spectroscopic ellipsometry and the optical transmission method*, *Appl. Phys. Lett.* **70**, 3209 (1997).

[32] R. Goldhahn, A. T. Winzer, V. Cimalla, O. Ambacher, C. Cobet, W. Richter, N. Esser, J. Furthmüller, F. Bechstedt, H. Luf, and W. J. Schaff, *Anisotropy of the dielectric function for wurtzite InN*, *Superlattices and Microstructures* **36**, 591 (2004).

[33] Q. Guo, M. Nishio, H. Ogawa, and A. Yoshida, *Optical properties of aluminum nitride*, *Phys. Rev. B* **55**, R15987 (1997).

[34] C. G. Olson, D. W. Lynch, and A. Zehe, *10-30-eV optical properties of GaN*, *Phys. Rev. B* **24**, 4629 (1981).

[35] G. Brockt and H. Lakner, *Probing the local dielectric:optical properties of group III-Nitrides by spatially resolved EELS on the nanometer scale*, *Materials Science and Engineering B* **59**, 155 (1999).

[36] T. Kawashima, H. Yoshikawa, and S. Adachi, *Optical properties of hexagonal GaN*, *J. Appl. Phys.* **82**, 3528 (1997).

[37] S. Logothetidis, J. Petalas, M. Cardona, and T. D. Moustakas, *Optical properties and temperature dependence of the interband transitions of cubic and hexagonal GaN*, *Phys. Rev. B* **50**, 18017 (1994).

[38] T. Wethkamp, *Optical Properties of Groupe-III-Nitrides in the Visible to Vacuu-Ultraviolet Spectral Range Investigated by Spectroscopic Ellipsometry*, PhD thesis, TU Berlin, 1999.

[39] T. Wethkamp, K. Wilmers, C. Cobet, N. Esser, W. Richter, O. Ambacher, M. Stutzmann, and M. Cardona, *Dielectric funktion of hexagonal AlN films determined by spectroscopic ellipsometry in the vacuum-uv spectral range*, *Phys. Rev. B* **59**, 1845 (1999).

[40] T. Wethkamp, K. Wilmers, N. Esser, W. Richter, O. Ambacher, H. Angerer, G. Jungk, R. L. Johnson, and M. Cardona, *Spectroscopic ellipsometry measurements of $Al_xGa_{1-x}N$ in the energy range 3-25 eV*, *Thin Solid Films* **313-314**, 745 (1998).

[41] L. X. Benedict, T. Wethkamp, K. Wilmers, C. Cobet, N. Esser, E. L. Shirley, W. Richter, and M. Cardona, *Dielectric function of wurtzite GaN and AlN thin films*, *Solid State Communications* **112**, 129 (1999).

[42] D. E. Aspnes, *The Accurate Determination of Optical Properties by Ellipsometry*, in *Handbook of Optical Constants of Solids*, edited by E. D. Palik, volume I, pages 89–112, Academic Press, Amsterdam, 1985.

[43] D. E. Aspnes, *Spectroscopic ellipsometry of solids*, in *Optical properties of solids: new developments*, edited by B. Seraphin, North-Holland Publishing Company, Amsterdam, 1975.

[44] D. Bagayoko, L. Franklin, and G. L. Zhao, *Predictions of electronic, structural, and elastic properties of cubic InN*, *J. Appl. Phys.* **96**, 4297 (2004).

[45] A. J. Fischer, W. Shan, J. J. Song, Y. C. Chang, R. Horning, and B. Goldenberg, *Temperature-dependent absorption measurements of excitons in $GaNepilayers$*, *Appl. Phys. Lett.* **71**, 1981 (1997).

[46] D. E. Aspnes, *Approximate solution of ellipsometric equations for optically biaxial crystals*, *J. Opt. Soc. Am.* **70**, 1275 (1980).

[47] D. W. Berreman, *Optics in stratified and anisotropic media: 4×4 matrix formulation*, *J. Opt. Soc. Am* **62**, 502 (1972).

[48] J. L. Birman, *Simplified LCAO Method for Zincblende, Wurtzite, and Mixed Crystal Structures*, *Phys. Rev.* **115**, 1493 (1959).

[49] W. R. L. Lambrecht, B. Segall, W. Suttrop, M. Yoganathan, P. Davaty, W. J. Choyke, J. A. Edmond, J. A. Powell, and M. Alouani, *Six-bilayer periodic structures in GaN grown on GaAs(001)*, *Appl. Phys. Lett.* **76**, 330 (2000).

[50] A. P. Lima, A. Tabata, J. R. Leite, S. Kaiser, D. Schikora, B. Schottker, T. Frey, D. J. As, and K. Lischka, *Growth of cubic InN on $InAs(001)$ by plasma-assisted molecular beam epitaxy*, *J. Cryst. Growth* **201-202**, 396 (1999).

[51] T. Suzuki, H. Yaguchi, H. Okumura, Y. Ishida, and S. Yoshida, *Optical Constants of Cubic GaN, AlN, and $AlGaN$ Alloys*, *Jpn. J. Appl. Phys. Part 2* **39**, L497 (2000).

[52] R. M. Feenstra, H. Chen, V. Ramachandran, and A. R. S. D. W. Greve, *Reconstructions of GaN and $InGaN$ surfaces*, *Appl. Surf. Sci.* **166**, 165 (2000).

[53] P. Drude, *Ueber die Gesetze der Reflexion und Brechung des Lichtes an der Grenze absorbirender Krystalle*, *Ann. Phys.* **32**, 584 (1887).

[54] P. Drude, *Bestimmung der optischen Constanten der Metalle*, *Ann. Phys.* **39**, 481 (1890).

[55] D. E. Aspnes and A. A. Studna, *High Precision Scanning Ellipsometer*, *Applied Optics* **14**, 220 (1975).

[56] H. G. Tompkins and E. A. Irene, *Handbook of Ellipsometry*, William Andrew Publishing, Norwich, 2005.

[57] J. Barth, R. L. Johnson, and M.Cardona, *Spectroscopic ellipsometry in the 6-35 eV region,* in *Handbook of Optical Constants of Solids*, edited by E. D. Palik, volume II, pages 213–246, Academic Press, Orlando, 1991.

[58] R. L. Johnson, J. Barth, M. Cardona, D. Fuchs, and A. M. Bradshaw, *Design and performance of a VUV ellipsometer, Nucl. Instr. Meth. Phys Res. A.* **290**, 606 (1990).

[59] R. M. A. Azzam and N. B.Bashara, *Ellipsometry and polarized light*, North-Holland Personal Library, Amsterdam, paperback edition, 1987.

[60] G. Stokes, *Trans. Cambridge Phil. Soc.* **9**, 399 (1852), [174].

[61] A. Röseler, *Infrared spectroscopic ellipsometry*, Akademie-Verlag, Berlin, 1990.

[62] O. Günther, *Kritische Punkte in der elektronischen dielektrischen Funktion von $GaAs$, $AlAs$, und $GaAs/AlAs$-Übergittern,* PhD thesis, TU Berlin, 1995.

[63] H. Mueller, *J. Opt. Soc. Am.* **38**, 661 (1948), [174].

[64] M. J. Walker, *Am. J. Phys.* **22 (4)**, 170 (1954), [174].

[65] C. Kunz, *Synchrotron Radiation - Techniques and Applications*, Springer-Verlag, Berlin, Heidelberg, New York, 1979.

[66] W. Gudat and C. Kunz, *Instrumentation for Spectroscopy and other Aplications,* in *Synchrotron Radiation - Techniques and Applications*, edited by C. Kunz, Springer-Verlag, Berlin, Heidelberg, New York, 1979.

[67] G. Reichardt, T. Noll, I. Packe, P. Rotter, J.-S. Schmidt, and W. Gudat, *Adaption of the BESSY I- 3m-Normal Incidence Monochromators to the BESSY II Source, NIM (A)* **467-468**, 458 (2001).

[68] M. Krumrey, E. Tegeler, J. Barth, M. Krisch, F. Schäfers, and R. Wolf, *Schottky type photodiodes as detectors in the VUV and soft x-ray range, Applied Optics* **27**, 4336 (1988).

[69] L. J. Terminello, A. B. McLean, A. Santoni, E. Spiller, and F. J. Himpsel, *Low pass filter for soft x-ray monochromators, Rev. Sci. Instrum.* **61**, 1626 (1990).

[70] D. W. Lynch and W. R. Hunter, *Comments on the Optical Constants of Metals and an Introduction to the Data for Several Metals,* in *Handbook of Optical Constants of Solids*, edited by E. D. Palik, volume I, Academic Press, 1985.

[71] V. G. Horton, E. T. Arakawa, R. N. Hamm, and M. W. Williams, *A triple reflection polarizer for use in the vacuum ultraviolet, Applied Optics* **8**, 667 (1996).

[72] F. Schäfers, H.-C. Mertins, A. Gaupp, V. Gudat, M. Mertin, I. Packe, F. Schmolla, S. D. Fonzo, G. Soullie, W. Jark, R. Walker, X. L. Cann, R. Nyholm, and M. Eriksson, *Soft-X-ray polarimeter with multilayer optics: complete analysis of the polarization state of light, Applied Optics* **38**, 4074 (1999).

[73] F. Schäfers, W. Peatman, A. Eyers, C. Heckenkamp, G. Schönhense, and U. Heinzmann, *High-flux normal incidence monochromator for circularly polarized synchrotron radiation, Rev. Sci. Instrum.* **57**, 1032 (1986).

[74] K.-J. Kim, *Characteristics of Synchrotron Radiation,* in *X-RAY DATA BOOKLET*, edited by A. C. Thompson and D. Vaughan, Lawrence Berkeley National Laboratory, second edition edition, 2001.

[75] U. Schade, 2004, BESSY GmbH, Albert-Einstein-Str.15, 12489 Berlin, Germany, priv. com.

[76] R. W. Collins and K. Vedam, *Optical properties of solids, Encycl. of Appl. Phys.* **12**, 285 (1995).

[77] R. L. Kronig, *ON THE THEORY OF DISPERSION OF X-RAYS, J. Opt. Soc. Am.* **12**, 547 (1926).

[78] P. Y. Yu and M. Cardona, *Fundamentals of Semiconductors*, Springer-Verlag, Berlin, 1996.

[79] P. Lautenschlager, P. B. Allen, and M. Cardona, *Temperature dependence of band gaps in Si and Ge, Phys. Rev. B* **31**, 2163 (1985).

[80] P. Lautenschlager, P. B. Allen, and M. Cardona, *Phonon-induced liftime brodenings of electronic states and critical points in Si and Ge, Phys. Rev. B* **33**, 5501 (1986).

[81] D. E. Aspnes, *Modulation Spectroscopy/Electric Field Effects on the Dielectric Function of Semiconductors,* in *Handbook On Semiconductors*, edited by T. S. Moss, volume II, pages 109–154, North-Holland Publishing Company, Amsterdam, 1980.

[82] L. V. Hove, *The Occurrence of Singularities in the Elastic Frequency Distribution of a Crystal, Phys. Rev.* **53**, 1189 (1953).

[83] J. R. Chelikowsky and M. L. Cohen, *Nonlocal pseudopotential calculations for the electronic structure of eleven diamond and zinc-blende semiconductors, Phys. Rev. B* **14**, 556 (1976).

[84] W. R. L. Lambrecht, B. Segall, J. Rife, W. R. Hunter, and D. K. Wickende, *UV reflectivity of GaN: Theory and experiment, Phys. Rev. B* **51**, 13516 (1995).

[85] M. Cardona and D. L. Greenaway, *Reflectivity of Gray Tin Single Crystals in the Fundamental Absorption Region, Phys. Rev.* **125**, 1291 (1962).

[86] M. Cardona and D. L. Greenaway, *Fundamental Reflectivity and Band Structure of ZnTe, CdTe, and HgTe, Phys. Rev.* **131**, 98 (1963).

[87] D. E. Aspnes, S. M. Kelso, and R. A. L. R. Bhat, *Optical properties of $Al_xGa_{1-x}As$, J. Appl. Phys.* **60**, 754 (1986).

[88] M. Cardona, *Modulation Spectroskopy*, in *Solid State Physics*, edited by F. Seitz, D. Turnbell, and H. Ehrenreich, volume 11, Academic Press, New York, 1969.

[89] Y. Toyozawa, M. Inoue, T. Inui, M. Okazaki, and E. Hanamura, *Coexistence of Local and Band Characters in the Absorption Spectra of Solids, J. Phys. Soc. Jpn.* **22**, 1337 (1967).

[90] D. E. Aspnes, C. G. Olson, and D. W. Lynch, *Electroreflectance of $GaAs$ and GaP to 27 eV using synchrotron radiation, Phys. Rev. B* **12**, 2527 (1975).

[91] W. H. Press, S. A. Teulolsky, W. T. Vetterling, and B. P. Flannery, *Numerical Recipes in C, The Art of Scintific Computing*, Cambridge University Press, New York, 2. edition, 1992.

[92] J.-T. Zettler and T. Trepk, 2003, LayTec GmbH, Helmholtzstr. 13/14, 10587 Berlin, Germany.

[93] J. M. Thijssen, *Computational Physics*, Cambridge University Press, Cambridge, 1999.

[94] N. E. Christensen and I. Gorczyca, *Optical and structural properties of III-V nitrides under pressure, Phys. Rev. B* **50**, 4397 (1994).

[95] W. R. L. Lambrecht, B. Segall, S. Strite, G. Martin, A. Agarwal, H. Morkoc, and A. Rockett, *X-ray photoelectron spectroscopy and theory of the valence band and semicore Ga 3d states in GaN, Phys. Rev. B* **50**, 14155 (1994).

[96] W. G. Schmidt, 2004, Institut für Festkörpertheorie und -optik, Friedrich-Schiller-Universität Jena, Fröbelstieg 1, 07743 Jena, Germany, priv. com.

[97] F. Bechstedt, J. Furthmüller, and J.-M. Wagner, *Electronic and vibrational properties of group-III nitrides: Ab initio studies, Phys. Stat. Sol. (c)* **0**, 1732 (2003).

[98] W. R. L. Lambrecht and M. Prikhodko, *Anisotropy of UV-reflectivity in wurtzite crystals: a comparison between GaN and $CdSe$, Solid State Communications* **121**, 549 (2002).

[99] K. Lawniczak-Jablonska, T. Suski, I. Gorczyca, N. E. Christensen, K. E. Attenkofer, R. C. C. Perera, E. M. Gullikson, J. H. Underwood, D. L. Ederer, and Z. L. Weber, *Electronic states in valence and conduction bands of group-III nitrides: Experiment and theory, Phys. Rev. B* **61**, 16623 (2000).

[100] P. Dudesek, L. Benco, C. Daul, and K. Schwarz, *d-to-s bonding in GaN, J. Phys.: Condens. Matter* **10**, 7155 (1998).

[101] Y.-N. Xu and W. Y. Ching, *Electronic, optical, and structural properties of some wurtzite crystals, Phys. Rev. B* **48**, 4335 (1993).

[102] D. E. Aspnes, J. B. Theeten, and F. Hottier, *Investigation of effektive-medium models of surface roughness by spectroscopic ellipsometry, Phys. Rev. B* **20**, 3292 (1979).

[103] D. A. G. Bruggeman, *Berechnung verschiedener physikalischer Konstanten von heterogenen Substanzen, Ann. Phys. (Leipzig)* **24**, 636 (1935).

[104] H. G. Tompkins, *A User's Guide to Ellipsometry*, Academic Press, San Diego, 1993.

[105] D. E. Aspnes, *Studies of surface, thin film and interface properties by automatic spectroscopic ellipsometry*, *J. Vac. Scl. Technol.* **18**, 289 (1980).

[106] N. V. Edwards, K. Jarrendahl, D. E. Aspnes, K. Robbie, G. D. Powell, C. Cobet, N. Esser, W. Richter, and L. D. Madsen, *Real-time assessment of selected surface preparation regimens for 4H-SiC surfaces using spectroscopic ellipsometry*, *Surface Science* **464**, 703 (2000).

[107] C. Cobet, *Die dielektrische Funktion verschiedener SiC-Modifikationen im Spektralbereich von 1,5 - 30 eV*, Diplomarbeit, Inst. f. Festkörperphysik, TU Berlin, 1999.

[108] B. Harbecke, B. Heinz, V. Offermann, and W. Theiß, *Far-Infrared Spectroscopy*, in *Optical Characterization of Epitaxial Semiconductor Layers*, edited by G. Bauer and W. Richter, pages 68–128, Springer-Verlag, 1996.

[109] D. W. Berreman and T. J. Scheffer, *Bragg reflection of light from single-domain cholesteric liquid-crystal films*, *Phys. Rev. Lett.* **25**, 577 (1970).

[110] H. Wöhler, G. Haas, M. Fritsch, and D. A. Mlynski, *Faster 4×4 matrix method for uniaxial inhomogeneous media*, *J. Opt. Soc. Am A* **5**, 1554 (1988).

[111] M. Schubert, *Polarization-dependent optical parameters of arbitrarily anisotropic homogenous layered systems*, *Phys. Rev. B* **53**, 4265 (1996).

[112] A. Röseler, *Problem of polarization degree in spectroscopic photometric ellipsometry (polarimetry)*, *J. Opt. Soc. Am. A* **9**, 1124 (1992).

[113] K. Hingerl, D. E. Aspnes, I. Kamiya, and L. T. Florez, *Relationship among reflectance-difference spectroscopy, surface photoabsorption, and spectroellipsometry*, *Appl. Phys. Lett.* **63**, 885 (1993).

[114] S. Logothetidis, M. Cardona, P. Lautenschlager, and M. Garriga, *Temperature dependence of the dielectric function and the interband critical points of $CdSe$*, *Phys. Rev. B* **34**, 2458 (1986).

[115] C. Cobet, T. Schmidtling, M. Drago, N. Wollschläger, N. Esser, W. Richter, R. M. Feenstra, and T. U. Kampen, *Surface termination during GaN growth by metalorganic vapor phase epitaxy determined by ellipsometry*, *J. Appl. Phys.* **94**, 6997 (2003).

[116] C. Cobet, T. Schmidtling, M. Drago, N. Wollschläger, N. Esser, W. Richter, and R. M. F. and, *In-situ ellipsometry: Identification of surface terminations during GaN growth*, *Phys. Stat. Sol. (c)* **0**, 2938 (2003).

[117] J. T. Wolan, C. K. Mount, and G. B. Hoflunda), *Chemical reactions induced by the room temperature interaction of hyperthermal atomic hydrogen with the native oxide layer on $GaAs(001)$ surfaces studied by ion scattering spectroscopy and x-ray photoelectron spectroscopy*, *J. Vac. Sci. Technol. A* **15**, 2502 (1997).

[118] V. K. Gupta, C. C. Wamsley, M. W. Koch, and G. W. Wicksb, *Native oxides and regrowth on III-N surfaces*, *J. Vac. Sci. Technol. B* **17**, 1249 (1999).

[119] K. Prabhakaran, T. G. Andersson, and K. Nozawa, *Nature of native oxide on GaN surface and its reaction with Al, Appl. Phys. Lett.* **18**, 3212 (1996).

[120] M. Eickhoff, R. Neuberger, G. Steinhoff, O. Ambacher, G. Müller, and M. Stutzmann, *Wetting behaviour of GaN surfaces with Ga- or N-face polarity, Phys. Stat. Sol. (b)* **228**, 519 (2001).

[121] S. A. Ding, S. R. Barman, K. Horn, and V. L. Alperovich, *Electronic structure of wurtzite $GaN(0001)$,* in *23rd International Conference on the Physics of Semiconductors*, edited by M. Scheffler and R. Zimmermann, volume 1, pages 525–528, World Scientific, 1996.

[122] E. A. Chowdhury, J. Kolodzey, J. O. Olowolafe, G. Qiu, G. Katulka, D. Hits, M. Dashiell, D. van der Weide, C. P. Swann, and K. M. Unruh, *Thermally oxidized AlN thin films for device insulators, Appl. Phys. Lett.* **70**, 2732 (1997).

[123] M. Drago and T. Schmidling, 2004, Inst. f. Festkörperphysik, Technische Universität Berlin, Hardenbergstraße 36, 10623 Berlin, Germany, priv. com.

[124] S. Peters, 2004, SENTECH Instruments GmbH, Carl-Scheele-Straße 16, 12489 Berlin Germany, priv. com.

[125] T. Schenk, *Investigation of III-nitride surfaces by Spectroscopic Ellipsometry*, diploma thesis, TU Berlin, 2004.

[126] C. Cobet, N. Esser, J. T. Zettler, W. Richter, P.Waltereit, O. Brandt, K. H. Ploog, S. Peters, N. V. Edwards, O. P. A. Lindquist, and M. Cardona, *Optical properties of wurtzite $Al_xGa_{1-x}N$ ($x< 0.1$) parallel and perpendicular to the c axis, Phys. Rev. B* **64**, 165203 (2001).

[127] P. Waltereit, O. Brandt, M. Ramsteiner, R. Uecker, P. Reiche, and K. H. Ploog, *Growth of M-plane GaN($1\bar{1}00$) on γ-LiAlO$_2$(100), J. Cryst. Growth* **218**, 143 (2000).

[128] P. Waltereit, O. Brandt, M. Ramsteiner, R. Uecker, P. Reiche, and K. H. Ploog, *Growth of M-Plane GaN($1\bar{1}00$): A Way to Evade Electrical Polarization in Nitrides, Phys. Stat. Sol. (a)* **180**, 133 (2000).

[129] C. Cobet, K. Wilmers, T. Wethkamp, N. V. Edwards, N. Esser, and W. Richter, *Optical properties of SiC investigated by spectroscopic ellipsometry from 3.5 to 10 eV, Thin Solid Films* **364**, 111 (2000).

[130] K. Schmidegg, 2004, Institut für Halbleiter- und Festkörperphysik, Johannes Kepler Universität, Altenbergerstr. 69, 4040 Linz, Austria, priv. com.

[131] S. Li and K. Lischka, 2004, Department of Physics, Universität Paderborn, Warburger Straße 100, 33098 Paderborn, Germany, priv. com.

[132] D. J. As, D. Schikora, and K. Lischka, *Molecular beam epitaxy of cubic III-nitrides on $GaAs$ substrates, Phys. Stat. Sol. (c)* **0**, 1607 (2003).

[133] X. L. Suna, Y. T. Wang, H. Yang, J. B. Li, L. X. Zheng, D. P. Xu, and Z. G. Wang, *The content calculation of hexagonal phase inclusions in cubic GaN films on $GaAs(001)$ substrates grown by metalorganic chemical vapor deposition*, *Thin Solid Films* **368**, 237 (2000).

[134] M. Cardona and G. Harbeke, *Optical properties and band structure of wurtzite-type crystals and rutile*, *Phys. Rev.* **137**, A1467 (1964).

[135] O. Zakharov, A. Rubio, X. Blase, M. L. Cohen, and S. G. Louie, *Quasiparticle band structures of six II-VI compounds: ZnS, $ZnSe$, $ZnTe$, CdS, $CdSe$, and $CdTe$*, *Phys. Rev. B* **50**, 10780 (1994).

[136] M. Cardona, *Infrared Dielectric Constant and Ultraviolet Optical Properties of Solids with Diamond, Zinc Blende, Wurtzite, and Rocksalt Structure*, *J. Appl. Phys.* **36**, 2181 (1965).

[137] M. Cardona, *Polarizatin effects in the ultraviolet reflection of crystals with wurtzite structure*, *Solid State Communications* **1**, 109 (1963).

[138] M. Cardona and G. Harbeke, *Optical Properties and Band Structure of Wurtzite-Type Crystals and Rutile*, *Phys. Rev.* **137**, A1467 (1965).

[139] T. K. Bergstresser and M. L. Cohen, *Electronic Structure and Optical Properties of Hexagonal $CdSe$, CdS, and ZnS*, *Phys. Rev.* **164**, 1069 (1967).

[140] M. Cardona and N. E. Christensen, *Spin-orbit splittings in AlN, GaN and InN*, *Solid State Communications* **116**, 421 (2000).

[141] W. R. L. Lambrecht and S. N. Rashkeev, *From Band Structures to Linear and Nonlinear Optical Spectra in Semiconductors*, *Phys. Stat. Sol. (b)* **217**, 599 (2000).

[142] D. Rönnow, L. F. Lastras-Martinez, and M. Cardona, *Isotope effects on the electronic critical points of germanium: Ellipsometric investigation of the E_1 and $E_1 + \Delta_1$ transitions*, *Eur. Phys. J. B* **5**, 29 (1998).

[143] C. Janowitz, M. Cardona, R. L. Johnson, T. Cheng, T. Foxon, O. Günther, and G. Junk, *Dielectric function of cubic GaN*, *BESSY Jahresbericht* , 230 (1994).

[144] S. Ghosh, P. Waltereit, O. Brandt, H. T. Grahn, and K. H. Ploog, *Polarization-dependent spectroscopic study of M-plane GaN on $\gamma - LiAlO_2$*, *Appl. Phys. Lett.* **80**, 413 (2002).

[145] M. Drago, T. Schmidtling, U. Pohl, S. Peters, and W. Richter, *InN metalorganic vapour phase epitaxy and ellipsometric characterisation*, *Phys. Stat. Sol. (c)* **0**, 2842 (2003).

[146] K. A. Mkhoyan, J. Silcox, E. S. Alldredge, N. W. Ashcroft, H. Lu, W. J. Schaff, and L. F. Eastman, *Measuring electronic structure of wurtzite InN using electron energy loss spectroscopy*, *Appl. Phys. Lett.* **82**, 1407 (2003).

[147] H. Lu, W. J. Schaff, L. F. Eastman, J. Wu, W. Walukiewicz, V. Cimalla, and O. Ambacher, *Growth of a-plane InN on r-plane sapphire with a GaN buffer by molecular-beam epitaxy*, *Appl. Phys. Lett.* **83**, 1136 (2003).

[148] V. Y. Davydov, V. V. Emtsev, I. N. Goncharuk, A. N. Smirnov, V. D. Petrikov, V. V. Mamutin, V. A. Vekshin, S. V. Ivanov, M. B. Smirnov, and T. Inushima, *Experimental and theoretical studies of phonons in hexagonal InN*, *Appl. Phys. Lett.* **75**, 3297 (1999).

[149] C. Yeh, Z. W. Lu, S. Froyen, and A. Zunger, *Zinc-blende-wurtzite polytypism in semiconductors*, *Phys. Rev. B* **46**, 10086 (1992).

[150] A. Garcia and M. L. Cohen, *First-principles ionicity scales. I. Charge asymmetry in the solid state*, *Phys. Rev. B* **47**, 4215 (1993).

[151] C. Persson, R. Ahuja, A. F. da Silva, and B. Johansson, *First-principle calculations of the dielectric function of zinc-blende and wurtzite InN*, *J. Phys.: Condens. Matter* **13**, 8945 (2001).

[152] D. Fritsch, H. Schmidt, and M. Grundmann, *Band dispersion relations of zinc-blende and wurtzite InN*, *Phys. Rev. B* **69**, 165204 (2004).

[153] V. Cimalla, V. Lebedev, U. Kaiser, R. Goldhahn, C. Foerster, J. Pezoldt, and O. Ambacher, *Polytype control and properties of AlN on silicon*, *Phys. Stat. Sol. (c)* **2**, 2199 (2005).

[154] A. Rubio, J. L. Corkill, M. L. Cohen, E. L. Shirley, and S. G. Louie, *Quasiparticle band structure of AlN and GAN*, *Phys. Rev. B* **48**, 11810 (1993).

[155] T. Koizumi, H. Okumura, K. Balakrishnan, H. Harima, T. Inoue, Y. Ishida, T. Nagatomo, S. Nakashima, and S. Yoshida, *Growth of M-plane GaN($1\bar{1}00$) on γ-LiAlO$_2$(100)*, *J. Cryst. Growth* **201/202**, 341 (1999).

[156] A. Nakadaira and H. Tanaka, *Metalorganic Vapor-Phase Epitaxial Growth and Characterization of Cubic $Al_xGa_{1-x}N$ Alloy*, *Jpn. J. Appl. Phys.* **37**, 1449 (1997).

[157] R. Goldhahn, C. Buchheim, V. Lebedev, V. Cimalla, O. Ambacher, C. Cobet, M. Rakel, N. Esser, U. Rossow, D. Fuhrmann, A. Hangleiter, S. Potthast, and D. As, *Dielectric function and critical points of the band structure for hexagonal and cubic GaN and AlN*, *BESSY Jahresbericht* (2004).

[158] Y. Danylyuk, S. Perooly, M. Rahman, and G. Auner, *Growth of a-plane AlN on r-plane sapphire by plasma source molecular beam epitaxy*, *Phys. Stat. Sol. (c)* **2**, 2228 (2005).

[159] V. Fiorentini, M. Methfessel, and M. Scheffler, *Electronic and structural properties of GaN by the full-potential linear muffin-tin orbitals method: The role of the d electrons*, *Phys. Rev. B* **47**, 13353 (1993).

[160] S. A. Ding, G. Neuhold, J. H. Weaver, P. Häerle, K. Horn, O. Brandt, H. Yang, and K. Ploog, *Electronic structure of cubic gallium nitride films grown on $GaAs$*, *J. Vac. Sci. Technol. A* **14**, 819 (1996).

[161] D. E. Aspnes, C. G. Olson, and D. W. Lynch, *Ordering and Absolute Energies of the L_6^c and X_6^c Conduction Band Minima in $GaAs$*, *Phys. Rev. Lett.* **37**, 766 (1976).

[162] M. Cardona, W. Gudat, E. E. Koch, M. Skibowski, B. Sonntag, and P. Y. Yu, *Core Transitions and Density of Conduction States in the III-V Semiconductors*, *Phys. Rev. Lett.* **25**, 659 (1970).

[163] P. Vogt, K. Lüdge, M. Zorn, M. Pristovsek, W. Braun, W. Richter, and N. Esser, *Surface structure of ordered $InGaP(001)$: The (2×4) reconstruction*, *Phys. Rev. B* **62**, 12601 (2000).

[164] O. Günther, C. Janowitz, G. Jungk, B. Jenichen, R. Hey, L. Däweritz, , and K. Ploog, *Comparison between the electronic dielectric functions of a $GaAs/AlAs$ superlattice and its bulk components by spectroscopic ellipsometry using core levels*, *Phys. Rev. B* **52**, 2599 (1995).

[165] P. V. et. al., 2005, Inst. f. Festkörperphysik, Technische Universität Berlin, Hardenbergstraße 36, 10623 Berlin, Germany, priv. com.

[166] M. Henzel and W. Göpel, *Oberflächenphysik des Festkörpers*, B.G. Teubner, Stuttgart, 2. edition, 1991.

[167] T. Sakurai and Y. Watanabe, *Advances in Scanning Probe Microscopy*, Springer-Verlag, Berlin, Heidelberg, New York, 2000.

[168] L. Reimer, *Scanning Electron Microscopy - Physics of Image Formation and Microanalysis*, Springer-Verlag, Berlin, Heidelberg, New York, 2. edition, 1998.

[169] A. Krost, G. Bauer, and J. Woitok, *High Resolution X-Ray Diffraction*, in *Optical Characterization of Epitaxial Semiconductor Layers*, edited by G. Bauer and W. Richter, pages 287–391, Springer-Verlag, Berlin, 1996.

[170] M. A. Herman, W. Richter, and H. Sitter, *Epitaxy*, Springer-Verlag, Berlin, Heidelberg, New York, 2004.

[171] O. Briot, *MOVPE growth of nitrides*, in *Group III Nitride Semiconductor Compounds*, edited by B. Gil, pages 19–69, Oxford University Press, New York, 1998.

[172] G. Popovici, H. Morkok, and S. N. Mohammed, *Deposition and properties of group III nitrides by molecular beam epitaxy*, in *Group III Nitride Semiconductor Compounds*, edited by B. Gil, pages 19–69, Oxford University Press, New York, 1998.

[173] N. Esser and J. Geurts, *Raman Spectroscopy*, in *Optical Characterization of Epitaxial Semiconductor Layers*, edited by G. Bauer and W. Richter, pages 129–202, Springer-Verlag, Berlin, 1996.

[174] D. Fuchs, *Spektroskopische Ellipsometrie im Vakuum-Ultraviolett-Spektralbereich*, PhD thesis, TU Berlin, 1990.

Nomenclature

Abbreviations

AES	Auger Electron Spectroscopy , page 139
AFM	Atomic Force Microscopy , page 139
ASA	Atomic Sphere Approximation
BESSY	Berliner Elektronenspeicherring-Gesellschaft für Synchrotronstrahlung
CP	Critical Point , page 33
DF	Dielectric Function
DFT	Density Functional Teory , page 38
DOS	Density Of States
EELS	Electron Energy Loss Spectroscopy
EMA	Effective Medium Approximation
FWHM	Full Width Half Maximum
JDOS	Joint Density Of States , page 33
LDA	Local Density Approximation , page 38
LEED	Low Energy Electron Diffraction , page 139
LMTO	Linear Muffin Tin Orbital
MBE	Molecular Beam Epitaxy , page 139
ML	MonoLayer
MOVPE	Metalorganic Vapour Phase Epitaxy , page 139
PAMBE	Plasma-Assisted Molecular Beam Epitaxy
PDOS	Partial Density Of States
PL	Photo Luminescence
REA	Rotating Analyser Ellipsometer
RMS	Root Mean Square

SEM	Scanning Electron Microscopy , page 139
UHV	Ultra High Vacuum
UV	Ultra Violet
VUV	Vacuum Ultra Violet
XPS	X-ray Photoelectron Spectroscopy
XRD	X-Ray Diffraction , page 139

Symbols

$\alpha(t)$	analyser angle, page 12
$\bar{\varepsilon}$	dielectric tensor (of a wurtzite crystal), page 53
$\bar{E}$	macroscopic electric field strength, page 29
$\bar{S}$	Stokes vector, page 15
χ	polariser angle, page 12
χ_e	electric susceptibility, page 29
$\Delta \equiv \arg(\rho)$	ellipsometric angle (phase), page 13
Δ_A	parameter of a non ideal analyser, page 16
δ_p, δ_s	phase shift of r_p, r_s, page 13
Γ	broadening parameter for optical transitions, page 33
$\hat{M}_A$	Mueller matrix of a rotating analyser, page 16
$\hat{M}_R$	Mueller matrix for a coordinate transformation , page 15
$\hat{M}_S$	Mueller matrix of the sample, page 16
κ	extinction coefficient, page 30
$\langle\varepsilon\rangle$	pseudodielectric (effective dielectric) function, page 14
μ_0	free space permeability, page 29
μ_{cv}	reduced effective mass, page 35
ω	angular frequency, page 30
ω_0	$m_e\omega_0^2 \equiv$ Hook's law restoring force, page 31
ω_p	plasma frequency, page 31
ϕ	angle of incidence, page 13

ϕ_{refr}	angle of refraction, page 13
$\psi \equiv \arctan \mid \rho \mid$	ellipsometric angle (amplitude), page 13
ψ_A	$\cos 2\psi_A \equiv$ degree of polarisation (analyser), page 16
ψ_P	$\cos 2\psi_P \equiv$ degree of polarisation (polariser), page 16
ρ	ellipsometric ratio r_p/r_s, page 13
σ	optical conductivity, page 29
$\tilde{n}$	(real) index of refraction, page 30
$\tilde{P}$	degree of polarisation, page 16
ε	dielectric function, page 29
ε_0	free space permittivity, page 29
$\varepsilon_\perp$	dielectric tensor components perpendicular to the c-axis (ordinary dielectric function), page 53
$\varepsilon_\parallel$	dielectric tensor component parallel to the c-axis (extraordinary dielectric function), page 53
φ_E	phase factor for a CP transition, page 35
$\vec{B}$	magnetic induction density, page 29
$\vec{D}$	dielectric displacement density, page 29
$\vec{H}$	magnetic field strength, page 29
$\vec{J}$	current density, page 29
A	amplitude of a CP transition, page 35
c	phase velocity of light in vacuum, page 30
C_2, S_2	Fourier coefficient, page 12
c_2, s_2	normalised Fourier coefficient (α_0, η-corrected), page 12
E	(photon) energy, page 30
E_{cv}	energy of a CP transition, page 33
$E_{ip/s}$	electric field components parallel/perpendicular to the plane of incidence of the light shining on the sample, page 13
$E_{rp/s}$	electric field components parallel/perpendicular to the plane of incidence after reflection on the sample, page 13
f_i	oscillator strength, page 31

$I(\alpha(t))$	intensity at the detector, page 12
I_0	average intensity at the detector, page 12
m_e	electron mass, page 31
n	complex refractive index, page 30
n_0	ambient complex refractive index, page 13
N_e	total number of electrons per unit volume, page 31
N_{eff}	effective number of electrons contributing to the optical properties, page 32
$r_{p/s}$	complex reflection coefficients parallel and perpendicular to the plane of incidence, page 13
$S_{0,1,2,3}$	Stokes parameter, page 15
v	phase velocity of light in a dielectric medium, page 30

List of Figures

List of Tables

Acknowledgement

Finally I want to express my thanks to all, who support and help me in this work. In particular I want to thank:

Prof. Wolfgang Richter and Priv. Doz. Dr. Norbert Esser for the opportunity to work in this project, as well as for the permanent interest, support, and a lot of helpful comments,

Prof. Mario Dähne for his interest on my results and the kindly support in the final period of this work,

Dr. Rüdiger Goldhahn for supplying several nitride samples and for instructive discussions in common beamtimes at BESSY,

Katrin Wilmers and Dr. Thorsten Wethkamp for the introduction concerning VUV-ellipsometry,

Munise Rakel for the collaboration and help in many beamtimes at BESSY,

Nils Wollschläger for his work in connection with the experiments on GaN surfaces,

Karsten Fleischer, who answers and suffers thousand of questions about computer problems, but also for exciting discussions and common experiments in surface physics,

Torsten Schmidtling and his permanent interest for the results, for many versatile assistance in case of experimental problems, as well as for the successful common experiments on GaN surfaces,

Massimo Drago, for supplying well defined MOVPE grown InN samples and common discussions about the mysteries of InN films/surfaces,

Werner Kaczmarek and all other members of the workshop, as well as Engelbert Eder for their prompt and committed support in case of technical or electronic problems,

all other members of the group of Prof. Richter for the motivating atmosphere, as well as for the pleasant and successful cooperation during the last year,

BESSY for various technical and scientific support during the beamtimes,

and, especially, my family for their continuous support and encouragements.

This work was supported by the BMBF (Bundesministerium für Bildung und Forschung) under 05 SE8KTA/3 and 05 KS4KTB/3.